The Dissertation Committee for Christopher Martin Bates Certifies that this is the approved version of the following dissertation:

Advanced Materials for Block Copolymer Lithography

Committee:

C. Grant Willson, Supervisor

Christopher W. Bielawski

Eric V. Anslyn

Hung-Wen Liu

Christopher J. Ellison

Advanced Materials for Block Copolymer Lithography

by

Christopher Martin Bates, B.S.

Dissertation

Presented to the Faculty of the Graduate School of

The University of Texas at Austin

in Partial Fulfillment

of the Requirements

for the Degree of

Doctor of Philosophy

The University of Texas at Austin

May 2013

Dedication

Dedicated to my parents.

Acknowledgements

I would specifically like to thank Professor Grant Willson for being the greatest advisor one could ask for. Many very talented graduate and undergraduate students that I have worked with over the last five years deserve recognition for their hard work. This project would not be where it is today without them. Special accolades go to Kathleen Sparks and Donna Martin – they have made my life so much easier during my time spent here at UT.

Advanced Materials for Block Copolymer Lithography

Christopher Martin Bates, Ph.D.

The University of Texas at Austin, 2013

Supervisor: C. Grant Willson

The multi-billion dollar per year lithography industry relies on the fusion of chemistry, materials science, and engineering to produce technological innovations that enable continual improvements in the speed and storage density of microelectronic devices. A critical prerequisite to improving the computers of today relies on the ability to economically and controllably form thin film structures with dimensions on the order of tens of nanometers. One class of materials that potentially meets these requirements is block copolymers since they can self-assemble into structures with characteristic dimensions circa three to hundreds of nanometers. The different aspects of the block copolymer lithographic process are the subject of this dissertation.

A variety of interrelated material requirements virtually necessitate the synthesis of block copolymers specifically designed for lithographic applications. Key properties for the ideal block copolymer include etch resistance to facilitate thin film processing, a large interaction parameter to enable the formation of high resolution structures, and thin film orientation control. The unifying theme for the materials synthesized herein is the presence of silicon in one block, which imparts oxygen etch resistance to just that domain. A collection of silicon-containing block copolymers was synthesized and characterized, many of which readily form features on approximately the length scale required for next-generation microelectronic devices.

The most important thin film processing step biases the orientation of block copolymer domains perpendicular to the substrate by control of interfacial interactions. Both solvent and thermal annealing techniques were extensively studied to achieve orientation control. Ultimately, a dual top and bottom surface functionalization strategy was developed that utilizes a new class of "top coats" and cross-linkable substrate surface treatments. Perpendicular block copolymer features can now be produced quickly with a process amenable to existing manufacturing technology, which was previously impossible. The development of etching recipes and pattern transfer processes confirmed the through-film nature of the features and the efficacy of both the block copolymer design and the top coat process.

Table of Contents

List of Tables

List of Figures

Chapter 1: History of Magnetic Media

1.1 Magnetic Recording

Technological innovations that have forever impacted modern life can often be difficult to precisely pinpoint in time. The scientific revolution nucleated the growth of modern scientific understanding, from the atomistic origins of matter to the universal motion of planets. Various agricultural revolutions throughout history have changed the availability of food for the masses. The industrial revolution led to the development of machines that enabled productivity that far surpassed anyone's (then) wildest dreams. These examples exemplify achievements of past centuries, but the 20th century has also seen myriad innovations. The development of commercial airlines and automobiles has redefined travel. Quantum mechanics transformed our understanding of the fundamental behavior of molecules. But perhaps the most impactful invention on our everyday lives has been the development of the computer, predicated by the integrated circuit. It is difficult to imagine a day removed from computers, the internet, and smart phones. Virtually all utilities we utilize daily run on computers and the number will certainly increase as "the cloud" centralizes control of our digital endeavors. However, one component encapsulated in the broad definition of "computers" likely goes underappreciated: magnetic data storage. Virtually all data is encoded merely as binary information, 1s and 0s. Historically this technology has been predicated on magneticial storage (although new technologies such as "flash" memory are gaining prevalence), which enabled the rapid growth of the computer industry. The vital role of magnetic storage is captured by a quote from Emerson Pugh, the Director of Technical Planning at IBM circa 1968 (1):

"The two most important technologies to be invented and developed during the second half of the 20th Century are magnetic disk storage and integrated circuits."
-Emerson Pugh, Director of Technical Planning at IBM ca. 1968

The history of magnetically encoding information can be traced back to Oberlin Smith, who conceived of the idea in 1878 but failed to produce a working device. Twenty years later, Valdemar Poulson demonstrated the Telegraphone (**Figure 1.1**) (*2*), which encoded sound waves on a steel wire and could replay them, albeit with significant static (*3*). **Figure 1.1** is reproduced with permission under the Creative Commons Attribution-Share Alike 2.5 generic license. His patent, if it were applicable today, would cover all magnetic storage technology. Poulson's device truly started a revolution, but like many technologies, magnetic recording took time to mature.

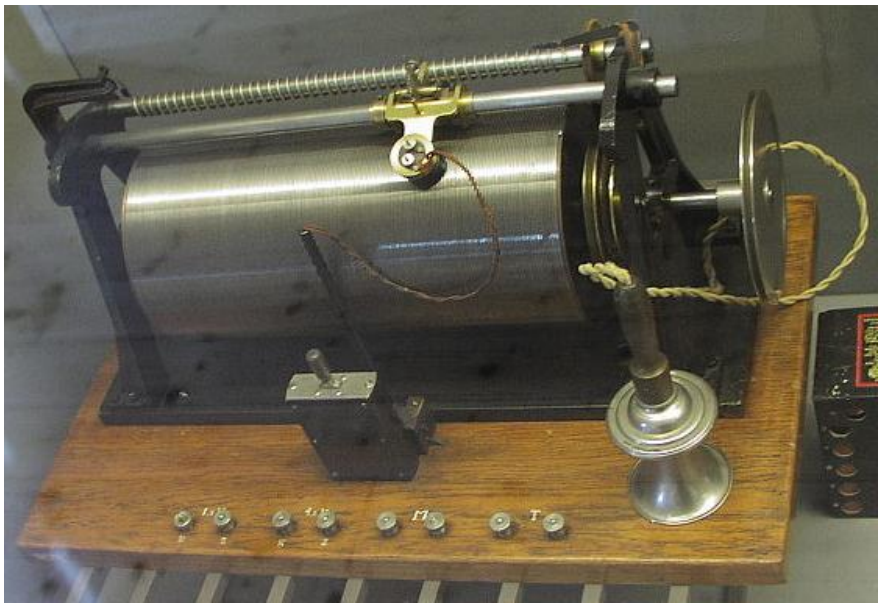

Figure 1.1: Picture of Valdemar Poulson's Telegraphone (1898), the first magnetic wire recorder.

Various improvements to Poulson's device were developed, including amplifiers to improve the playback volume and tape-based storage media. However, arguably the next ground-breaking development occurred with the introduction of the IBM Random Access Method of Accounting and Control (RAMAC) (*3*) file disk in 1956 (**Figure 1.2A**) (*4*). A moving hard disk head was incorporated in conjunction with a rotating magnetic platter. This enabled fast "random" access to any desired piece of information

on demand, on the order of milliseconds, in contrast to the relatively slow magnetic wire or tape which had to be wound or rotated to the correct position for data retrieval.

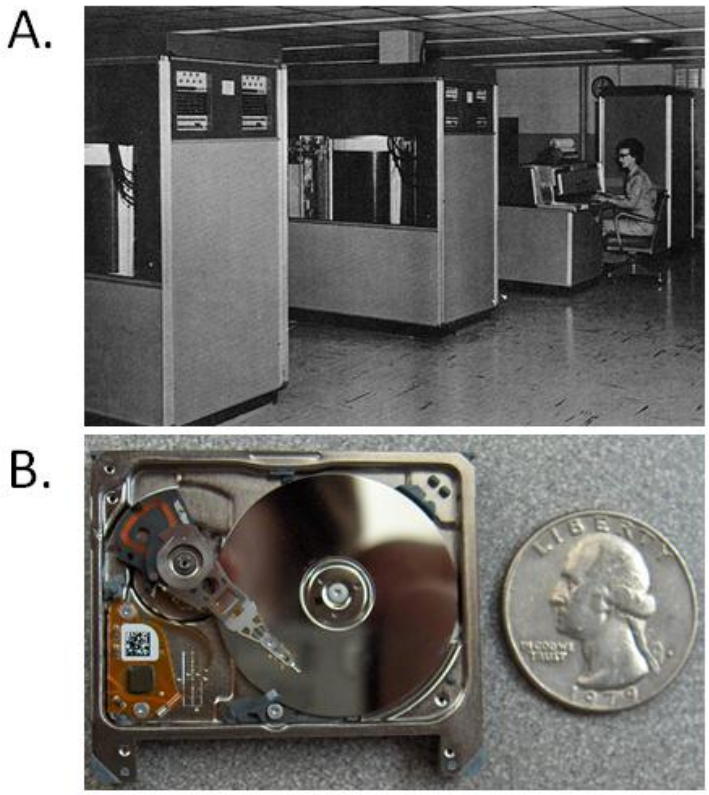

Figure 1.2: **A)** IBMs 5 megabyte RAMAC disk drive weighed more than 1 ton (1956). **B)** A 1" Seagate hard disk drive with 5 GB capacity about the size of a quarter (2006). Both images are public domain.

A comparison of the RAMAC to today's hard disk drives exemplifies the trends in miniaturization observed within the past ~60 years. The RAMAC weighed over a ton, contained more than 50 platters, had an areal density of 2 Kbits/in^2 (*5*), and cost $650 in 1956 (the equivalent of $5150 in 2010). Today, mass-produced 1" commercial disk drives with many gigabits of storage capacities (**Figure 1.2B**) (*6*) can be purchased for around $100. The massive increase in density and decrease in size of hard disk drives are

captured qualitatively in **Figure 1.3** (*7*). Ever-increasing demand drives innovation in technologies that enable increases in disk drive areal densities.

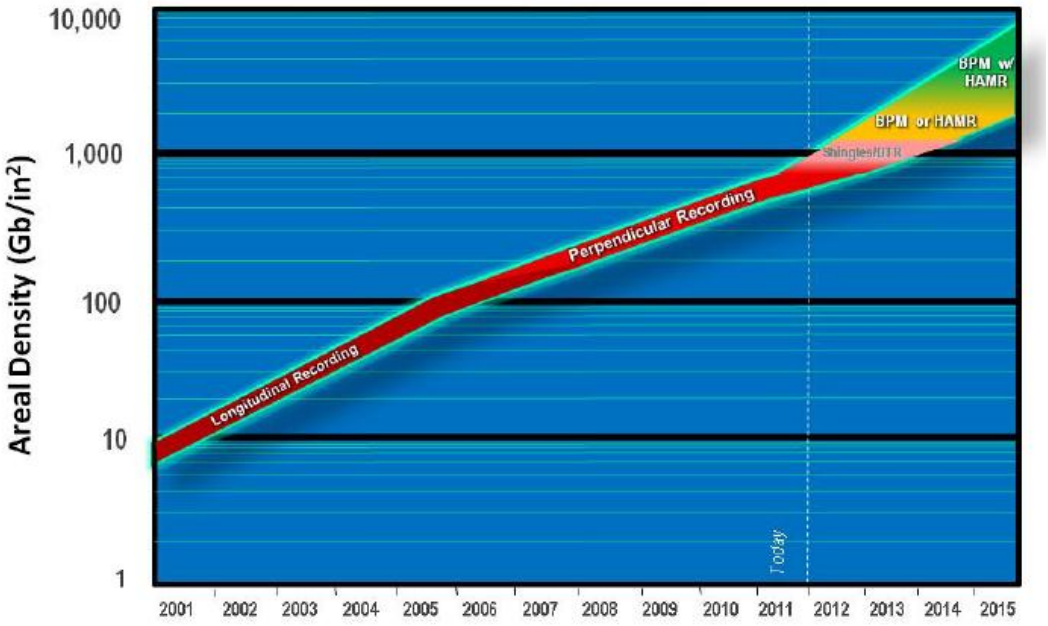

Figure 1.3: Recent trends in hard disk drive manufacturing. Reprinted with permission from Ye, Z. et al., S. V. Proc. SPIE 2012, 8323, 1. Copyright 2012 SPIE.

Current (the year 2013) high density magnetic disk drive platters are based on "conventional multigrain media" (CMM) technology (**Figure 1.4**) (*8*). Thin films (ca. 10 nm) of metallic alloys are either grown or deposited on the platter (*9*), resulting in the random placement of metallic crystalline grains. Alloys typically include ferromagnetic cobalt for its high coercivity properties, although other metals are under investigation (*10*). The disk drive head is then mechanically programmed to separate the circular platter into individually addressable regions. Data tracks run around the circumference of the disk at a constant radius. Each data track is further separated into individual bit cells. Small chunks of the magnetic material are thus arbitrarily grouped together and are referred to as bits. Each bit represents one piece of binary information (a 1 or a 0), yet contains on the order of 100 magnetic grains (*11*). A high resolution transmission

electron microscopy (TEM) image of the crystalline grains of a CoCrPt-TiO_2 alloy is shown in **Figure 1.5** (*12*). Each grain is on the order of 10 nm in diameter. In operation, the disk is rotated at about 7200 rpm, and the head can independently move to address individual bits of information. This is no small feat. The relative speed between the head and the disk is ≥10 m/s with a separation distance of only ~25 nm. A good analogy is a 747 jet flying just a few inches off of the ground without a single collision (*10*), which would catastrophically and irreversibly destroy the plane and all of its passengers, equivalent to the disk drive and all of its data. It is a remarkable technology, but unfortunately CMM has almost reached the maximum density achievable, approximately 1 Tbit/in^2.

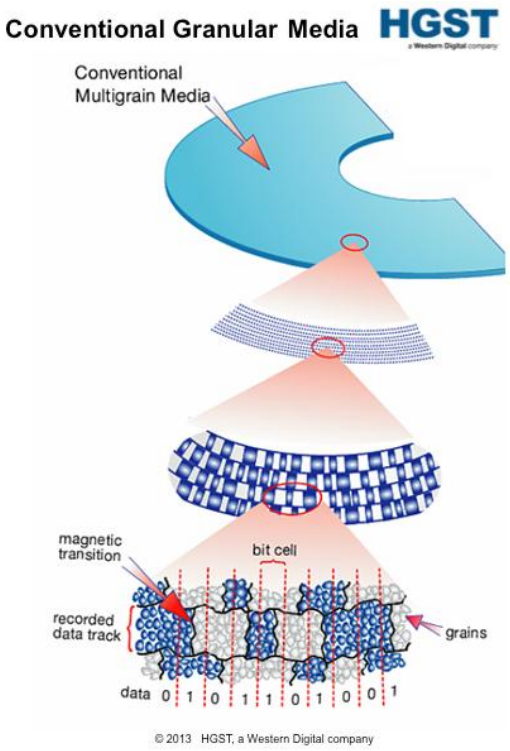

Figure 1.4: Schematic representation of conventional multigrain media magnetic platters utilized in current high density disk drives. Reused with permission from Hitachi Global Storage Technologies. Copyright 2013, HGST, a Western Digital Company.

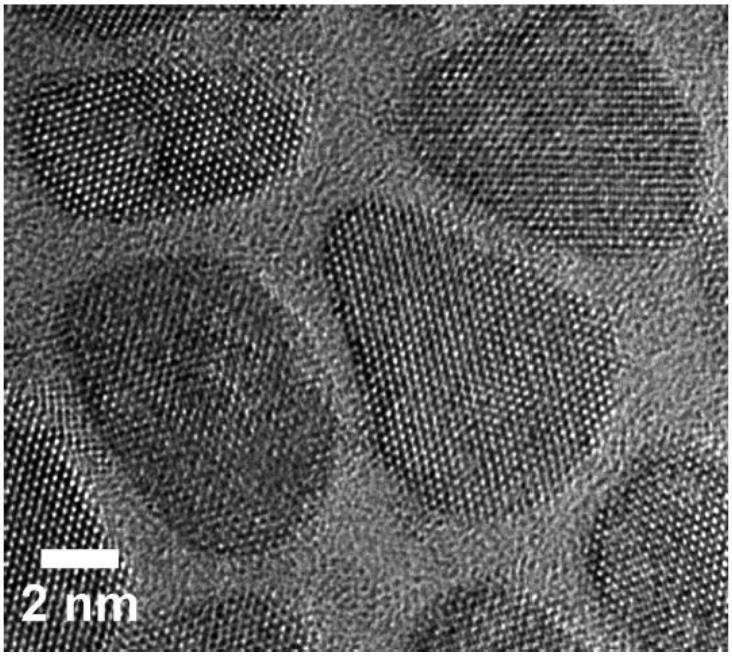

Figure 1.5: Aberration corrected high resolution transmission electron microscope image of a CoCrPt-TiO_2 magnetic alloy used in conventional multigrain media. Different crystalline grains (ca. 6-10 nm in diameter) can be observed contained within oblong oval shapes separated by an intergranular phase. Reprinted with permission from Hossein-Babaei et al., Nano Letters 2012. Copyright 2012 American Chemical Society.

The underlying cause for the CMM density limitations relates to a phenomenon called the superparamagnetic limit. The meaning of this limitation requires a brief description of terms related to magnetism (*5*). Ferromagnetic materials have molecular or atomic magnetic dipole moments that are strongly coupled to each other and pointing in the same general direction. The sum of these dipoles produces a macroscopic magnetic dipole moment that results in magnetic properties. These materials, such as alloys containing cobalt, are used as the magnetic layers in disk drives. In contrast, paramagnetic materials have molecular or atomic magnetic dipole moments that are only weakly coupled to each other. Thermal energy alone is enough to randomly align them

such that there is no permanent macroscopic magnetic dipole moment. Paramagnets can have their magnetic moments aligned in the presence of an applied field, but when the field is removed the dipole moments relax back to a random orientation. Ferromagnetic materials can be transformed into paramagnetic materials by heating to above their Curie temperature. This represents a problem for the ferromagnetic materials used in magnetic disk drives due to the superparamagnetic equation (**Equation 1.1**).

$$K_u V > c k_B T \qquad \textbf{Eq. 1.1}$$

K_u represents the anisotropy energy density (units: energy/volume), V is the volume of the switchable unit, c is a constant related to long-term storage stability, k_B is Boltzmann's constant (energy/temperature), and T is the absolute temperature. The anisotropy energy density determines how much energy is required to change the magnetization of the bit of a given volume; the higher the value, the more energy is required and the higher the demands placed on the read/write head. $k_B T$ represents the thermal energy of the system (T>300 K in most hard drives) (*13*). The stability constant is generally in the range of 40-80 for 10 year magnetization stability, but can vary depending on the target product application (*11*). The physical interpretation of equation 1 is that to maintain the desired individual bit magnetization for at least 10 years, the product of the anisotropy energy and the volume must be greater than the thermal energy of the environment (*14*). Herein lies the problem with increasing the density using CMM technology. Increasing density demands either less grains per bit or smaller individual grain volumes V (so that more grains can be packed into the same disk platter area). Fewer grains per bit results in signal-to-noise problems and will not suffice (*11*). Since stability requirements don't change (constant c) and both k_B and operating temperature T are constant, decreasing V requires increasing K_u so the product $K_u V$ is still greater than $ck_B T$. Unfortunately, limitations in read/write head technology have virtually maxed out

K_u, which implies that V is already at a minimum (*11*). CMM technology has reached its limit. However, there remains hope in the form of bit-patterned media (BPM).

Bit-patterned media relies on a fundamentally different approach to creating magnetic domains. Instead of many randomly placed grains of magnetic material collectively comprising individual bits, magnetic domains are lithographically defined such that they are isolated by a non-magnetic material (**Figure 1.6**) (*8*). The increased possible density of BPM is related to magnetic coupling (*9*). In CMM, individual grains (**Figure 1.5**) are only weakly coupled to each other and behave as individual switching volumes. The volume term that goes into the superparamagnetic equation is the volume of an individual grain, but ca. 100 grains make up an individual bit. In contrast, each bit in BPM is magnetically isolated from its surroundings and all of the polycrystalline grains contained within each bit are strongly coupled to each other. Each bit acts as a single switching volume that is the sum of the volumes of all the grains it is comprised of. **Figure 1.7** qualitatively describes this difference (*8*). If each bit in CMM is comprised of 100 equivalent grains, the volume that goes into the superparamagnetic equation is the volume of an individual grain, while the same size bit in BPM has a volume 50 times greater. Thus, BPM potentially offers two orders of magnitude increase in density compared to CMM. The density limit for BPM corresponds with each bit containing only 1 grain.

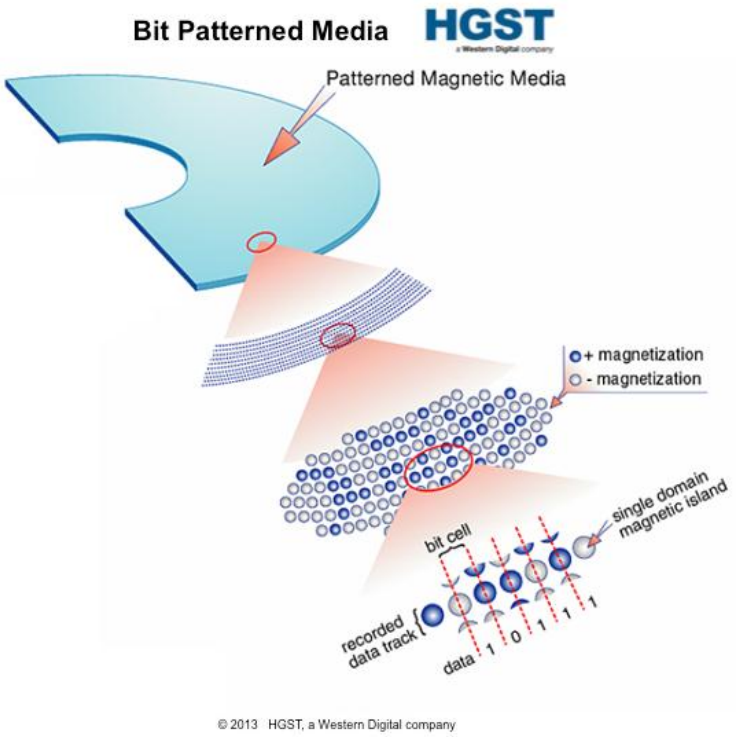

Figure 1.6: Schematic representation of bit-patterned media, the proposed next-generation magnetic media technology. Reused with permission from Hitachi Global Storage Technologies. Copyright 2013, HGST, a Western Digital Company.

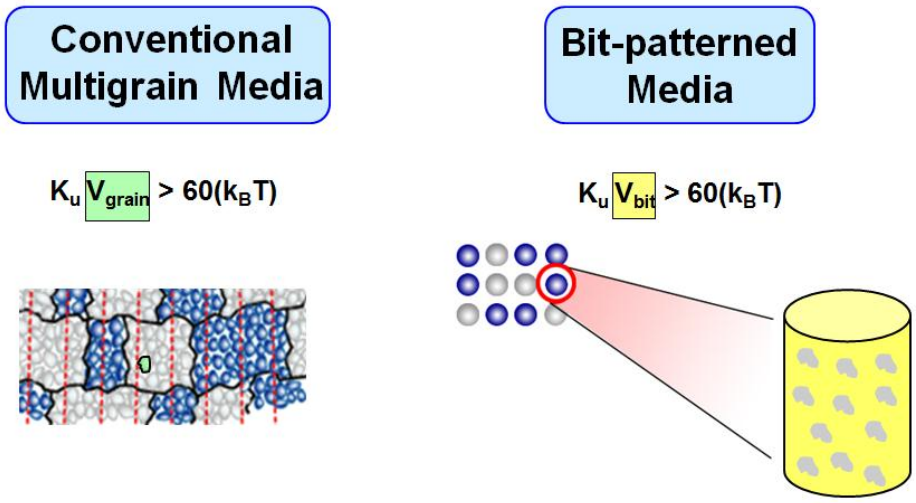

Figure 1.7: Qualitative comparison of the volumes that contribute to the superparamagnetic equation for CMM and BPM technologies. The volume term for CMM is that of an individual magnetic grain (green), while for BPM it is the volume of an entire bit (yellow, which is comprised of many grains). Part of the CMM image is from Figure 4.

The challenge for realizing BPM thus lies in patterning. How does one make an array of dots separated by non-magnetic material? The most vexing problem of the patterning process involves the size of individual bits. A geometric analysis of a large area (in lithographic terms) composed of hexagonally-packed dots says that to achieve 1 Tbit/in^2 of dots (1,000,000,000,000 bits) requires a center-to-center distance between dots (the pitch) to be 27 nm. The diameter of each individual dot must then be <14 nm. This length scale poses a serious challenge for state-of-the-art 193 nm immersion photolithography. Single patterning technology is limited to 36 nm features (half-pitch) (*15*). Double and even triple patterning can potentially reach the required length-scale but this involves very many costly steps (*15*). Step and Flash Imprint Lithography (SFIL) (*16*) can provide sub-10 nm resolution (*17, 18*) and commercial imprint tools are available that are capable of printing hundreds of disks per hour on both sides (*7*). What is required to enable SFIL is a template. While electron beam lithography has sub-10 nm

resolution (*19*), the cost of writing a perfect template is prohibitive since the write time is so slow. It is estimated that writing a 95 mm platter at a density of 1 Tbit/in^2 would require 1 month (*20*). There must be a cheaper alternative to pattern imprint templates to realize economically-viable BPM that is the subject of this dissertation.

1.2 Block Copolymer Self-Assembly

Polymers consist of long chains of repeating monomeric small molecules covalently linked together. In general, there exist many different types of polymers, which can be classified based on the sequence in which their monomer units are connected (**Figure 1.8**). The control of sequence has been the subject of extensive polymer chemistry research for many years and remains critically important when designing materials for tailored applications (*21*). Of particular interest to the present research is the block architecture. Block copolymers (BCPs) can self-assemble into ordered structures on the length scale of ca. 3-100 nm (**Figure 1.9**) (*22, 23*) and potentially offer an economic route to form BPM structures. The self-assembly process is predicated on the notion that most polymers will not mix but instead phase separate from each other. A mixture of phase-incompatible ("macrophase separated") homopolymers generally forms domains >>1 μm in size (*24*). However, the covalent bond connecting each block in a block copolymer prevents macrophase separation and restricts the size of the "microphase separated" domains to approximately the dimensions of the block copolymer chain. Features and pitches <50 nm in size are typical and reports of sub-10 nm features are becoming more prevalent (*25, 26*).

Homo	AAAAAAAAAAAA
Block	AAAAAABBBBBB
Random	ABBAABABABBB
Tapered	ABBBAABBAAAB

Figure 1.8: Different classifications of polymers based on their sequence.

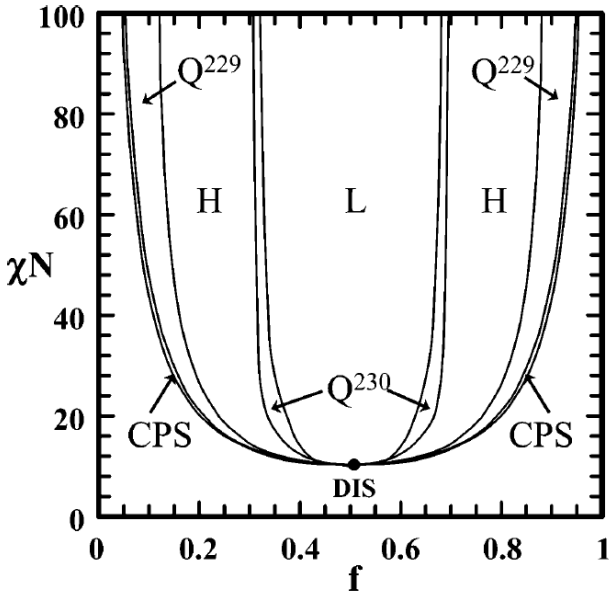

Figure 1.9: Theoretical AB diblock copolymer phase diagram demonstrating the different common morphologies. Reprinted with permission from Cochran, E. W. et al., Macromolecules 2006, 39, 2449. Copyright 2006 American Chemical Society.

Block copolymer self-assembly primarily depends on three variables: the volume fraction of each block (f_A, f_B, …), the interaction parameter (χ), and the overall degree of polymerization (N). The relative volume fractions (x-axis, **Figure 1.9**) mainly control the morphology of the material. Approximately equal volume fractions (f_A=f_B=0.5) result in equal sized alternating lines (lamella). As the amount of one block is decreased, a reduction in interfacial area between the two blocks drives a change in morphology through hexagonally packed cylinders and finally to spheres of one block dispersed in a matrix of the other. Since the theoretical phase diagram is symmetric about f_A=0.5, the minor component can consist of either block depending on the synthesis of the material. The interaction parameter χ takes the general form of **Equation 1.2**. Qualitatively, χ captures the phase-incompatibility of the blocks with each other; a high value represents a strong driving force for the blocks to remain microphase separated.

$$\chi = \frac{\alpha}{T} + \beta \qquad \textbf{Eq. 1.2}$$

Microphase separation also depends on the overall degree of polymerization, N. Since the entropy of mixing contribution to the overall free energy is inversely proportional to N (*27*), higher values of N lead to a reduction of entropy and less favorable mixing. At a given volume fraction, the product χN (y-axis, **Figure 1.9**) determines if a block copolymer will form an ordered structure or remain disordered. At f_A=0.5, in order to form a self-assembled morphology, χN≥10.5. The domain periodicity (the pitch, D, also referred to as L_0 for lamella-forming BCPs) also depends on both χ and N. **Equation 1.3** shows this relationship in the strong segregation limit (χN>>10.5). Since D scales much more strongly with N than χ, smaller pitches (features) can be obtained by simultaneously decreasing N and increasing χ, with χN≥10.5.

$$D \sim aN^{2/3}\chi^{1/6} \qquad \textbf{Eq. 1.3}$$

As the number of blocks and types of monomers increases, the aforementioned morphologies become difficult to predict *a priori* (*21*). This dissertation focuses on lamella- and cylinder-forming AB diblock and ABA triblock copolymers, which have similar and relatively well-understood theoretical phase diagrams (*28*) that qualitatively agree with the example shown in **Figure 1.9**.

1.3 Block Copolymer Thin Film Self-Assembly

The general strategy utilized to leverage BCP self-assembly for lithographic applications involves a series of thin film processing steps (**Figure 1.10**). Each step is briefly described here and discussed in much greater detail in the following chapters. The first step is to spin coat an alignment layer that enables the formation of perpendicular BCP features in the subsequent annealing step. Chapter 3 will discuss

alignment layer synthesis, characterization, and use. Chapter 2 details the synthesis of silicon-containing block copolymers, which can be cast as a thin film onto a surface treatment by spin coating. The design and synthesis of BCP materials generally influences the choice of alignment layer, thus a discussion about BCP materials naturally precedes the alignment layer chapter. Annealing is generally accomplished by either exposing the BCP thin film to solvent vapor or by heating the sample to provide mobility to the BCP to rearrange into an energetically favorable orientation and alignment. Chapter 4 leverages solvent annealing, while Chapters 6 and 7 utilize new materials that enable thermal annealing of materials that has traditionally been impossible. The last step involves removing one block and potentially transferring the pattern into a specific underlying material. Chapter 5 will discuss process optimization using a dry etch process known as reactive ion etching.

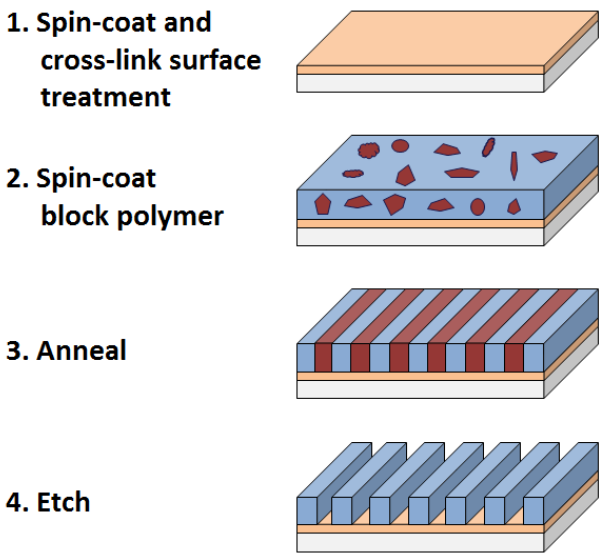

Figure 1.10: Idealized schematic of BCP thin film self-assembly for lithographic applications. A lamella-forming BCP morphology is pictured.

1.4 Material Design

An understanding of both block copolymer self-assembly and lithographic thin film processes results in a set of idealized material requirements for both the surface treatment layer and the block copolymer. The choice of surface treatment is generally dependent on the specific BCP, thus material design starts with the block copolymer. In particular, the block copolymer must be synthesizable by established controlled polymerization methods, have a high χ (for a small minimum feature size), be amenable to thin film orientation control and processing, and be etch resistant (for ease of RIE pattern transfer). Furthermore, the ideal BCP candidate would be glassy for structural stability, non-crystalline to prevent crystallization-induced defectivity (*29*), and non-metal containing for ease of integration into existing lithographic facilities. Each requirement introduces unique difficulties that must be addressed and overcome. The materials described within this dissertation aim to meet all of the ideal material requirements.

1.5 Collaborative Efforts

All of the work reported in this dissertation has been a collaborative effort between many members of both the Willson and Ellison research groups at The University of Texas at Austin. In particular, past and present graduate students Jeffrey R. Strahan, Julia D. Cushen, Michael J. Maher, William J. Durand, Gregory Blachut, and undergraduate students Morgan W. Schulze, Leon M. Dean, Jeffrey Ting, Anthony Thio, Litan Li, and Brennen Mueller, have made significant contributions and have been invaluable resources. Since this project embodies many different aspects of chemistry and engineering, including small molecule and polymer synthesis, characterization, thin film assembly, and microscopy, collaborations have been the key to success. It would be impossible to separate out individual contributions from the whole, but every effort has been made to give credit within this dissertation where appropriate to those that produced specific sets of data.

Chapter 2: Silicon-containing Block Copolymers

2.1 BACKGROUND

Reactive ion etch-resistant block copolymers have been a major research initiative over the past ~12 years and studies on the topic have been reported in great detail in the literature (*30*-*32*). The driving force to develop etch-resistant BCP materials derives from the potential simplification of pattern transfer thin film processes. BCP materials that can act as a hard mask and resist reactive ion etching should widen the process latitude of the etch processes significantly. The most common strategies used to incorporate etch-resistant groups into one block either involve the covalent incorporation of an etch-resistant heteroatom or the selective segregation of etch-resistant functionality during thin film processing. For example, the most common heteroatoms covalently incorporated into one block are silicon and iron. Most silicon-containing blocks consist of either poly(dimethylsiloxane) or poly(methacrylate oligomeric silsesquioxane). Examples of block copolymers containing one of these blocks include: poly(styrene-*block*-dimethylsiloxane) (PS-*b*-PDMS) (*33*), poly(2-vinylpyridine-*block*-dimethylsiloxane) (P2VP-*b*-PDMS) (*34*), poly(lactide-*block*-dimethylsiloxane-*block*-lactide) (PLA-*b*-PDMS-*b*-PLA) (*35*) poly(styrene-*block*-methacrylate polyoligomeric silsesquioxane) (PS-*b*-PMAPOSS), and poly(methacrylate-*block*-methacrylate polyoligomeric silsesquioxane) (PMMA-*b*-PMAPOSS) (*36*). Fe-containing blocks usually consist of a poly(ferrocenyldimethylsilane) block (which also includes silicon); for example poly(ferrocenyldimethylsilane-block-methyl methacrylate) (PFS-*b*-PMMA) (*37*). In contrast, the selective segregation strategy utilizes BCPs that can preferentially interact (non-covalently) with the chosen etch resistant group. Examples include organosilicate segregation into the poly(ethylene oxide) domain of poly(styrene-*block*-ethylene oxide) (*38*) and the interaction of gold with the poly(4-vinylpyridine) block of poly(styrene-*block*-4-vinylpyridine) (PS-*b*-P4VP) (*39*). Etch resistant moieties such as aluminum can also be introduced during etch processes (*40*).

The aforementioned strategies and materials have benefits and drawbacks. PDMS-containing block copolymers generally have high χ values and can form extremely high resolution structures. For instance, the χ value of PS-*b*-PDMS (*41*) at 150 ^{0}C is about 10 times larger than PS-*b*-PMMA (*42*). Wan et al. have reported impressive high resolution thin film patterns with a pitch on the order of 10 nm using PS-*b*-PDMS (*43*). However, the major drawback of PDMS is its low T_g (-127°C) which remains a concern for self-assembled structural integrity, pattern transfer, and pattern defectivity. POSS-containing block copolymers can also form relatively small structures (*36*), but have a significantly skewed phase diagram due to the large volume of the POSS cage that can make synthesis challenging. They are also relatively expensive and potentially crystalline, which can introduce defects. Selective segregation strategies generally require processing steps in addition to those outlined in Chapter 1 and the successful process window can often be both quite narrow and BCP dependent.

After evaluating the extensive body of work reported in the literature including the aforementioned etch-resistance strategies, our group decided to pursue the synthesis of monomers with covalently-incorporated silicon functional groups. These monomers can then be used to produce a library of different block copolymers depending on the choice of monomer for the other block(s). Most of the work in this dissertation revolved around three different block copolymers synthesized at the University of Texas: poly(styrene-*block*-trimethylsilylisoprene), poly(styrene-*block*-methyltrimethylsilylmethacrylate), and poly(styrene-*block*-trimethylsilylstyrene-*block*-styrene). Each block copolymer was synthesized using anionic polymerization, which is the living polymerization method with the tightest control of molecular weight, molecular weight distributions (colloquially "polydispersity"), and yield (albeit with limited functional group tolerance) (*44*). These block copolymers utilize three different types of silicon-containing monomers and two different block copolymer architectures (AB and ABA).

Each material has a number of advantages and disadvantages that will be described in detail. While block copolymer synthesis can be quite challenging and

complicated, many thin film experiments can be performed with a single BCP. For instance, there have been hundreds of papers written on PS-*b*-PMMA and PS-*b*-PDMS. The three block copolymers reported herein have produced a large collection of experimental data and have greatly improved our understanding of thin film self-assembly processes. This chapter focuses on the synthesis and characterization of the Si-BCPs, while subsequent Chapters 4, 5, 6, and 7 describe thin film studies.

2.2 POLY(STYRENE-*BLOCK*-TRIMETHYLSILYLISOPRENE)

The first silicon-containing monomer investigated was trimethyl(2-methylenebut-3-en-1-yl)silane ("trimethylsilylisoprene", TMSI). This work is adapted with permission from C. M. Bates et al., J. Polym. Sci., Part A: Polym. Chem. 2013, 51, 290. Isoprene is known to undergo anionic polymerization and has been used to make both diblock (*45*) and triblock (*46*) copolymers anionically. It was surmised that a silicon-containing isoprene derivative would also undergo anionic polymerization and could be copolymerized with styrene. The synthesis of TMSI monomer (**Scheme 2.1**) was accomplished by Kumada coupling of commercially available chloroprene (generously provided by Nissan Chemical Company) and ((trimethylsilyl)methyl)magnesium chloride (*47*). TMSI monomer was isolated in 60% yield after distillation.

Anionic polymerization was performed with both styrene and TMSI monomers to form a diblock copolymer. A detailed description of the anionic polymerization setup (including custom glassware) can be found in the dissertation of Jeffrey R. Strahan (*48*). The first step involved extensive purification of both monomers to ensure that there was no water or oxygen present. Styrene monomer was carefully purified by distillation over dibutyl magnesium two times. TMSI monomer was purified over *n*-butyllithium two times, with the mixture of TMSI and *n*-butyl lithium kept in an ice bath at 4°C. In the case of isoprene monomer, the mixture of isoprene and *n*-butyllithium must remain cold to prevent exothermic polymerization of isoprene. Since isoprene is low boiling, the exotherm can create very high pressures very quickly in a sealed glass vessel and result in an explosion. To be safe, TMSI monomer was handled in the same way as isoprene. The

monomers were subsequently distilled into air-free glass burettes and freeze-pump-thawed three times to remove any trace oxygen still present. At this point, the monomers were considered to be free of both water and air and were subjected to anionic polymerization. Purified styrene was dissolved in cyclohexane (obtained from a dry solvent system) and initiated with *sec*-butyl lithium (**Scheme 2.2**), which resulted in generation of an appropriate bright burnt orange color. After 12 h, an aliquot of the polystyrene anion was extracted from the reactor and injected into degassed methanol. The PS homopolymer provided important information about the first block and was used as a point of comparison with the subsequent diblock material. TMSI monomer was then added to the reactor which resulted in a colorless solution that was stirred for 12 h. After degassed methanol was added to the reactor to quench the living anions, the polymer was isolated by precipitation and analyzed.

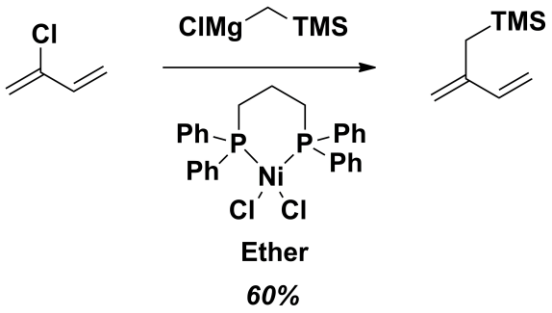

Scheme 2.1: Synthesis of TMSI monomer.

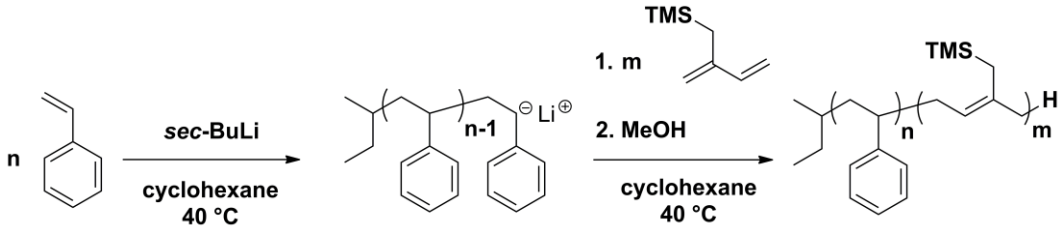

Scheme 2.2: Synthesis of PS-*b*-PTMSI.

Size exclusion chromatograms (SEC) of the polystyrene aliquot and the diblock copolymer are shown in **Figure 2.1**. The polystyrene (blue curve on the right)

completely shifts to the left towards higher molecular weight after block growth (green curve, PS-*b*-PTMSI). Complete conversion of all living polystyrene chains to PS-*b*-PTMSI chains was achieved. If some PS chains failed to react, the green curve would likely be bimodal with one peak maximum overlapping with the PS homopolymer blue curve, which is not observed. The data in **Table 2.1** calculated form the SEC data and ^{1}H NMR are consistent with excellent control of molecular weight and chain length dispersity for both the polystyrene block and the diblock copolymer. Differential scanning calorimetry performed under a nitrogen atmosphere shows the presence of two glass transition temperatures (T_g(PTMSI)= -35°C, T_g(PS)=104°C) that suggest microphase separation of the two blocks (**Figure 2.2**).

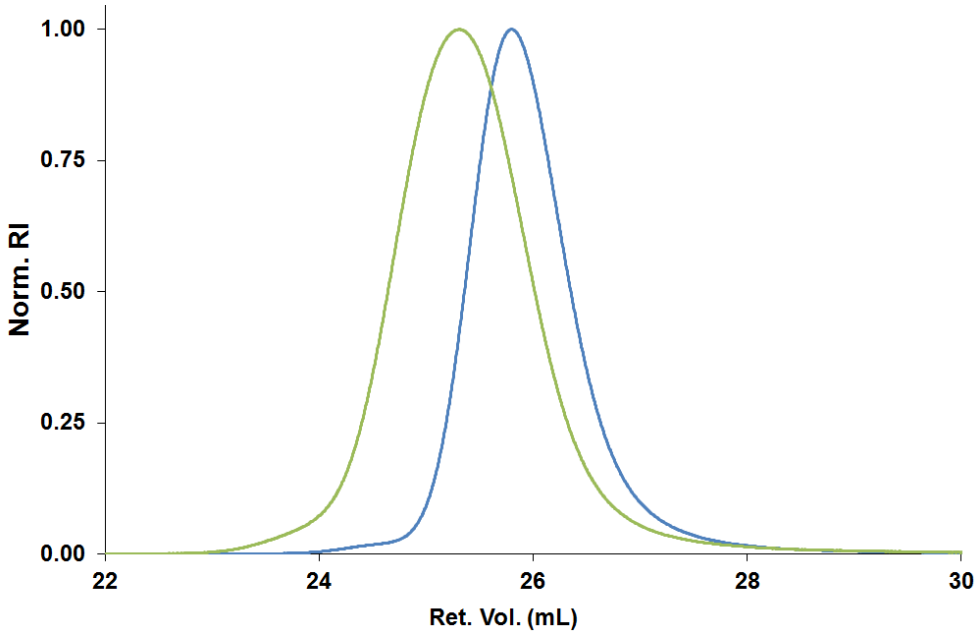

Figure 2.1: SEC trace of the polystyrene aliquot (blue, right) and PS-*b*-PTMSI (green, left).

Table 2.1: SEC data for the synthesis of PS-*b*-PTMSI.

Sample	M_n (kDa)	Dispersity[a]
PS aliquot[a]	54.2	1.00
Block[b]	68.3	1.02

[a] Calculated relative to a polystyrene standard, dn/dc=0.185.

[b] M_n calculated by ^{1}H NMR = $M_{n\text{-PS}} + M_{n\text{-PTMSI}}$, dispersity calculated by SEC relative to a polystyrene standard.

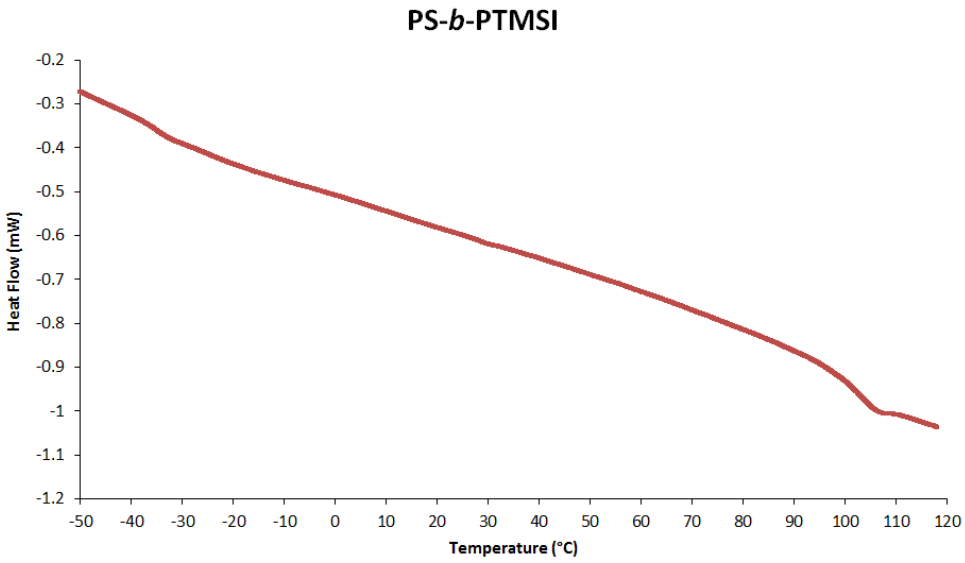

Figure 2.2: DSC trace on heating of PS-*b*-PTMSI. T_g(PTMSI)= -35°C, T_g(PS)=104°C.

Based on the volume fractions (0.83:0.17 PS:PTMSI) as calculated by ^{1}H NMR, it was expected that the morphology would be either hexagonally packed cylinders or body-centered cubic spheres. Small angle X-ray scattering data (**Figure 2.3**) were collected and analyzed relative to the expected extensively-studied block copolymer bulk morphologies (*49*). After the BCP was annealed at 170°C for 3 h under a nitrogen atmosphere, the material showed signs of an ordered morphology, with $4^{1/2}$q*, $7^{1/2}$q*, and $12^{1/2}$q* reflections most closely matching those expected for hexagonally-packed cylinders ($3^{1/2}$q*, $4^{1/2}$q*, $7^{1/2}$q*, $9^{1/2}$q*, $12^{1/2}$q*). The underlying cause of the missing $3^{1/2}$q* and $9^{1/2}$q* peaks is unclear, but missing SAXS peaks have been observed in other

block copolymer systems (*50*). Based on the q* value of 0.0153 $Å^{-1}$, the d_{100} domain spacing (assuming a hexagonally-packed cylinder morphology), was calculated to be 41.1 nm.

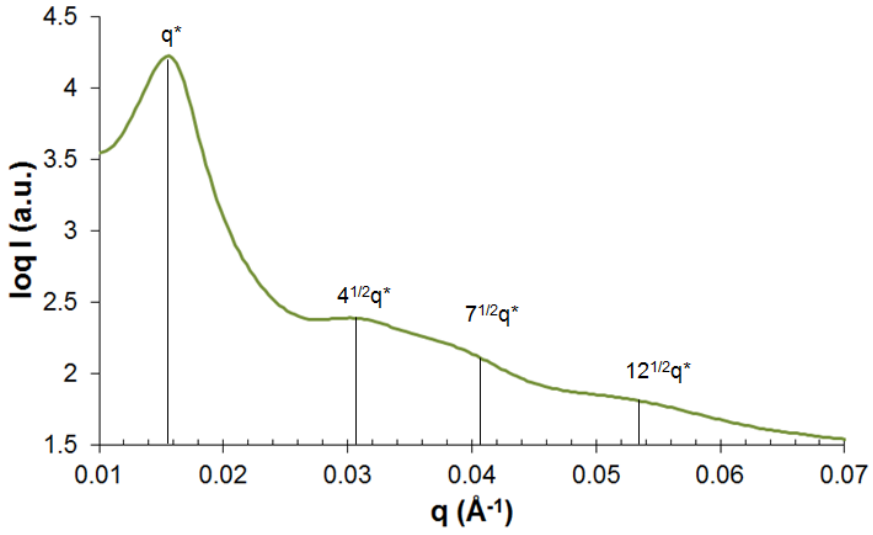

Figure 2.3: Small angle X-ray scattering data, collected at 25 ^{0}C, of PS-*b*-PTMSI thermally annealed at 170 ^{0}C for 3 h under a nitrogen purge.

During the course of initial thermal studies with PS-*b*-PTMSI, it was discovered that the block copolymer undergoes some sort of degradation process when thermally annealed in the presence of air. This is evidenced by a change in the SEC data of bulk samples annealed under vacuum (**Figure 2.4**). The molecular weight of the bulk sample decreases as it is heated hotter and longer which corresponds with a shift of the peak maximum to longer retention time (to the right). Significant low molecular weight tailing also becomes evident. The calculated molecular weight and dispersity data (**Table 2.2**) confirm that the bulk sample has significantly lower molecular weight and a higher dispersity than the as-synthesized material.

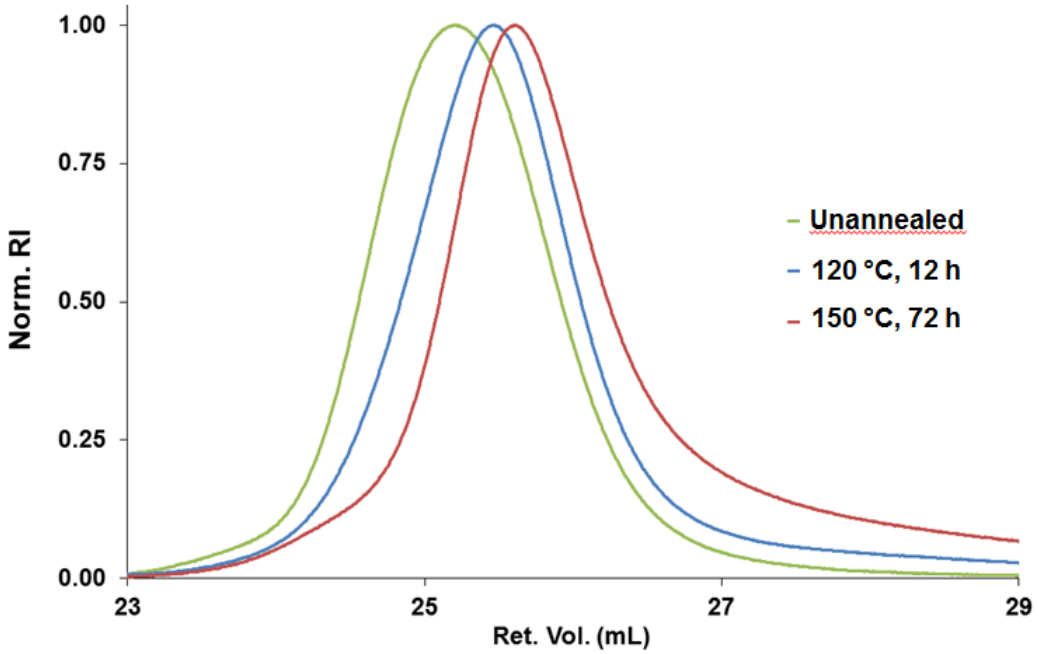

Figure 2.4: SEC data indicating thermal degradation of bulk samples of PS-*b*-PTMSI heated under vacuum.

Table 2.2: SEC data demonstrating thermal degradation of PS-*b*-PTMSI.

Sample	M_n (kDa)[a]	Dispersity[a]
Original Polymer	68.3	1.02
120°C, 12 h	47.6	1.23
150°C, 72 h	36.9	1.47

[a] SEC data calculated relative to a polystyrene standard.

Isothermal TGA data run under a nitrogen purge gas at 150°C (**Figure 2.5**) indicate only miniscule mass loss as a function of time, which suggests one of two degradation scenarios. Either the degradation products are non-volatile and do not manifest as a change in mass during the TGA run or the block copolymer is sensitive to a component in the air which speeds up degradation. Since the TGA was run under a nitrogen atmosphere, presumably air would not be present in quantities large enough to

cause degradation. While the data do not conclusively indicate one scenario, given potential thermal instabilities, alternative annealing techniques were examined with PS-*b*-PTMSI.

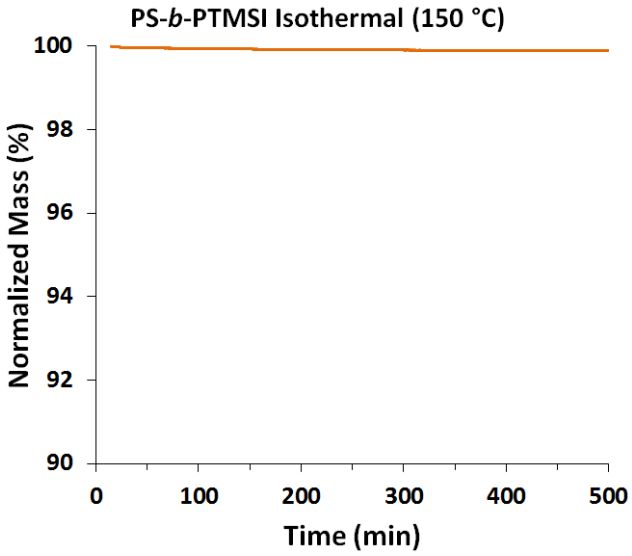

Figure 2.5: Isothermal TGA data of PS-*b*-PTMSI at 150°C indicates no mass loss as a function of time.

Solvent annealing is an alternative annealing technique that can overcome traditional thermal annealing limitations. In the case of the present study, it was anticipated that even successful thermal annealing would likely produce parallel-oriented features with a TMSI-rich wetting layer at the free surface due to the low surface energy of silicon-containing polymers (*33*). Thus, subsequent efforts were focused on using solvent annealing to obtain assembly of PS-*b*-PTMSI, which will be discussed in Chapter 4. An additional potential problem is the low T_g of the PTMSI block (-35°C). While significantly higher than other rubbery blocks such as PDMS, the T_g is still lower than room temperature. Potential concerns related to structural stability, defectivity, and low T_g led to the investigation of alternative silicon-containing block copolymers.

Due to thermal degradation issues and a low glass transition temperature, the χ value of PS-*b*-PTMSI was not thoroughly investigated. It is currently unclear how the minimum feature size of PS-*b*-PTMSI relates to that of PS-*b*-PMMA, PS-*b*-PDMS, and other extensively-studied block copolymers, although it is likely comparable to PS-*b*-PMMA.

2.3 POLY(STYRENE-*BLOCK*-METHYLTRIMETHYLSILYLMETHACRYLATE)

Methyltrimethylsilylmethacrylate (MTMSMA, **Figure 6**) is an attractive alternative to TMSI monomer for several reasons. Polymethacrylates generally have higher T_g values than polyisoprenes, which could potentially mitigate defectivity concerns. MTMSMA is also commercially available at relatively low cost with good purity, which greatly shortens the pre-polymerization preparation time requirements. The anionic polymerization of PS-*b*-PMTMSMA followed established procedures for PS-*b*-PMMA (*51*).

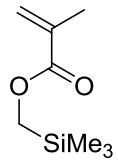

Figure 2.6: Methyltrimethylsilylmethacrylate (MTMSMA) monomer is commercially available.

Styrene was purified in the same was as previously described. MTMSMA was purified by two distillations into CaH_2 to remove water. The dry monomer was distilled into a burette and freeze-pump-thawed to remove oxygen. Unlike the PS-*b*-PTMSI block, PS-*b*-PMTMSMA was synthesized with THF as a solvent at -78°C, which is typical for PS-*b*-PMMA block copolymers (*44*). The cold temperature is required to prevent side reactions between anions and THF. Polystyrene was initiated with *sec*-butyllithium and propagated for 4 hours. A small aliquot was extracted from the reactor for analysis. Subsequently, 1,1-diphenylethylene (DPE) was added as a crossover

moiety, which resulted in an immediate change of solution color from burnt orange to bright red. DPE adds only one unit to living polystyrene anions, and the resulting anion enables efficient initiation of a subsequent methacrylate block. The steric bulk of DPE prevents 1,4 and 1,2 addition to the methacrylate and instead results in exclusively 3,4 addition (*52*). The presence of LiCl in the reactor slows down propagation of the methacrylate polymerization and allows for excellent control of molecular weight and chain length dispersity (*53*). After the DPE was reacted for 3 h to ensure complete conversion of polystyrenyl anions, MTMSMA was added and reacted for 3 h. Termination of the polymerization and isolation of the polymer resulted in a white powder.

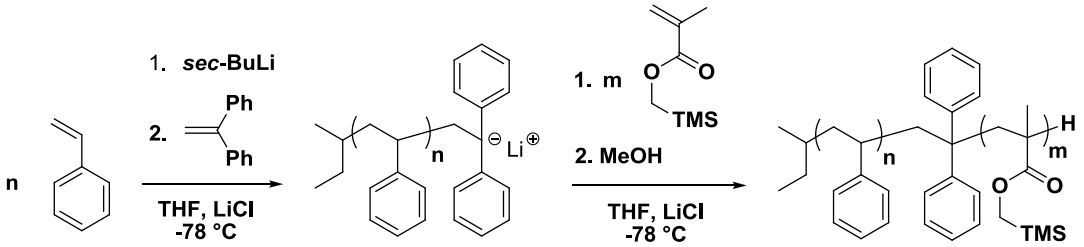

Scheme 2.3: Synthesis of PS-b-PMTMSMA.

Analysis of PS-*b*-PTMSI by SEC shows good control of molecular weight and chain length dispersity (**Figure 2.7**). Careful examination of the block copolymer peak (green, left) shows a small partially-resolved secondary shoulder peak. The maximum of the second peak appears to elute at the same time as the PS homopolymer. A small amount of termination of polystyrenyl anions either during aliquot extraction or more likely during diphenylethylene crossover is probably the cause. Regardless, the overall dispersity of both the PS block and PS-*b*-PMTMSMA remains relatively low (**Table 2.3**, 1.17) and is considered acceptable. The volume fractions calculated by ^{1}H NMR, (PS:PMTMSMA=0.66:0.34) correspond well with the expected volume fractions based on the feed ratio. Based on these volume fractions and the symmetric diblock copolymer theoretical phase diagram, PS-*b*-PMTMSMA should self-assemble into a hexagonally-packed cylinder morphology with cylinders of PMTMSMA in a matrix of PS.

Cylinder-forming PS-*b*-PMTMSMA

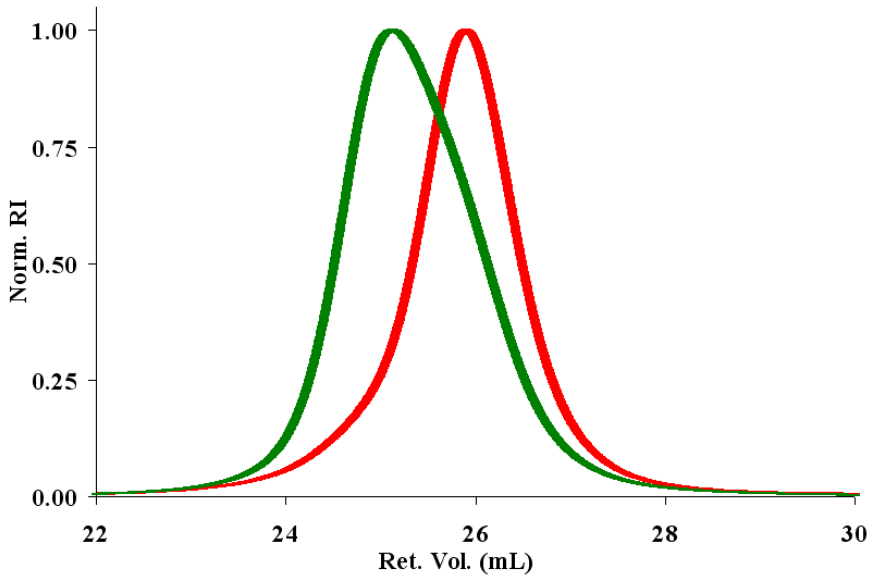

Figure 2.7: SEC trace of cylinder-forming PS-*b*-PMTMSMA.

Table 2.3: SEC data for PS-*b*-PMTMSMA

Sample	Mn (kDa)[a]	Mw (kDa)[a]	Dispersity
PS Aliquot	60.0	70.1	1.17
PS-*b*-PMTMSMA	75.2	87.8	1.17

[a] Calculated relative to a polystyrene standard.

Small angle X-ray scattering data (**Figure 2.8**) collected with a synchrotron radiation are consistent with a hexagonally-packed cylinder morphology. Bragg peak reflections at $3^{1/2}$q*, 2q*, and $7^{1/2}$q* are expected and observed. Based on the position of the q* peak (0.0128 Å), the d_{100} spacing is calculated to be 52.4 nm. **Figure 2.9** shows the calculated spacing of the hexagonally-packed cell based on the SAXS data.

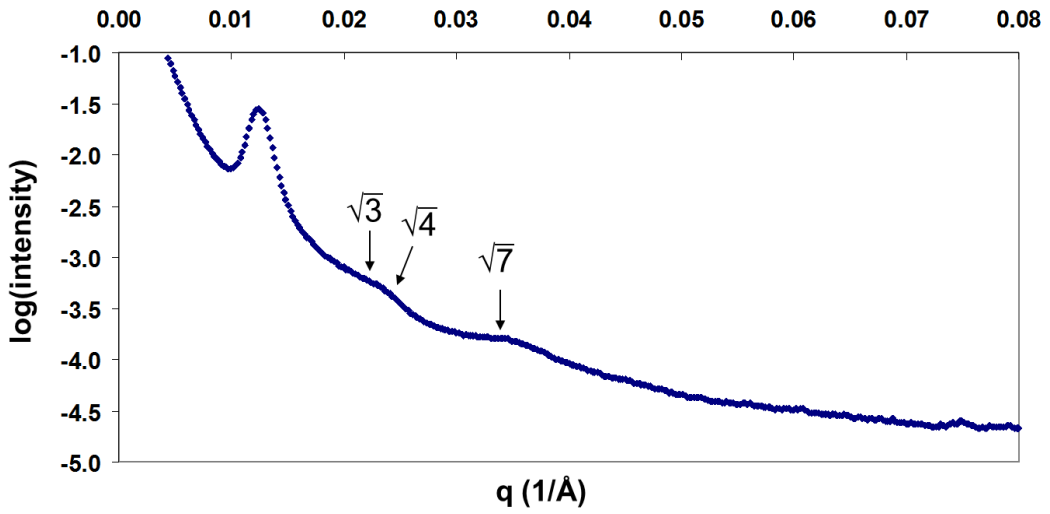

Figure 2.8: Small angle X-ray scattering data for cylinder-forming PS-*b*-PMTMSMA at 170°C. The domain spacing d_{100} is calculated to be 52.4 nm from the relationship $d_{100}=2\pi/q^*$.

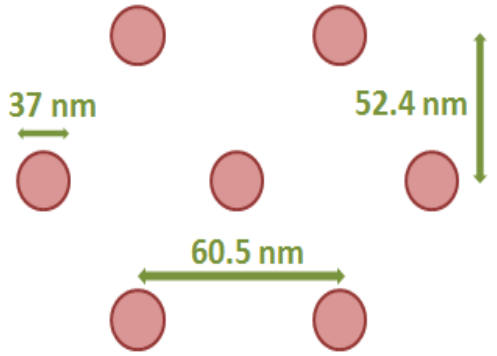

Figure 2.9: Calculated hexagonally-packed cell dimensions based on SAXS data.

Analysis of PS-*b*-PMTMSMA with DSC shows the presence of one strong glass transition at 105°C (**Figure 2.10**) which is attributed to the PS block. The lack of an observed T_g for the PMTMSMA block could be due to a small change in the heat capacity between $T<T_g$ and $T>T_g$. Alternatively, it is possible that the block copolymer

is disordered and the miscible blocks produce only one observed T_g. However, given the scattering data, the heat capacity explanation seems more plausible. Temperature-ramp TGA analysis of PS-*b*-PMTMSMA indicates good thermal stability with degradation starting around 300°C.

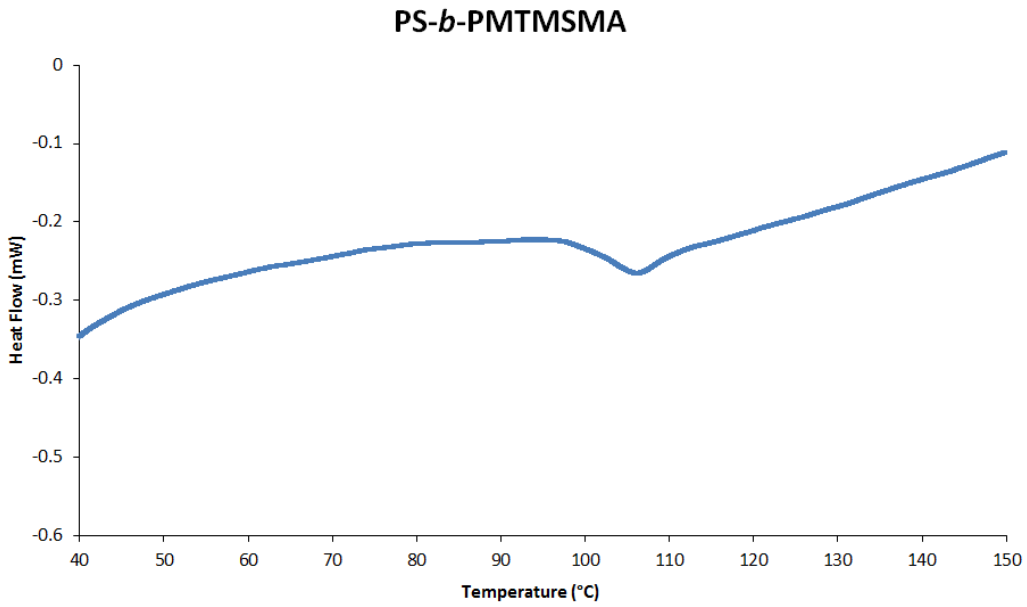

Figure 2.10: DSC trace on heating of cylinder-forming PS-*b*-PMTMSMA. Data were acquired at 10°C/min. One T_g is observed at 105°C.

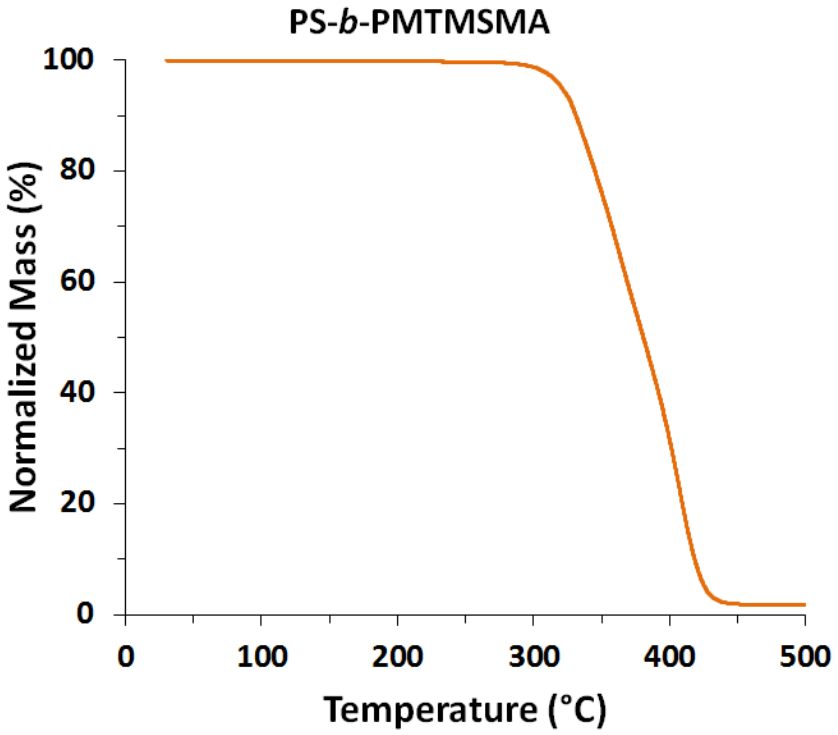

Figure 2.11: TGA degradation data of cylinder-forming PS-*b*-PMTMSMA. Data were acquired at 10°C/min.

Julia D. Cushen performed extensive synthesis and characterization work to calculate the χ value of PS-*b*-PMTMSMA by rheology and absolute intensity SAXS. The calculations can be quite complex and the details will be reported by Julia in her dissertation. **Equation 2.1** shows the result of her calculations, with α=18.9 and β=0.021. At 150°C, the value of χ=0.066 is about two times larger than PS-*b*-PMMA (0.030 at 150°C) (*54*). PS-*b*-PMTMSMA potentially enables a significant density increase of features compared to PS-*b*-PMMA. Efforts were thus made to orient thin films of PS-*b*-PMTMSMA (see Chapter 4).

$$\chi = \frac{18.9}{T} + 0.021$$ **Eq. 2.1**

Equation 2.1: Calculated χ value for PS-*b*-PMTMSA. Experiments were performed by Julia D. Cushen using absolute intensity SAXS.

2.4 POLY(STYRENE-*BLOCK*-TRIMETHYLSILYLSTYRENE-*BLOCK*-STYRENE)

An ABA triblock copolymer, poly(styrene-*block*-trimethylsilylstyrene-*block*-styrene) (PS-*b*-PTMSS-*b*-PS), was also synthesized anionically. The ABA architecture was pursued in addition to AB diblock copolymers because previous studies (29, 30) suggest that ABA triblock copolymers with relative interfacial energies $\gamma_B<\gamma_A$ adopt a perpendicular orientation in thin films more readily than AB diblocks. The effects of interfacial energies, surface energetics, and thermal orientation control will be greatly expounded in subsequent chapters.

Trimethylsilylstyrene (TMSS) monomer was synthesized by the Grignard reaction of 4-chlorostyrene (ClSty) with trimethylsilyl chloride (TMSCl) (**Scheme 2.4**). ClSty was added to a heterogeneous mixture of magnesium metal in THF with catalytic 1,2-dibromoethane and stirred for 30 minutes at 65°C, which resulted in partial dissolution of the magnesium and a dark brown solution. The mixture was cooled to 0°C and TMSCl was added dropwise. After 1.5 h, the reaction was quenched and TMSS was isolated by fractional distillation in moderate yield.

Both the TMSS and styrene monomers were purified with dibutylmagnesium in the same way as discussed previously. Anionic polymerization was performed using potassium naphthalenide and α-methylstyrene (**Scheme 2.5**). Potassium napthalenide, a radical anion, reacts with α-methylstyrene to form an α-methylstyrene radical anion (*44*). Two α-methylstyrene radical anions then recombine to form a bifunctional anionic oligomeric initiator α-methylstyrene tetramer dianion, which has a characteristic bright red color (*44*). Subsequent addition of TMS monomer resulted in polymer propagation in two directions. After 4 h, the TMSS reaction was complete and styrene was added to the reactor. This resulted in styrene growth from both ends of the polymer chain. The

polymerization was quenched after 4 h. The resulting block copolymer has an ABA triblock architecture, with A blocks of PS and a B block of PTMSS. Note that the tetramer initiator of α-methylstyrene leaves a small oligomeric unit at the midpoint of the PTMSS block. Since the length of the oligomeric unit is significantly shorter than the length of the PTMSS half blocks on either side, its effect is ignored and should not impact the block copolymer self-assembly.

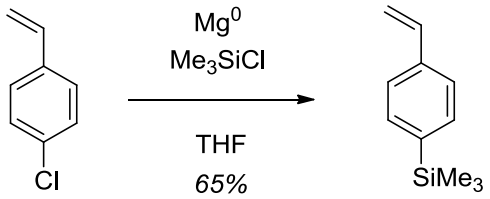

Scheme 2.4: Synthesis of TMSS monomer.

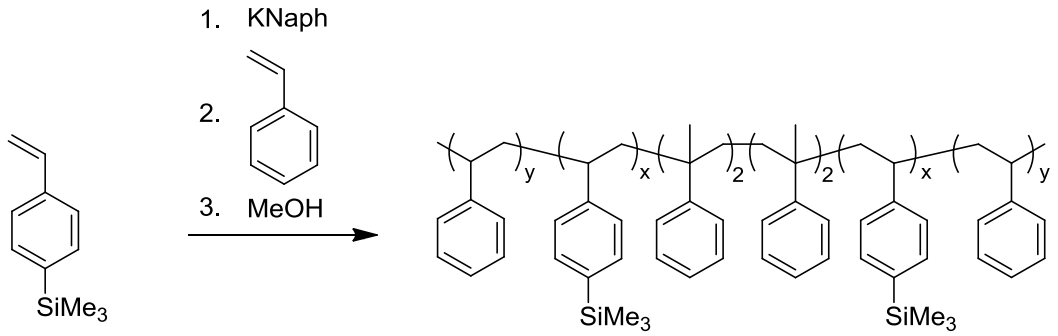

Scheme 2.5: Anionic polymerization of PS-*b*-PTMSS-*b*-PS.

Size exclusion chromatograms of the PTMSS aliquot and PS-*b*-PTMSS-*b*-PS (**Figure 2.12**) show good control of the polymerization and low dispersity values for both the aliquot and block (**Table 2.4**). The volume fractions as calculated by ^{1}H NMR (0.48:0.52 PTMSS:PS) suggest a lamella-forming morphology. Syncotron SAXS data (**Figure 2.13**) further support a lamellar morphology with Bragg peaks at q* and 3q*. Note that lamella-forming morphologies also have an allowed 2q* reflection, which disappears for symmetric block copolymers with volume fractions 0.50:0.50 (*49*). The calculated volume fractions of 0.48:0.52 PTMSS:PS are within error of 0.50:0.50 given a

~5% error in the ^{1}H NMR integrals. Based on the location of the q* peak (0.021 Å), the periodicity of the block copolymer is L_0=30 nm, which corresponds with individual line widths of 15 nm (**Figure 2.14**).

Lamella-forming PS-*b*-PTMSS-*b*-PS

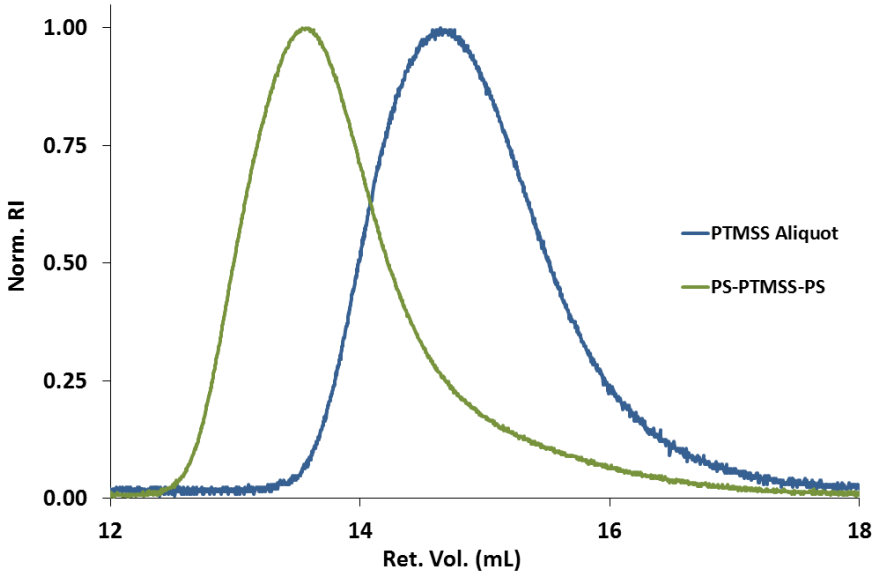

Figure 2.12: SEC data demonstrating the synthesis of lamella-forming PS-*b*-PTMSS-*b*-PS.

Table 2.4: Molecular weight and dispersity data for lamella-forming PS-*b*-PTMSS-*b*-PS.

Sample	M_n (kDa)	M_w (kDa)	Dispersity
PTMSS aliquot[a]	38.0	41.0	1.08
PS-*b*-PTMSS-*b*-PS[b]	79.1	94.9	1.20

[a]Molecular weight data calculated using PTMSS dn/dc=0.138 (*55*).

[b]M_n calculated using ^{1}H NMR, dispersity data calculated using SEC with PS-*b*-PTMSS-*b*-PS dn/dc=0.280.

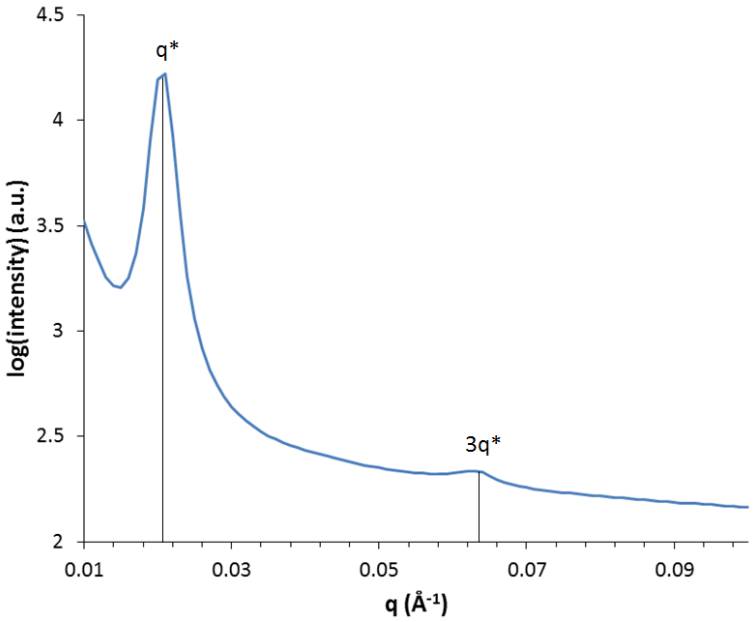

Figure 2.13: SAXS profile of lamella-forming PS-*b*-PTMSS-*b*-PS with characteristic Bragg reflections at q* and 3q*. The extinction of 2q* is expected for symmetric block copolymers. L_0=30.

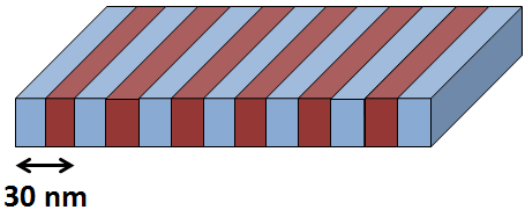

Figure 2.14: Bulk dimensions of lamella-forming PS-*b*-PTMSS-*b*-PS as calculated by SAXS.

Julia D. Cushen spent a significant amount of time characterizing the χ value for PS-*b*-PTMSS-*b*-PS by absolute intensity SAXS (*56*). The details of the calculation will be reported by her at a later date. Eq. 2 shows the value of chi with α=2.09 and β=0.019. At 150°C, the value of χ is 0.024. This number is slightly smaller but comparable to the

value of χ (0.039) for PS-*b*-PMMA at 150°C. PS-*b*-PTMSS-*b*-PS will not produce the highest resolution features. However, there are potential advantages with a triblock architecture. As further explained in Chapter 6, triblock copolymers are potentially easier to orient in thin films than their diblock copolymer counterparts (*57, 58*). A detailed analysis of the thin film behavior of PS-*b*-PTMSS-*b*-PS is left to Chapters 4, 6, and 7.

$$\chi = \frac{2.09}{T} + 0.019 \qquad \textbf{Eq. 2.2}$$

Equation 2.2: Calculated χ value for PS-*b*-PTMSS-*b*-PS. Experiments were performed by Julia D. Cushen using absolute intensity SAXS.

Cylinder-forming PS-*b*-PTMSS-*b*-PS

Cylinder-forming PS-*b*-PTMSS-*b*-PS was also synthesized analogous to the lamella-forming material. Again, SEC data (**Figure 2.15**, **Table 2.5**) show good control the polymerization with clean growth of the second block. ^{1}H NMR was used to calculate the PTMSS:PS relative volume fractions as 0.31:0.69. SAXS analysis of the sample shows a q and 2q* peak. The allowed $3^{1/2}$q* is apparently not resolved and possibly overlaps with the relatively broad 2q* peak. The row-to-row domain spacing, d_{100} is 33 nm as calculated from the SAXS data. The volume fractions and the SAXS data (**Figure 2.16**) were used to calculate a cylinder diameter of 22 nm. **Figure 2.17** summarizes the calculated cylinder domain geometry.

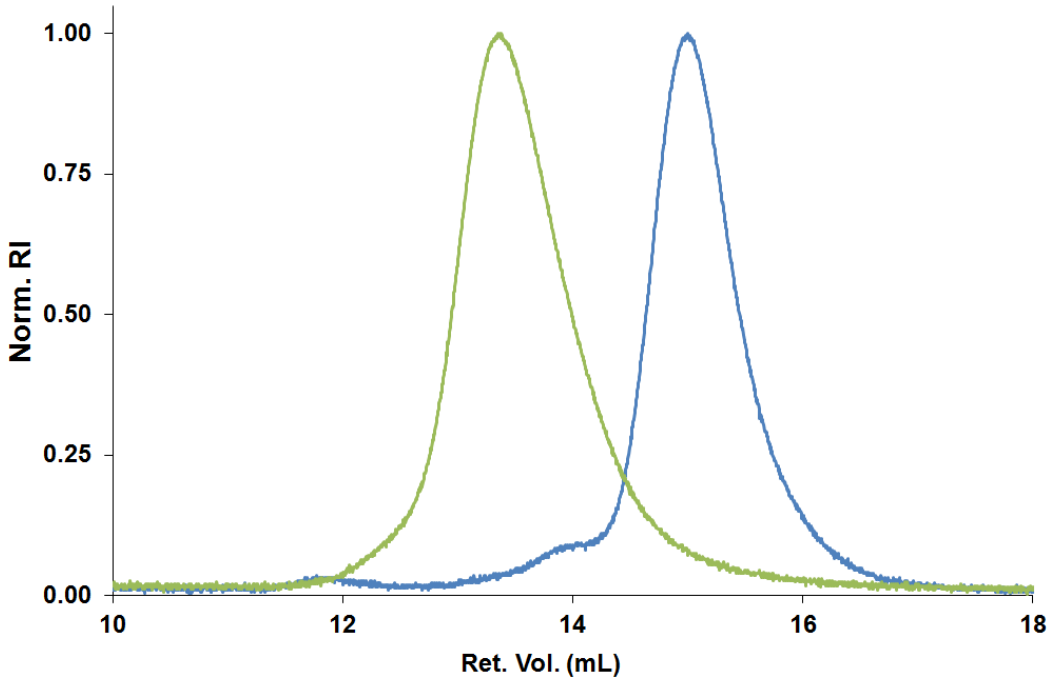

Figure 2.15: SEC data demonstrating the synthesis of cylinder-forming PS-*b*-PTMSS-*b*-PS. Green curve (left): PS-*b*-PTMSS-*b*-PS; Blue curve (right): PS aliquot.

Table 2.5: Molecular weight and dispersity data for cylinder-forming PS-*b*-PTMSS-*b*-PS.

Sample	M_n (kDa)	M_w (kDa)	Dispersity
PTMSS aliquot[a]	33.3	36.0	1.08
PS-*b*-PTMSS-*b*-PS[b]	108.6	126.0	1.16

[a]Molecular weight data calculated using PTMSS dn/dc=0.138 (*55*).

[b]M_n calculated using ^{1}H NMR, dispersity data calculated using SEC with PS-*b*-PTMSS-*b*-PS dn/dc=0.280.

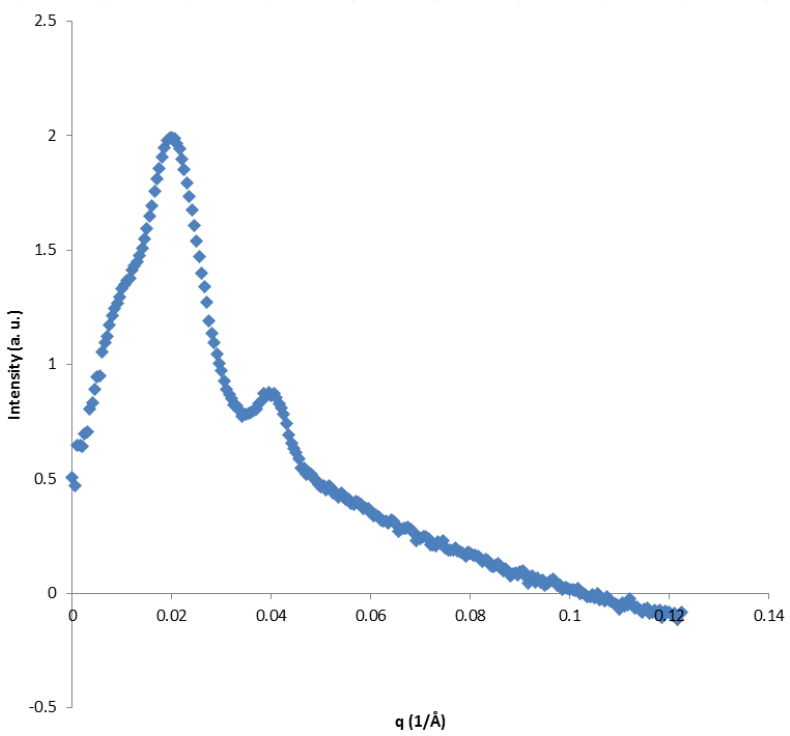

Figure 2.16: Cylinder-forming PS-*b*-PTMSS-*b*-PS small angle X-ray scattering data. The calculated domain spacing is d_{100}= 33 nm.

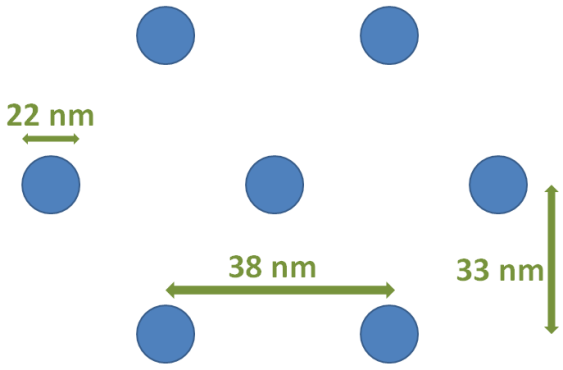

Figure 2.17: Calculated unit cell dimensions for cylinder-forming PS-*b*-PTMSS-*b*-PS (cylinders of PTMSS) based on SAXS data.

2.5 EXPERIMENTALS:

Poly(styrene-*block*-trimethylsilylisoprene):

Reagents:

Styrene, *n*-butyllithium (1.4 M in toluene), *sec*-butyllithium (2.5 M in hexanes), di-*n*-butylmagnesium (1 M in heptane), and cyclohexane were purchased from Sigma-Aldrich. Custom glassware was purchased from ChemGlass and made by the University of Texas at Austin Chemistry glass shop.

Trimethylsilylisoprene:

In a modification of a procedure from Sakurai *et al.* (**Scheme 1**) (*47*), a 250 mL RBF with condenser was charged with freshly ground Mg turnings (2.2 g, 92.2 mmol), a catalytic amount of dibromoethane, diethyl ether (100 mL), and a stir bar. After stirring for 15 min at rt, the reaction mixture was brought to reflux, and chloromethyltrimethylsilane (10.6 mL, 76.8 mmol) was added drop-wise over 30 min. In a separate 1 L RBF with addition funnel, a mixture of 1,3-bis(diphenylphosphino)propane nickel(II) chloride (1.3 g, 2.3 mmol), freshly distilled chloroprene (9.0 mL, 97.6 mmol, bp = 58-61°C, 760 torr), and diethyl ether (500 mL) was stirred at 0°C. After nearly complete Mg consumption (2 h), the pale-gray Grignard solution was cooled, added drop-wise to the dark-red, chloroprene mixture over 30 min, and stirred overnight at rt. The yellow solution was quenched with H_2O (500 mL) and extracted with ether (3 x 250 mL); the organic layers were combined, dried over $MgSO_4$, filtered, and concentrated *in vacuo*. Trimethyl-(2-methylene-but-3-enyl)silane ("trimethylsilylisoprene," TMSI) was isolated by distillation (57-60°C, 66 torr) in moderate yield (6.5 g, 60%) as a clear liquid; ^{1}H NMR (400 MHz, $CDCl_3$, δ, ppm): 6.380 (ddd, J = 17.6, 10.8, 0.4 Hz, 1H), 5.121 (dd, J = 17.6, 0.4 Hz, 1H), 5.052 (dd, J = 10.4, 0.4 Hz, 1H), 4.903 (m, 1H), 4.794 (s, 1H), 1.711 (d, J = 0.8 Hz, 2H), 0.007 (s, 9H); ^{13}C NMR (400 MHz, $CDCl_3$, δ, ppm): 144.141, 139.915, 114.142, 113.606, 21.190, -

1.250; IR (NaCl): 3084, 2955, 2897, 1588, 1248, 851 cm^{-1}; HRMS (ESI, *m/z*): $[M+H]^+$ calcd for $C_8H_{16}Si$, 141.1021; found, 141.1023.

Purification:

All purifications and polymerizations were performed under vacuum or in an argon atmosphere using standard Schlenk techniques (*51*).

Styrene:

To two 500 mL Schlenk flasks, di-*n*-butylmagnesium (*ca.* 1.5 mL for every 5 g styrene) was added in the glove box, and the solvent was removed *in vacuo* with the Schlenk line. Styrene monomer was freeze-pump-thawed three times in a third 500 mL Schlenk flask. The styrene monomer was then distilled trap-to-trap through a flame-dried short path into the first dry di-*n*-butylmagnesium Schlenk flask and then stirred for an hour at room temperature. The styrene was then trap-to-trap distilled again into the second di-*n*-butylmagnesium Schlenk flask and stirred for an hour at room temperature, then distilled trap-to-trap into a flame-dried and pre-weighed burette.

Trimethylsilylisoprene:

Careful fractional distillation of as-synthesized TMSI was found to be extremely important, as residual chloroprene appears to prevent initiation and/or propagation of the anionic polymerization of TMSI. Fractionally distilled TMSI was vacuum distilled twice from *n*-butyllithium, using the same procedure as described for the styrene monomer, but taking care not to allow the temperature of the TMSI and *n*-butyl lithium slurry to rise above 0°C (to prevent explosive exothermic polymerization). Extreme caution must be taken during distillation of TMSI monomer over purification reagents. The purified TMSI monomer was then trap-to-trap distilled into a flame-dried and pre-weighed burette.

Cyclohexane:

Cyclohexane was passed through a Pure Solv MD-2 solvent purification system containing two activated alumina columns to remove trace water and a copper supported redox catalyst to remove oxygen. The purified cyclohexane was added to a 500 mL Schlenk flask directly from the purification system.

Anionic Polymerization:

Anionic polymerization of P(S-*b*-TMSI) (**Scheme 2.2**) followed the general procedure described by Bailey *et al.* for synthesizing poly(styrene-*block*-isoprene) (*45*). Purified styrene (16 g, 154 mmol, 421 eq.) polymerization was initiated with *sec*-butyllithium (0.26 mL, 0.36 mmol, 1 eq.) at 40°C in cyclohexane (240 mL), which resulted in the development of a red, clear solution over the course of 5 min. After 12 h, a 5 mL aliquot of the polystyrene was extracted from the reactor for analysis and terminated with degassed methanol. Purified TMSI monomer (5.87 g, 41.9 mmol, 114.8 eq) was then added to the reactor drop-wise over the course of 3 minutes; the solution almost instantly turned colorless at the beginning of the addition. TMSI was reacted for 12 h, followed by addition of degassed methanol to quench the living anions. The block copolymer was precipitated in methanol, filtered, and freeze dried from a 10 wt % benzene solution with 0.25 wt % butylated hydroxytoluene (BHT) inhibitor to prevent oxidative degradation of the PTMSI backbone. The volume fraction of PS:PTMSI was calculated to be 0.83:0.17 as determined by ^{1}H NMR, assuming the density of the PTMSI block is equal to that of polyisoprene, as reported by Fetters *et al*. (*59*).

Synthesis of poly(styrene-*block*-methyltrimethylsilyl methacrylate)

Reagents:

Styrene, *n*-butyllithium (1.4 M in toluene), *sec*-butyllithium di-*n*-butylmagnesium (1 M in heptane), calcium hydride (CaH_2, reagent grade powder, ca. 0-2 mm, 90-95%), diphenylethylene, and lithium chloride were purchased from Sigma-Aldrich.

Methyltrimethylsilyl methacrylate (MTMSMA) was purchased from Gelest and uninhibited tetrahydrofuran (THF) was purchased from JT Baker. Basic alumina (Brockman activity I, 60-325 mesh) was purchased from Fischer. Custom glassware was purchased from ChemGlass and made by the University of Texas at Austin Chemistry glass shop.

Purification:

All purifications and polymerizations were performed under an argon atmosphere using standard Schlenk techniques (*60*).

Styrene:

To two 500 mL Schlenk flasks, di-*n*-butylmagnesium (ca. 1.5 mL for every 5 g styrene) was added in the glove box, and the solvent was removed *in vacuo* with the Schlenk line. Styrene monomer was freeze-pump-thawed three times in a third 500 mL Schlenk flask. The styrene monomer was then distilled trap-to-trap through a flame-dried short path into the first dry di-*n*-butylmagnesium Schlenk flask and was stirred for an hour at room temperature. The styrene was then trap-to-trap distilled again into the second di-*n*-butylmagnesium Schlenk flask followed by an hour of stirring at room temperature. Finally, the styrene was trap-to-trap distilled into a flame-dried and pre-weighed burette.

Methyltrimethylsilylmethacrylate:

Methyltrimethylsilylmethacrylate was first filtered through basic alumina to remove inhibitor, followed by addition of the monomer to a 500 mL Schlenk flask and three freeze-pump-thaw-cycles. To two 500 mL Schlenk flasks, calcium hydride (ca. 5 g per 5 g MTMSMA) was added and the flasks were pump/purged three times with argon gas. MTMSMA was trap-to-trap distilled through a flame-dried short path into the first CaH_2 flask. The MTMSMA was then trap-to-trap distilled again into the second CaH_2

Schlenk flask followed by an hour of stirring at room temperature. Finally, the MTMSMA was trap-to-trap distilled into a flame-dried and pre-weighed burette.

Tetrahydrofuran:

Tetrahydrofuran was passed through a Pure Solv MD-2 solvent purification system containing two activated alumina columns to remove trace water and a copper supported redox catalyst to remove oxygen. The purified THF was added to a 500 mL Schlenk flask directly from the purification system.

Diphenylethylene:

1,1-diphenylethylene was vacuum distilled twice from *n*-butyllithium and stored in a glove box.

Anionic Polymerization of poly(styrene-block-methyltrimethylsilyl methacrylate):

A polymerization reactor was charged with a stir bar and LiCl (5 eq., 0.09 g, 2.21 mmol) followed immediately by five flame-drying cycles to remove trace water and oxygen. Purified THF (249 mL) was added to the reactor and the temperature reduced to ca. -78 ^{0}C with a dry-ice isopropanol bath. For the remainder of the polymerization the pressure in the reactor was maintained at approximately 3 psi. *sec*-butyllithium (1 eq., 0.32 mL, 0.44 mmol) initiator (measured volumetrically) was introduced into the reactor via syringe and allowed to stir for 5 minutes. The following process describes the monomer "seeding" process, which is used to reduce polydispersity in the synthesized polymers (*61*). A slight molar excess of purified styrene monomer relative to *sec*-butyllithium was added to the stirred solution of solvent and initiator to initiate all living chain ends, which resulted in an immediate solution color change from colorless (styrene monomer) to orange (styrenyl anions with a lithium counter-cation in THF). After 15 minutes, the seeding process was considered complete and the remaining styrene monomer was added dropwise to the reactor (total styrene: 360 eq., 16.6 g, 159 mmol). The temperature of the solution was always maintained at or below -65 ^{0}C. 4 hours after

the start of the seeding process, a 5 mL aliquot of polystyrene (PS) was extracted from the reactor and precipitated in degassed methanol. Diphenylethylene (5 eq., 0.39 mL, 2.21 mmol) (measured volumetrically) was then introduced into the reactor by syringe, which resulted in the immediate formation of clear, red solution. After 3 hours of stirring, the MTMSMA monomer was seeded, which immediately rendered the solution colorless, and after 15 minutes the remaining MTMSMA was added dropwise (total MTMSMA: 131 eq., 9.97 g, 57.9 mmol). After 3 hours, 5 mL of degassed methanol was injected into the reactor and stirring was continued for 30 minutes. The reactor was then vented to air. The solution was precipitated in methanol, filtered, and freeze-dried from a 10 wt% benzene solution, resulting in a white, powdery solid. The cylinder-forming poly(styrene-*block*-methyltrimethylsilyl methacrylate) (PS-*b*-PMTMSMA) was found to have 66 vol% PS and 34 vol% PMTMSMA using mol% values obtained by ^{1}H NMR and density values reported by Fetters (*59*), assuming PMTMSMA has the same density as PMMA. Small angle X-ray scattering data indicates a d_{100} distance of 49 nm for the cylinder-forming PS-*b*-PMTMSMA.

Synthesis of poly(styrene-*block*-trimethylsilylstyrene-*block*-styrene)*:*

Trimethylsilylstyrene monomer:

In a modified procedure of Chaumont et al. (*62*), freshly ground magnesium (2 eq, 5.262 g, 216.5 mmol) was added to a three neck 500 mL RBF with a stir bar, outfitted with a reflux condenser, addition funnel, septum, and pump/purged three times with nitrogen and placed under dynamic nitrogen. Dry THF (130 mL) was added followed by 1 mL of 4-chlorostyrene and three drops of dibromoethane. Upon refluxing the solution, a brown color developed over 10 minutes, after which the remaining 4-chlorostyrene (total: 1 eq, 15.0 g, 108.2 mmol) was added. Subsequently, trimethylsilyl chloride (2 eq, 23.52 g, 216.5 mmol) was added dropwise and stirred for 1.5 h. The reaction was then quenched with the stepwise addition of isopropanol, methanol, and water, diluted with diethyl ether and washed with water. The water layer was extracted three times with

diethyl ether, the organic fractions were combined, washed with brine, and dried over $MgSO_4$. The slightly cloudy, colorless liquid was filtered and dried *in vacuo*, followed by distillation (b.p. 65-68°C, 7 torr) to yield a clear, colorless liquid in ca. 65% yield. ^{1}H NMR ($CDCl_3$) δ ppm: 7.50 (dd, *J* = 27, 9 Hz, 4H), 6.77 (dd, *J* = 18, 12 Hz, 1H), 5.84 (d, *J* = 18 Hz, 1H), 5.32 (d, *J* = 12 Hz, 1H), 0.35 (s, 9H). ^{13}C NMR ($CDCl_3$): 141 (1C), 139 (1C), 138 (1C), 136 (2C), 126 (2C), 115 (1C), 0 (3C) ppm. IR: 3062.89, 3008.08, 2955.87, 2896.70, 1629.11, 1598.29, 1543.93, 1500.20, 1389.34, 1248.15, 1208.53, 1115.63, 1104.81, 1115.63, 1028.18 cm^{-1}.

Poly(styrene-block-trimethylsilylstyrene-block-styrene)

Potassium naphthalenide (KNaph) was prepared according to literature procedure (*63*). Styrene and trimethylsilylstyrene (TMSS) monomers were each purified two times by distillation over di-*n*-butylmagnesium. PS-*b*-PTMSS-*b*-PS was synthesized by sequential anionic polymerization under an Ar atmosphere using well-established Schlenk line techniques (*44*, *51*, *64*). Potassium naphthalenide (1.46 mL, 0.17 M) was used to initiate approximately 4 units of α-methylstyrene (0.059 g, 0.000499 mol) in a stirred solution of THF (78 mL) at -78°C, which instantly turned bright red and was reacted for *ca.* 2 hr. Trimethylsilylstyrene was then "seeded" using 10 drops of monomer to evenly initiate all chains. After 5 minutes, the remaining trimethylsilylstyrene (5.12 g, 0.0290 mol) was added dropwise to the reactor, ensuring the reactor internal temperature remained less than -65°C. Four hours after the addition of TMS, a polytrimethylsilylstyrene (PTMSS) aliquot was extracted from the reactor, and styrene (5.19 g, 0.0499 mol) was added dropwise to the reactor. After 4 more hours, degassed methanol (~3 mL) was rapidly added to the reaction mixture to quench all living anions. The resulting polymer was precipitated in methanol to yield a white powder, filtered, and dried *in vacuo*. Lamellar-forming P(S-*b*-TMSS-*b*-S) was characterized by SEC (Figure 12) and SAXS (Figure 13) and found to have periodicity L_0=30 nm as calculated by $L_0=2\pi/q^*$, where q* is the primary scattering peak. IR: 3061, 3026, 2954, 2925, 2851, 1600, 1493, 1452, 1399, 1248, 1115 cm^{-1}. The volume fraction as calculated by ^{1}H

NMR: 48:52 vol% PTMSS:PS, using a density of PS=0.969 g/cm^3 (*59*) and PTMSS=0.965 g/cm^3 (measured).

2.6 CONCLUSIONS:

Several Si-BCPs were successfully synthesized and characterized. The low T_g and thermal instabilities of PS-*b*-PTMSI drove the development of alternative Si-BCPs. Both PS-*b*-PMTMSMA and PS-*b*-PTMSS-*b*-PS appeared to have significantly improved properties, with high T_g and thermal stability.

2.7 ACKNOWLEDGEMENTS:

Dr. Jeffrey Strahan contributed to the anionic synthesis of PS-*b*-PMTMSMA and PS-*b*-PTMSI, along with undergraduate research assistant Morgan W. Schulze. The PS-*b*-PTMSS-*b*-PS triblock copolymers and the lamella-forming PS-*b*-PMTMSMA were synthesized by Julia D. Cushen from the Ellison group.

Chapter 3: Substrate Surface Treatments

3.1 Surface Energy

The control of interfaces is crucial for thin film block copolymer orientation control. The underlying reason relates to the concept of surface energy (γ), which is the energetic penalty for creating a surface (**Equation 3.1**), where ∂G represents the change in Gibbs free energy, ∂A is the change in area, and (n, T, P) represents constant moles, temperature, and pressure (*65*). Surface energy and interfacial energy are used interchangeably herein, but it should be pointed out that surface energies reported in literature are generally with air as a reference (i.e. the second material in contact with the polymer. When considering thin film block copolymer orientation control, while the top interface is often air (or solvent), the substrate interface consists of the block copolymer in contact with a second polymer or small molecule, not air. Care must be taken when attempting to compare surface energies with air and then extrapolating the expected behavior to other types of interfaces.

$$\gamma = \left(\frac{\partial G}{\partial A} \right)_{n,T,P} \qquad \textbf{Eq. 3.1}$$

Equation 1 actually represents a surface energy density (it has units of energy per area), but it will be referred to as surface energy throughout the rest of this document for brevity. Typical units of the surface energies discussed herein are in mN/m (milli-Newtons per meter) by convention, which equal J/m^2 (joules per meter squared). Surface energy is thus related to the area of the surface created and the amount of increased energy associated with that surface. The concept of surface energy is not necessarily intuitive; a few examples will be provided and should help provide a basic understanding and feel for what it means. The surface energy of water (73 mN/m) (*66*) is relatively high compared to organic soft materials, but why? **Figure 3.1** shows a schematic of a cross-section of a collection of water molecules. (Of course, in reality the water molecules extend in three dimensions, which are ignored for simplicity).

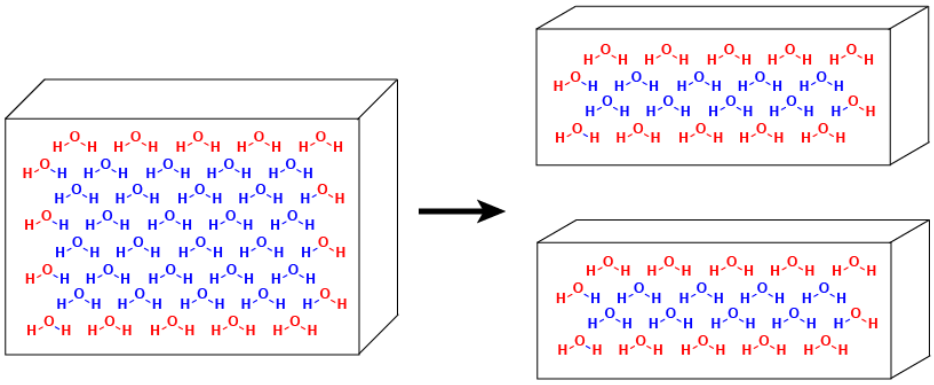

Figure 3.1: The creation of surface area leads to the reduction in favorable intermolecular interactions and leads to the increase of energy due to the surface.

The box on the left of **Figure 3.1** contains water molecules in two different environments, bulk (blue) and at a surface (red). Bulk water molecules (blue) can maximize their favorable intermolecular interactions (including hydrogen bonding) because they are surrounded by the maximum number of other water molecules. In contrast, water molecules at the surface are lacking some intermolecular interactions because they are not fully surrounded by other water molecules. When the box containing water molecules on the left side of **Figure 3.1** is split into two (on the right side of **Figure 3.1**), it creates more surface area and results in an increased number of surface water molecules in contact with the air rather than with other water molecules (**Figure 3.1**, red). In general, these intermolecular interactions with a second material (for instance, H_2O-air interactions) will be weaker than the intermolecular interactions of the same type of molecules (H_2O-H_2O), and leads to an increase in energy as area is created. This energy increase is surface energy. From the simplistic argument used in **Figure 3.1**, it can be surmised that surface energy is related to the number of missing bonds (or intermolecular interactions) (N), the bond or interaction strengths (ε), and the density of atoms on the surface (ρ), as shown in **Equation 3.2** (*65*). The ½ factor is due to the creation of two surfaces when splitting the box into two pieces.

$$\gamma = \frac{1}{2} N \varepsilon \rho \qquad \textbf{Eq. 3.2}$$

Thus, stronger intermolecular interactions result in a higher surface energy because there is a larger energetic penalty for reducing the number of intermolecular contacts as surface is created. There are five types of intermolecular interactions, ranked approximately from strongest to weakest (*67*, *68*): charge-charge (~500 kJ/mol), ion-dipole (~100 kJ/mol), dipole-dipole (~0.03-1 kJ/mol), dipole-induced dipole, and induced dipole-induced dipole (London dispersion forces, ~1 kJ/mol). For comparison purposes, covalent bond strengths are on the order of 200-800 kJ/mol, and hydrogen bonds are 10-40 kJ/mol (*67*). In reality there are many other factors that influence surface energy, including higher-order neighbor interactions, crystal structure, surface reorganization, and molecular segregation, but **Equation 3.2** provides some valuable insight into the behavior of materials presented herein.

In practice, surface energy values are extremely hard to measure with acceptable accuracy or precision (*69*). While a *very* rough estimate of the surface energy of a given polymeric material can be calculated from static or dynamic contact angle experiments (possibly within 5-10 mN/m) using three different types of liquids (*70*), these measurements are approximations that are imprecise and difficult to reproduce. One of the great challenges associated with contact angle measurements is the choice of liquids, which necessarily cannot dissolve or sorb into the polymeric material under evaluation. Even slight swelling can significantly impact measured contact angles. There is a reasonable chance that one liquid can be found which will not interact with the polymer, but three liquids is nearly impossible. Other notable potential difficulties include drop size consistency, surface roughness, contact angle hysteresis, surface contaminants, and surface chemical heterogeneities. An excellent discussion about contact angle measurement difficulties and potential solutions can be found in Strobel et al. (*71*). More easily utilized than calculated surface energies are the relative values of only water

contact angles. These values loosely correspond to polarity, which is related to surface energy (more polar things generally have higher surface energy due to their strong intermolecular interactions, as evidenced by the argument above using water molecules). **Figure 3.2** shows rough estimates of the surface energies of different types of materials.

Figure 3.2: Rough estimates of the surface energies of fluorinated, silylated, non-polar organic, and polar materials.

Figure 3.2 provides some insight into the approximate surface energies of materials containing different types of functional groups. As materials go from being polar (water, surface energy 73 mN/m) to less polar (polystyrene, surface energy ca. 40 mN/m) (*33*), intermolecular interactions decrease, and the energetic penalty for creating a surface also decreases. Importantly, the incorporation of silicon into a material such as poly(trimethysilylstyrene), poly(methyltrimethylsilylmethacrylate), or poly(dimethylsiloxane) reduces the surface energy drastically to around 25 mN/m (*33*, *69*). A similar (and potentially larger) decrease in surface energy is observed when fluorine is incorporated into a material (*72*). What is the underlying cause of such a large dependence of surface energy on functional groups?

Fluorine

The largest source of intermolecular interactions in non-polar molecules is London dispersion forces (induced dipole-induced dipole), since there are no significant permanent dipole moments. These forces can account for almost 100% of the

intermolecular forces in non-polar molecules (like Ne-Ne and CH_4-CH_4 interactions), but require polarizable bonds (*67*). For example, the dependence of the strength of intermolecular forces on bond polarizability is nicely captured with the halogen series, F_2, Cl_2, Br_2, I_2. Fluorine is the least polarizable, has the weakest intermolecular forces, and is a gas, as is chlorine. Bromine is more polarizable, has stronger intermolecular forces, and is a liquid. Iodine is the most polarizable, has the strongest intermolecular forces, and is a solid. To consider the effect of fluorine on surface energy, it is simplest to compare a fully-fluorinated hydrocarbon, such as perfluorohexane, to its unfluorinated counterpart, hexane. Fluorine is extremely electronegative and thus creates large C-F bond dipoles throughout the molecule, but the overall molecular is non-polar (*73*). The C-F bonds have low polarizability because fluorine does not significantly share the bonding electrons, which results in significantly fewer London dispersion forces relative to hexane. As a result, perfluorinated hexane will have a significantly lower surface energy than hexane. While the presence of molecular dipoles in polar molecules will result in London dispersion forces contributing less to the overall sum of intermolecular interactions, the local non-polarizable C-F bonds coupled with surface reorganization at interfaces allows for fluorine to be expressed at the surface and still results in extremely low surface energies (*72*).

Silicon

The low surface energy of silicon can be attributed to its atomic size. To a first approximation surface energy is related to the number of atoms on a surface (**Equation 3.2**). Comparing the size of a silicon atom (van der Waals radius 2.1 Å) to a carbon atom (van der Waals radius 1.68 Å) (*74*), a crude approximation based only on size says the number of carbon atoms that can fit on a surface is approximately 1.56 times larger than the number of silicon atoms. This factor (1.56) is approximately the surface energy of hydrocarbon materials relative to silylated materials. Of course, as discussed above, many other factors must be considered, and size has to be balanced with polarizability. However, experimental evidence clearly demonstrates silicon-containing materials have

surface energies on the order of fluorinated materials (or slightly higher), which is significantly lower than hydrocarbons and polar molecules (*66, 69, 75*).

3.2 BLOCK POLYMER SUBSTRATE SURFACE NEUTRALIZATION

Block polymer thin film orientation control usually requires surface functionalization. The present discussion will involve the orientation of a BCP that only depends on the nature of the substrate interactions; a more detailed description involving all interfaces is postponed until Chapters 6 and 7. The purpose of the substrate surface treatment is to balance the interfacial interactions between each block and the surface such that there is no preference for a single block to interact with the substrate surface. **Figure 3.3** demonstrates the different wetting scenarios at a constant film thickness of $1*L_0$. Note that the there are two possible ways to achieve parallel-oriented lamella; either the blue or red block is exclusively in contact with the bottom surface. In contrast, perpendicular lamellae necessarily have both the blue and red blocks in contact with the surface. The key to induce perpendicular lamella is to choose an alignment layer that produces equal differences in interfacial energy ($\Delta\gamma$) between each block and the surface (red block: $\Delta\gamma_{Red\text{-}surface}$, blue block: $\Delta\gamma_{Blue\text{-}surface}$).

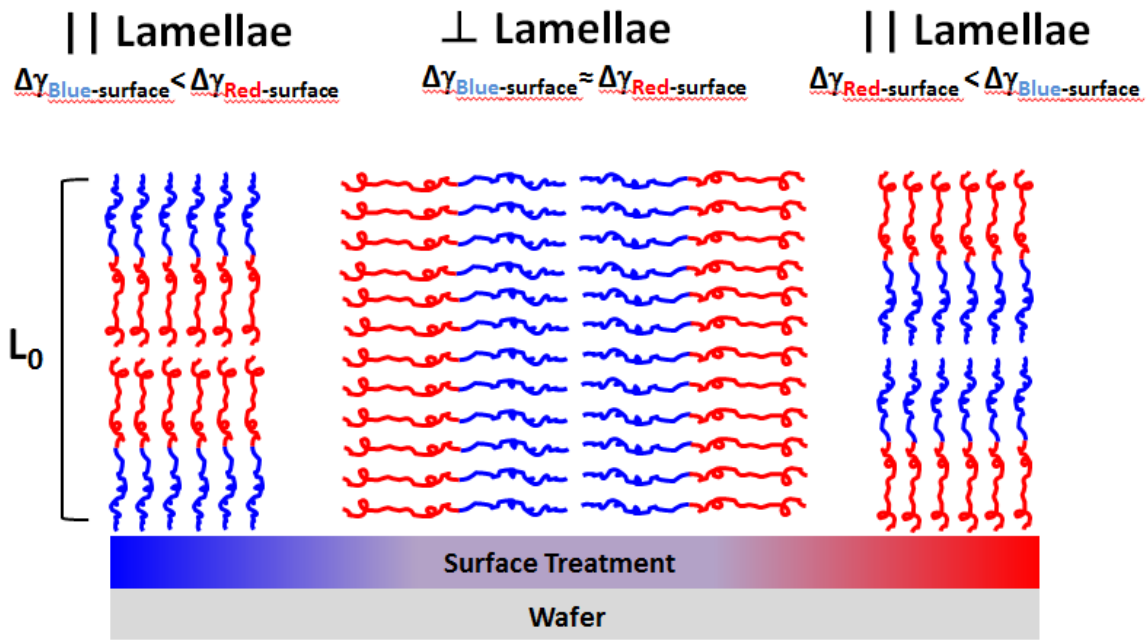

Figure 3.3: Three different substrate surface wetting scenarios for a lamella-forming BCP. Left: the blue block wets the surface which results in parallel lamella; middle: both blocks wet the surface which results in perpendicular lamella; right: the red block wets the surface which results in parallel lamella.

BC thin film behavior has been studied by many researchers (*76-79*) and a recent review (*80*) has highlighted the importance of film thickness and interfacial interactions in dictating the BC orientation. One method of inducing cylinder or lamellar domains to orient perpendicular to the substrate is by treating the substrate with a surface modification agent such that the surface has an interfacial energy between that of each block. This type of substrate surface has been termed "neutral" because the enthalpic penalty for each block to establish contact with the substrate is approximately equal (*76*). If this condition is not appropriately met, the cylinders or lamellae will usually lie parallel to the substrate with the block that most prefers the surface wetting the substrate.

The thickness of the BC film can also influence the orientation of the BC. This effect is often attributed to differences between the overall film thickness and multiples of the bulk domain periodicity (L_o) of the BC, which can be convoluted with the nature of the interfacial interaction at the substrate and free surface (*80*). If the film thickness is not commensurate with the bulk domain periodicity, the BC may be forced to assemble with a domain spacing or periodic structure that is not consistent with those in bulk or it may form islands of varying thickness. This "frustration" phenomenon was first described by Russell (*79*).

3.3 POLY(STYRENE-*BLOCK*-METHYL METHACRYLATE) SURFACE TREATMENTS

The first thin film work performed on the project utilized the ubiquitous poly(styrene-*block*-methyl methacrylate) (PS-*b*-PMMA) block copolymer. This work is reprinted with permission from C. M. Bates et al., Langmuir 2011, 27, 2000. The etch selectivity between the PS and PMMA domains is relatively small, but the material is relatively easy to orient in thin films. The BCP provided a framework to develop surface treatment synthesis and thin film techniques. The lessons learned in the initial surface treatment studies with PS-*b*-PMMA were extremely valuable and subsequently applied to the Si-BCPs.

A variety of surface treatment techniques have been reported to yield surfaces for controlling BC orientation. Reports by Nealey (*81*), Baker (*82*), and Daillant (*83*) describe the use of chlorosilanes and their subsequent oxidation to control BC orientation, which can also be used in conjunction with a gradient technique (*84*) to yield a distribution of surface energies on a single wafer. Earlier it was shown that a substrate coated with a random copolymer of styrene and methyl methacrylate induces perpendicular orientation of PS-*b*-PMMA (*85*). This approach was further optimized by incorporation of a hydroxyl end-group that can bond to the substrate surface to prevent random copolymer diffusion into the block copolymer thin film (*86*). The term 'brush' was applied to polymeric surface treatments that produced chains bound to the surface

through reaction of the single terminal hydroxyl group with silanol groups on the substrate surface (*87*). Additional research revealed that the molar composition of the random copolymer surface treatment affects the water contact angle, and by forming "non-preferential interactions" between the treated surface and either block of the BC, these materials induced the BC to orient perpendicular to the substrate (*76, 86, 88, 89*). Small variations in contact angle, and thus surface energy, have been shown to be sufficient to bias BC orientation. For poly(styrene-*r*-methyl methacrylate) used for alignment of associated BCs, the estimated surface energies at 170°C are 29.9 mN/m (polystyrene homopolymer) and 30.2 dyn/cm (poly(methyl methacrylate) homopolymer), a difference of less than 1% (*86*).

Due to long reaction times required to form a covalent bond between a polymeric end-group and the substrate surface, subsequent reports have described use of random terpolymers that incorporate cross-linking chemistry to quickly yield a robust, neutral surface. Like covalently-bound brushes, the chains in these cross-linked films will not diffuse into block copolymer thin films applied on top. Several cross-linking functional groups have been exploited for this application including acrylates (*90*), epoxides (*90*), benzocyclobutanes (*91*), and benzyl azides (*92*). Although not properly representative of traditional polymer brush architecture, the term "brush" has also been applied to these cross-linked surface treatments.

Rather than manipulating the mole ratio of surface treatment components in random terpolymers containing monomer 1 with crosslinking functionality, and monomers 2 and 3 that are identical to the monomers in the BC, we proposed a simpler approach for generating neutral surfaces obtained by cross-linking substituted styrenes (*69*). This approach was started in collaboration with Dr. Jeffrey R. Strahan in our group and simplified surface modification by incorporating a small amount of 4-vinylbenzyl azide into a polymer composed mostly of a para-substituted styrene. The substituted styrene majority component primarily defines the surface energy of the treated substrate

while the 4-vinylbenzyl azide in the copolymer undergoes thermal reactions responsible for cross-linking (*93*) through highly reactive nitrene intermediates (*94*). In the event that uncross-linked polymer remained after the heating step, it could be removed by solvent washing the cross-linked surface before spin coating the block copolymer on top.

A distinguishing feature of the substituted styrene work from the random terpolymer approach discussed above (*90*-*92*) is that random terpolymers used for manipulating surface energy require a truly random architecture. If this is not achieved, the modified surface may display regions differing in interfacial energy driven by partial phase separation of polymer segments rich in one monomer. This would render the surface non-neutral and randomly chemically patterned in a way that would be detrimental to driving uniform BC orientation. There are also inherent difficulties related to random terpolymer synthesis including reactivity ratio differences, monomer mixture drift, and polymer composition drift. These issues can be addressed by restricting monomer conversion to low levels (e.g., less than 15%) in batch polymerizations but in that case a substantial amount of monomer must be recovered or discarded. Alternatively, one or more monomers can be added continuously in a semi-batch polymerization, but this complicates the synthetic procedure.

Our viewpoint was that the use of two completely different monomer species (e.g., a methacrylate and a styrene as seen in previous work) to control surface energy is unnecessary because the variety of functional groups available on styrene derivatives. Since there is already a wealth of information in the literature regarding PS-*b*-PMMA, and since it is generally regarded as the easiest block copolymer to orient in thin films, it was chosen as the block copolymer to demonstrate the efficacy of the styrene-only surface treatments. However, since substituted styrenes presumably give access to a much larger range of surface energies it was envisioned that this technique could also be applied to non-traditional functional block copolymers such as poly(styrene-*block*-dimethylsiloxane) (*33*), poly(lactide-*block*-dimethylsiloxane-*block*-lactide) (*35*),

poly(ferrocenyldimethylsilane-*block*-dimethylsiloxane) (*95*), and poly(α-methylstyrene-*block*-4-hydroxystyrene) (*96*) whose block segments have vastly different surface energies compared to PS and PMMA. In addition, making random co-polymers of some of these systems is challenging. The synthesis of substituted styrene polymers with <10% 4-vinylbenzylazide has the advantage that a copolymer composed of two styrenic monomers can be synthesized using traditional and inexpensive initiators such as azobisisobutyronitrile (AIBN) instead of more complicated schemes involving nitroxide-mediated (*86*) or reversible-addition-fragmentation chain transfer (RAFT) (*92*) polymerization techniques. The benzyl azide moiety (*92*) was chosen as the cross-linking agent because of its synthetic accessibility and short thermal cross-linking reaction times.

During the course of the substituted styrene synthesis and characterization work (reported by Strahan (*48*) and Bates et al. (*69*)) it was actually discovered than an even simpler system effected the same control of PS-*b*-PMMA orientation as substituted styrene derivatives. Polymers containing only styrene and 4-vinylbenzylazide monomers (poly(styrene-*random*-4-vinylbenzylazide), PS-*r*-PVBzAz) could be used to control the orientation of PS-*b*-PMMA to varying degrees of success depending on the relative ratio of polystyrene:poly(4-vinylbenzylazide).

The serendipitous discovery of perpendicular cylinders observed on PS-*r*-PVBzAz prompted a set of experiments probing the effect of the crosslinked poly(4-vinylbenzyl azide) content on the orientation of PS-*b*-PMMA. A series of five random copolymers of polystyrene and poly(4-vinylbenzyl azide) were synthesized with compositions between 5-100 mol% PVBzAz (**Table 3.1**). Five different thicknesses of PS-*b*-PMMA films were spin-coated onto each of these random copolymers and the BC orientation was studied by AFM (**Figure 3.4**). Full AFM images are provided in **Figures 3.5-3.9**. L_0 is defined as the row-to-row distance (d_{100}) of the cylinders; as measured by bulk SAXS experiments L_0=34.7 nm (*48*). Some PS-*b*-PMMA films were rough (±5 nm) and displayed regions of mixed morphology or differing feature density as a function of

the local thickness, e.g., the PS-*b*-PMMA film 25 nm in thickness prepared on 5 mol% PVBzAz. In these cases, the AFM images shown in **Figure 3.5** were selected to show the boundary between distinct regions of different orientation so that all were faithfully represented in one image. Full AFM images are provided **Figures 3.6-3.10**. Many PS-*b*-PMMA films, such as the 25 nm thick film on 28 mol% PVBzAz, were homogenous and displayed the same orientation and feature density over the entire film. Generally, 28 mol% poly(4-vinylbenzyl azide) provided the widest range of BC film thicknesses that produced dense perpendicular cylinders, but dense perpendicular cylinders were also achieved for other selected cases such as the 75 nm thick film on 56 mol% poly(4-vinylbenzyl azide). It is especially interesting to note that even the crosslinked homopolymer of poly(4-vinylbenzyl azide) induced dense perpendicular cylinders at 75 nm BC film thickness. To the authors' knowledge this is the first example of a single component surface treatment that can produce dense perpendicular cylinders of P(S-*b*-MMA) after thermal annealing without also prepatterning the substrate either physically or chemically. It should be noted that there are examples of single-component neutralization layers for block copolymers such as poly(styrene-*block*-ethylene oxide) with organosilicate additives (*97*) which have been successfully combined with directed self-assembly to yield excellent control of lamellar features within surface topographic features (*38*).

Table 3.1: Characterization of PS-*r*-PVBzAz.

mol% PVBzAz	M_w (kDa)[a]	M_n (kDa)[a]	Dispersity[a]
5	21.6	11.6	1.85
28	35.4	13.9	2.54
49	35.2	13.0	2.71
56	40.1	17.3	2.32
100	49.9	34.2	1.46

[a] Measured relative to polystyrene standards

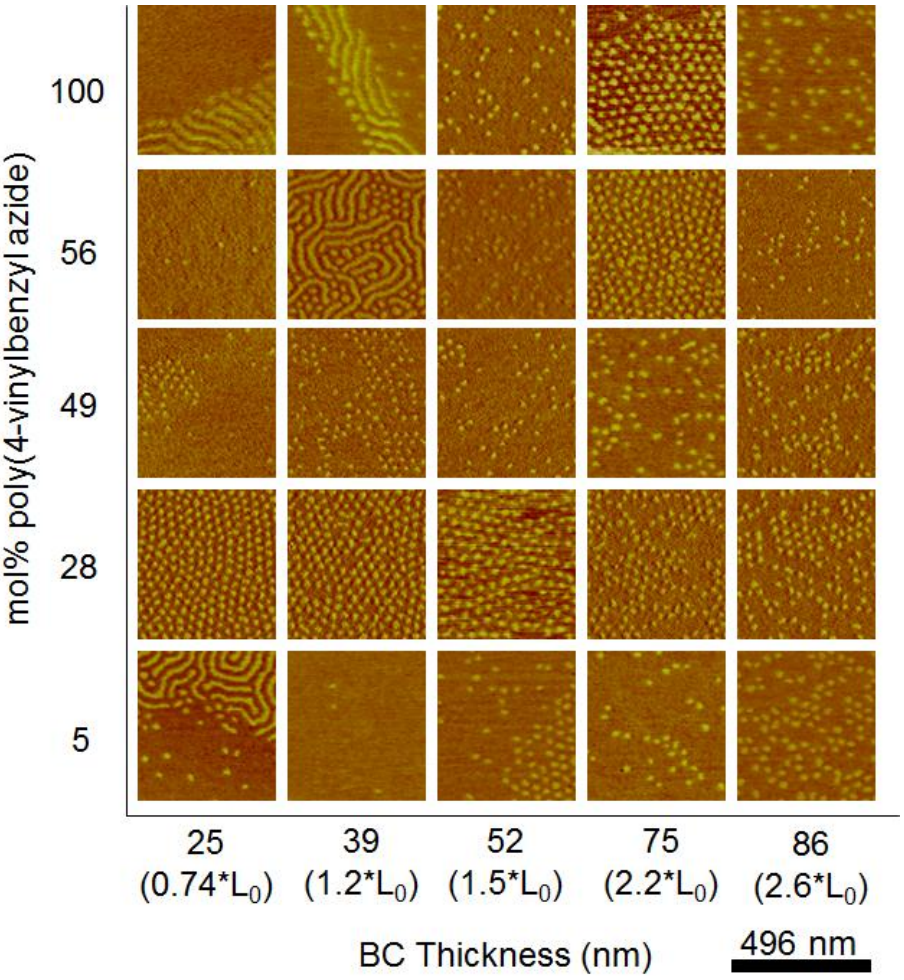

Figure 3.4: AFM images of five PS-*b*-PMMA film thicknesses on five different PS-*r*-PVBzAz random copolymers of various compositions. The AFM images were chosen to be representative of the entire sample.

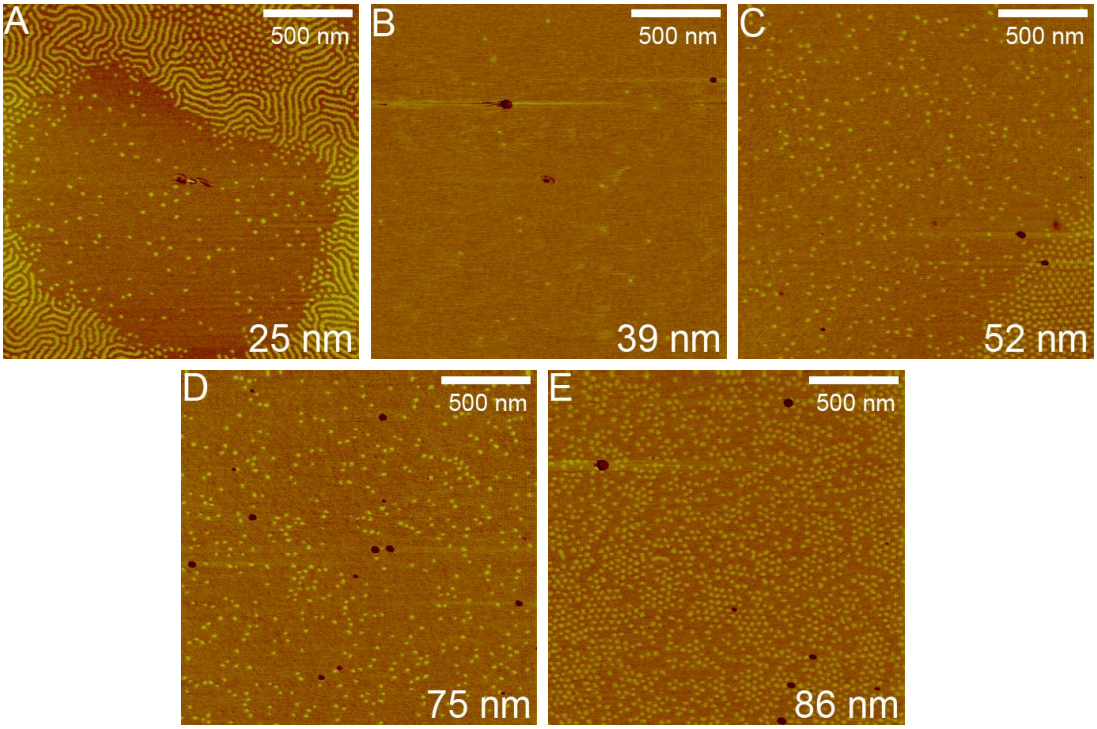

Figure 3.5: Full AFM images of PS-*r*-PVBzAz with 5 mol% VBzAz.

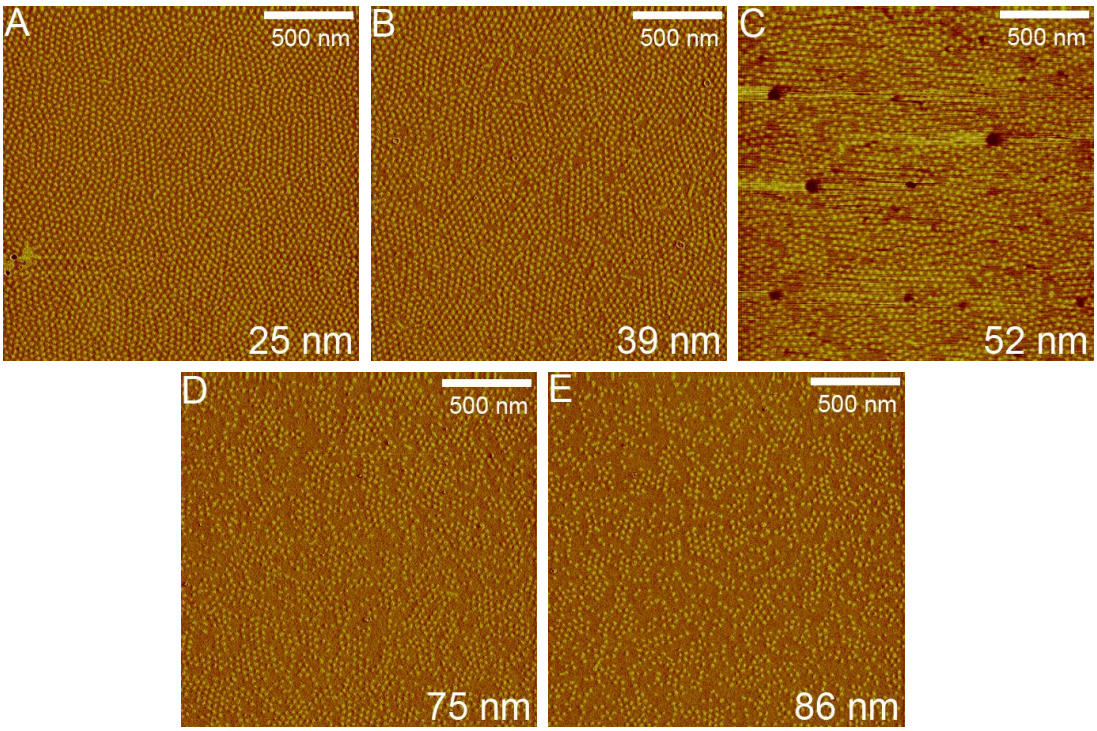

Figure 3.6: Full AFM images of PS-*r*-PVBzAz with 28 mol% VBzAz.

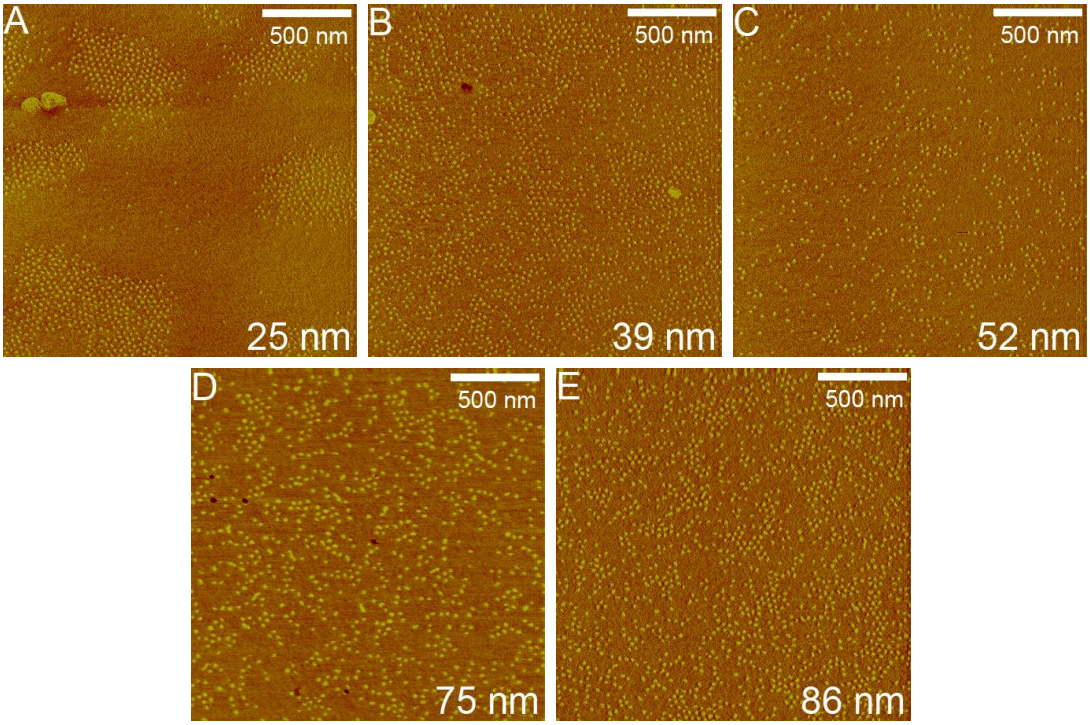

Figure 3.7: Full AFM images of PS-*r*-PVBzAz with 49 mol% VBzAz.

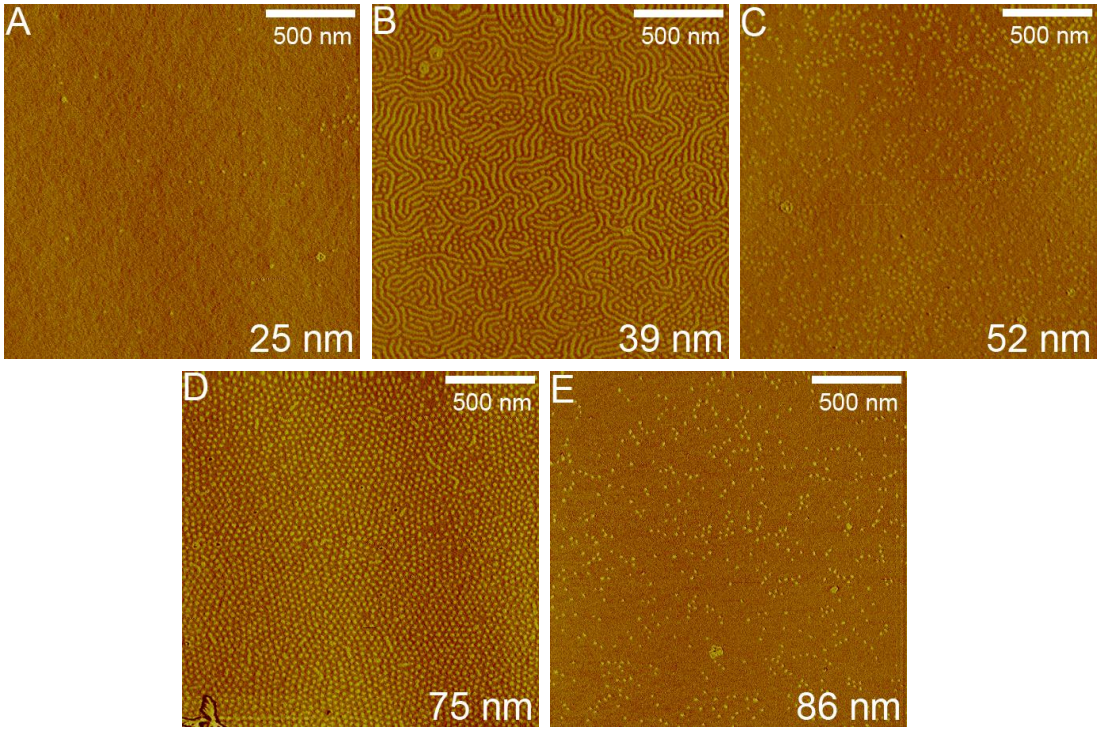

Figure 3.8: Full AFM images of PS-*r*-PVBzAz with 56 mol% VBzAz.

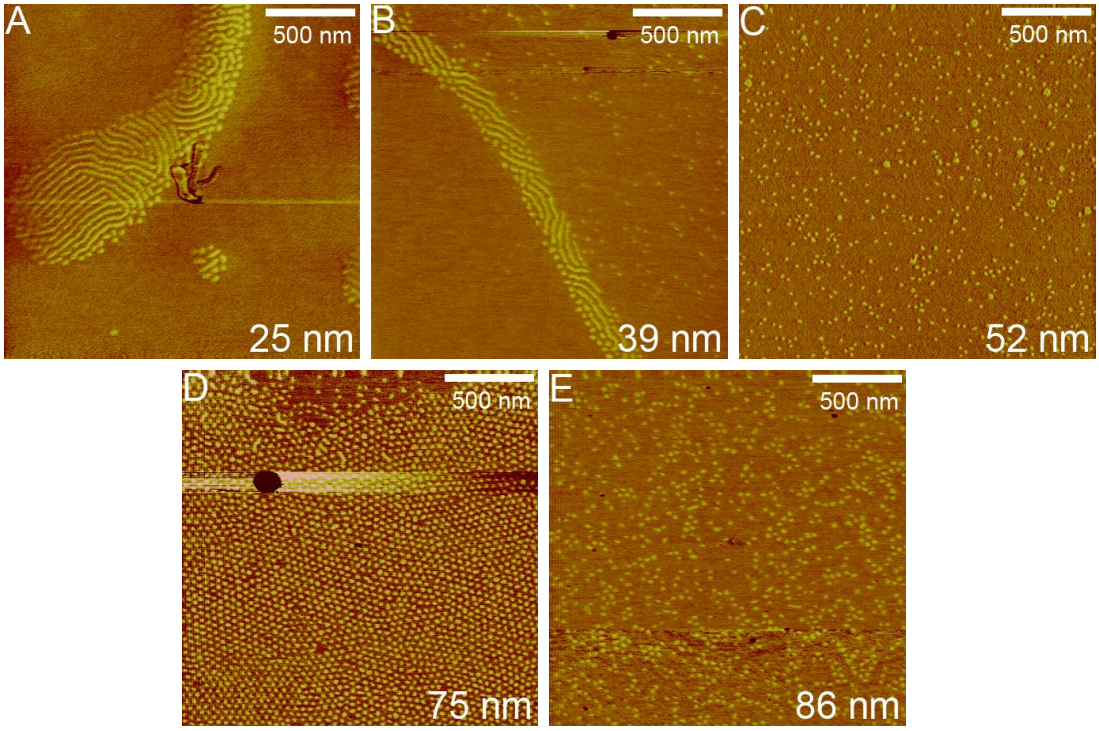

Figure 3.9: Full AFM images of PS-*r*-PVBzAz with 100 mol% VBzAz.

Much effort was exerted in an attempt to quantify the surface energy of the different PS-*r*-PVBzAz copolymer surface treatments. Unfortunately, the relatively low precision (±1 dyn/cm) of the calculated surface energies did not allow identification of a trend in the values as a function of molar composition. The authors' current hypothesis is that the surface energies of the crosslinked homopolymer of poly(4-vinylbenzyl azide) is similar enough to polystyrene that it cannot be distinguished with a contact angle measurement within the error of the measurement.

The thermolysis products of PS-*r*-PVBzAz with PVBzAz content ranging from 5-100 mol% were found to be neutral surface treatments for inducing perpendicular orientation of PS-b-PMMA over the entire composition range studied. We believe that the cross-linked homopolymer of poly(4-vinylbenzyl azide) is the first example of a single-component surface treatment that produces perpendicular orientation of PS-*b*-

PMMA after thermal annealing without chemically or physically prepatterning the surface.

3.4 PS-*r*-PVBzAz Experimentals:

PS-*r*-PVBzAz:

The synthesis of the PS-*r*-PVBzAz copolymers followed synthetic procedures from literature (*69*). Styrene (20 mmol) and 4-vinylbenzyl chloride (0.62 mmol) were copolymerized by refluxing THF (20 mL) for 48 h in the presence of AIBN initiator (20 mg). The polymer was isolated by precipitation in 0°C MeOH, filtered, and dried *in vacuo* which resulted in a white powder. The mol ratio of styrene to vinyl benzyl chloride was determined by ^{1}H-NMR. Taking into account this ratio, poly(4-chloromethyl styrene) (1.0 g) and sodium azide (3 wt equiv/VBzCl) were dissolved in DMF (20 mL) and stirred overnight at rt. The polymer was precipitated in MeOH, filtered, re-dissolved in THF (10 mL), and stirred with H_2O (1 mL) to remove any unreacted salts. Finally, the polymer was isolated by precipitation in 0°C MeOH, filtered, and dried *in vacuo* to yield the surface treatment as a white powder. Typical yields over these two steps from monomer mass were 50%; IR (KBr) ≈ 2100 cm^{-1}. The benzyl protons undergo a complete shift from 4.5 ppm (VBzCl) to 4.3 ppm (VBzAz) by ^{1}H NMR upon azide functionalization. Molecular weight and dispersity data for the series of different compositions are shown in **Table 3.1**.

Surface Treatment with PS-*r*-PVBzAz:

A film of PS-*r*-PVBzAz was spin coated from a 1.0 wt% solution in toluene at 3770 rpm for 30 sec onto a wafer that had been triple rinsed with IPA and acetone, respectively. The wafer was immediately baked at 250°C for 5 min to cross-link the film. The wafer was then submerged in toluene for 2 min, blown dry, submerged again for 2 min, and blown dry. Typical film thicknesses as determined by ellipsometry were 10-20 nm. The extent of random copolymer cross-linking was studied by FTIR. Representative

surface treatments were spin-coated onto NaCl salt disks and the integral of the azide peak (2100 cm^{-1}) was compared before and after the cross-linking reaction. The polymer with 8 mol% poly(4-vinylbenzyl azide)) showed 100% cross-linking, while poly(4-vinylbenzyl azide) homopolymer had greater than 90% cross-linking after 5 minutes at 250°C. Atomic force microscopy (AFM) was used to determine surface roughness values for XST-H, a representative surface treatment, over a 2x2 μm area. It was found that the average roughness R_a = 0.277 nm and the root-mean square roughness R_q = 0.349 nm. This is generally considered to be a "smooth" polymer film (*98-100*).

3.5 SURFACE TREATMENTS FOR SILICON-CONTAINING BCPS

The main focus of this dissertation research was to orient silicon-containing block copolymers in thin films. The aforementioned interface neutralization methods become more difficult to control as the difference in block surface energies diverges, since even small variations in interfacial composition can cause preferential interactions between one block and the surface, resulting in a parallel orientation. Additionally, the range of accessible surface energies with the PS-*r*-PVBzAz copolymers described above is likely not large enough to accommodate the large $\Delta\gamma$ of Si-BCPs. The synthesis of random copolymers composed of a silicon-containing monomer and a non-silicon-containing monomer was ultimately deemed a more flexible route towards controlling surface treatment composition over a larger range. Since the surface energies of the silicon-containing homopolymer and non-silicon containing homopolymer should represent the approximate extremes of surface energies of the two blocks, this architecture should provide access to a neutral interface at some intermediate composition. The majority of the silicon-containing surface treatment work was aimed at controlling the orientation of poly(styrene-*block*-methyltrimethylsilylmethacrylate) (see Chapter 2 for the synthesis and Chapter 4 for thin film work). Random copolymers composed of styrene and methyltrimethylsilylmethacrylate were thus synthesized. Analogous to the PS-*r*-PVBzAz surface treatments, vinylbenzyl chloride was added as a third component and converted to poly(4-vinylbenzylazide) post polymerization to provide crosslinking functionality.

The first step to produce the poly(styrene-*random*-methyltrimethylsilylmethacrylate-r*andom*-4-vinylbenzyl chloride) (PS-*r*-PMTMSMA-*r*-PVBzCl) surface treatments was the measurement of the reactivity ratios of each monomer combination. In theory, using these ratios, accurate copolymer compositions can be predicted based purely on the feed ratios. Polymerizations were run to low conversion to prevent monomer drift, which can cause the instantaneous copolymer composition to change with time because of differences in monomer reactivity ratios (*101*). The theory behind reactivity ratios will first be described and then applied to the styrene, MTMSMA, VBzCl terpolymer system.

3.6 Reactivity Ratio Models

Two-component Model

First, consider a two component model where two monomers (A and B) are copolymerized. The growing chain end (either A radical or B radical) can add either an A or B monomer. The result is 4 possible different reaction rates (k_{11}, k_{12}, k_{22}, and k_{21}, **Figure 3.10**). Two reactivity ratios can be defined as the rate of homo-propagation versus cross-propagation for a given monomer chain end, r_{12} and r_{21} (**Equation 3.3**). These reactivity ratios can be used in combination with the copolymer equation (**Equation 3.4**), which relates the change in monomer concentration to the reactivity ratios and the feed monomer concentrations. It is then straightforward to write the copolymer equation in terms of the polymer composition (M_1/M_2) as a function of the reactivity ratios and monomer feeds.

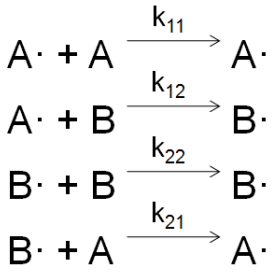

Figure 3.10: Possible propagation scenarios involving a two-component random copolymer synthesized via conventional free radical polymerization.

$$r_{ij} = \frac{reactivity - monomer_i : monomer_i}{reactivity - monomer_i : monomer_j} = \frac{k_{ii}}{k_{ij}} \qquad \textbf{Eq. 3.3}$$

Equation 3.3: Definition of reactivity ratios, r_{ij} as a function of rate constants k_{ii} and k_{ij}.

$$\frac{d[M_1]}{d[M_2]} = \frac{[M_1]\left(r_{12}[M_1] + [M_2]\right)}{[M_2]\left([M_1] + r_{21}[M_2]\right)} \qquad \textbf{Eq. 3.4}$$

Equation 3.4: The copolymer equation (Mayo-Lewis model).

$$\frac{M_1}{M_2} = \frac{r_{12}\left(\frac{m_1}{m_2}\right) + 1}{r_{21}\left(\frac{m_2}{m_1}\right) + 1}$$

$M_i \equiv d[M_i]$ Concentration of monomer *i* in the polymer

$m_i \equiv [M_i]$ Concentration of monomer *i* in the feed **Eq. 3.5**

Equation 3.5: The copolymer equation rewritten in terms of the reactivity ratios and feed concentrations.

$$\frac{f(1-F)}{F} = -r_{12}\left(\frac{f^2}{F}\right) + r_{21}$$

$f = \frac{[M_1]}{[M_2]}$ Concentration ratio in the feed

$F = \frac{d[M_1]}{d[M_2]}$ Concentration ratio in the copolymer **Eq. 3.6**

Equation 3.6: The copolymer equation is transformed into the form y=mx+b and the reactivity ratios, r_{12} and r_{21}, can extracted by finding the slope and intercept of the best-fit line.

Three-component Model

The Mayo-Lewis two component model can be extended to three components using the Alfrey-Goldfinger model (*102*). The addition of a third monomer creates another set of rate constants (**Figure 3.11**) and reactivity ratios (**Equation 3.3**) that must be accounted for in the kinetic equations. Equations analogous to the Mayo-Lewis model but incorporating a third monomer can be written that relate the polymer composition (M_i) to the monomer feed ratios (m_i) (**Equation 3.7** and **Equation 3.8**).

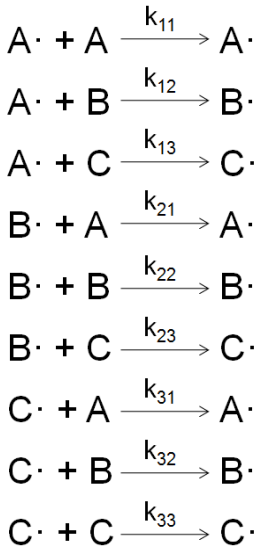

Figure 3.11: Possible propagation scenarios involving a three-component random terpolymer synthesized by uncontrolled free radical polymerization.

$$\frac{M_1}{M_2} = \frac{m_1\left(\frac{m_1}{r_{21}r_{31}} + \frac{m_2}{r_{21}r_{32}} + \frac{m_3}{r_{23}r_{31}}\right)\left(m_1 + \frac{m_2}{r_{12}} + \frac{m_3}{r_{13}}\right)}{m_2\left(\frac{m_1}{r_{12}r_{31}} + \frac{m_2}{r_{13}r_{32}} + \frac{m_3}{r_{13}r_{32}}\right)\left(m_2 + \frac{m_1}{r_{21}} + \frac{m_3}{r_{23}}\right)} \qquad \textbf{Eq. 3.7}$$

Equation 3.7: Alfrey-Goldfinger model for predicting the composition of random terpolymers (M_1, M_2, and M_3) based on the monomer feed ratios (m_1, m_2, m_3) and the reactivity ratios (r_{ij}) (*102*).

$$\frac{M_1}{M_3} = \frac{m_1\left(\frac{m_1}{r_{21}r_{31}} + \frac{m_2}{r_{21}r_{32}} + \frac{m_3}{r_{23}r_{31}}\right)\left(m_1 + \frac{m_2}{r_{12}} + \frac{m_3}{r_{13}}\right)}{m_3\left(\frac{m_1}{r_{13}r_{21}} + \frac{m_2}{r_{12}r_{23}} + \frac{m_3}{r_{13}r_{23}}\right)\left(m_3 + \frac{m_1}{r_{31}} + \frac{m_2}{r_{32}}\right)} \qquad \textbf{Eq. 3.8}$$

Equation 3.8: Alfrey-Goldfinger model for predicting the composition of random terpolymers (M_1, M_2, and M_3) based on the monomer feed ratios (m_1, m_2, m_3) and the reactivity ratios (r_{ij}) (*102*).

3.7 Measurement of PS, PMTMSMA, and VBzCl Reactivity Ratios

The use of the Alfrey-Goldfinger model requires knowledge of 6 pairs of reactivity ratios: r_{12}, r_{13}, r_{21}, r_{23}, r_{31}, r_{32}. Here, styrene is defined as monomer 1, methyltrimethylsilylmethacrylate as monomer 2, and vinylbenzyl chloride as monomer 3. Each reactivity ratio can be extracted using the two component model (specifically **Equation 3.6**) with each pair of monomers. The reactivity ratios were subsequently used with the three component model to predict the copolymer composition as a function of the feed ratio.

For each pair of monomers, three sets of reactions were set up (**Schemes 3.1-3.3**) with different feed compositions, which were determined gravimetrically. The reactions were run neat at 90°C with benzoyl peroxide as the thermal initiator. After one hour, each reaction as quenched at 0°C and isolated by precipitation. Low conversions (~5% as calculated by mass recovery) were intentionally achieved to prevent monomer drift. The presence of residual monomer due to the low conversion necessitated reprecipitation of each polymer at least four times. ^{1}H NMR was used to calculate the composition of the polymers, which were compared with the feed ratios (**Tables 3.2-3.4**). Together, these data were used to extract all of the required reactivity ratios (**Figures 3.12-3.14**). A summary of all of the calculated reactivity ratios is provided in **Table 3.5**.

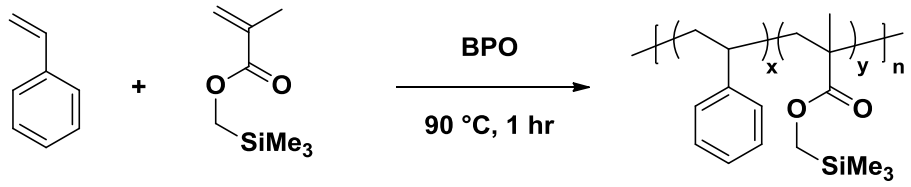

Scheme 3.1: Synthesis of PS-*r*-PMTMSMA at low conversion for the determination of reactivity ratios.

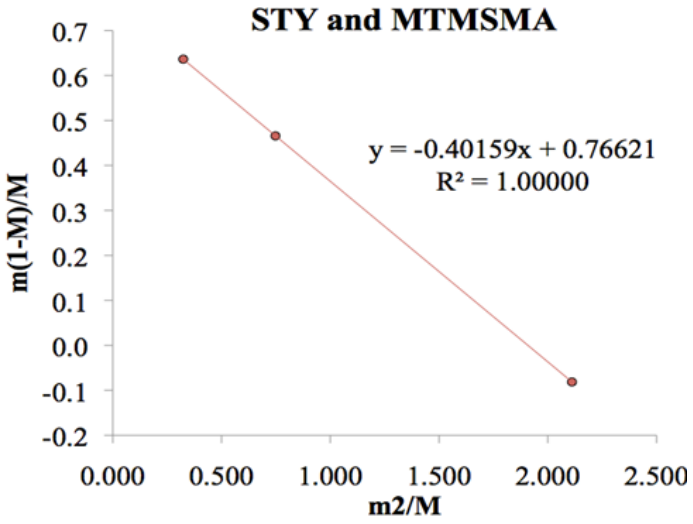

Figure 3.12: Calculation of the reactivity ratios between styrene and methyltrimethylsilylmethacrylate monomers (r_{12} and r_{21}).

Table 3.2: Summary of feed and copolymer compositions for PS-*r*-PMTMSMA.

	Feed		Measured	
Reaction	Styrene	MTMSMA	Styrene	MTMSMA
1	0.40	0.60	0.436	0.564
2	0.60	0.40	0.630	0.370
3	0.75	0.25	0.744	0.256

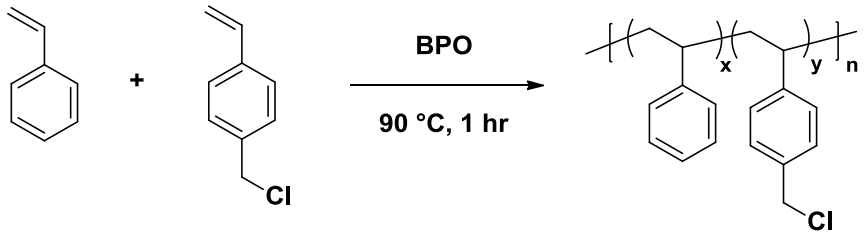

Scheme 3.2: Synthesis of PS-*r*-PVBzCl at low conversion for the determination of reactivity ratios.

Table 3.3: Summary of feed and copolymer compositions for PS-*r*-PVBzCl.

	Feed		Measured	
Reaction	Styrene	VBzCl	Sty	VBzCl
1	0.4	0.6	0.367	0.633
2	0.68	0.32	0.489	0.511
3	0.75	0.25	0.552	0.448

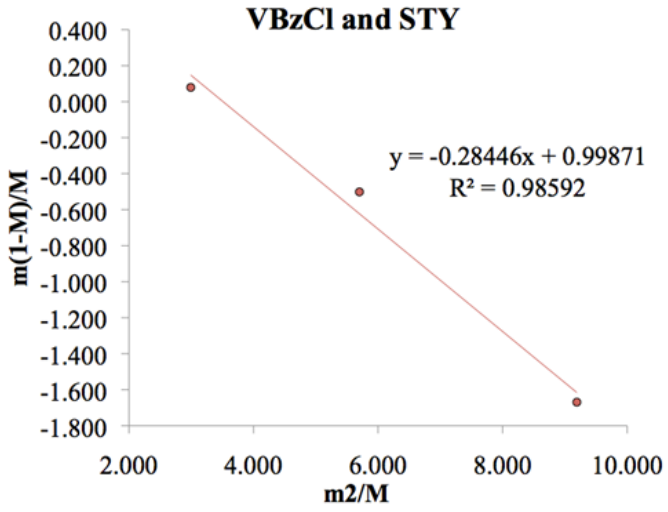

Figure 3.13: Calculation of the reactivity ratios between vinylbenzyl chloride and styrene monomers (r_{31} and r_{13}).

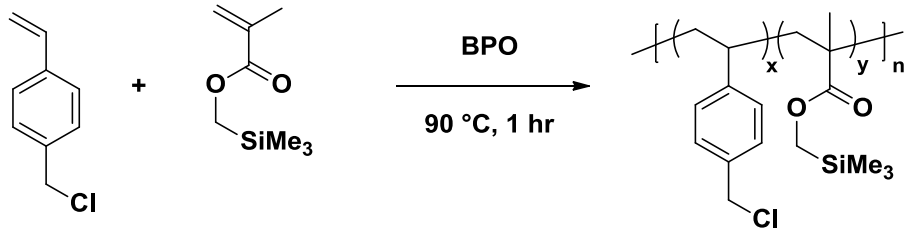

Scheme 3.3: Synthesis of PVBzCl-*r*-PMTMSMA at low conversion for the determination of reactivity ratios.

Table 3.4: Summary of feed and copolymer compositions for PVBzCl-*r*-PMTMSMA.

	Feed		Measured	
Reaction	MTMSMA	VBzCl	MTMSMA	VBzCl
1	0.4	0.6	0.292	0.708
2	0.68	0.32	0.522	0.478
3	0.75	0.25	0.596	0.404

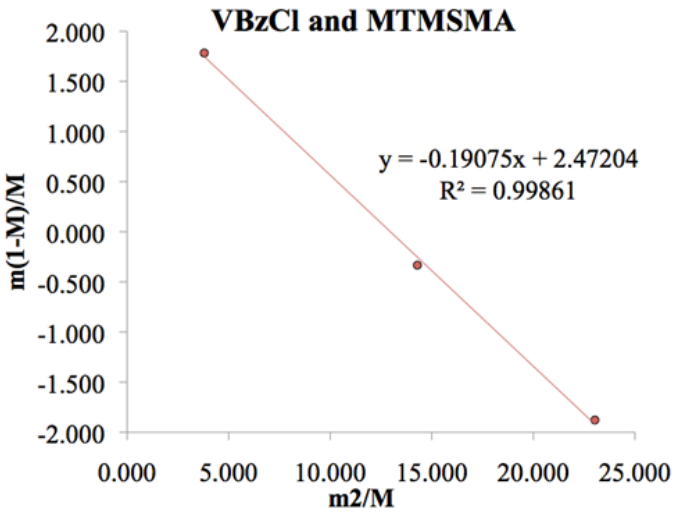

Figure 3.14: Calculation of the reactivity ratios between methyltrimethylsilylmethacrylate and vinylbenzyl chloride monomers (r_{23} and r_{32}).

Table 3.5: Summary of reactivity ratios between styrene, methyltrimethylsilylmethacrylate, and vinylbenzyl chloride monomers.

Combination	Reactivity Ratio	Value
STY-MTMSMA	r_{12}	0.766
MTMSMA-STY	r_{21}	0.402
MTMSMA-VBzCl	r_{23}	0.191
VBzCl-MTMSMA	r_{32}	2.523
VBzCl-STY	r_{31}	0.886
STY-VBzCl	r_{13}	0.284

Reactions utilizing the calculated reactivity ratios (**Table 3.2**) were used to directly compare the Mayo-Lewis and Alfrey-Goldfinger models (**Figure 3.15**). Interestingly, the Alfrey-Goldfinger model seems to do slightly better than the Mayo-Lewis model, but the differences are relatively subtle. It is possible that with such a small feed ratio of PVBzCl in the reaction, the Mayo-Lewis model is still somewhat accurate. This would probably not be possible with higher PVBzCl feed ratios. Regardless, the Alfrey-Goldfinger model does a relatively good job at predicting copolymer compositions within the error of the calculated ^{1}H NMR polymer composition.

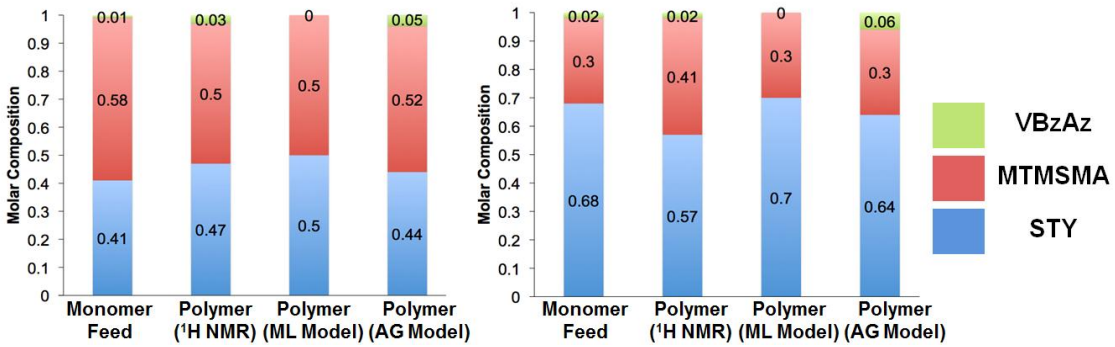

Figure 3.15: Comparison of the monomer feed ratio, polymer composition as calculated by ^{1}H NMR, and the Mayo-Lewis and Alfrey-Goldfinger models.

3.8 PS-*r*-PMTMSMA SURFACE TREATMENT SYNTHESIS:

With reactivity ratios in hand, PS-*r*-PMTMSMA-*r*-PVBzCl surface treatment precursors were synthesized by uncontrolled free radical polymerization using benzoyl peroxide as an initiator in neat monomer. Reactions were heated at 90°C for 1 h and were quenched in ice water. A summary of the calculated compositions is shown in **Table 3.6**. Crosslinkable surface treaments were then synthesized from the PS-*r*-PMTMSMA-*r*-PVBzCl precursors. Sodium azide was added to a solution of PS-*r*-PMTMSMA-*r*-PVBzCl copolymers dissolved in DMF and the slurry was stirred for 18 h. The milky white opaque solution was precipitated. After isolation of the PS-*r*-PMTMSMA-*r*-PVBzAz surface treatments by precipitation, ^{1}H NMR showed complete conversion of PVBzCl to PVBzAz as evidenced by a shift in the broad benzyl position resonance in the from ~4.5 (PVBzCl) to ~4.3 (PVBzAz). Furthermore, the presence of azide was verified with infrared spectroscopy with a sharp peak ca. 2100 cm^{-1}. The dispersity values of the surface treatments listed in **Table 3.6** are unusually low for uncontrolled free radical polymerizations. Because the molecular weights calculated relative to PS standards, they do not represent the true molecular weight of the copolymers and thus there could be discrepancy in the dispersities.

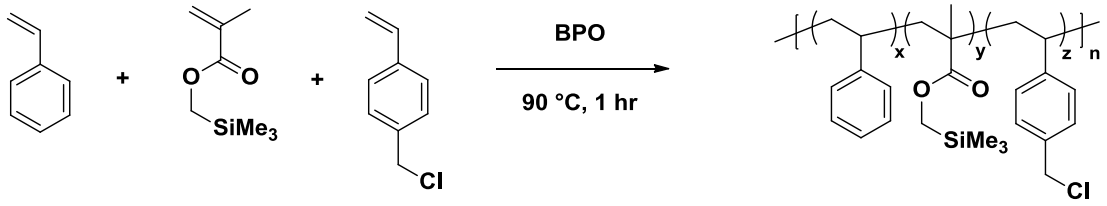

Scheme 3.4: Synthesis of PS-*r*-PMTMSMA-*r*-PVBzCl copolymers. The composition of the copolymer was predicted using the Alfrey-Goldfinger terpolymer model.

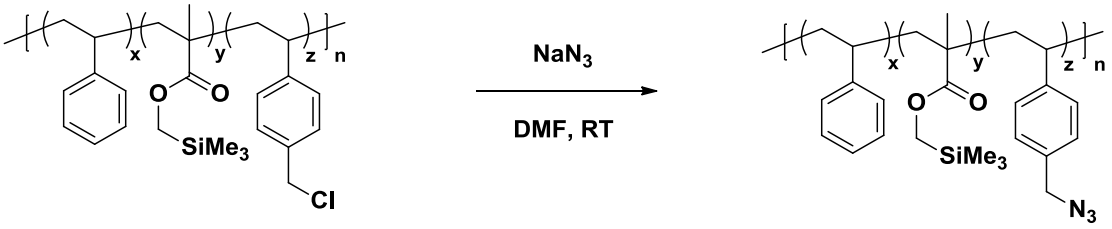

Scheme 3.5: Synthesis of PS-*r*-PMTMSMA-*r*-PVBzAz by installation of crosslinkable azide moieties on the vinylbenzyl chloride position.

Table 3.6: Composition analysis of PS-*r*-PMTMSMA-*r*-PVBzAz surface treatments as calculated by ^{1}H NMR and GPC.

Sample	%PS	%PMTMSMA	%PVBzCl	Mn	Mw	Dispersity
Mat-SM-1	47	50	3	175,340	207,740	1.18
Mat-SM-2	65	31	4	108,250	132,820	1.23
Mat-SM-3	76	21	3	86,220	104,080	1.21
Mat-SM-4	51	47	2	123,450	158,240	1.28

3.9 PS-*R*-PMTMSMA COPOLYMER EXPERIMENTALS

General Procedures For Surface Treatment Synthesis

Reactivity Ratio Calculation

A 100 mL round bottom flask was charged with a stir bar, vinylbenzyl chloride (0.60 eq., 7.930 g, 52.2 mmol), methyltrimethylsilylmethacrlate (0.40 eq., 6 g, 34.8 mmol), and benzoyl peroxide (0.0006 eq., 20 mg, 0.080 mmol). The solution was

degassed for 20 minutes with ultra-high purity argon gas and subsequently placed in an oil bath at 90°C. After 1 hr, the solutions were quenched in an ice bath at 0°C for 10 minutes and precipitated into methanol. The white powder was isolated by filtration, and reprecipitated into methanol three times (dissolved in 10 mL THF). A total mass of 1.008 g PVBzCl-*r*-PMTMSMA was isolated in 4.0% conversion. Composition (^{1}H NMR, mol%) PVBzCl:PMTMSMA=47:53. ^{1}H NMR ($CDCl_3$, δ, ppm): 6.4-7.4 (br, m), 4.2-4.4 (br, s), 0.2-3.8 (br, m), -0.2-0.2 (br, s).

Mat Precursor

A 100 mL round bottom flask was charged with a stir bar, styrene (0.41 eq., 6.03 g, 57.6 mmol), methyltrimethylsilyl methacrylate (0.58 eq., 14.03 g, 81.0 mmol), vinylbenzyl chloride (0.01 eq., 0.31 g, 1.40 mmol), and benzoyl peroxide (0.000736 eq., 24.9 mg, 0.103 mmol). The solution was degassed for 20 minutes with ultra-high purity argon gas and subsequently placed in an oil bath at 90°C. After 1 hr, the solutions were quenched in an ice bath at 0°C for 10 minutes and precipitated into methanol. The white powder was isolated by filtration, and reprecipitated into methanol three times (dissolved in 10 mL THF). A total mass of 1.008 g poly(styrene-*r*-methyltrimethylsilyl methacrylate-*r*-vinylbenzyl chloride) was isolated in 4.9% conversion. Composition (^{1}H NMR, mol%) PS:PMTMSMA:PVBzCl=47:50:3. ^{1}H NMR ($CDCl_3$, δ, ppm): 6.4-7.4 (br, m), 4.2-4.4 (br, s), 0.2-3.8 (br, m), -0.2-0.2 (br, s).

Surface Treatment – Mat-SM-1, 2, 3, 4

A 50 mL round bottom flask was charged with a stir bar, 1 g of poly(styrene-*r*-methyltrimethylsilylstyrene-*r*-vinylbenzyl chloride) (1 eq.), sodium azide (6 mass eq. for every vinylbenzyl chloride, 197 mg, 3.03 mmol), and 20 mL DMF. The reaction was stirred for 18 h. The DMF was removed *in vacuo*, the polymer was redissolved in toluene and washed three times with water to remove residual unreacted sodium azide, followed by precipitation into methanol. The white powder was isolated by filtration and dried *in vacuo* with >90% mass recovery. The broad benzyl position resonance in the ^{1}H

NMR completely shifted from ~4.5 (PVBzCl) to ~4.3 (PVBzAz) and the presence of azide was verified with infrared spectroscopy with a sharp peak ca. 2100 cm^{-1}. ^1H NMR ($CDCl_3$, δ, ppm): 6.40-7.40 (br, m), 4.40-4.60 (br, s), 0.20-3.80 (br, m), -0.20-0.20 (br, s).

3.10 NON-SILICON CONTAINING SURFACE TREATMENTS

Very recently, a set of non-silicon-containing and cross-linkable substrate surface treatments with an apparent wide range of accessible surface energies was developed. The impetus to create an additional class of XSTs stemmed from anticipated problems during pattern transfer etching processes. For the same reason that silicon introduces etch resistance into a BCP, its presence in a substrate surface treatment would create an etch resistant layer below the BCP film. While etch resistance is intentionally included in the BCP, its presence in the PS-*r*-PMTMSMA-*r*-PVBzAz XSTs was only introduced to access a wide range of surface energies. The etch-resistant alignment layer would quite possibly interfere with subsequent pattern transfer and is clearly not the ideal XST material. A superior XST would replace the PMTMSMA component with a non-silicon-containing monomeric unit of comparable surface energy.

We were inspired by a recent report by Kennemur et al. (*54*) in which they detailed the synthesis and bulk characterization of poly(4-*tert*-butylstyrene-*block*-methyl methacrylate) (PtBuS-*b*-PMMA). The χ value is apparently quite large, since they report that the BCP can self-assemble into bulk periodicities down to L_0=14 nm. The implication is that the poly(4-*tert*-butylstyrene) block has a significantly lower surface energy than the PMMA block. XSTs composed of PtBuS, PMMA, and cross-linkable PVBzAz provide a potential convenient route to a universal, non-silicon-containing surface treatment.

A series of random copolymers of the design poly(4-*tert*-butylstyrene-*random*-methyl methacrylate-*random*-vinylbenzyl azide) (PtBuS-*r*-PMMA-*r*-PVBzAz) were synthesized (**Scheme 3.6**) analogously to the aforementioned XSTs. The first step in the synthesis was the characterization of the reactivity ratios of the various monomer pairs to enable accurate copolymer compositions to be targeted. Four of the six required

reactivity ratios were found in the Polymer Handbook (*103*). The VBzCl-tBuS and tBuS-VBzCl pairs were measured using the Mayo-Lewis Model (**Figure 3.16**).

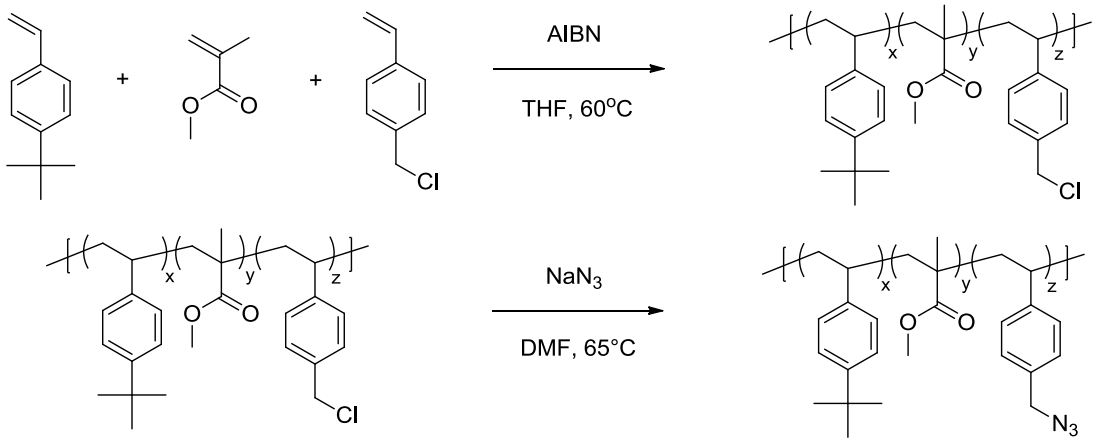

Scheme 3.6: Synthesis of PtBuS-*r*-PMMA-*r*-PVBzAz surface treatments.

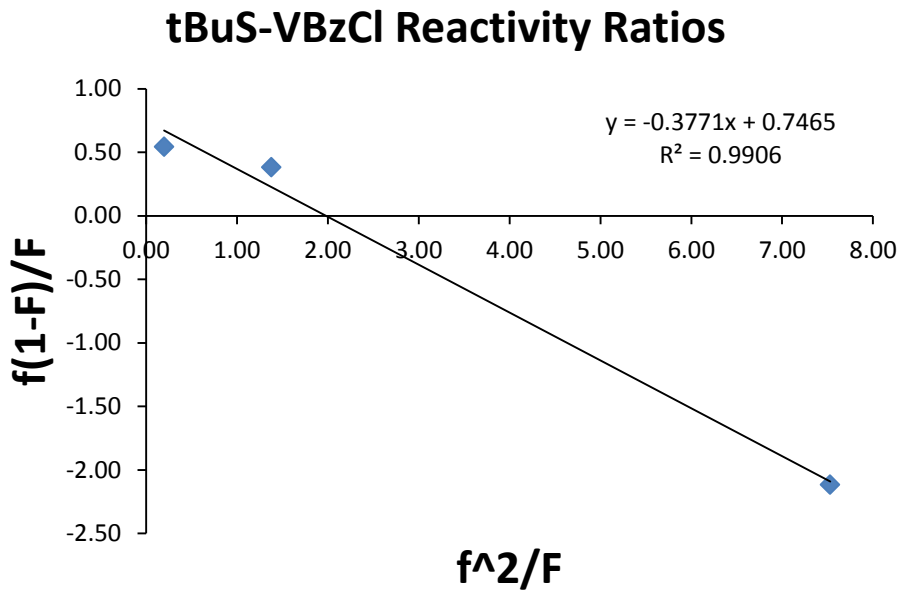

Figure 3.16: Reactivity ratio calculation for 4-*tert*-butylstyrene and 4-vinylbenzyl chloride.

Table 3.7: Summary of reactivity ratio pairs between 4-*tert*-butylstyrene, methyl methacrylate, and 4-vinylbenzyl chloride.

Combination	Reactivity Ratio	Value	Literature Value
tBuS-MMA	r_{12}	0.500	*
MMA-tBuS	r_{21}	0.440	*
MMA-VBzCl	r_{23}	0.408	*
VBzCl-MMA	r_{32}	0.910	*
VBzCl-tBuS	r_{31}	0.747	
tBuS-VBzCl	r_{13}	0.377	

The knowledge of all the relevant reactivity ratio pairs enabled the precise synthesis of a set of PtBuS-r-PMMA-r-PVBzAz XSTs. **Table 3.8** lists the series of synthesized XSTs and compares the polymerization feed ratio, composition as calculated by combustion analysis, and predicted composition based on the reactivity ratios (from the aforementioned Alfrey-Goldfinger model).

The use of combustion analysis was crucial for the accurate calculation of XST compositions; ^{1}H NMR integrals were found to be significantly more inaccurate. Combustion analysis was performed by Midwest Microlab, LLC. Four different elemental mass percentages were measured for each sample (C, H, O, and N or Cl depending on whether the sample was the VBzCl precursor or the VBzAz XST). A set of three reported elemental percentages, either [C, H, and O] or [C, H, and (Cl or N)] was used to calculate the composition of the sample. Based on the number of moles of each element in each repeat unit structure (4-tertbutylstyrene, methyl methacrylate, and vinylbenzyl chloride or azide), Microsoft Excel® Solver was used to minimize the difference between each mass% measured and the mass% for each element that would be calculated based on an initial guess of the relative mole ratios of each monomer. Solver changed the values of the initially guessed mole percentages until the sum of the mean squared errors between each calculated elemental mass% and the actual measured mass%

was minimized. MSE were generally very low, on the order of <0.01. Only one solution was found for each sample.

Table 3.8: Compositions (in mole fractions) for the series of synthesized PtBuS-*r*-PMMA-*r*-PVBzAz XSTs calculated with combustion analysis.

Sample	Feed (mole fraction)			Composition (mole fraction, combustion)			Predicted (Reactivity Ratios)		
XST-14	0.10	0.85	0.05	0.14	0.77	0.08	0.13	0.79	0.08
XST-21	0.15	0.80	0.05	0.21	0.71	0.08	0.19	0.74	0.07
XST-34	0.31	0.64	0.05	0.34	0.59	0.07	0.33	0.60	0.07
XST-36	0.27	0.68	0.05	0.36	0.56	0.08	0.30	0.63	0.07
XST-40	0.37	0.58	0.05	0.40	0.53	0.07	0.37	0.56	0.07
XST-46	0.475	0.475	0.05	0.46	0.48	0.06	0.46	0.48	0.06
XST-46-2	0.45	0.50	0.05	0.46	0.46	0.08	0.43	0.50	0.07
XST-51	0.50	0.45	0.05	0.51	0.43	0.06	0.46	0.46	0.07
XST-68	0.76	0.19	0.05	0.68	0.25	0.07	0.68	0.25	0.07

Internal consistency checks to verify the calculated compositions were performed in two ways. First, a few of the PtBuS-*r*-PMMA-*r*-PVBzCl samples measured with [C, H, O, and Cl] were compared to the same sample after the azide reaction measured with [C, H, O, and N] (**Table 3.9**). VBzCl-42 corresponds with XST-40, VBzCl-47 corresponds with XST-46-2, and VBzCl-50 corresponds with XST-51. In each case, the numbers agree within a couple percent.

Table 3.9: Comparison of the calculated compositions of select PtBuS-*r*-PMMA-*r*-PVBzCl precursors with the corresponding XSTs, PtBuS-*r*-PMMA-*r*-PVBzAz.

	The answer Using C ,H, O			The answer Using C, H, Cl		
	PtBuS	PMMA	PVBzCl	PtBuS	PMMA	PVBzCl
VBzCl-42	0.42	0.49	0.08	0.42	0.50	0.08
VBzCl-47	0.47	0.44	0.09	0.47	0.44	0.09
VBzCl-50	0.50	0.43	0.07	0.50	0.42	0.07
	The answer Using C ,H, O			The answer Using C, H, Cl		
	PtBuS	PMMA	PVBzCl	PtBuS	PMMA	PVBzCl
XST-40	0.40	0.53	0.07	0.40	0.53	0.07
XST-46-2	0.46	0.46	0.08	0.46	0.46	0.08
XST-51	0.51	0.44	0.05	0.51	0.43	0.06

The second internal consistency check involved comparing the calculated results for a given XST sample using two different sets of elements, [C, H, O] and [C, H, N]. Virtually identical results were found in both cases for each XST sample (**Table 3.10**).

Table 3.10: Comparison of the calculated compositions (in mole fraction) of XSTs with elements [C, H, O] compared to [C, H, N].

	The answer Using C ,H, O				The answer Using C, H, N			
	PtBuS	PMMA	PVBzAz	Sum	PtBuS	PMMA	PVBzAz	Sum
XST-14	0.14	0.74	0.13	1.00	0.14	0.77	0.08	1.00
XST-21	0.21	0.72	0.07	1.00	0.21	0.71	0.08	1.00
XST-34	0.34	0.60	0.05	1.00	0.34	0.59	0.07	1.00
XST-36	0.36	0.57	0.07	1.00	0.36	0.56	0.08	1.00
XST-40	0.40	0.53	0.07	1.00	0.40	0.53	0.07	1.00
XST-46	0.46	0.49	0.06	1.00	0.46	0.48	0.06	1.00
XST-46-2	0.46	0.46	0.08	1.00	0.46	0.46	0.08	1.00
XST-51	0.51	0.44	0.05	1.00	0.51	0.43	0.06	1.00
XST-68	0.68	0.25	0.07	1.00	0.68	0.25	0.07	1.00

A select set of XST samples were used extensively with the second generation top coats reported in Chapter 7. Their SEC traces are shown in **Figure 3.17** and the molecular weight and dispersity data are summarized in **Table 3.11**. The SEC traces of the remaining XSTs reported in **Table 3.8** are shown in **Figure 3.18 and 3.19** and also summarized in **Table 3.11**.

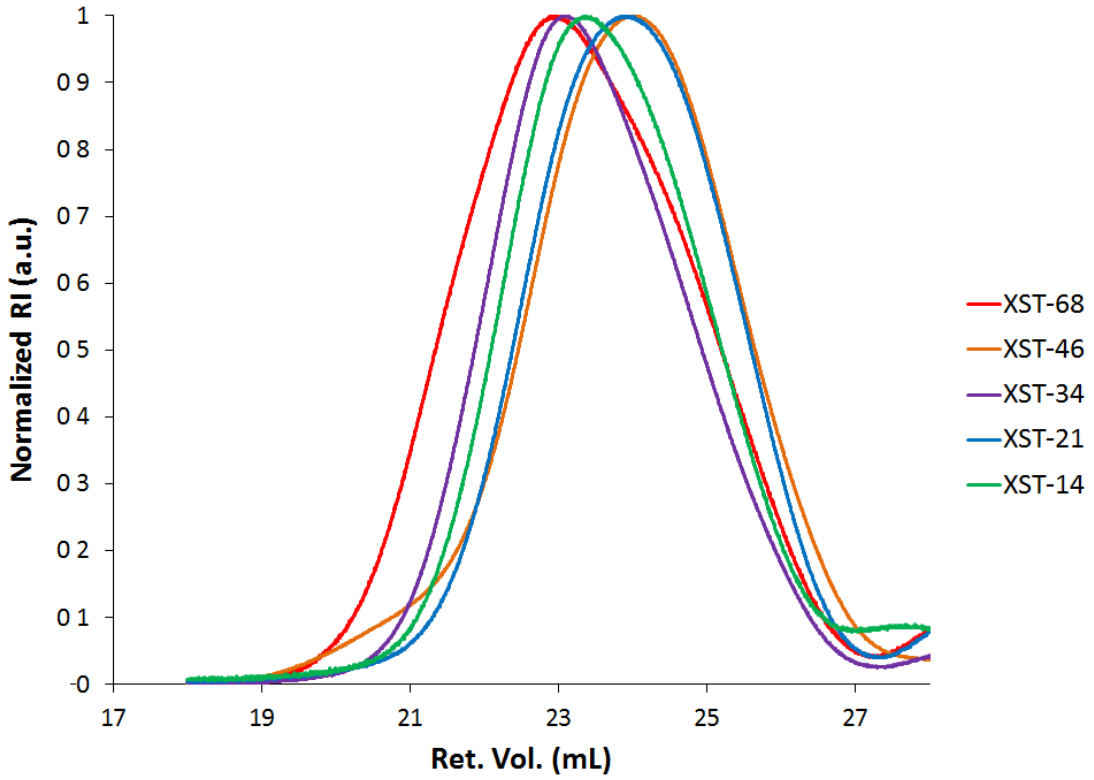

Figure 3.17: SEC traces for five select XSTs that are used in Chapter 7. Samples are named with the mole percent of the PtBuS component.

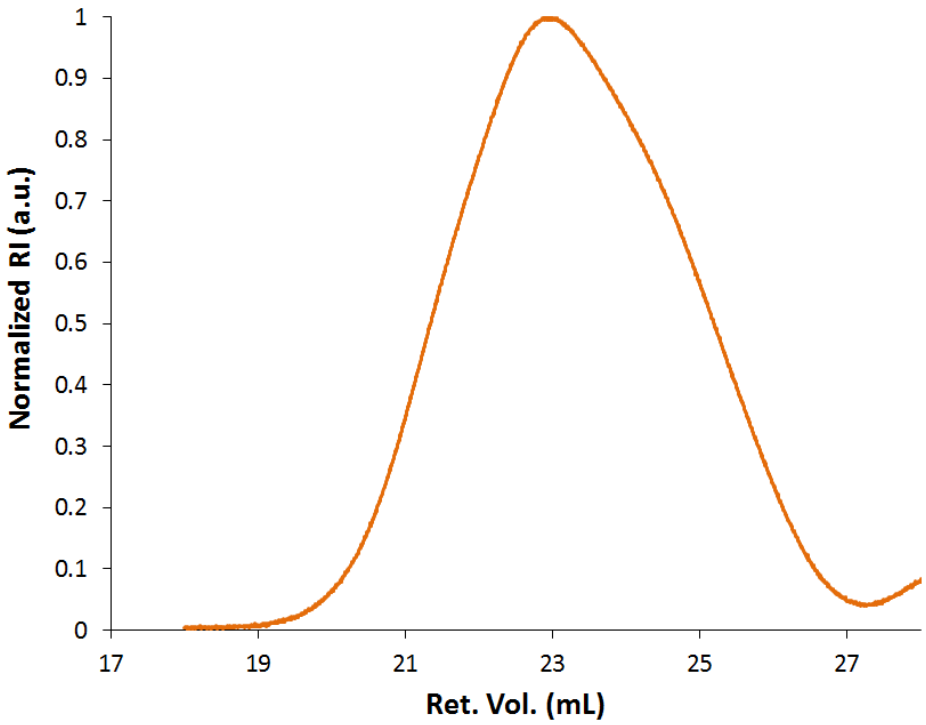

Figure 3.18: SEC trace of XST-36.

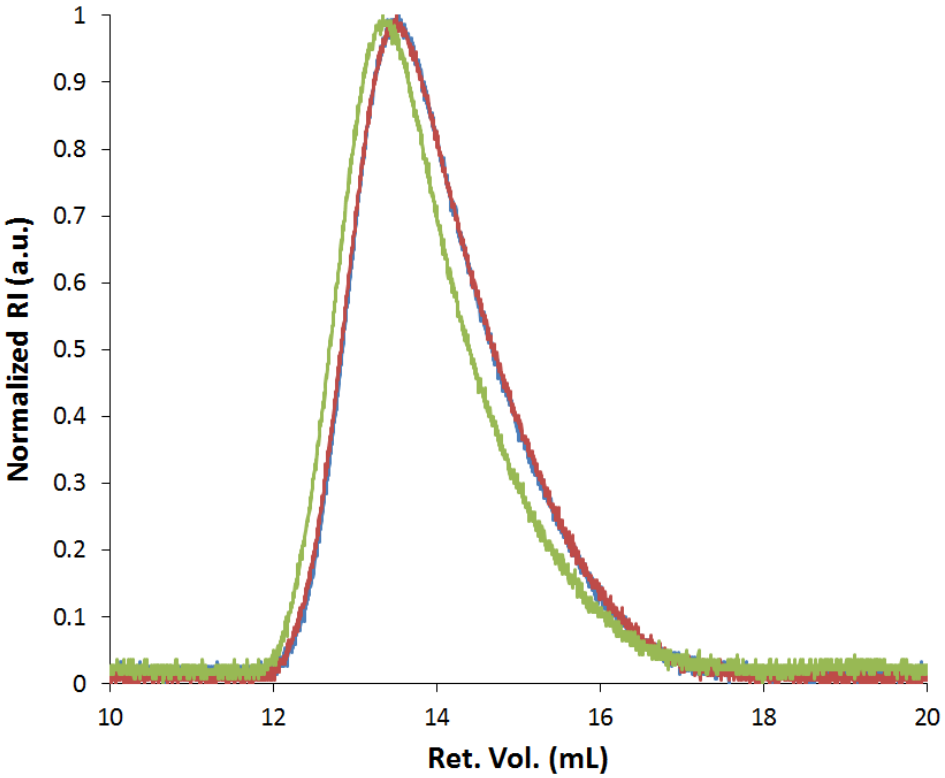

Figure 3.19: SEC trace XSTs. These data were collected on different set of SEC columns than the aforementioned XSTs that causes the elution time to differ.

Table 3.11: Molecular weight and dispersity data for the PtBuS-*r*-PMMA-*r*-PVBzAz XSTs. Data were collected in THF at 23°C relative to a polystyrene standard using triple detect calibration.

	Mole Fraction					
-	PtBuS	PMMA	VBzAz	M_n	M_w	Đ
XST-14	0.14	0.77	0.08	31593	43697	1.38
XST-21	0.21	0.71	0.08	24094	34450	1.43
XST-34	0.34	0.59	0.07	34248	49155	1.44
XST-36	0.36	0.56	0.08	35384	61793	1.75
XST-40	0.40	0.53	0.07	54339	77291	1.42
XST-46	0.46	0.48	0.06	26140	45170	1.73
XST-46-2	0.46	0.46	0.08	49932	72188	1.45
XST-51	0.51	0.43	0.06	84827	120256	1.42
XST-68	0.68	0.25	0.07	26980	40490	1.50

3.11 PTBUS-*R*-PMMA COPOLYMER EXPERIMENTALS:

Reactivity ratio calculation between 4-*tert*-butylstyrene and 4-vinylbenzyl chloride:

4-tert-butylstyrene and 4-vinylbenzyl chloride were purified by stirring with basic alumina for 15 min. The slurry was filtered and the purified monomers were used immediately. A 100 mL three-necked round bottom flask fitted with a reflux condenser, septum, and 14/20 ground glass hose adapter was charged with a stir bar, 4-*tert*-butylstyrene (0.2 eq, 5.000 g, 31.2 mmol), 4-vinylbenzyl chloride (0.8 eq, 19.04 g, 125 mmol), azoisobutyronitrile (0.01 eq, 256 mg, 1.56 mmol) and 13 mL of THF. Three separate reactions were prepared with various relative feed ratios of the monomers (tBuS:VBzCl 0.2:0.8, 0.5:0.5, and 0.8:0.2). The mixture was stirred to dissolve the AIBN and degassed for 20 minutes by bubbling dry nitrogen through with a needle. The reaction was placed under dynamic nitrogen and heated at 65°C in an oil bath for 1 hr. The reaction was cooled to 0°C in an ice bath and precipitated into methanol. The white powder was redissolved in THF, reprecipitated in methanol two more times to remove unreacted monomer, and dried *in vacuo* at 65°C. A total mass of 1 g was isolated in ~5%

yield. Conversion was intentionally kept low to avoid monomer drift. The relative ratio of PtBuS:PVBzCl was measured by ^{1}H NMR, which was possible because both the benzyl protons of VBzCl and the aromatic protons are reasonably well separated from other peaks. The feed ratios and calculated compositions are shown in **Table 3.12**.

Table 3.12: Feed and polymer ratios for the polymerizations used to calculate the reactivity ratios between 4-*tert*-butylstyrene and 4-vinylbenzyl chloride. Polymer mole fractions were measured by ^{1}H NMR.

	Mole Fraction Feed		Mole Fraction Polymer	
	tBuS	VBzCl	PtBuS	PVBzCl
Reaction 1	0.20	0.80	0.24	0.76
Reaction 2	0.50	0.50	0.42	0.58
Reaction 3	0.80	0.20	0.68	0.32

PtBuS-*r*-PMMA-*r*-PVBzCl Mat Precursor:

The following is a representative procedure for the synthesis of the poly(4-*tert*-butylstyrene-*random*-methyl methacrylate-*random*-4-vinylbenzyl chloride) XST precursor polymers. All three monomers were purified by stirring with basic alumina for 15 minutes and vacuum filtered to remove the alumina. All monomers were clear and colorless after purification. A 100 mL three-necked round bottom flask fitted with a reflux condenser, septum, and 14/20 ground glass hose adapter was charged with a stir bar, 4-*tert*-butylstyrene (0.37 eq, 15.335 g, 95.7 mmol), methyl methacrylate (0.58 eq, 15 g, 150 mmol) 4-vinylbenzyl chloride (0.05 eq, 1.974 g, 12.9 mmol), azoisobutyronitrile (0.01 eq, 424 mg, 2.586 mmol) and 22.5 mL of THF. The mixture was stirred to dissolve the AIBN and degassed for 15 min by bubbling dry N_2 gas through a needle. The reaction was heated for 1 hr in an oil bath at 65°C and cooled to 0°C in an ice bath. The polymer was precipitated in methanol, redissolved in THF and reprecipitated two more times into methanol to remove unreacted monomer. The fine white powder was dried in

vacuo at 65°C. A total mass of 1.572 g was isolated in 5% yield. Conversion was intentionally kept low to prevent monomer drift.

PtBuS-*r*-PMMA-*r*-PVBzAz representative procedure:

The following is a representative procedure for the synthesis of the poly(4-*tert*-butylstyrene-*random*-methyl methacrylate-*random*-4-vinylbenzyl azide) XST. A 50 mL round bottom flask was charged with a stir bar, 1.572 g of poly(4-*tert*-butylstyrene-*random*-methyl methacrylate-*random*-4-vinylbenzyl chloride), sodium azide (806 mg, 12.4 mmol), and 20 mL DMF. More than three mass equivalents of sodium azide for every mass equivalent of VBzCl were added to ensure complete conversion of VBzCl to VBzAz. The slurry was heated at 65°C for 19 hr 40 min, quenched at 0°C in an ice bath, and precipitated into methanol. The polymer was redissolved in THF and reprecipitated two additional times into methanol to remove excess sodium azide. The polymer was dried in vacuo at 65°C. A total isolated mass of 221 mg in 14% yield was obtained. Total isolated mass yields were variable for the azide reaction and generally ranged from ~14-50%.

3.12 CONCLUSIONS:

A variety of PS-*r*-PVBzAz surface treatments were synthesized and shown to be effective at controlling the orientation of cylinder-forming PS-*b*-PMMA. Surprisingly, even the homopolymer of PVBzAz enabled partial perpendicular orientation. Two sets of surface treatments with a presumably large accessible range of surface energies were synthesized; silicon-containing PS-*r*-PMTMSMA-*r*-PVBzAz and non-silicon containing PtBuS-*r*-PMMA-*r*-PVBzAz. Surface treatments with targeted compositions were made possible by utilizing the measured reactivity ratios between each pair of monomers. For the silicon-containing surface treatments the monomers were styrene, MTMSMA, and 4-vinylbenzyl chloride; for the non-silicon containing surface treatments the monomers were 4-*tert*-butylstyrene, methyl methacrylate, and 4-vinylbenzyl chloride. The three-component Alfrey-Goldfinger model was shown to predict terpolymer composition better

than the two-component Mayo-Lewis model in the case of the PtBuS-*r*-PMMA-*r*-PVBzAz XSTs.

3.13 ACKNOWLEDGEMENTS:

The original synthesis of PS-*b*-PMMA was done in collaboration with Joshua Katzenstein of the Ellison group and Dr. Jeffrey Strahan, who also reported many substituted styrene and self-assembled monolayer surface treatments in his dissertation (*48*). Undergraduate research assistant Jeffrey Ting made significant contributions to the synthesis of PS-*r*-PMTMSMA-*r*-PVBzAz surface treatments. He is currently a graduate student at the University of Minnesota. Undergraduate Benjamin B. Bamgbade also made contributions to the XST-H surface treatment thin film work. Leon Dean, Anthony Thio, and Litan Li contributed to the PtBuS-r-PMMA-r-VBzAz XST synthesis and characterization.

Chapter 4: Solvent Annealing

4.1 Orientation control

The control of block copolymer feature orientation in thin films is crucial for most applications. The most common morphologies utilized are lamella- and cylinder-forming BCPs. If a bulk morphology is obtained uniformly throughout the film, **Figure 4.1** shows the two possible orientations (perpendicular and parallel) of lamella-forming and cylinder-forming BCPs. Parallel lamellae are lithographically useless; from the top down, there are no nanoscale features present. Perpendicular lamellae produce line-space patterns that can potentially be leveraged for lithography. Parallel cylinders also potentially produce line-space type patterns but with rounded edges. From a pattern transfer standpoint, the rounded edges potentially introduce significant difficulties. Perpendicular lamellae are generally highly preferred and are sought instead of parallel cylinders. A fundamentally different type of pattern is produced from perpendicular cylinders. From the top down, they appear as hexagonally-packed arrays of dots. These two basic types of structures (lines and dots) are being investigated for different applications. While perpendicular cylinders were originally slated to be used for bit patterned media, perpendicular lamella are now being sought (*104*); in combination with rotary electron beam lithography, the lamella can be cut into small rectangular arrays of bits. Line-space patterns are also required for high density thin film transistor applications (*105*). Perpendicular cylinders are currently used to produce IBM's Air Gap® technology (*80*) and will likely be used to pattern contact holes between lithographic layers in next generation computer chips (*106*).

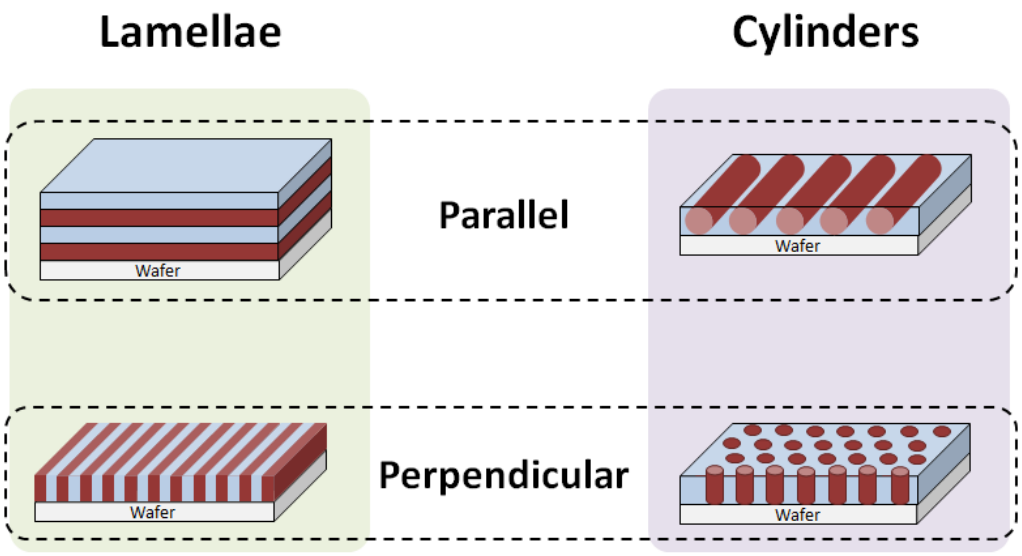

Figure 4.1: Perpendicular and parallel orientations of lamella-forming and hexagonally-packed cylinder-forming block copolymers. Note that perpendicular lamellae (desired) and parallel cylinders (less desirable) appear identical from the top down by SEM and AFM but differ in interfacial curvature.

4.2 ALIGNMENT

Many of the applications listed above not only require orientation control of BCP features (parallel vs. perpendicular) but also control of alignment - the direction the BCP features point in the plane of the film and regularity of the pattern. The technique used to control alignment is referred to as "Directed Self-Assembly" (DSA) and involves either chemical (chemoepitaxy (*107, 108*)) or physical (graphoepitaxy (*32, 109*)) pre-patterning of the wafer. Preferential interactions between one or multiple blocks and a given surface are then used to guide the alignment of the block copolymer with or against the pre-pattern. Regular arrays of straight lines, bent lines, and dots can be formed using DSA (**Figures 4.2 and 4.3**) (*20, 110-112*). DSA is predicated on the control of orientation (i.e. orientation control is required before DSA can be utilized to control feature alignment).

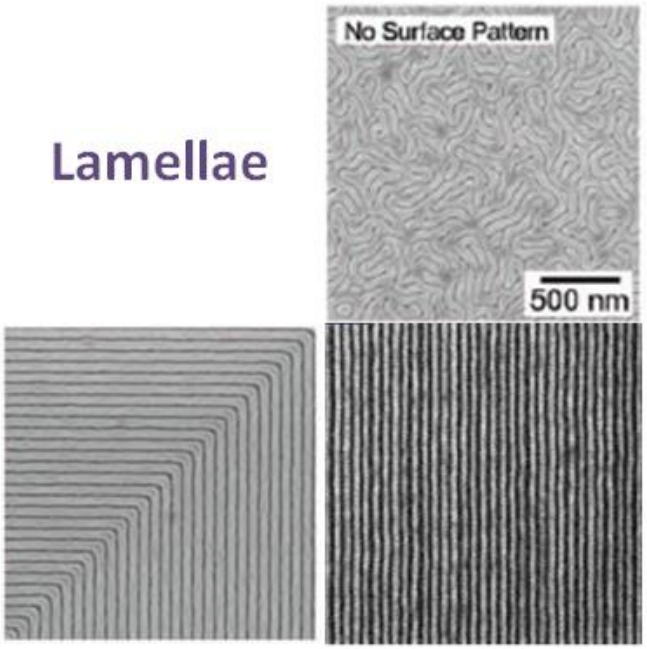

Figure 4.2: Top: undirected perpendicular lamellae. Directed self-assembly of perpendicular lamellae can produce straight or bent lines. Reused with permission from Stoykovich, M. P. et al., Science 2005, 308, 1442. Copyright AAAS 2005.

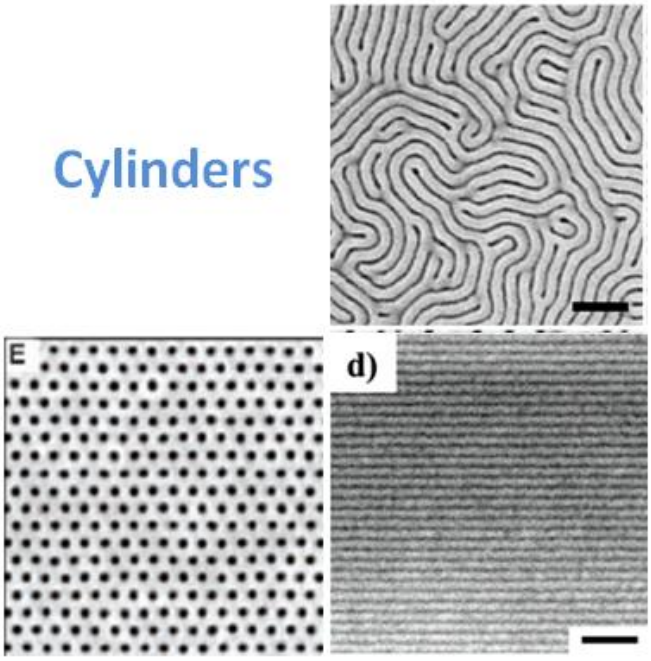

Figure 4.3: Top: Undirected parallel cylinders. Reprinted with permission from Han, E. et al., Macromolecules 2008, 41, 9090. Copyright 2008 American Chemical Society. Lower right: Directed self-assembly of parallel cylinders can produce straight lines (with curved sidewalls). Reprinted with permission from Edwards, E. W. et al., Macromolecules 2006, 39, 3598. Copyright 2006 American Chemical Society. Lower left: directed self-assembly of perpendicular cylinders produces arrays of dots. Reused with permission from Ruiz, R. et al., Science 2008, 321, 936. Copyright 2008 AAAS.

4.3 ORIENTATION TECHNIQUES

There exist two methods of annealing block copolymer thin films, thermal and solvent annealing. In general, as-cast block copolymer films are not well self-assembled and are kinetically trapped in a useless non-equilibrium morphology formed during the spin coating process. The basic role of both annealing techniques is the same – to give the BCP mobility and enact a rearrangement of chains into the desired self-assembled

morphology, orientation, and/or alignment. However, thermal and solvent processes are drastically different.

Thermal annealing involves heating a BCP thin film to a temperature greater than the T_g of both blocks, which provides the BCP mobility to rearrange into its minimum energy state. Chapter 3 describes the importance of interfacial energies on BCP orientation and discusses substrate surface treatments that bias the orientation of BCPs. However, reality is complicated by a second interface, the top, which is general significantly more difficult to control. Chapters 6 and 7 will discuss in great detail control of the top interface. In the interim, it is noted that previously, through-film perpendicular orientations of BCP features produced by thermal annealing could only be achieved with PS-*b*-PMMA. Both high-χ and silicon-containing polymers have historically required the solvent annealing technique to orient features perpendicular to the substrate.

Solvent annealing orients BCP morphologies by a fundamentally different mechanism (**Figure 4.4**) than thermal annealing. Usually solvent annealing experiments are performed in a closed environment (such as a jar) or in a chamber with a constant flow of solvent and carrier gas. Each block absorbs solvent(s) from the atmosphere (likely different amounts) that swell(s) the domains and plasticizes the polymer, i.e. the BCP glass transition temperatures are depressed. The ideal solvent annealing experiment sorbs just enough solvent into the block copolymer to reduce the T_g to below room temperature, which gives the block copolymer chains enough mobility to reorganize. The reason solvent annealing can produce perpendicular BCP orientation is due to a change in the nature of the interfacial interactions of each block with the different surfaces. The presence of solvent in both blocks and the atmosphere of gas at the top interface minimizes the difference in interfacial energy between each block and the top interface, since all materials contain significant amounts of solvent. It is thus possible to achieve perpendicular BCP orientations with solvent annealing that would otherwise be impossible with thermal annealing alone.

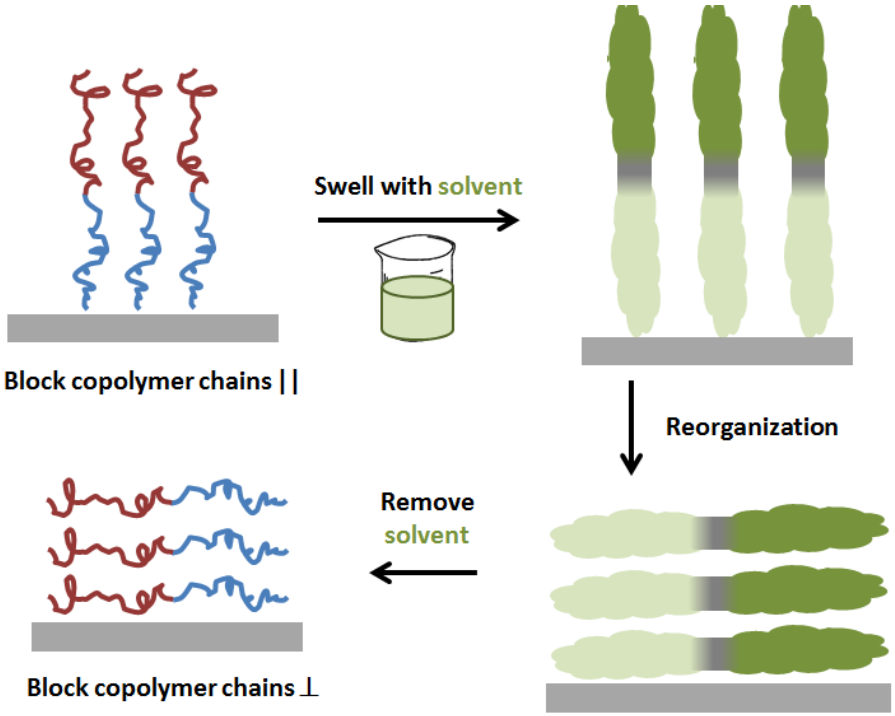

Figure 4.4: The solvent annealing process enables the production of perpendicular BCP feature orientations. Pictured is the desired transformation of parallel features lamellae into perpendicular ones.

Solvent annealing has several drawbacks. Many ill-defined and non-equilibrium morphologies can be achieved that can be difficult to predict or rationalize *a priori*. The processing variable space is also quite large and includes control of chamber dimensions, solvent(s), solvent partial pressure(s), temperature, time, film thickness, changes in film thickness as a function of solvent uptake, substrate surface, and solvent evaporation rate. Ideally each of these variables must be separately understood and optimized for each new block copolymer material. The interaction parameter χ is dependent on specific solvent conditions and usually decreases with solvent uptake if both blocks sorb the same solvent (*34*) (**Equation 4.1**). If χ_{A-B} is the bulk value, after the block copolymer absorbs solvent and partitions a fraction of it at the A-B interface (ϕ_s) the χ value is reduced to χ_{eff}, which is the value that impacts the self-assembly process. The more solvent that is

absorbed by each block, the more each block "appears" like the same solvent, and the less of the energetic driving force to keep the blocks separated. Eventually as enough solvent is sorbed by the blocks, they become miscible.

$$\chi_{eff} = \chi_{A-B}(1-\phi_s) \qquad \textbf{Eq. 4.1}$$

Realistically it is virtually impossible to optimize all of the variables simultaneous, so initial screening studies are performed to identify possible solvent candidates that produce a self-assembled BCP pattern. Each variable is optimized as needed until an acceptable thin film pattern is produced for a given material. Clearly the process is not ideal, but it was until very recently a necessity. As will be discussed in Chapter 6, perpendicular orientations of both high-χ and silicon-containing block copolymers can now be achieved with thermal annealing. However, at the outset of the project thermal annealing was not possible and solvent annealing was pursued with PS-*b*-PMTMSMA, PS-*b*-PTMSI, and PS-*b*-PTMSS-*b*-PS.

4.4 POLY(STYRENE-*BLOCK*-TRIMETHYLSILYLISOPRENE)

The first thin film processing work utilized PS-*b*-PTMSI. There were two main goals of the thin film work: 1) to self-assemble the block copolymer in the thin film and 2) to control the arrangement (i.e. orientation and alignment) of the self-assembled domains. As discussed in Chapter 2, thermal degradation at modest temperatures necessitated the use of solvent annealing to self-assemble the thin film morphology. However, at the outset of the thin film processing work, it was not entirely clear whether the morphology of the block copolymer is hexagonally-packed cylinders or spheres. While the SAXS pattern suggests cylinders, the volume fraction of PS:PTMSI=0.83:0.17 lies very close to the order-order transition from cylinders to spheres. Small differences in the relative swelling ratio of each block could result in an order-order transition between the bulk cylinders and spheres or even lamellae, so care must be taken in the

interpretation of the solvent annealing results. Once an appropriate solvent was identified for self-assembly, control of the orientation (both perpendicular to the substrate) and alignment (how the domains are arranged in the plane of the film) were investigated.

Solvent annealing

To determine an appropriate solvent that creates self-assembled structures in thin films, an initial screening of solvents of different polarities was performed (**Figures 4.5-4.9**). BCP film thicknesses of 40 nm on bare silicon wafers containing native oxide were exposed to solvent vapor in a jar for 1 h with a tight cap. The results illustrate a number of difficulties associated with solvent annealing in general. First, the self-assembly process often results in non-equilibrium morphologies that are difficult to interpret. Samples annealed in cyclohexane showed strange swollen dot patterns that are likely micelle-like structures that lack order. The lack of hexagonally-closed packed structures rules out bulk cylinder or sphere morphologies. Decahydronaphthalene showed very faint line patterns that could be interpreted as parallel cylinders or perpendicular lamella. However, the difficulty in imaging the structures suggests that they are either sub-surface features (potentially with a wetting layer on top) or that solvent annealing changed the value of χ and blurred the interface between the blocks. Dioxane, anisole, 2-methoxyethyl ether, chloroform, PGMEA, and cyclohexanone showed dot patterns that could be interpreted as perpendicular cylinders, but the dots mostly lack local hexagonal packing. More likely, the morphology transitioned to spheres with either overlap of multiple layers, a kinetically trapped partially self-assembled state, or an off-axis crystal lattice causing a distortion in the expected BCC or FCC sphere packing. Benzene, ethyl acetate, 1-butanol, isopropanol, 1-propanol, ethanol, acetonitrile, DMSO, and water all showed “mixed” morphologies - a combination of intermixed dots and lines.

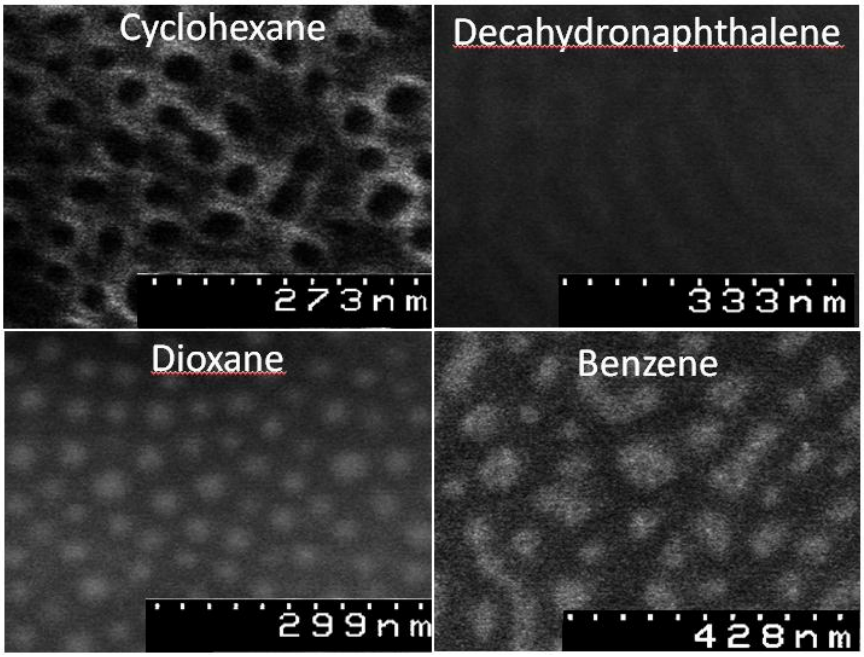

Figure 4.5: PS-*b*-PTMSI solvent annealed with various solvents for 1 hr.

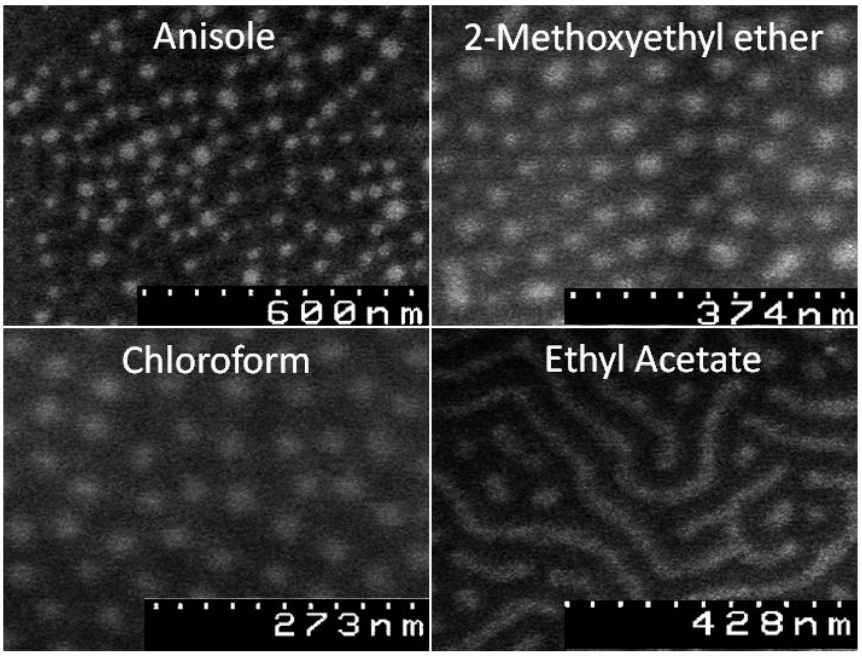

Figure 4.6: PS-*b*-PTMSI solvent annealed with various solvents for 1 hr.

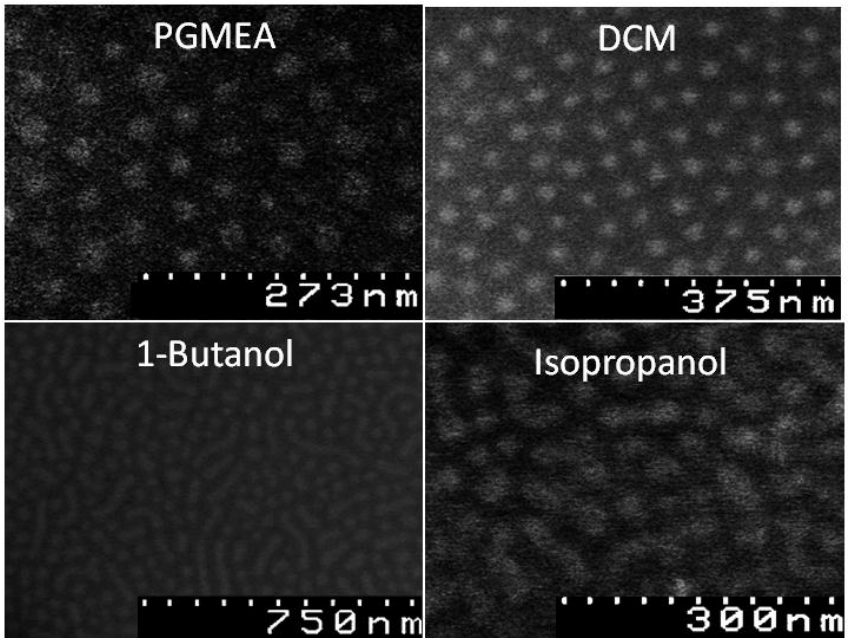

Figure 4.7: PS-*b*-PTMSI solvent annealed with various solvents for 1 hr.

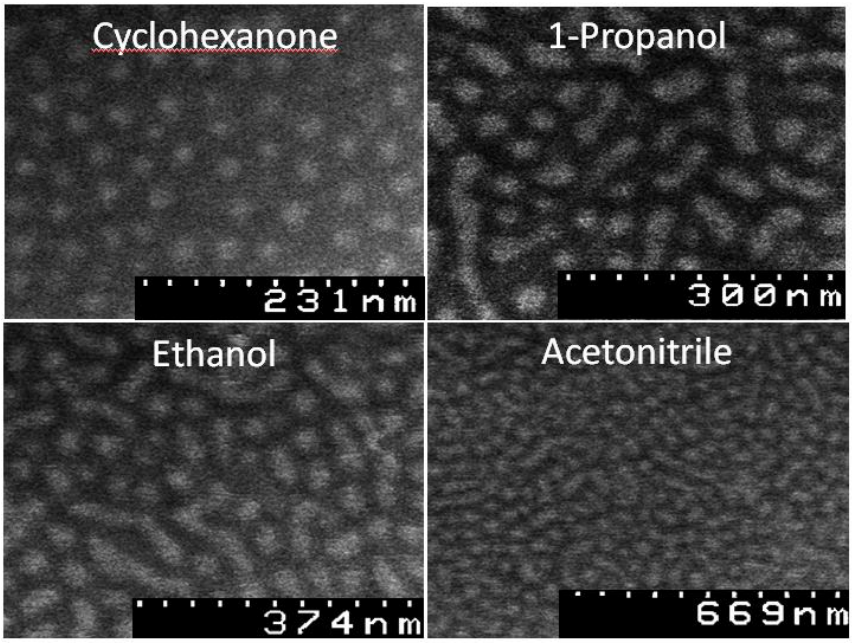

Figure 4.8: PS-*b*-PTMSI solvent annealed with various solvents for 1 hr.

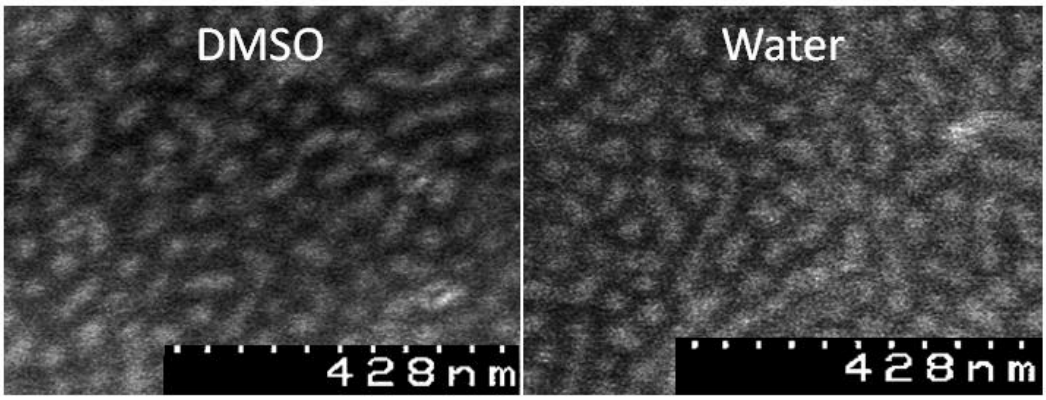

Figure 4.9: PS-*b*-PTMSI solvent annealed with various solvents for 1 hr.

In an attempt to get more consistent thin film self-assembly, PS-*b*-PTMSI was solvent annealed on a crosslinked polystyrene surface treatment. While likely not a truly neutral surface for thermal annealing, it was considered potentially significantly closer to the surface energy of the non-polar polystyrene and polytrimethylsilylisoprene blocks than the native SiO_2 oxide surface, which is quite polar. A silicon wafer with a thin (*ca.* 6 nm) cross-linked polystyrene surface treatment (X-PS mat, generously provided by Professor Paul F. Nealey's group) was coated with PS-*b*-PTMSI and subjected to solvent vapor annealing for various times. After an SF_6 etch (more etching details can be found in Chapter 5), scanning electron microscopy was used to determine the block copolymer morphology and orientation. Solvent annealing was optimized using several additional solvents, substrates and annealing times in order to obtain acceptable assembly of the block copolymer. It was found that exposing the block copolymer to an atmosphere of either diethyl ether for 5 h or toluene for 1.5 h produced reasonably good assembly. As shown in **Figure 4.10A and 4.10B** (*113*), both annealing conditions produced regions containing a "fingerprint" pattern indicative of either perpendicular lamellae or parallel cylinders. Based on the block volume fractions (0.83:0.17 PS:PTMSI) and the aforementioned SAXS data, it is suspected that the features are parallel cylinders, but phase transitions can occur as a result of the solvent partition function between the blocks (which influences the volume fractions) (*114, 115*), so a definitive thin film

morphological assignment could not be made in the absence of additional information. These data were encouraging though because of the increased consistency of the self-assembled structures as compared to **Figures 4.5-4.9**, which were misshapen and irregular.

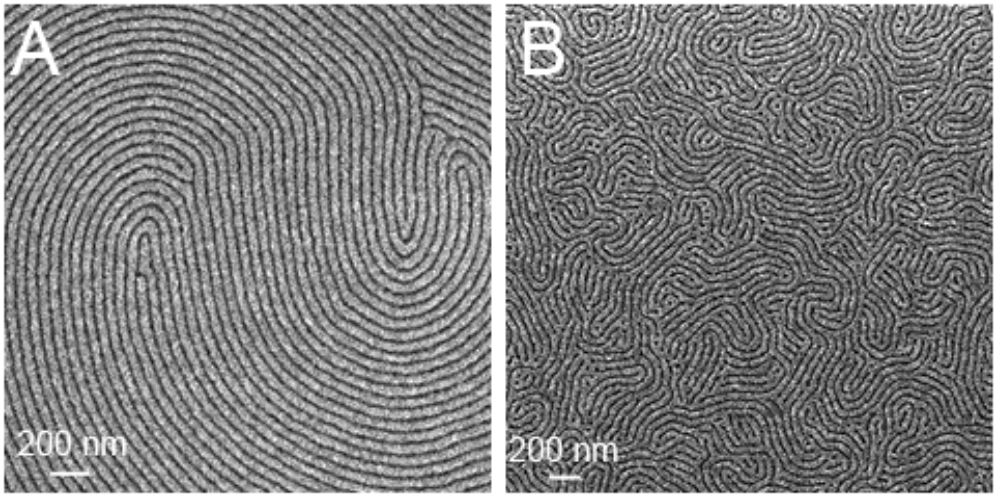

Figure 4.10: SEM image of PS-*b*-TMSI on a cross-linked polystyrene surface treatment (X-PS). **A)** annealed with diethyl ether for 5 h. **B)** Annealed with toluene for 1.5 h.

Solvent annealing using toluene generally produced more uniform and consistent self-assembly in shorter periods of time, while diethyl ether tended to yield a non-uniform film with large regions where the polymer apparently did not assemble. Thus, toluene was chosen for subsequent graphoepitaxially-guided self-assembly studies using PS-*b*-PTMSI on pre-patterned wafers provided by SEMATECH (**Figure 4.11**). Assembling the block copolymer on a patterned substrate produced markedly different self-assembly behavior than on a flat X-PS mat. Assembly of the block in between gratings (**Figure 4.12**) yielded no lithographically useful structure, but the region adjacent to the gratings revealed the coexistence of perpendicular and parallel cylinders (**Figures 4.12 and 4.13A**), illustrated by both hexagonally-packed dot and "fingerprint" type patterns. It is possible that small film thickness variations produced during the spin-

coating process lead to commensurability effects that govern the BC orientation (*116*), but regardless of the cause, the dual orientation provides insight into the block copolymer thin film morphology as-annealed by toluene, which is now assigned as hexagonally-packed cylinders. **Figures 4.13B and 4.14** shows the effect of the toluene-annealed sample confined within a Fresnel zone plate. Interestingly, relatively well-aligned hexagonally-packed cylinders are observed within the trench. Furthermore, there appear to be few grain boundaries present, suggesting some level of long-range order induced by the graphoepitaxial assembly, which is extremely important for industrial applications using block copolymers (*117*). The apexes of the trenches show a slightly mixed but predominantly parallel cylinder morphology. The current hypothesis is that the film thickness of the swollen block copolymer is different within the trench and above it, which leads to commensurability effects at least partially contributing to the observed orientation differences. The solvent-annealed block copolymer confined between pre-patterned posts (**Figure 4.13C and 4.15**) also produced perpendicular cylinders between the posts. The self-assembled perpendicular cylinders were subsequently etched using an O_2 RIE, which was expected to remove the matrix material and leave the silicon-rich cylinders intact (more information about etching can be found in Chapter 5). Tilted SEM of the etched sample (**Figure 4.13D**) indeed demonstrated the efficacy of the etch process, with significant removal of the PS matrix and hexagonally packed dots left on the substrate.

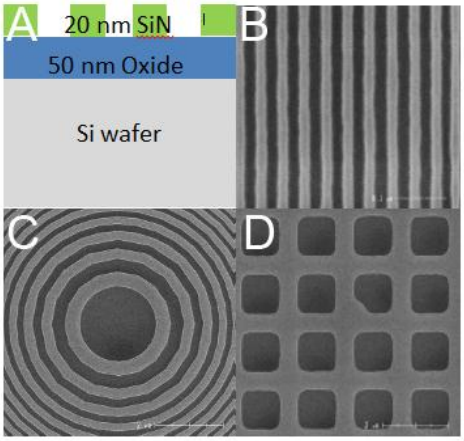

Figure 4.11: **A)** The pre-patterned wafers used in this work consisted of 20 nm thick SiN features on a 50 nm oxide layer. Representative features include **B)** gratings **C)** Fresnel plate zones and **D)** programmed defects.

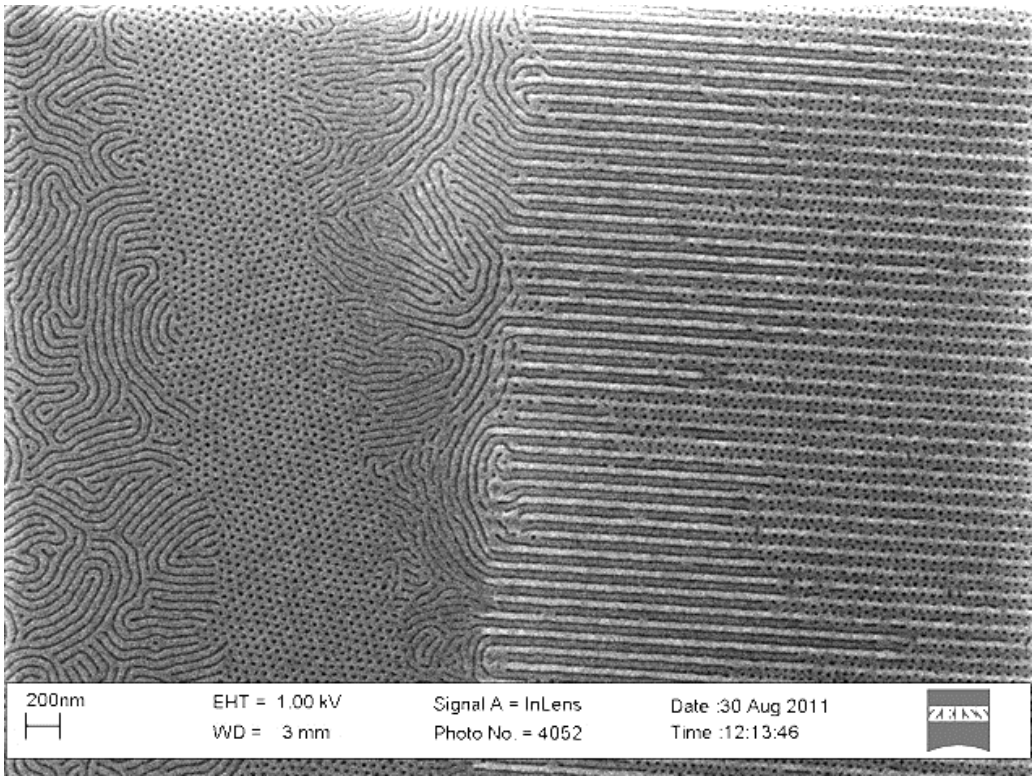

Figure 4.12: PS-*b*-PTMSI solvent annealed in toluene for 1.5 h on cross-linked polystyrene at the edge of pre-patterned gratings. The coexistence of parallel and perpendicular cylinders can be seen in the left half of the image.

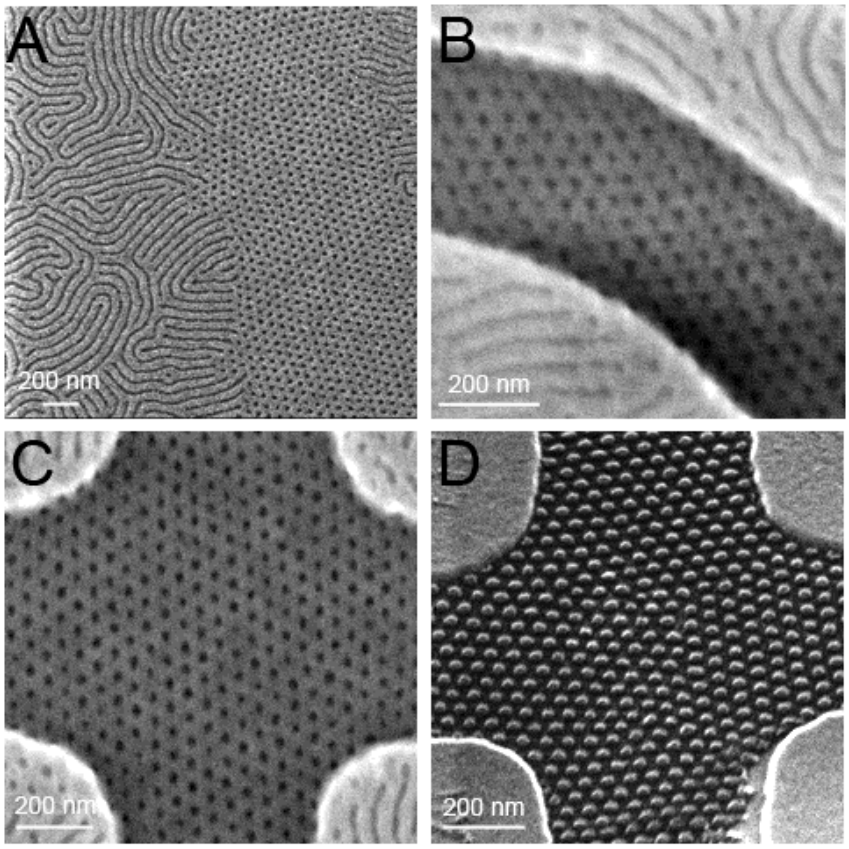

Figure 4.13: SEM images of etched PS-*b*-PTMSI annealed with toluene for 1.5 h on pre-patterned substrates with a polystyrene cross-linked surface treatment. Key: **A)** A region near pre-patterned gratings which shows the coexistence of parallel and perpendicular cylinders. **B)** Graphoepitaxial assembly of perpendicular cylinders confined within a trench of a Fresnel zone plate. Parallel cylinders can be seen on the apexes. **C)** Graphoepitaxial assembly of perpendicular cylinders between pre-patterned posts. Mixed (perpendicular and parallel coexisting) morphologies can be observed on the pillar apexes. **D)** Tilted view of perpendicular cylinders confined between pillars, analogous to Figure 5C.

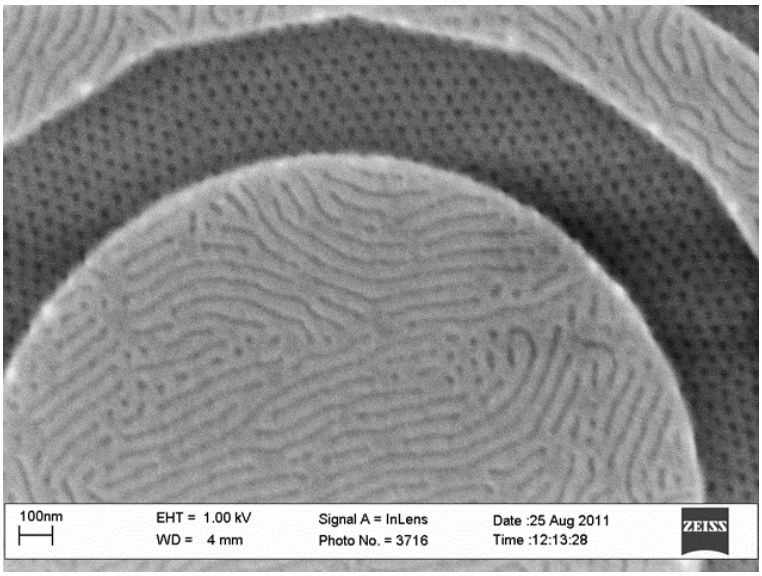

Figure 4.14: PS-*b*-PTMSI solvent annealed in toluene for 1.5 h on cross-linked polystyrene surface treatment on a pre-patterned Fresnel zone plate.

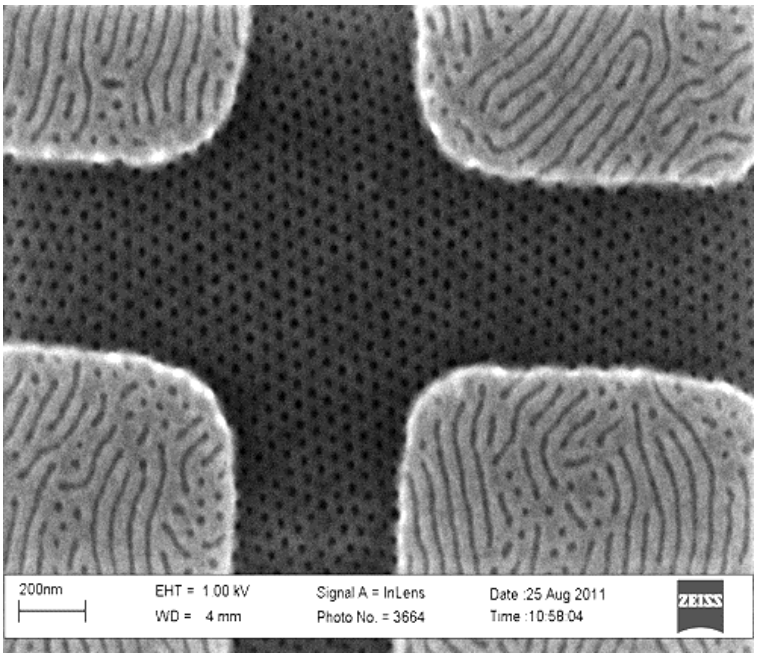

Figure 4.15: PS-*b*-PTMSI solvent annealed in toluene for 1.5 h on cross-linked polystyrene surface treatment on pre-patterned posts.

Unfortunately, the PTMSI block has a low T_g (<< room temperature) that potentially introduces flow and defects during pattern transfer steps. While the orientation control and graphoepitaxial alignment results were encouraging from the perspective of gaining a deeper understanding of thin film processes, the material was ultimately abandoned in favor of other high-χ silicon-containing BCPs.

4.5 POLY(STYRENE-*BLOCK*-METHYLTRIMETHYLSILYLMETHACRYLATE)

PS-*b*-PMTMSMA was designed to improve upon PS-*b*-PTMSI in two ways: 1) PMTMSMA has a higher T_g (>> room temperature) than PTMSI and 2) MTMSMA monomer is commercially available, which simplifies polymerization preparation significantly. Both lamella and cylinder-forming BCPs were synthesized. The cylinder-forming sample is described in Chapter 2 and is extensively used herein. During the solvent annealing phase of the project, cylinders were still the targeted morphology for bit patterned media and were thus most heavily pursued. Julia D. Cushen synthesized a large number of lamella samples to fully characterize the χ value of the material; the data will be reported separately by her. A significant amount of effort was expended on trying to solvent anneal cylinder-forming PS-*b*-PMTMSMA. An initial screening of 24 solvents with a wide range of dielectric constants (**Table 4.1**) (*118-122*) yielded no self-assembled patterns after 1 h of annealing using bare silicon as a surface treatment. Furthermore, at 5.5 h, most films dewet and the ones that did not still yielded no pattern. All attempts to vary block copolymer film thickness also resulted in no block copolymer self-assembly. Eventually it was discovered that using DMF to solvent anneal cylinder-forming PS-*b*-PMTMSMA for ~5.5 hr resulted in self-assembly of line-space patterns that were interpreted as parallel cylinders (**Figure 4.16**).

Table 4.1: Initial solvent screening with cylinder-forming PS-*b*-PMTMSMA yielded no self-assembly.

Solvent	Dielectric Constant
pentane	1.84
heptane	1.9
cyclopentane	1.97
hexanes	2.02
cyclohexane	2.02
decahydronaphthalene	2.2
1,4-dioxane	2.2
benzene	2.3
anisole	4.33
diethyl ether	4.34
chloroform	4.81
ethyl acetate	6.02
2-methoxyethyl ether	7.7
PGMEA	8.3
DCM	9.1
cyclohexanone	16.1
1-butanol	17.8
IPA	18.3
2-butanone	18.5
1-propanol	20.1
ethanol	24.3
acetonitrile	36.6
DMF	36.7
DMSO	47.2
water	80

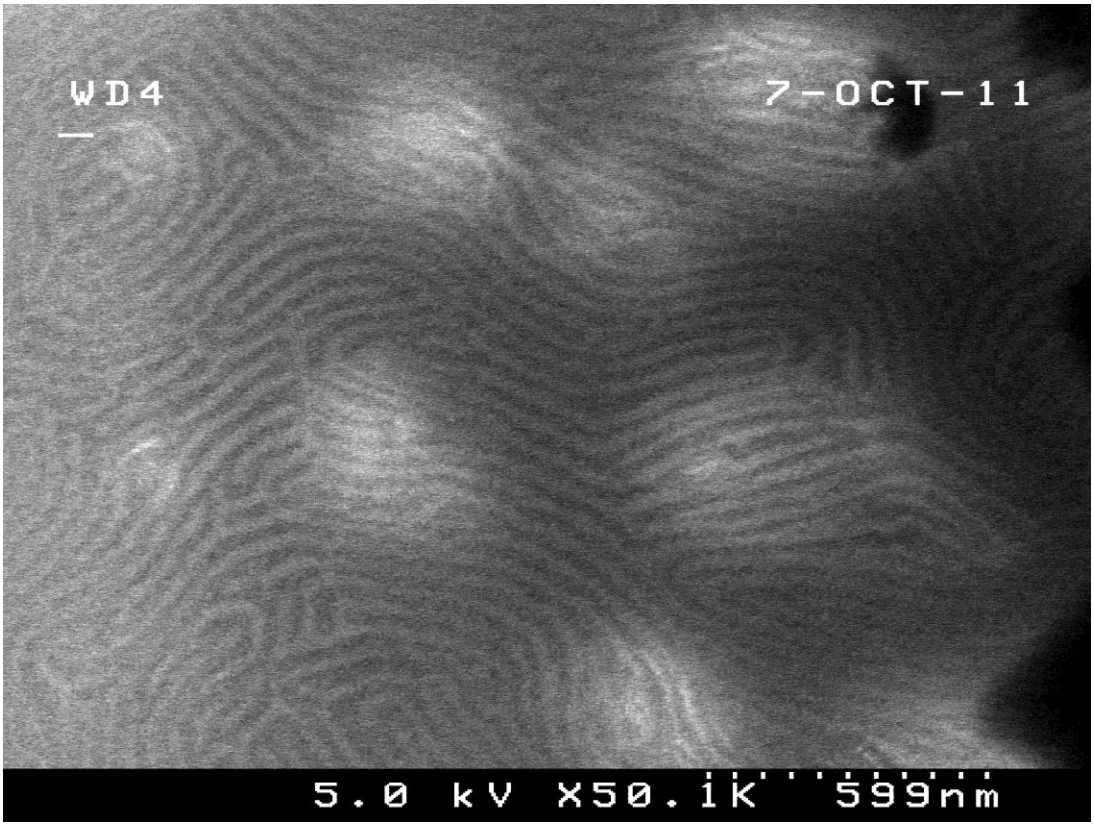

Figure 4.16: Cylinder-forming PS-*b*-PMTMSMA (52 nm) cast on bare silicon wafer (no surface treatment), solvent annealed with DMF for 5.5 hr. The sample was etched with SF_6 followed by O_2 (UT formula). SF_6: Pressure=50 mTorr, RF=20 W, ICP=50 W, SF_6 Flow=5 sccm, Ar flow=45 sccm, Temp=15°C, time=15 sec; O_2: Pressure=20 mTorr, RF=80 W, ICP=50 W, O_2 Flow=75 sccm, Ar flow=75 sccm, Temp=15°C, time=30 sec.

It was hypothesized that, similar to PS-*b*-PTMSI, using more appropriate surface treatments would potentially limit thin film dewetting and improve the self-assembly of the BCP. Unfortunately, none of the solvents listed in **Table 4.1** produced any self-assembly for cylinder-forming PS-*b*-PMTMSMA solvent annealed on Mat SM-1, Mat SM-2, Mat SM-3, Mat-SM-4, or X-PS (see Chapter 3 for mat materials). However, cylinder-forming PS-*b*-PMTMSA annealed in DMF for ~5.5 h on the PS-*r*-PMTMSMA-

r-PVBzAz crosslinked random copolymer Mat-SM-2 resulted in line-space patterns that seem more well-defined and regular than those observed on bare silicon (**Figure 4.17**). Note that the film was etched to expose the BCP pattern (see Chapter 5 for more etching details). The white dots in **Figure 4.16** are believed to be artifacts of a non-optimal etch process. While not the most desired thin film orientation, this was the first observed self-assembly of PS-*b*-PMTMSMA. Changing the surface treatment to a presumably less-optimal X-PS mat resulted in considerably worse assembly with DMF as a solvent; the best assembly was observed at 5.5 h (**Figure 4.18**) and is still highly defective. Longer annealing times caused dewetting to occur.

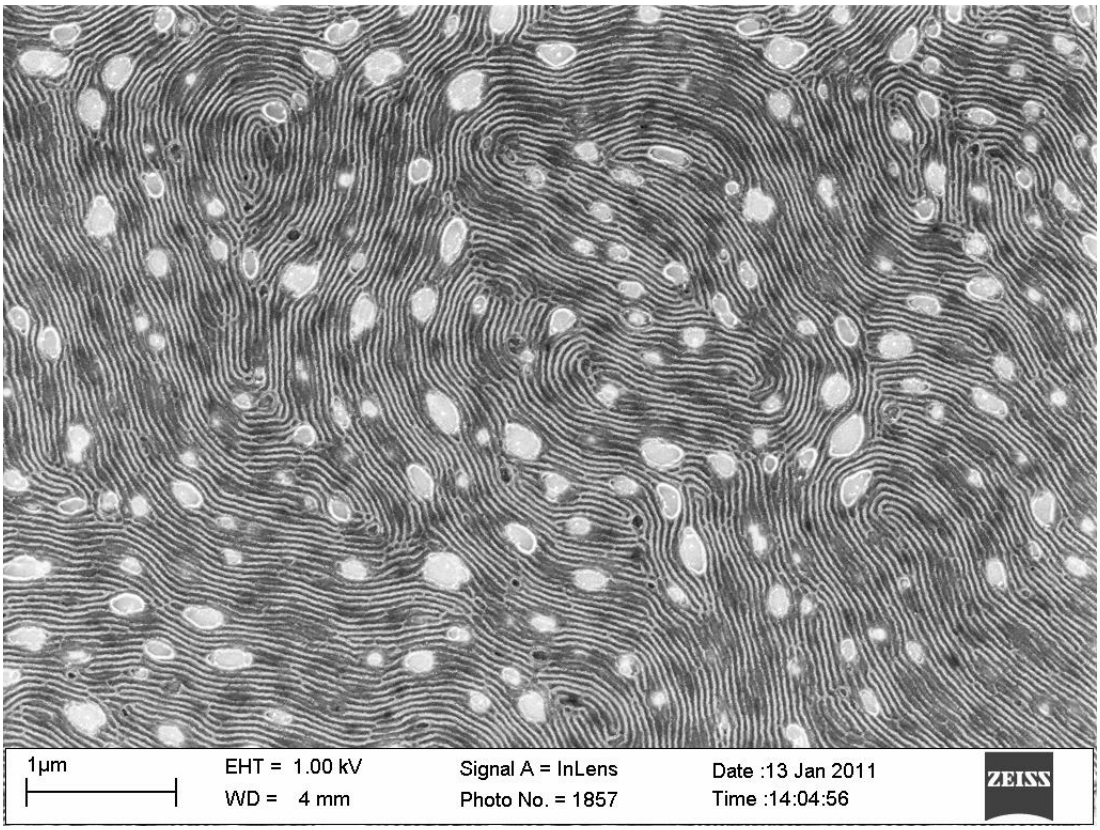

Figure 4.17: Cylinder-forming PS-*b*-PMTMSMA (54 nm) on surface treatment Mat-SM-2 (PS:PMTMSMA:PVBzAz=65:31:4), solvent annealed with DMF for 5.5 hr. Relatively well-formed lines are suggestive of parallel cylinders, and this type of pattern was observed across large regions of the wafer. The light spots are likely artifacts of the 6 sec SF_6 etch process.

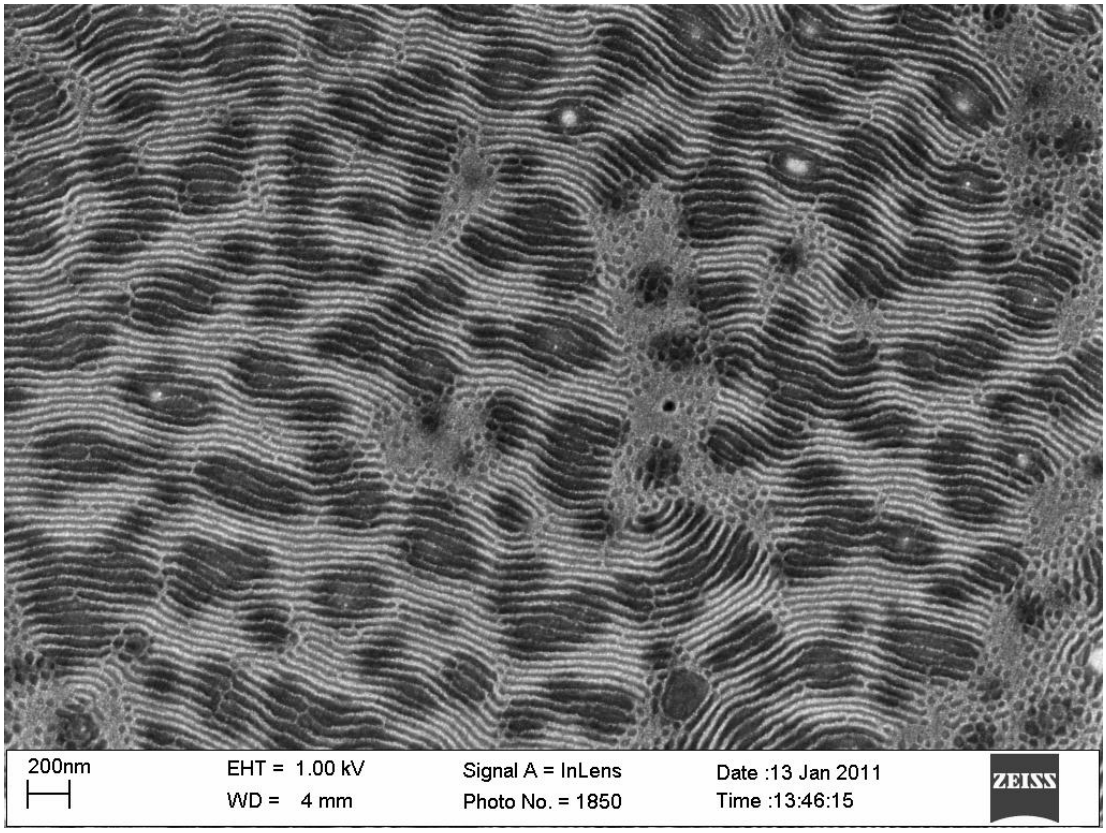

Figure 4.18: Cylinder-forming PS-*b*-PMTMSMA (54 nm) on surface treatment X-PS, solvent annealed with DMF for 5.5 hr.

The extreme difficulty in finding solvents that produce self-assembly of PS-*b*-PMTMSMA was quite surprising and frustrating. Most BCP materials found in the literature have a variety of solvents that create self-assembled patterns (*34, 115, 123*); the conditions of the annealing can then be tuned to create the desired orientation and alignment of the features. In the case of PS-*b*-PMTMSMA, the only solvent that even produced a pattern is DMF, and it only formed what we believe is parallel cylinders, which is not ideal. Over a year and a half were already invested in the BCP thin film work. Rather than continue a likely fruitless effort to further control the orientation by solvent annealing, we decided to demonstrate the graphoepitaxial alignment of the features within pre-patterned silicon trenches. Such a process has been demonstrated

with PS-*b*-PMMA (*105*) and PS-*b*-PDMS cylinders (*123*) and the potential to utilize higher χ silicon-containing BCPs than PS-*b*-PMMA could potentially be useful for next generation DSA.

The process first involved creating "trenches" on the silicon substrate (**Figure 4.19**). One patterning method available involves an additive rather than subtractive process; instead of selectively removing a portion of the silicon to create a trench, terraces are formed using a negative electron beam lithography resist, hydrogensilsesquioxane (HSQ). Exposed regions of the resist crosslink and become insoluble upon development (*19*). Subsequent O_2 passivation renders the crosslinked Si_xO_y material similar to the native SiO_2 oxide on the silicon wafer (*124*). A scanning electron micrograph of the oxidized HSQ lines is shown in **Figure 4.20**. A surface treatment can be spin-coated over the silicon posts and within the trench, followed by a block copolymer (**Figure 4.21**). Note that the block copolymer is quite sensitive to the width of the trench relative to the periodicity of the BCP (*125*). The dimensions of the trench influence the ability of the BCP to self-assemble into its energetically favorable state without added extension or compression. Mismatch between the trench size and the BCP periodicity can create undesired frustrated morphologies and defects (*126*) or affect the relative alignment of the BCP features and the pre-patterns (*32*).

After application of the BCP, the film was solvent annealed using DMF for 5.5 h. **Figure 4.22** shows the results of the solvent annealed and etched film. Relatively good alignment of the parallel cylinders within the 500 nm trench is observed – the cylinders lie parallel to both the plane of the substrate and the trench walls. Note that other trench widths did not produce BCP features consistently parallel to the trench walls, the best and most aligned assembly was observed within the 500 nm trench. This trench width corresponds with 8.3*c where c is the calculated bulk center-to-center distance of 60.5 nm. This is relatively consistent with the 8 observed cylinders populating the trench. However, the as-measured center-to-center distance of the cylinders in the SEM image is 46 nm, which is closer to the bulk d_{100} distance of 52.4 nm. One plausible explanation is that the DMF-swollen BCP has different dimensions than the thermally annealed bulk

BCP. Furthermore, roughness on the trench sidewall seems to indicate some dewetting, which may be contributing to a frustrated self-assembled state. Additional experiments seem to indicate that the sidewall roughness is indeed from partial dewetting of the BCP annealed in DMF and not from the electron beam lithography.

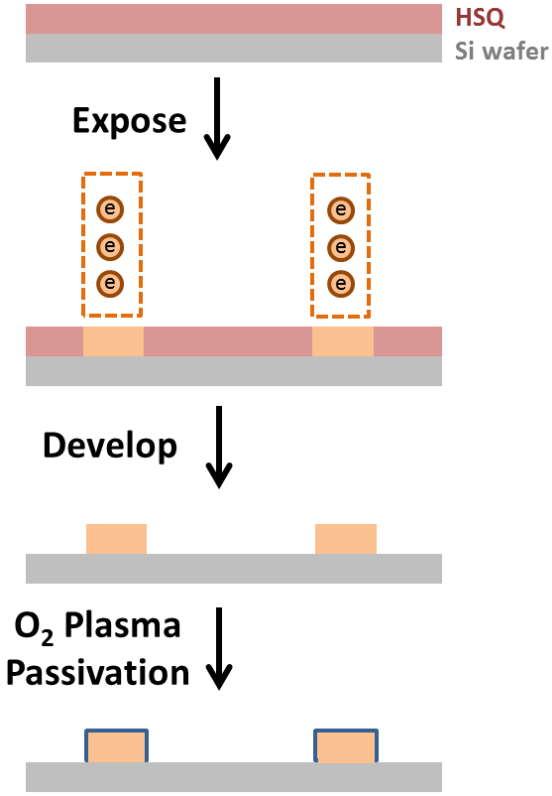

Figure 4.19: Schematic of the process used to pattern trenches in silicon by an additive process. HSQ negative electron beam lithography resist is crosslinked in exposed regions. After development of unexposed regions, Si_xO_y material remains and is passivated with a quick O_2 plasma etch.

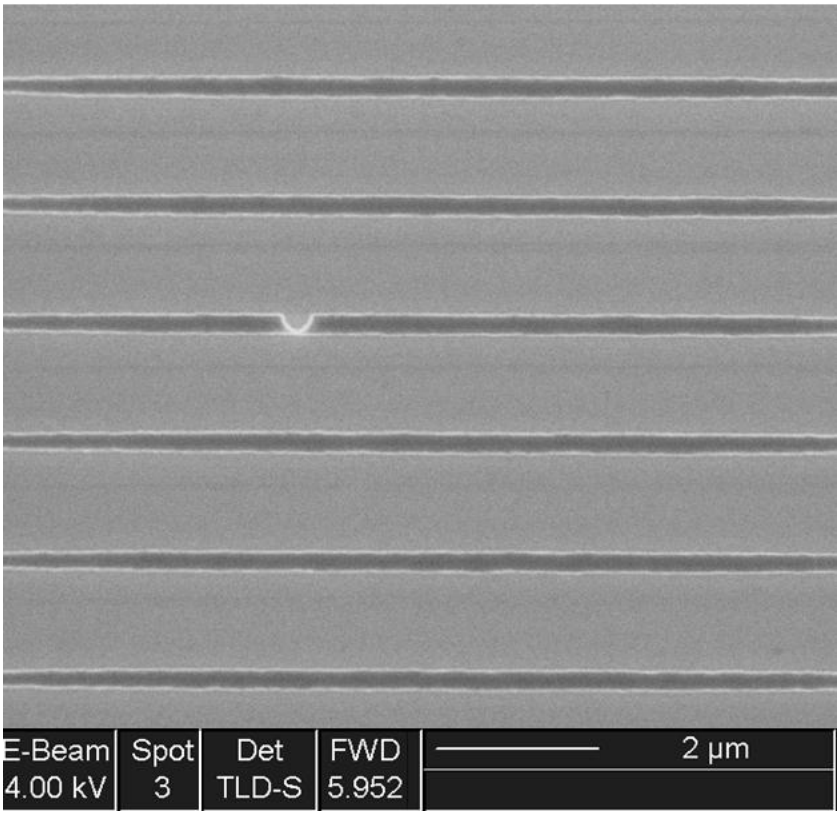

Figure 4.20: Lines printed with hydrogen silsesquioxane, a negative electron beam lithography resist, for use as a directing template for PS-*b*-PMTMSMA. Electron beam lithography was performed at the University of Wisconsin-Madison. The lines were developed in tetramethylammonium hydroxide and exposed to O_2 plasma for 20 sec to oxidize the surface of the resist.

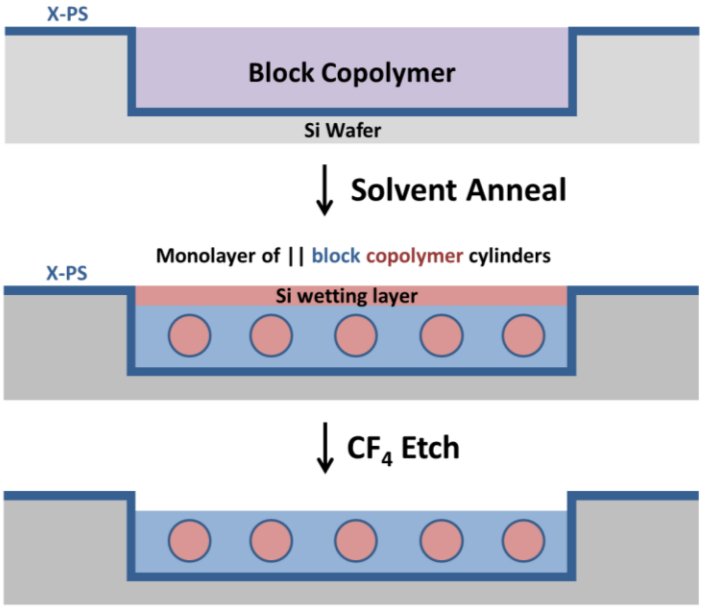

Figure 4.21: Schematic of graphoepitaxial alignment of PS-*b*-PMTMSMA within pre-patterned silicon trenches. Circles represent cylinders coming in and out of the plane of the page, both parallel to the substrate and trench walls.

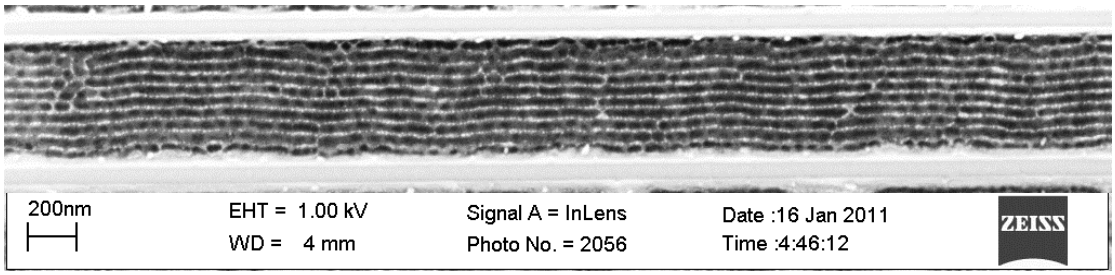

Figure 4.22: Graphoepitaxial alignment of cylinder-forming PS-*b*-PMTMSMA (~54 nm thick) on X-PS surface treatment solvent annealed with DMF for 5.5 hr. HSQ trenches patterned by e-beam lithography appear as light stripes. The sample was etched with a 6 sec SF_6 etch prior to imaging. Cylinders in between the HSQ can be seen running parallel to the trench walls.

Alignment was also achieved in thicker trenches 940 nm wide (**Figure 4.23**). The alignment was again characterized by trench sidewall roughness. The best results with the wider trenches were again observed with a ca. 55 nm thick BCP on an 11 nm thick crosslinkable XST-H PS mat. Similar to **Figure 4.23**, defectivity was also observed with discontinuous individual cylinders. Cylinders also failed to align throughout the entire length of the trench and only tended to align reasonably well near the ends. Shear fields have been demonstrated to align BCP domains within thin films (*127*) and it is possible they contribute to the alignment of the PS-*b*-PMTMSMA cylinders at the ends of the trenches.

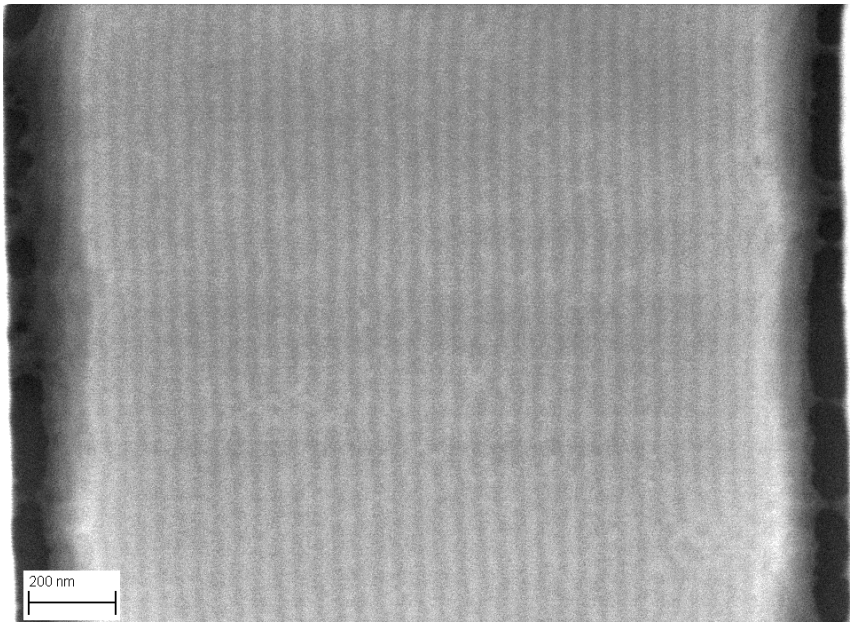

Figure 4.23: Graphoepitaxial alignment of 55 nm thick PS-*b*-PMTMSMA within a trench 940 nm wide on an XST-H crosslinkable PS mat. The trench was patterned by photolithography and kindly provided by Tokyo Ohka Kogyo (TOK).

Although the best orientation control on non-patterned substrates was obtained with DMF as a solvent and Mat SM-2 as a substrate surface (**Figure 4.17**), the best results on patterned substrates (**Figure 4.22**) were obtained using an X-PS mat. One

possible explanation is related to the addition of extra interfaces (along the trench wall) with the patterned substrates. In the case of parallel cylinders, it is actually more energetically favorable to have trench walls that are preferential towards the majority block (*128*). While it is difficult to infer what the interfacial preferences are of each block in the DMF swollen state, it is possible that Mat-SM-2 is more neutral towards both blocks than X-PS, which is presumably preferential towards the majority polystyrene block. The differences between these surface treatments may become more pronounced with the increased interfacial area of the patterned silicon.

Ultimately the use of PS-*b*-PMTMSMA was abandoned because of the extreme difficulty in controlling both the orientation and alignment of cylinder and lamella features in thin films. On paper, the BCP appears to meet all of the requirements of an ideal lithographic BCP material: it is readily synthesizable by anionic polymerization, both monomers are commercially available, it has a higher χ than PS-*b*-PMMA, and both blocks have a T_g>room temperature. Unfortunately, PS-*b*-PMTMSMA exemplifies the difficulties encountered with the multi-faceted field of lithography. Materials must meet all of the required experimental attributes to be useful; failure to perform acceptably in even one crucial aspect can be a death sentence. The underlying cause of the difficulties encountered is not entirely clear but they necessitated the investigation of alternative Si-BCPs.

4.6 POLY(STYRENE-*BLOCK*-TRIMETHYLSILYLSTYRENE-BLOCK-STYRENE)

Solvent annealing of cylinder-forming PS-*b*-PTMSS-*b*-PS was investigated as an alternative to both PS-*b*-PTMSI and PS-*b*-PMTMSMA. Similar to PS-*b*-PMTMSMA, both blocks (PS and PTMSS) have T_g >> room temperature. Ultimately, the downside to PS-*b*-PTMSS-*b*-PS is that its χ value is slightly lower than even PS-*b*-PMMA, which makes it significantly less attractive as a next-generation lithographic material. Never-the-less, some solvent annealing work was performed concurrently with the synthesis and characterization of its χ value (which took a considerable amount of time and effort, mainly by Julia D. Cushen). A set of solvents was initially screened (**Figures 4.24-4.27**)

and immediately produced significantly more promising self-assembly than solvent annealed PS-*b*-PMTMSMA. Virtually all solvents tested induced some self-assembled thin film pattern. Cyclohexane, DCM, 1-butanol, IPA, cyclohexanone, 1-propanol, ethanol, DMSO, and water produced mixed morphologies and were discarded. PGMEA produced line-space patterns that could be interpreted as parallel cylinders or perpendicular lamella and were also discarded. However, unlike PS-*b*-PMTMSMA, benzene, anisole, and 2-methoxyethyl ether produced hexagonally-packed dot patterns. While it is difficult to differentiate between spheres and perpendicular hexagonally-packed cylinders in a thin film without doing additional characterization such as syncotron grazing incidence small angle x-ray scattering (GISAXS), the initial results appeared quite promising. Larger field images of anisole, 2-methoxyethyl ether, and benzene are shown in **Figures 4.28-4.30**. The measured cylinder diameters from **Figures 4.28-4.30** are relatively consistent: anisole (24 nm), benzene (25 nm), and 2-methoxyethyl ether (25 nm). Thin film measurements agree relatively closely to the bulk cylinder diameter of 22 nm as calculated by SAXS. It is possible the solvents are causing some slight swelling of the features. Benzene exhibited slightly more dispersity in cylinder diameter and shape than both anisole and 2-methoxyethyl ether. However, 2-methoxyethyl ether did show some "worm-like" structures that are interpreted as parallel cylinders (i.e. it produced a slightly mixed morphology).

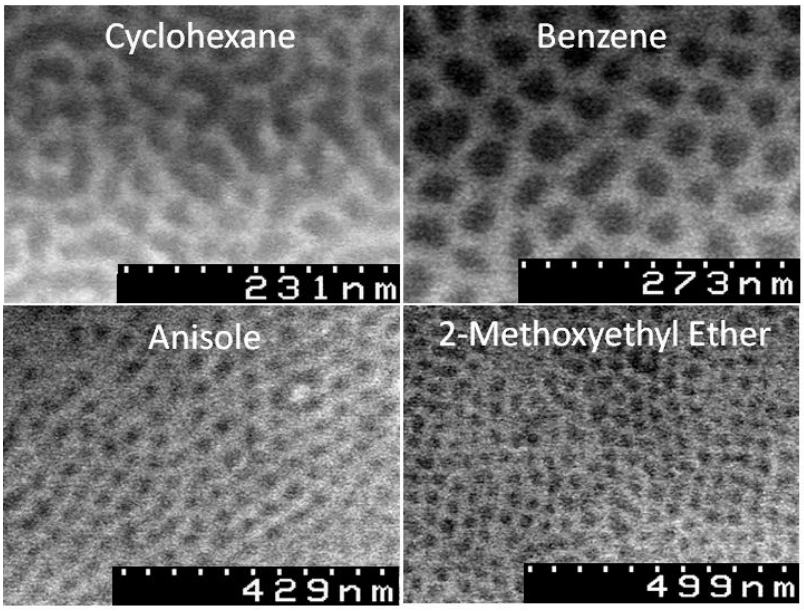

Figure 4.24: PS-*b*-PTMSS-*b*-PS solvent annealed for 1 h with various solvents on native SiO_2.

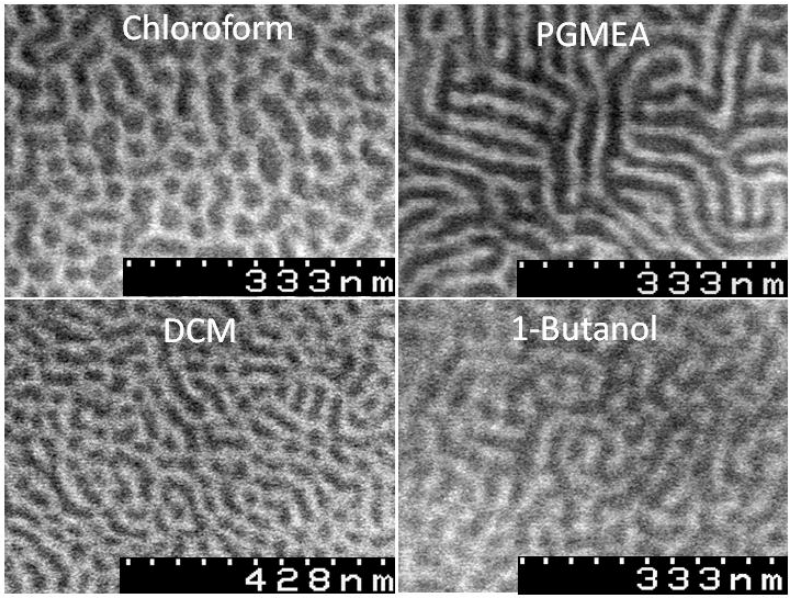

Figure 4.25: PS-*b*-PTMSS-*b*-PS solvent annealed for 1 h with various solvents on native SiO_2.

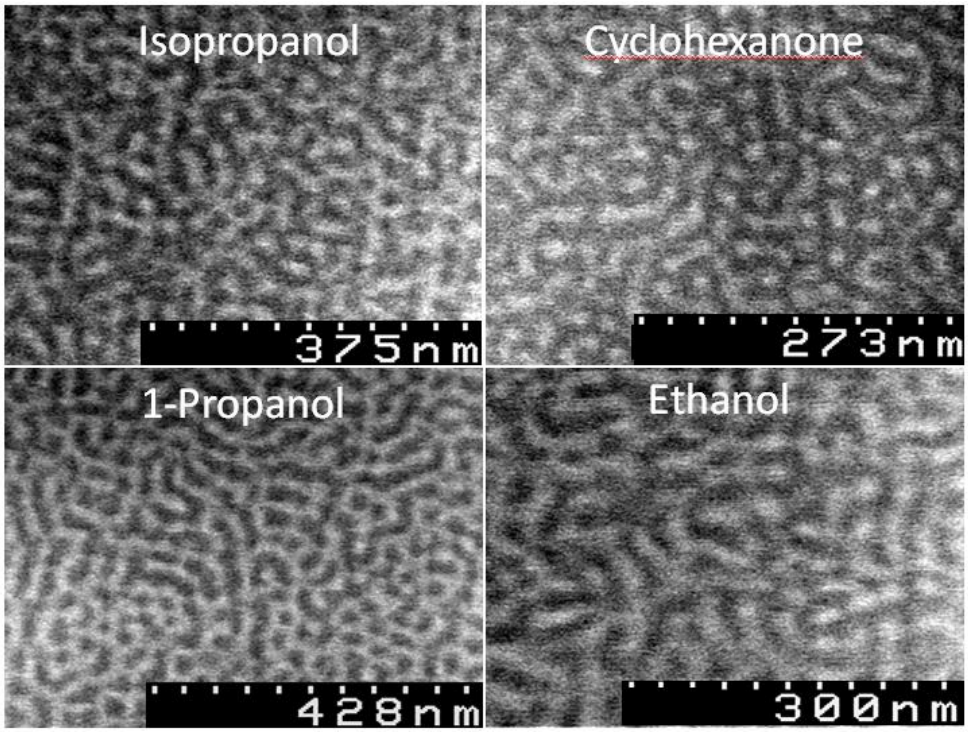

Figure 4.26: PS-*b*-PTMSS-*b*-PS solvent annealed for 1 h with various solvents on native SiO_2.

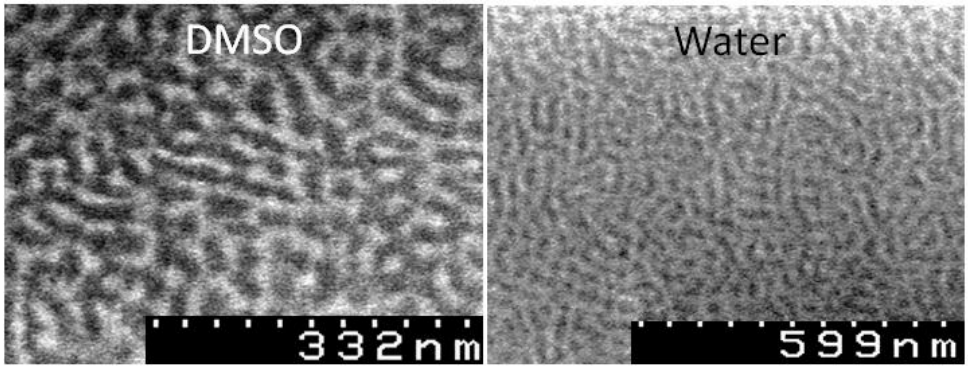

Figure 4.27: PS-*b*-PTMSS-*b*-PS solvent annealed for 1 h with various solvents on native SiO_2.

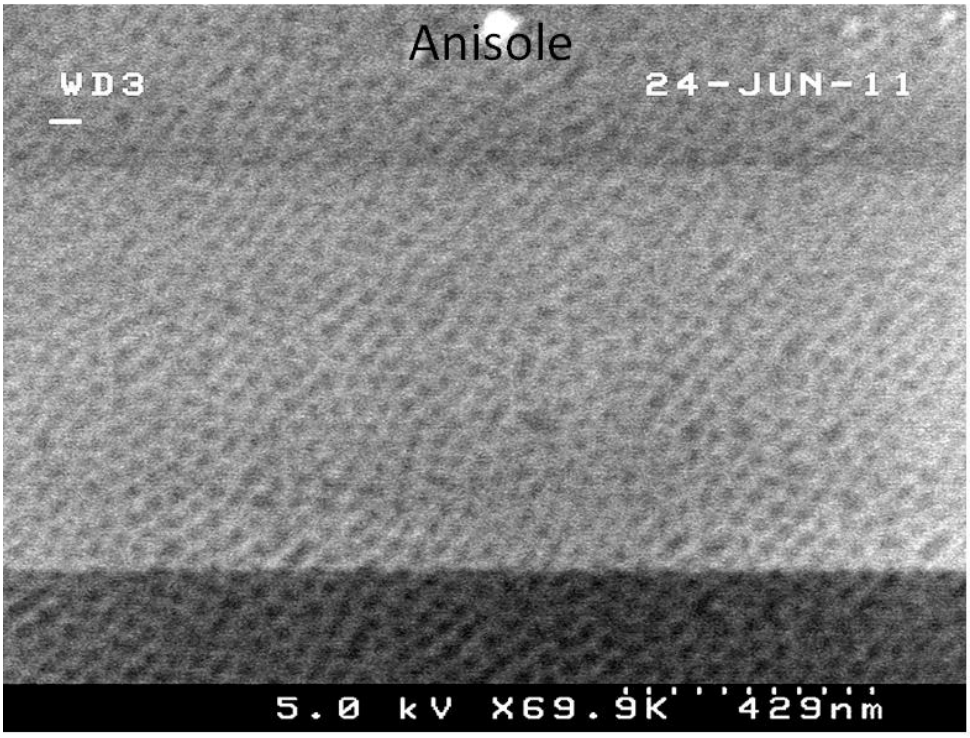

Figure 4.28: Larger field of PS-*b*-PTMSS-*b*-PS solvent annealed for 1 h with anisole.

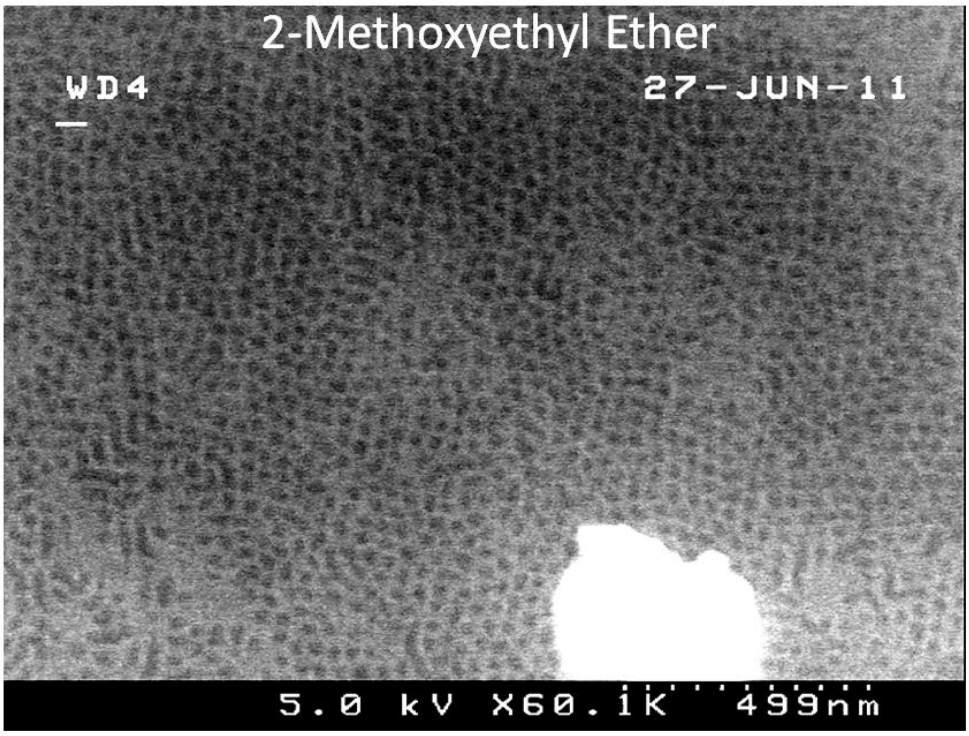

Figure 4.29: Larger field view of PS-*b*-PTMSS-*b*-PS solvent annealed for 1 h with 2-methoxyethyl ether.

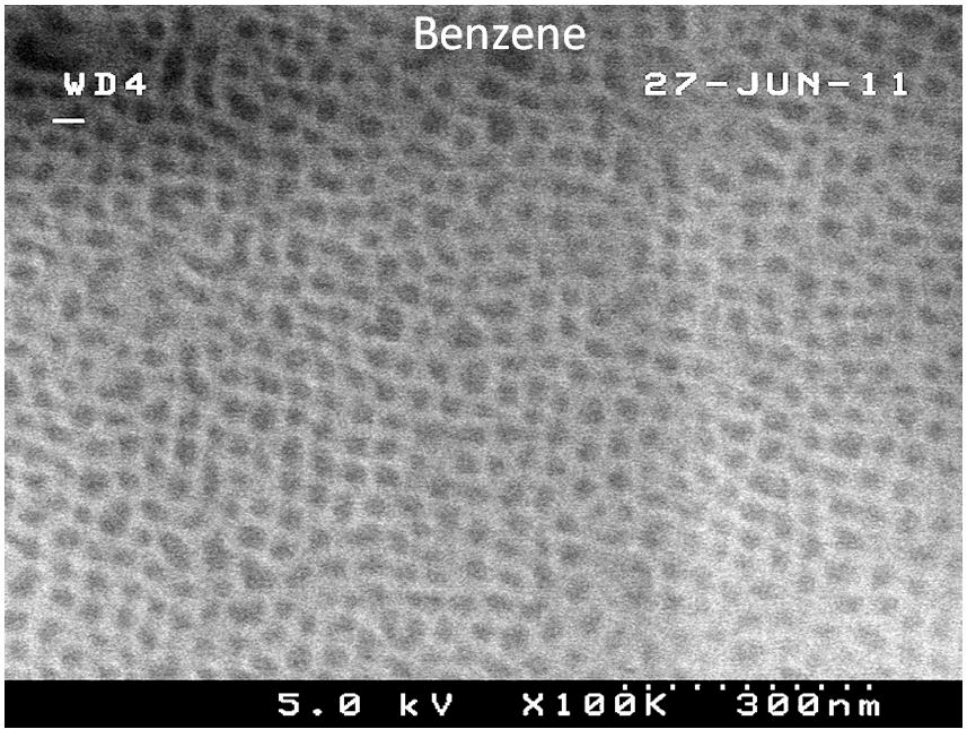

Figure 4.30: Larger field view of PS-*b*-PTMSS-*b*-PS solvent annealed for 1 h with benzene.

4.7 EXPERIMENTALS:

PS-*b*-PTMSI Thin Film procedures:

Preparation of polymer films:

A clean silicon wafer with native oxide (*ca.* 4 nm) was cleaned by immersion in piranha etch solution (7:3 H_2SO_4 to H_2O_2) at 130°C for 30 min. However, no significant difference in the assembly of the block copolymer was observed between Si wafers with and without piranha treatment. (The patterned wafers provided by SEMATECH were not treated with piranha solution to prevent damage to the features of the wafer. Instead, these samples were sonicated with chlorobenzene). The wafers were blown dry and a 0.2 wt% solution of crosslinkable hydroxy-terminated poly(styrene-*random*-

benzocyclobutane) (7.8 wt% BCB, referred to as "X-PS mat") in toluene was spin coated at 4000 rpm, which produced a 5-6 nm film. The film was subsequently crosslinked by baking under a nitrogen atmosphere at 250°C for 5 min, which resulted in a polymer "mat" surface treatment. Solutions of approximately 1 wt% PS-*b*-PTMSI in toluene were then spin-coated on top of the mat at 3500 rpm in order to achieve film thicknesses of ≈40 nm, commensurate with the cylinder-to-cylinder distance obtained by small angle X-ray scattering measurements.

Solvent Annealing and Reactive Ion Etching:

A wafer fragment bearing the BC thin film was placed in a 20 mL scintillation vial containing a smaller, 7 mL vial containing 5 mL solvent. Toluene annealing was performed for 1.5 h, diethyl ether annealing was performed for 5 h. After annealing, the films were etched with an SF_6 plasma for a short time in order to remove the wetting layer formed by the Si containing block. Some samples had a subsequent etch performed with O_2 plasma to remove the styrene block and thereby produce a physical pattern based on the original assembled block copolymer structure.

PS-*b*-PMTMSMA Thin Film Procedures:

General Thin Film Experimental:

For samples with a substrate surface treatment, a 0.2 wt% solution of surface treatment (for instance, Mat-SM-1) in toluene was spin coated onto an oxygen plasma cleaned silicon wafer. The surface treatment was cross-linked at 250°C for 5 minutes under a nitrogen atmosphere. Subsequently, the wafer was quickly cooled to room temperature followed by submersing in toluene for 2 minutes and blown dry twice to remove residual uncross-linked polymer, which resulted in a surface treatment thickness of 8 nm. In the case of samples with no surface treatment, the block copolymer was spin-coated directly onto the silicon wafer. Various concentration block copolymer solutions were used to produce the desired block copolymer film thicknesses. For instance, a 1.8

wt% solution of lamella-forming PS-*b*-PMTMSMA (bulk L_0=27.1 nm) in toluene was spin-coated at 3000 rpm to give a block copolymer film thickness of 51 nm. The thin films were solvent annealed with various solvents for variable amounts of time. The film was subsequently etched on a custom-built reactive ion etch tool at the University of Wisconsin-Madison with the following recipe developed by Professor Paul Nealey's group to remove a silicon air-interface wetting layer: pressure=10 mT, ICP power=300 W, RIE power=40 W, Gas flow rate (sccm)= 35 Ar, 5 SF_6, 9 C_4F_8, 5 backside He (for cooling), temperature=20°C, time=6 sec.

Graphoepitaxy pre-patterns:

Patterns produced by electron-beam lithography (**Figures 4.20 and 4.22**) were created as follows. A 6% solution of hydrogen silsesquioxane was purchased commercially from Dow Corning and cast at 3000 rpm to give a ca. 110 nm film. The resist was exposed using a LEO VP-1550 Scanning Electron Microscope with variable dose at the University of Wisconsin-Madison. The pattern was subsequently developed in 25% TMAH at room temperature and rinsed with flowing deionized water for 30 sec.

The pre-patterned wafer used for the graphoepitaxial alignment in **Figure 4.23** was produced by photolithography and kindly provided by Tokyo Ohka Kogyo (TOK).

X-PS Mat

Cross-linkable polystyrene mat, hydroxy-terminated poly(styrene-*random*-benzocyclobutane) (7.8 wt% BCB), was produced by Professor Paul Nealey's group at the University of Wisconsin-Madison.

4.8 CONCLUSIONS:

Solvent annealing was performed on three Si-BCPs: PS-*b*-PTMSI, PS-*b*-PMTMSMA, and PS-*b*-PTMSS-*b*-PS. The most success was achieved with PS-*b*-PTMSI, which was both oriented with solvent and aligned within graphoepitaxial pre-patterns. PS-*b*-PMTMSMA was also partially aligned graphoepitaxially. However, due

to both the lack of solvents that induced the desired perpendicular orientation of the self-assembled pattern and the high levels of defectivity observed in the thin films, PS-*b*-PMTMSMA was ultimately abandoned. PS-*b*-PTMSS-*b*-PS appears potentially amenable to solvent annealing since many solvents induce self-assembly.

Solvent annealing was ultimately abandoned for two reasons. First, there are severe difficulties associated with solvent annealing. As demonstrated with PS-*b*-PTMSI, PS-*b*-PMTMSMA, and PS-*b*-PTMSS-*b*-PS, the annealing conditions can differ drastically for each BCP. While some success was found with PS-*b*-PTMSI and PS-*b*-PTMSS-*b*-PS, serious further optimization would be necessary for each material in order to realize device level perfection. Even the best images obtained (PS-*b*-PTMSI, **Figure 4.15**; PS-*b*-PMTMSMA, **Figure 4.22**, PS-*b*-PTMSS-*b*-PS, **Figure 4.28**) contained significant numbers of defects in a relatively small area. Second, the integration of solvent annealing with DSA is the subject of current research in the field and is not well-resolved. Rather than focus on a repetitive cycle of solvent annealing optimization for the aforementioned BCPs, our attention turned towards alternative methods of orientation control, which is the subject of Chapters 6 and 7.

4.9 ACKNOWLEDGEMENTS:

Solvent annealing and etching work for PS-*b*-PTMSI was done in collaboration with Professor Paul F. Nealey from the University of Wisconsin-Madison and one of his graduate students, Marco A. Bedolla Pantoja. Leon M. Dean, an undergraduate research assistant, was pivotal in much of the solvent annealing and thin film work. Logan J. Santos also made significant contributions to the solvent annealing work.

Chapter 5: Reactive Ion Etch Process Optimization

5.1 Thin Film Etching Background

The ultimate goal of the BCP thin film self-assembly work reported herein is to selectively remove one block and leave the second block intact, a process which will be referred to as "BCP pattern development." The nanoscale physical relief pattern that results can then be manipulated into desired structures through subsequent processing. Myriad post-development techniques exist to achieve such pattern transfer that include dry etching into metal (*129*) or single crystal silicon (*130*), growth of silicon dioxide within nanoscopic pores (*131*), and metal deposition and liftoff techniques (*11*, *132*). The work herein aims to develop a process for BCP pattern development.

5.2 Wet Etching

BCP pattern development is most often accomplished using either wet or dry etching. Wet etching involves rinsing away one block with solvent after selective degradation of either that block or the covalent junction between the two blocks. For instance, the covalent bonds along the backbone of the PMMA block of PS-*b*-PMMA can be degraded with UV light. Subsequent treatment of the film with aqueous acetic acid rinses away the degradation products and leaves only the self-assembled PS domain behind (*133*). Unfortunately, the aspect ratio (height/width) of features produced by wet etch processes is limited due to pattern collapse caused by capillary forces (Figure 5.1) (*134-136*). The critical aspect ratio before pattern collapse scales with feature size and is ~3 with 30 nm pitch line-space domains. A preferable alternative to wet etching is a dry etch process known as reactive ion etching (RIE), which utilizes plasmas that can produce much higher aspect ratio structures than wet etching (*137*).

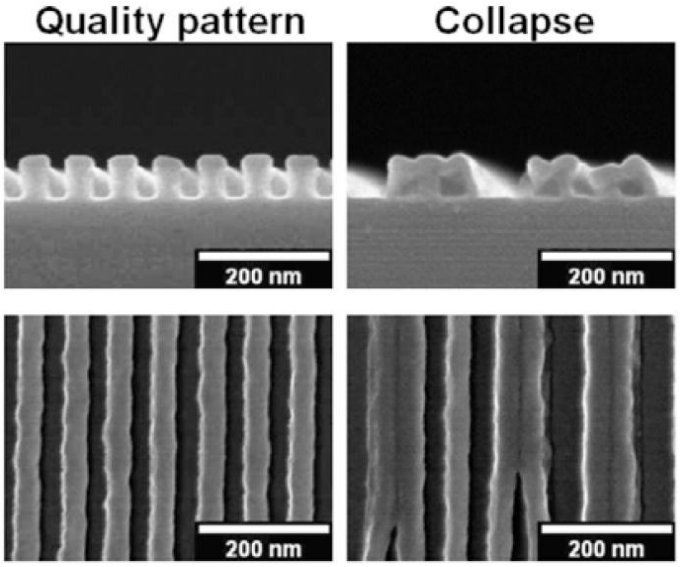

Figure 5.1: Examples of PMMA lines patterned by electron-beam lithography exposed to solvent, undamaged (left) and collapsed (right). Line collapse is caused by capillary forces produced by the development solvent and limits the aspect ratio (height/width) of thin film features etched by a wet process. Reprinted with permission from Mohammad, M. A. et al., Microelectronic Engineering 2010, 87, 1104. Copyright 2012 Microelectronic Engineering.

5.3 REACTIVE ION ETCHING

A basic parallel-plate capacitively coupled etcher involves two parallel electrodes separated by void space. A gas or combination of gases is introduced into the space between the electrodes and a plasma is generated by the application of a potential. A complex mixture of ions and neutral species is formed, some of which are highly reactive (*138*). The exact composition of reactive species is quite complex and depends upon the type of gas(es) used and the input variables of the system. The molecular and atomic species that are formed can subsequently undergo a variety of reactions. **Scheme 5.1** lists some generic types of gas and solid phase reactions that can occur in the plasma etcher (*138*).

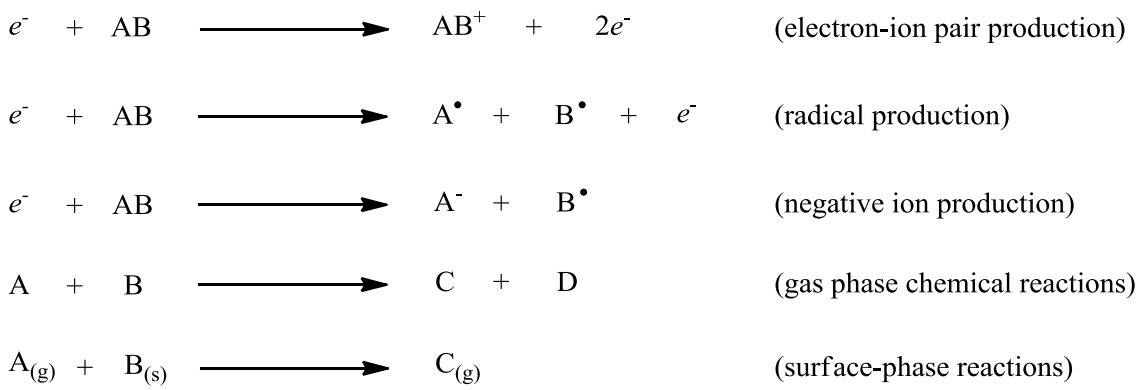

Scheme 5.1: Generic reactions that can occur in a plasma.

Plasmas can be used to controllably remove thin film material by physical and/or chemical mechanisms. Physical etching results from the bombardment of the thin film by gas phase ions that are accelerated by the electric field towards the surface of the film. These charged species sputter away material non-selectively, but can do so anisotropically. The acceleration of ions perpendicular to the plane of film results in faster vertical etch rates and slower horizontal etch rates. In contrast, chemical etching involves the reaction of ions or radicals with chemical moieties in the thin film to produce volatile products. Chemical etching can provide selectivity between different materials if their chemical composition is sufficiently different. Both physical and chemical mechanisms can also work synergistically, whereby ion bombardment reduces the activation energy necessary for chemical reactions to take place between the etch gas species and functional groups within the thin film (*139*). The surface-phase reaction from **Scheme 5.1** is of particular importance for the removal thin film material. Solid thin film material can be reacted with gaseous species to form gaseous product(s) that can be removed by vacuum. The choice of gaseous species is thus crucial for each etch process.

5.4 Requirements for 2 Etch Processes

At the outset of the RIE process optimization described in this chapter, two orthogonal etch process recipe goals were targeted: 1) a process to selectively remove the non-silicon containing block of the Si- BCPs described within this dissertation ("BCP pattern development") and 2) a process of capable of removing silicon-containing wetting layers at the top interface of annealed BCP thin films. None of these etch chemistries are fundamentally new; they have all been well-established within the literature. However, etch recipes are notoriously dependent on precise instrument specifications consistent with both literature (*139*) and personal experience. The values of input variables reported in the literature generally produce different results on separate tools. The development of specific etch formulations was thus required for the BCP materials utilized herein. Individually-tailored recipes were developed for the tool at UT Austin using the same basic etch chemistries found within the BCP thin film literature. This chapter focuses on the development of these etch recipes – the specific application of the recipes for thin film studies is reported within each individual chapter where applicable.

5.5 Process #1: O_2 Reactive Ion Etch

A BCP development process is required for most oriented BCP film, regardless of annealing method, as a prerequisite for subsequent pattern transfer processes. Techniques that circumvent pattern development requirements, such as molecular transfer printing, will not be discussed (*140*). Additionally, while some BCPs can be imaged directly by SEM with no contrast enhancement required (such as PS-*b*-PMMA), many BCPs require additional processing before the features can be observed. Arguably the simplest method is to create a physical pattern from the self-assembled and oriented BCP, which process #1 also achieves. Thus, process #1 can be used for both pattern development and as a diagnostic tool to determine the success or failure of the self-assembly and orientation processes.

RIE pattern development processes require careful design of materials to produce selectivity between the two domains. Sufficient etch contrast (i.e. a large difference in

etch rates between the blocks) must be achieved such that one block can be selectively removed without excessive damage to the second block. All of the BCPs synthesized and reported in Chapter 3 incorporate silicon into one block for O_2 etch selectivity. When a silicon-containing material with >10 wt% silicon is exposed to an oxygen plasma reactive ion etch (O_2 RIE), the silicon quickly forms solid SiO_2, which acts as an etch barrier. In contrast, material composed of carbon, hydrogen, and oxygen (the other block) reacts to form gaseous products that can be removed by vacuum (**Scheme 5.2**) (*141*). Selectivities on the order of 15:1 or greater have been reported in the literature (*142*). In contrast, all-organic block copolymers such as PS-*b*-PMMA generally have low etch selectivities (etch rate PMMA:PS) around 3 (*137, 143*), although a selectivity of up to 7 has been claimed recently (*144*).

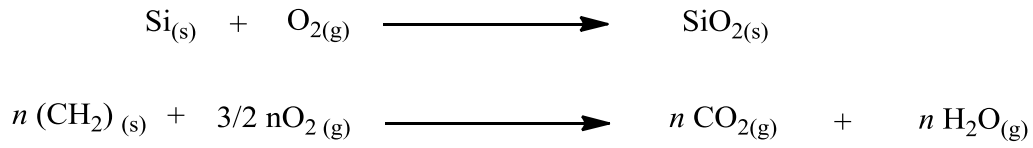

Scheme 5.2: Possible O_2 plasma etch reactions.

5.6 PROCESS #2: SF_6 REACTIVE ION ETCH

The need for process #2 stemmed from both the initial solvent annealing work described in Chapter 4 and the interpretation of negative results. A significant portion of time was spent solvent annealing thin films of PS-*b*-PMTMSMA and virtually every result produced no self-assembled pattern as observed by SEM. Unfortunately, it is not often that a negative result conclusively proves an experimental fact. That is, what caused the BCP film to lack a self-assembled pattern? It could be that the solvent choice was wrong. However, equally likely is that the block copolymer cannot be observed by SEM. The application of process #1 to the solvent annealed samples should mitigate contrast concerns, but an additional level of complexity is introduced because of the large surface energy difference between the silicon-containing block and the second block. If there are even slightly preferential interactions between the solvent-containing vapor phase and one block, that block can form a wetting layer at the top interface (a point

addressed further in Chapter 6). If the wetting layer consists of the non-silicon-containing block, it should not be of concern since the O_2 RIE process #1 will remove it and develop the BCP pattern sequentially. However, if the wetting layer is silicon-rich, it will effectively hide the features of the BCP. The O_2 RIE process will immediately stop at the wetting layer and the film will not etch. **Figure 5.2a** shows a schematic of a silicon-containing wetting layer formed from a PS-*b*-PDMS sample (*33*). The presence of the PDMS wetting layer at the top interface of the film masks the presence of parallel cylinders; even after 1 min of O_2 RIE (**Figure 5.2b**), the features are difficult to see. However, a brief 5 sec CF_4 etch, followed by a 1 minute O_2 etch (**Figure 5.2c**) cleanly and clearly exposes the self-assembled parallel cylinder pattern. The good possibility that silicon-containing wetting layers formed with the BCP samples reported in Chapter 4 thus necessitated the development of a fluorinated etch formula for analytical purposes.

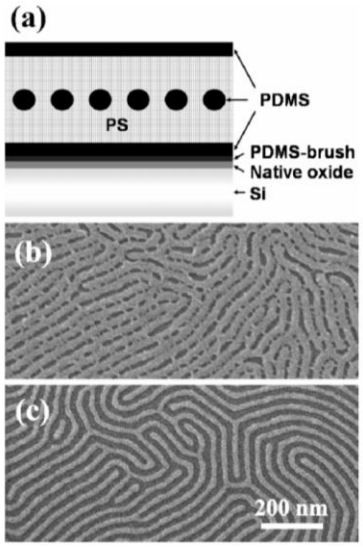

Figure 5.2: **A)** Silicon-containing wetting layers can hide the self-assembled features of Si-BCPs (pictured, PS-*b*-PDMS). **B)** Even after 1 minute of O_2 reactive ion etching, the BCP pattern is difficult to clearly observe. **C)** 5 sec of a CF_4 etch for removal of the wetting layer, followed by a 1 min O_2 etch produces a clear image. Reprinted with permission from Jung, Y. S. et al., Nano Letters 2007, 7, 2046. Copyright 2007 American Chemical Society.

Fluorine-containing gases including SF_6 and CF_4 can be used to etch silicon (**Scheme 5.3**) (*145, 146*). The resulting fluorinated silicon compounds such as SiF_4 are gaseous and can be removed by vacuum. In contrast to O_2 RIE, many of the fluorinated compounds containing C, H, and O are also gaseous. Thus, selectivity is not expected. SF_6 was chosen as the Si etch gas because it was readily available on the etch tool at UT-Austin.

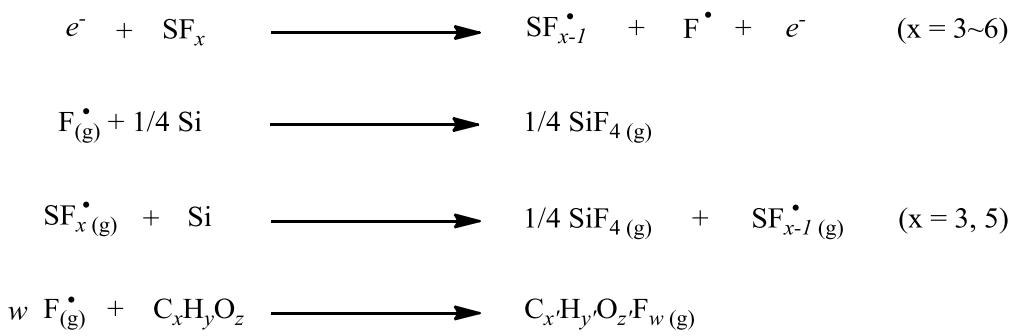

Scheme 5.3: Possible SF_6 plasma etch reactions.

5.7 EVALUATION CONSIDERATIONS

Important considerations for evaluating each etch process include etch rate, selectivity, and anisotropy. A low etch rate is preferred (on the order of 0.1 nm/sec or less) for all of targeted BCP processes. The thin nature of the films (<50 nm) and inconsistencies in the plasma at low run times due to startup transients necessitates slow and controlled etching. In contrast, etch tools are generally designed to etch fast. The semiconductor industry strives to minimize processing time and maximize throughput. A large selectivity (the relative etch rates of different materials) is required for the BCP development process but is unimportant for the wetting layer etch. Anisotropy is necessary for the BCP development and pattern transfer steps to maintain feature size and sidewall profiles, but is not necessary for the wetting layer etch. Etch rates and selectivities were the primary focus of the present optimization studies; anisotropy was not quantitatively evaluated herein.

5.8 ETCHING TOOL

An Oxford Plasmalab 80+ (**Figure 5.3**) located at the Texas Materials Institute was used for all of the etch studies reported herein. It runs in inductively coupled plasma (ICP) mode, which decouples the ion density and the ion flux (*147*). The result is the ability to form a higher ion and radical density plasma at a lower pressure than more classical reactive ion etching tools. The potential difference used to accelerate the ions towards the wafer can be controlled independently of the number of ions and radicals present in the plasma. It is possible that a better process can be obtained with this additional level of control, but the downside is that the number of variables to optimize increases. The tool software provides the ability to change six types of variables: the chamber pressure, RF power (related to the accelerating potential), ICP power (for lighting the plasma), gas flow rate(s), time, and temperature of the wafer chuck. Each of these variables can have significant impact on the etch process and must be studied and controlled carefully. Unfortunately, etch processes are known to depend not only linearly on individual variables but on higher order correlations between variables (*139*). Second and third order correlations obfuscate experimentalists' intuition for tuning a process and significantly hamper the rapid development of optimized experimental conditions.

Figure 5.3: Oxford Plasmalab 80+ inductively coupled reactive ion etcher at UT-Austin used for the etch studies reported herein.

5.9 EXPERIMENTAL DESIGN

The goal of the optimization process was to understand how the different etch input variables controlled through the software correlate to some metric that can be measured experimentally. Etch rates and selectivities can be calculated with etched homopolymer films by measuring the difference between the as-cast and etched film thicknesses. Homopolymer films give a rough estimate of BCP etching conditions, although some deviations are expected (*137*). Polystyrene (PS) was chosen as a model hydrocarbon polymer since it is commercially available at low cost and many of the

BCPs reported in Chapter 3 contain a polystyrene block. A model silicon-containing homopolymer poly(methyltrimethylsilylmethacrylate) (PMTMSMA) was chosen because at the time, PS-*b*-PMTMSMA was of the most interest to us. The etch rate of PMTMSMA and other silicon-containing polymers is expected to vary slightly, but PMTMSMA should provide a valuable metric to evaluate the efficacy of a given set of etch conditions. Initial work correlated the input variables with etch rates and selectivities for PS and PMTMSMA with O_2 RIE.

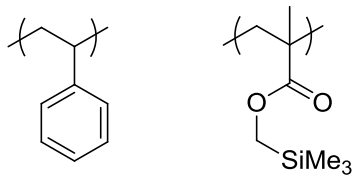

Figure 5.4: Model homopolymers used for the etch process optimization experiments. Left: PS hydrocarbon model; right: PMTMSMA silicon-containing model.

The large number of possible input variables necessitated the careful design of experiments to both minimize the number of experiments performed and maximize the amount of data collected from the set of experiments. The software package JMP IN® was used to guide the design of a set of experiments and can be used to produce statistically meaningful correlations between input variables (*139*). A full factorial design was chosen to probe the realistic maximum, minimum, and midpoint of each input variable. The basic concept can be illustrated for a three input variable system with a cube (**Figure 5.5**). The vertices of the cube represent the smallest and largest possible value for each input variable. The entire processing space (every possible combination of the three variables) is represented by the volume. Experiments performed only at vertices (and possibly midpoints of the cube for additional confidence) (**Figure 5.5**, black and gray dots) enable correlations between variables to be deduced and general trends to be elucidated. The present study seeks to determine how the etch rate and selectivity of the process change as a function of each input variable.

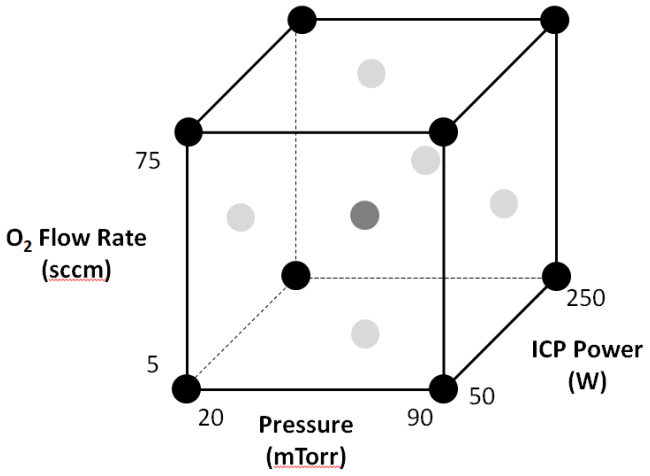

Figure 5.5: Process space for a hypothetical three input variable system.

5.10 O_2 Etch Optimization

It is crucial to pick endpoints for each input variable that provide a large workable process space. Additionally, each point to be experimentally tested must result in a valid set of data. For instance, if the plasma could not light or sustain at a given pressure, the entire collection of data is statistically compromised and invalidated. Initial experiments found that etching with only O_2 gas resulted in very fast etch rates that were unworkable. A diluent gas (Argon) was introduced to the feed to attempt to decrease the etch rate. To reduce the number of required combinatorial experiments, temperature was held constant at a 15°C set point (16-18°C actual). Cryo-etching (T ~ -100°C) has found some success in BCP patterning (*148*), but the Oxford tool used herein was unable to sustain -100°C. There were thus 5 input variables to study: O_2 flow rate, Ar flow rate, chamber pressure, RF power, and ICP power. Flow rate minima were determined to be 5 sccm; smaller numbers caused some formulas to not ignite the plasma. Maxima of 75 sccm were chosen near the limit of the tool. The chamber pressure minimum was determined to be 20 mTorr; smaller values often failed to ignite the plasma. The maximum chamber pressure of 90 sccm was near the limit of the tool. RF and ICP power minima and maxima were again selected to ensure that the plasma ignited for all formulas tested.

Values larger than the maxima frequently caused voltage out of range errors. Time was held constant at 45 sec for direct comparison of the etch formulas. Values longer than 30 sec seemed to result in stable plasmas and etch rates.

Table 5.1 lists the measured PS etch rates and PS:PMTMSMA selectivity results for each etch formula that represents a combination of maxima, minima, and midpoints within the selected process space. Multiple conclusions can be drawn from this data. A very high selectivity (~16) was achieved with formula #29. This is not surprising since PMTMSMA contains 16 wt% silicon; high selectivities should be possible. The high selectivity can be qualitatively justified because formula #29 has a high flow rate of O_2 and little Ar diluent. This combination results in a large chemical etching contribution and minimized anisotropic physical bombardment. Since chemical O_2 etching provides the selectivity in an O_2 RIE, a high selectivity results. Unfortunately, formula #29 also has a very high etch rate (PS etch rate ~ 4 nm/sec) which proved to be difficult to control with BCP samples.

The opposite result is observed with formula #13; a relatively slow and controlled etch (PS etch rate~0.46 nm/sec) occurs with only a modest etch selectivity between PS and PMTMSMA (~4). Initially it was surprising that another formula with high O_2 flow rate would result in a low selectivity. The underlying reason may relate to the increased Argon flow rate (75 sccm) and/or could be the result of higher-order input variable correlations.

Table 5.1: O_2 reactive ion etching optimization using PS and PMTMSMA.

Formula	Pressure	RF Power	ICP Power	O_2 Flow	Ar Flow	Time	PS Etch rate (nm/sec)	Selectivity
1	20	10	50	5	75	45	0.41	1.37
2	90	80	250	5	75	45	3.68	8.78
3	20	10	50	75	5	45	0.48	1.87
4	20	80	250	75	5	45	6.12	12.20
5	20	10	250	5	5	45	2.21	6.27
6	90	10	250	5	5	45	0.67	2.10
7	55	45	150	40	40	45	2.83	8.88
8	20	80	250	75	75	45	4.91	10.14
9	90	10	50	5	5	45	0.20	0.66
10	20	80	50	75	5	45	3.15	8.83
11	90	80	250	75	75	45	5.00	12.89
12	20	80	50	75	75	45	2.90	8.24
13*	20	10	50	75	75	45	0.46	3.83
14	90	10	50	75	5	45	0.13	0.87
15	90	10	50	75	75	45	0.18	1.16
16	55	45	150	40	40	45	2.61	9.87
17	20	80	50	5	75	45	2.11	6.22
18	20	80	50	5	5	45	3.23	8.46
19	90	80	50	5	75	45	3.16	11.10
20	90	80	250	5	5	45	0.61	3.60
21	20	10	50	5	5	45	0.33	1.79
22	20	80	250	5	75	45	2.90	8.14
23	55	45	150	40	40	45	2.24	10.28
24	90	80	50	5	5	45	2.86	12.39
25	90	10	250	75	5	45	0.51	2.43
26	90	80	50	75	75	45	2.67	12.01
27	90	10	50	5	75	45	0.41	2.21
28	20	10	250	75	5	45	1.92	9.16
29*	90	80	250	75	5	45	3.87	16.07
30	20	80	250	5	5	45	5.37	13.99
31	20	10	250	5	75	45	0.62	2.33
32	90	10	250	5	75	45	0.45	1.97
33	90	10	250	75	75	45	0.45	2.00
34	20	10	250	75	75	45	1.33	5.65
35	90	80	50	75	5	45	2.49	9.25

[a]Selectivity is defined as the etch rate of polystyrene divided by the etch rate of PMTMSMA.

*Indicates a formula used for subsequent block copolymer studies.

JMP IN® statistical analysis confirmed the observed trend between etch rate and selectivity (**Figure 5.6**). For pressure, RF power, ICP power, O_2 flow, and Ar flow, as each variable is changed, selectivity and PS etch rate are intrinsically coupled and change together. When the etch rate decreases, so does the selectivity. The process is most sensitive to RF power (the response surface has the highest slope). Unfortunately, the general trends preclude the development of a most optimal formula within the process space. Both formulas 13 and 29 were used on BCP samples with some success. Generally formula 13 (slower and less selective) was found to be more reproducible for the thin BCP films utilized in this dissertation.

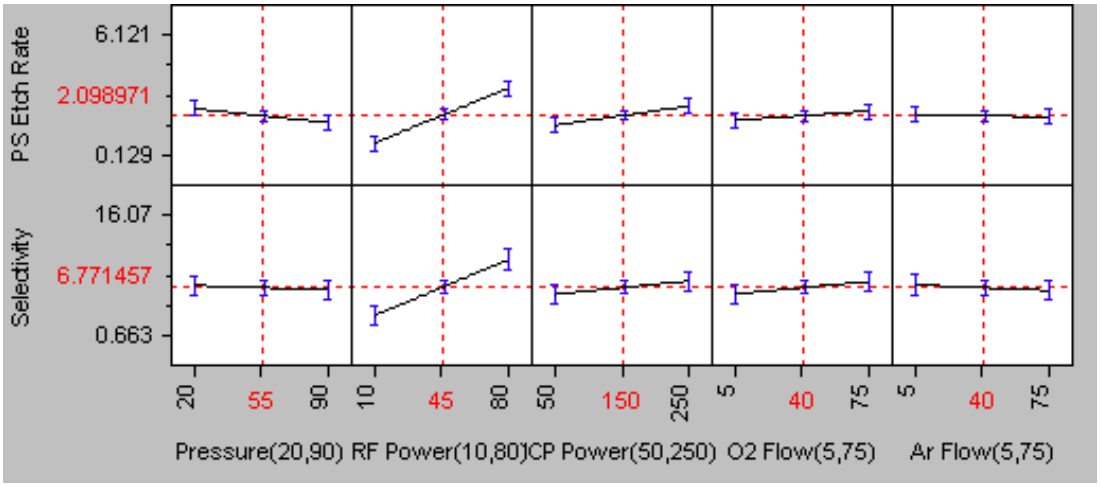

Figure 5.6: The relationship between the different etch input variables, PS etch rate, and etch selectivity (PS:PMTMSMA etch rate).

5.11 SF_6 Etch Optimization

The development of a fluorinated etch formula followed the same approach as the development of an O_2 formula, with one simplification. Fluorinated etches are poorly

selective, i.e. in principal, they will not etch PS and PMTMSMA at different rates. The ideal formula will etch PMTMSMA at the slowest rate to provide the most controllable process. The same full factorial design that used for the O_2 etch optimization was used with the same process space (endpoints and midpoints) for each input variable. The only change was the replacement of O_2 gas with SF_6. The change of gas was found to have no effect on the stability of the plasma – it ignited for all input variable formulations.

Table 5.2 details the results of the SF_6 optimization. Formula 6 (PMTMSMA etch rate=0.11 nm/sec), formula #1 (PMTMSMA etch rate=0.13 nm/sec), formula #17 (PMTMSMA etch rate=0.16 nm/sec), and formula #18 (PMTMSMA etch rate=0.16 nm/sec) were found to have the slowest etch rates. The differences in the etch rates is relatively small but some formulas caused unanticipated effects on PS homopolymer films. Formula #1 apparently deposited material onto PS homopolymer (the film thickness increased) and was discarded. Formulas #6 and #18 both etched PS homopolymers significantly faster than formula #17. The source of this etch rate discrepancy could be attributed to some deposition processes. The exact chemistry of the plasma and its interaction with PS and PMTMSMA homopolymers is unknown. Realistically, formulas #6, #17, and #18 could all be effective for wetting layer removal. Formula #17 was selected for further etching studies because it exhibits the slowest PS etch rate and relatively slow PMTMSMA etch rate. It is possible that formulas within the process space (but not at the endpoints or midpoint) would have an even slower PMTMSMA etch rate, but 0.16 nm/sec was deemed slow enough to continue with wetting layer etch studies.

Table 5.2: SF_6 reactive ion etching optimization using PMTMSMA.

Formula	Pressure	RF Power	ICP Power	SF_6 Flow	Ar Flow	Time	PMTMSMA Etch rate (nm/sec)
1	90	10	250	75	75	45	0.13
2	20	10	250	75	75	45	8.29
3	90	80	50	75	5	45	1.59
4	20	10	50	5	75	45	1.29
5	90	80	250	5	75	45	9.17
6	20	10	50	75	5	45	0.11
7	20	80	250	75	5	45	15.97
8	20	10	250	5	5	45	5.50
9	90	10	250	5	5	45	0.61
10	55	45	150	40	40	45	1.31
11	20	80	250	75	75	45	16.23
12	90	10	50	5	5	45	0.52
13	20	80	50	75	5	45	3.59
14	90	80	250	75	75	45	1.80
15	20	80	50	75	75	45	2.57
16	20	10	50	75	75	45	0.59
17*	90	10	50	75	5	45	0.16
18	90	10	50	75	75	45	0.16
19	55	45	150	40	40	45	1.21
20	20	80	50	5	75	45	4.42
21	20	80	50	5	5	45	3.53
22	90	80	50	5	75	45	3.83
23	90	80	250	5	5	45	4.08
24	20	10	50	5	5	45	0.70
25	20	80	250	5	75	45	10.78
26	55	45	150	40	40	45	1.24
27	90	80	50	5	5	45	3.75
28	90	10	250	75	5	45	0.68
29	90	80	50	75	75	45	2.16
30	90	10	50	5	75	45	0.41
31	20	10	250	75	5	45	7.24
32	90	80	250	75	5	45	1.90
33	20	80	250	5	5	45	13.78
34	20	10	250	5	75	45	4.37
35	90	10	250	5	75	45	2.10

*Indicates a formula used for subsequent block copolymer studies.

5.12 Evaluation of O_2 and SF_6 etch formulas using BCPs

Initial wetting layer etch studies presented a conundrum. If solvent annealing produces a morphology that is masked by a silicon-containing wetting layer, the morphology cannot be observed without an SF_6 etch. But if solvent annealing does not produce a self-assembled pattern, there will also be no observable features. Thus, if the SF_6 etch yields no pattern, is it because the SF_6 etch is ineffective, or is the SF_6 etch acceptable but the solvent annealing produced no pattern? A third possibility is that the SF_6 etch is indeed effective, but the morphology cannot be observed without additional O_2 RIE development. The only way to solve this set of inter-related predicaments is to solvent anneal a BCP, try various combinations of SF_6 and O_2 etches at various etch depths, and repeat if necessary. Both SF_6 formula #17 and O_2 formula #13 (or #29) must be used in combination to identify an appropriate process. The process identified with a single Si-BCP will ideally be applicable to all of the Si-BCPs under study with minimal perturbations to processing conditions.

Cylinder-forming PS-*b*-PMTMSMA (**Figure 5.7**) was chosen as the first Si-BCP to study because the PMTMSMA block was used as the model homopolymer for the O_2 and SF_6 etch recipe development. Additionally, it was the highest χ material synthesized at UT-Austin at the time. Relatively smooth 54 nm BCP films were cast on bare silicon with native oxide. The BCP film was subsequently annealed in DMF for 5.5 h. Solvent annealing was performed in a tightly capped 125 mL jar (Fisher, catalog no. 02-911-455) at room temperature and atmospheric pressure. Within the jar was an uncapped 20 mL vial (Fisher, catalog no. 03-337-15) with ca. 5 g DMF. The precise amount of DMF in the interior container did not seem impact the solvent annealing results, but the lid to the container was found to be crucial. Solvent annealing with a white Fisher cap that contained a polymeric inner lining always failed, likely either because the cap did not form a great seal or more likely because the inside lining absorbs solvent, a process that somehow interferes with BCP annealing. The annealing process also failed if the lid was

not sealed tightly. Solvent annealing with a black Fisher lid containing an aluminum lining resulted in a noticeable change in the film color from off black to cloudy and blue. The blue color is not necessarily indicative of successful solvent annealing and probably results from surface roughness induced by the solvent annealing process. DMF is not the ideal solvent for the annealing process. However, with PS-*b*-PMTMSMA successful solvent annealing occurred concomitant with the change in color, which did not occur in films annealed with white lids or loose caps. Solvent annealed films were subsequently divided and exposed to RIE conditions.

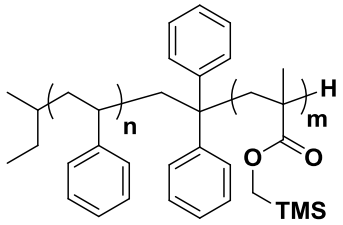

Figure 5.7: Cylinder-forming PS-*b*-PMTMSMA used for initial wetting layer etch studies.

A control sample of PS-*b*-PMTMSMA annealed in DMF for 5.5 h and only exposed to O_2 RIE formula #13 is shown in **Figure 5.8**. Surface roughness is observed, but no self-assembled features are present, which suggests the presence of a silicon-containing wetting layer. PS-*b*-PMTMSA samples were subsequently used in combination with SF_6 and O_2 RIE formulas to elucidate effective etch processes.

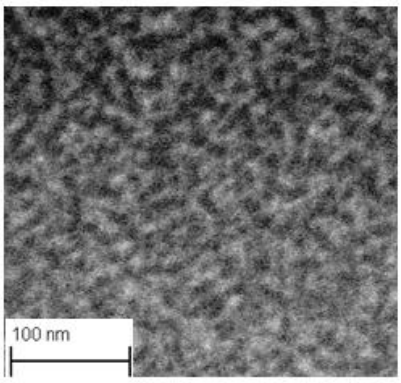

Figure 5.8: PS-*b*-PMTMSMA annealed in DMF for 5.5 h and exposed only to O_2 RIE for 30 sec.

An etch matrix was performed on DMF-annealed samples of PS-*b*-PMTMSMA. SF_6 etching was always performed before O_2 etching because of the anticipated silicon-containing wetting layer. Three different SF_6 etch depths (10, 18, and 25 nm) were targeted using SF_6 formula #17 and the PMTMSMA homopolymer film etch rate. Pieces of these films were set aside and not exposed to an O_2 etch (O_2 etch depth=0 nm). Separate pieces of each of these films were subsequently exposed to O_2 formula #13 (targeted etch depth=15 nm) or formula #29 (targeted etch depth=30 nm). Etch depths of 15 and 30 nm were calculated by the PS homopolymer etch rate. Formula #29 (selectivity=16) was etched deeper than formula #13 (selectivity=4) because it was anticipated that the higher selectivity would prevent significant damage to the PMTMSMA block and enable a deeper etch. Additionally, the etch rate is so fast that a slightly longer etch could help to produce a more uniform plasma. The etched sample was imaged by SEM to determine if BCP self-assembly could be observed (**Figure 5.9**). Each SEM image corresponds with an entirely different sample exposed to SF_6 and then for some samples O_2. Samples were never re-exposed to additional etching, i.e. 15 nm O_2 etch depth is an entirely different sample than 30 nm O_2 etch depth.

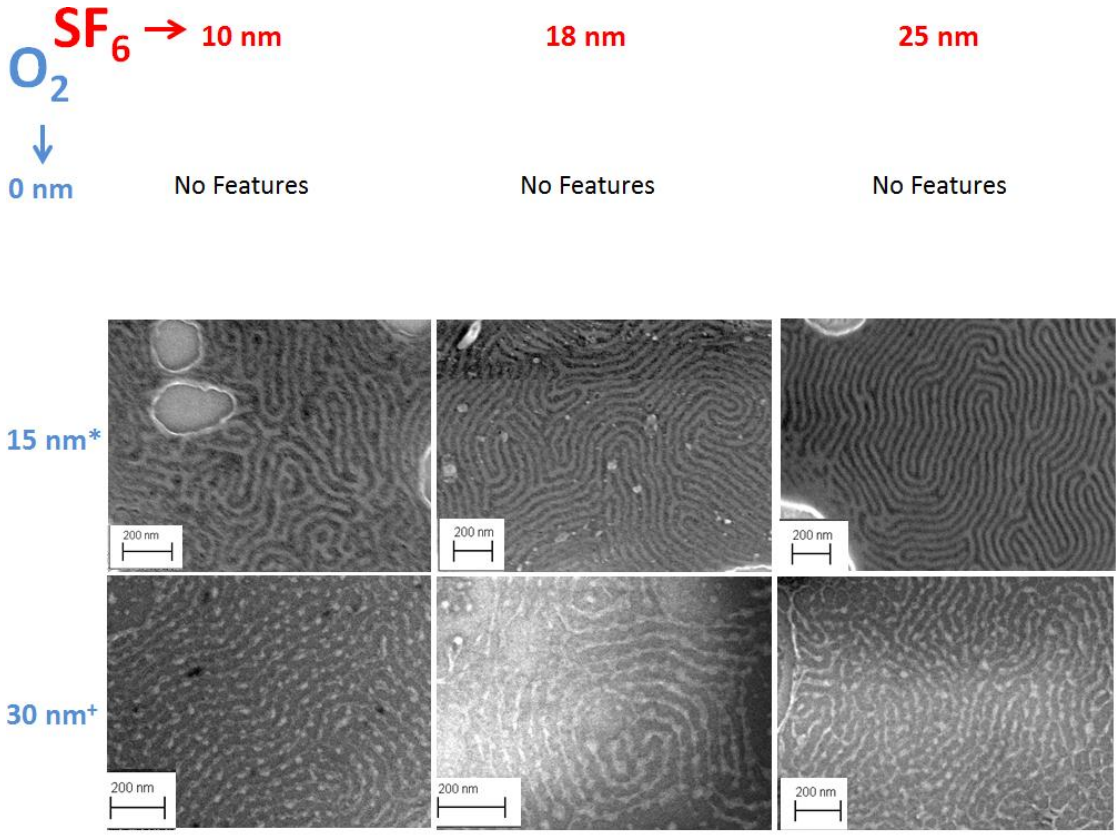

Figure 5.9: Etch study of cylinder-forming PS-*b*-PMTMSMA, solvent annealed with DMF for 5.5 h, using various combinations of SF_6 and O_2 reactive ion etching.
*Etched using O_2 Formula #13, PS etch rate=0.46 nm/sec, selectivity=3.83.
+Etched using O_2 Formula #29, PS etch rate=3.87 nm/sec, selectivity=16.1.
SF_6 Formula #17, PMTMSMA etch rate=0.16 nm/sec.

The trends in **Figure 5.9** are quite encouraging. Samples exposed to SF_6 and not to O_2 lack BCP features at 10, 18, and 25 nm SF_6 etch depths. These results alone do not directly establish the efficacy of the SF_6 etch formula. Further development of the block copolymer using both the low and high selectivity O_2 formulas shows evidence of BCP features that are likely parallel cylinders. The SF_6 etch formula is clearly effective. The actual BCP etch depth produced by the SF_6 and O_2 formulas is unclear. Both 18 and 25 nm SF_6 etch depths appear to produce cleaner BCP lines than the 10 nm etch depth. It is

possible that the silicon-containing wetting layer is completely removed between 10 and 18 nm etch depths. The calculated homopolymer etch depths could also differ from the BCP etch characteristics, which has been experimentally observed in the literature (*137*). Clean BCP features were obtained with O_2 formula #13 (slow with low selectivity) at a 15 nm etch depth. In contrast, the lines produced with formula #29 (fast and less selective) appear significantly over-etched at all three SF_6 etch depths. Possible problems with formula #29 include the fast etch rate and poor anisotropy, which was not optimized. Effective etch formula combinations were nevertheless identified using SF_6 formula #17 in combination with O_2 formula #13.

An identical etch matrix was also performed on anisole-annealed samples of PS-*b*-PTMSS-*b*-PS (**Figure 5.10, Figure 5.11**). Again, SF_6 etching was always performed before O_2 etching. Three different SF_6 etch depths (10, 18, and 25 nm) were targeted using SF_6 formula #17 and the PMTMSMA homopolymer film etch rate. Pieces of these films were set aside and not exposed to an O_2 etch (O_2 etch depth=0 nm). Separate pieces of each of these films were subsequently exposed to O_2 formula #13 with targeted etch depths of 15 and 30 nm; formula #29 was not used due to the aforementioned problems.

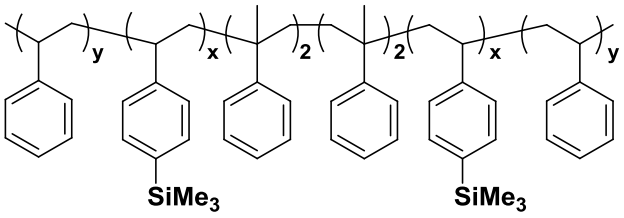

Figure 5.10: PS-*b*-PTMSS-*b*-PS used for wetting layer etch studies.

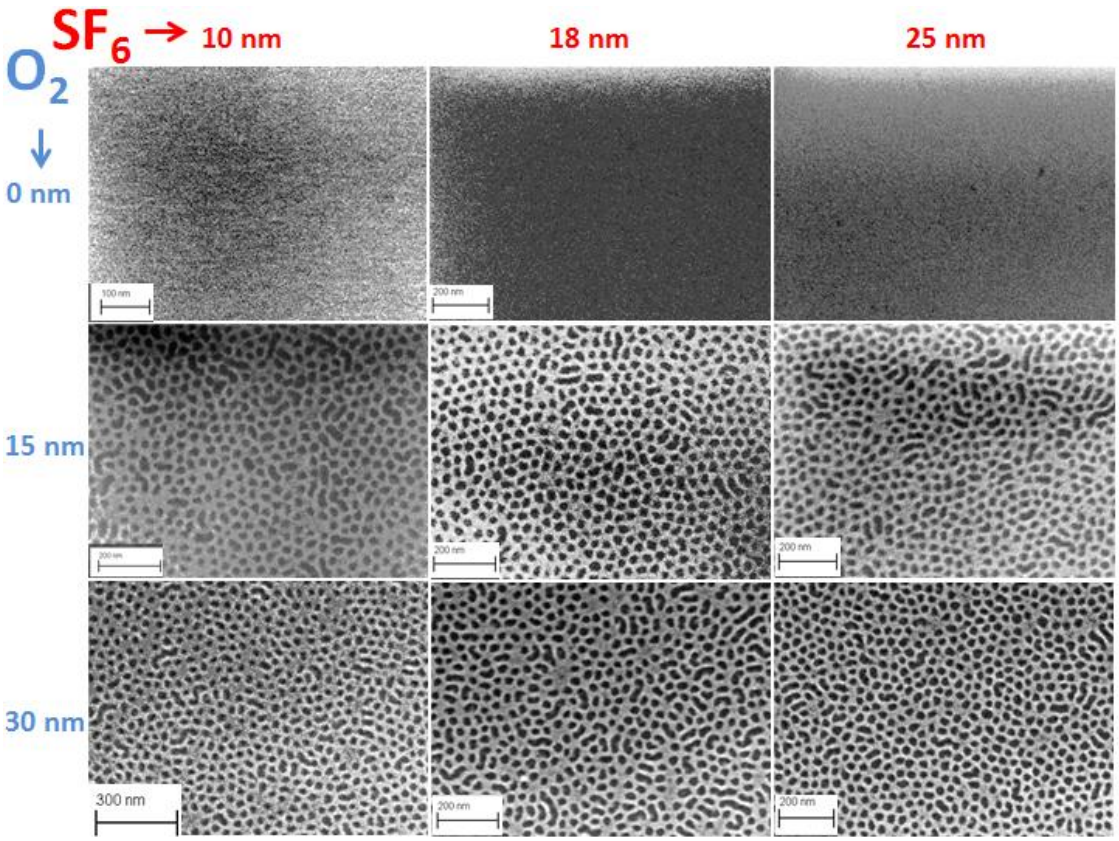

Figure 5.11: Etch study of cylinder-forming PS-*b*-PTMSS-*b*-PS, solvent annealed with anisole for 1 h, using various combinations of SF_6 and O_2 reactive ion etching. Axis labels correspond with targeted etch depths based on model polymer etch studies. For all samples, SF_6 etching was performed first, followed in some cases by O_2 etching. The following formulas were used. O_2 etch (formula #13): Pressure=20 mTorr, RF=10 W, ICP=50 W, O_2 flow=75 sccm, Ar=75 sccm, PS etch rate=0.46 nm/sec, selectivity=3.83; SF_6 etch (formula #17): Pressure=90 mTorr, RF=10 W, ICP=50 W, SF_6 flow=75 sccm, Ar=5 sccm, PMTMSMA etch rate=0.16 nm/sec.

The trends in **Figure 5.11** for PS-*b*-PTMSS-*b*-PS are in good agreement with those observed in **Figure 5.9** for PS-*b*-PMTMSMA. Samples etched only with SF_6 show featureless films at all SF_6 etch depths. Exposure to O_2 for both 15 and 30 nm etch

depths shows clear evidence of BCP self-assembly with an apparent mixed morphology (perpendicular and parallel cylinders intermixed). The silicon-rich wetting layer can be removed with a 10 nm SF_6 etch depth, but the BCP must be at least partially developed with O_2 before the pattern can be observed. All O_2 etch depths effectively show the same pattern, although the 30 nm depth target possibly creates higher aspect ratio features than the 15 nm depth target. The over-etch problems observed with O_2 formula #29 applied to PS-*b*-PMTMSMA is not observed with a targeted etch depth of 30 nm using O_2 formula #13 on PS-*b*-PTMSS-*b*-PS. This experimental finding further supports the hypothesis that the fast etch rate is the source of the apparent over-etch with formula #29.

5.13 CONCLUSIONS:

SF_6 and O_2 etch formulas were developed that enable the removal of Si wetting layers and BCP development. Two optimized O_2 formulas provide either slow etch rates with relatively low selectivity, or fast etch rates with very high selectivity. Unfortunately, within the available process space on the Oxford Plasmalab 80+, it is impossible to achieve a slow and selective O_2 etch. The use of alternative etch tools may ultimately provide the necessary control and selectivity. The combination of SF_6 and O_2 etch formulas nevertheless provides a valuable method of evaluating new BCP materials, annealing methods, and thin film processing conditions. The efficacy of the etch formulas was demonstrated with two Si-BCPs, PS-*b*-PMTMSMA and PS-*b*-PTMSS-*b*-PS and should also be applicable to other Si-BPCs.

5.14 ACKNOWLEDGEMENTS:

Leon M. Dean greatly assisted in the development of the etch processes in this chapter.

Chapter 6: Top Coats for Thermal Annealing

6.1 Background

Solvent annealing can induce perpendicular orientation of both silicon-containing BCPs high-χ BCPs (*26*), but this process has important shortcomings including dewetting, long annealing times, deformation of the structures (*115*), and incompatibility with processes commonly used in nanomanufacturing. Thermal annealing remains a considerable challenge because perpendicular orientation of features requires control of both the substrate (bottom) and top interfaces of the film. Much of the work in this chapter was first reported in C. M. Bates et al., Science 2012, 338, 775 and is reprinted with permission from AAAS (*149*). Additional published information can be found in Seshimo et al. (*150*).

The orientation challenge stems from the fact that, in the absence of solvent or other components, there exist three possible equilibrium arrangements of a lamella-forming AB diblock copolymer thin film (**Figure 6.1**). There are two possible orientations (parallel and perpendicular) with three different interfacial wetting scenarios (horizontal symmetric, horizontal asymmetric, and perpendicular). Horizontal symmetric and horizontal asymmetric are both representative of a parallel orientation; horizontal symmetric has the same block in contact with the substrate and the top interface, while horizontal asymmetric has one block in contact with the substrate and the other block in contact with the top interface. Perpendicular orientations have both blocks in contact with both interfaces. In contrast to the over-simplified picture painted in Chapter 2 (which only discussed substrate interfacial interactions), the orientation and interfacial wetting actually depend on both the bottom and top interfaces. When thermally annealed, the minimum energy state is largely determined by interfacial interactions with both surfaces (*84*). Thus, achieving desirable orientations demands control of the interfacial interactions.

Mathematically, there are as many as four pairs of interfacial energies to be considered: $\gamma_{A\text{-}Top}$, $\gamma_{A\text{-}Bot}$, $\gamma_{B\text{-}Top}$, $\gamma_{B\text{-}Bot}$, where γ is the interfacial interaction energy, the subscripts A and B refer to the two blocks of a two-component block copolymer, and "Bot" and "Top" refer to the bottom and the top surface respectively. Orientations of lamella perpendicular to the substrate occur when the difference between the individual block interfacial energies with each surface are minimized; that is, $\Delta\gamma_{Top} \sim \Delta\gamma_{Bot} \sim 0$, where $\Delta\gamma_{Top} \equiv |\gamma_{B\text{-}Top} - \gamma_{A\text{-}Top}|$ and $\Delta\gamma_{Bot} \equiv |\gamma_{B\text{-}Bot} - \gamma_{A\text{-}Bot}|$. Surfaces that have this characteristic are referred to as "neutral." As these differences deviate from near 0, lamella form in an orientation that creates planes of blocks parallel to the substrate that have a single block in contact with each surface. Horizontal symmetric or asymmetric wetting is then determined by the scenario results in the lowest overall interfacial energy.

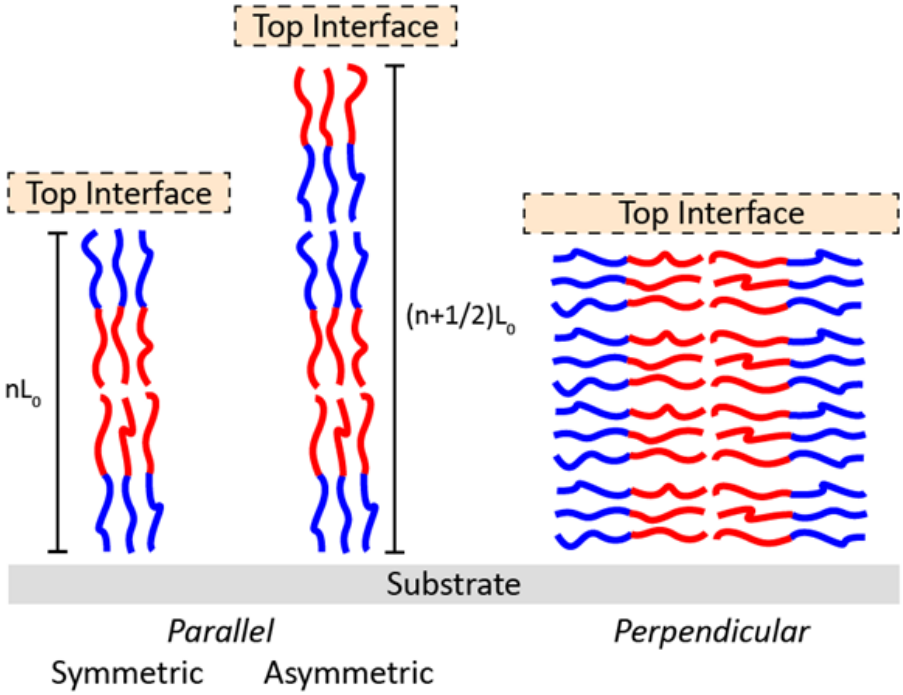

Figure 6.1: Three thin film orientations of a lamella-forming AB diblock copolymer.

The commensurability of the as-cast BCP thickness with the characteristic bulk length scale of the BCP (L_0) also plays a crucial role in determining the energetically-

favorable orientation and interfacial wetting of the BCP features (*151*). Film thickness quantization of parallel-oriented BCPs to thicknesses commensurate with L_0 can result in the formation of either island or hole topography (**Figure 6.2**). BCPs that produce symmetric wetting (such as non-polar BCPs on a non-polar substrate with air as the top interface), the most energetically-favorable thin film state for a parallel orientation is integer multiples of L_0 (denoted by black dashed lines). When the as-cast film thickness (D) is coated as $D \neq n*L_0$ and heated, the BCP film spontaneously undergoes quantization of film thickness to integer multiples of L_0. Such quantization alleviates the energetic penalty associated with overly stretching or compressing chains. In the case of $L_0 < D < 1.5*L_0$, the majority of the BCP film goes down to $1*L_0$ thickness and the "excess" BCP creates islands of materials at $2*L_0$ thickness. Polymer chains with both $1*L_0$ and $2*L_0$ thicknesses are characterized by the same wetting characteristics at each interface. The same block is in contact with both the top and bottom interfaces. When $D < L_0$, the majority of the film adopts $1*L_0$ thickness, with holes at $0*L_0$ scattered throughout the film since there is not enough polymer material to fully cover the substrate at $1*L_0$ thickness. The inverse quantization conditions are true with a BCP that adopts asymmetric wetting. Parallel orientation is favored at $D = (n+1/2)*L_0$. When the as-cast film thickness $D \neq (n+1/2)*L_0$, islands form when $D=1/2*L_0 < D < 1*L_0$ and holes when $1*L_0 < D < 1.5*L_0$. BCP film thickness quantization is suppressed under the conditions of neutral interfaces with a perpendicular BCP orientation. The BCP chains can adopt a length corresponding with L_0 in the plane of the film irrespective of film thickness (**Figure 6.1**). Control of BCP film thickness is thus crucial for thermal annealing processes.

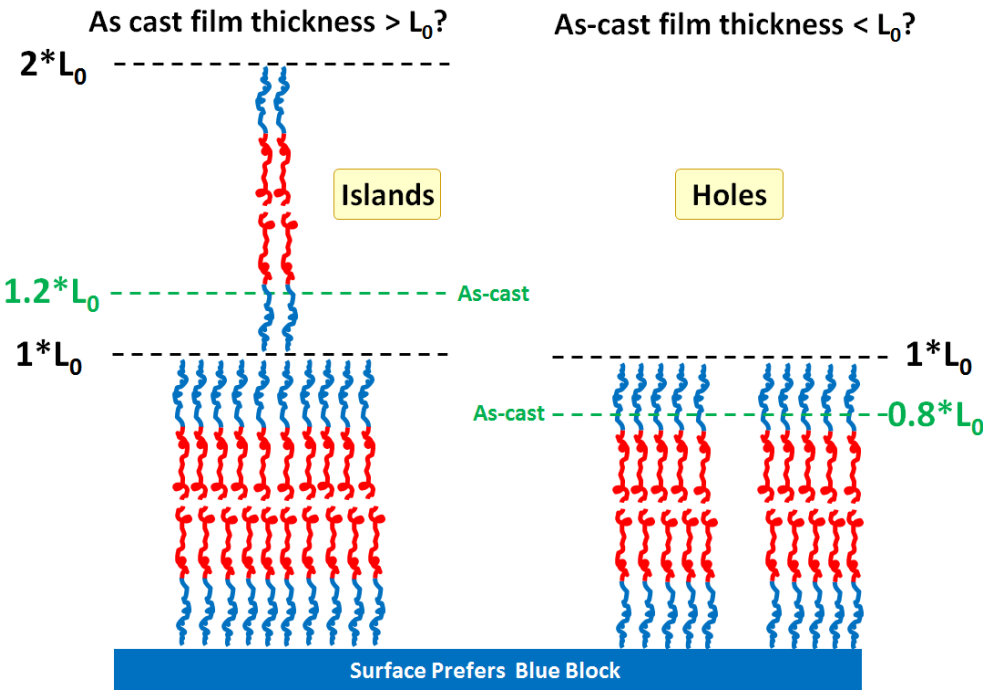

Figure 6.2: Quantization of film thickness to integer multiples of L_0 ($n*L_0$) for a symmetrically-wetting BCP results in island and hole formation concurrent with parallel lamellae.

As discussed in Chapter 2, substrate interfacial interactions can be controlled through a variety of methods, including grafting a polymer or monolayer to functional groups on a surface (*86*), cross-linking a spin-coated polymer film on a surface (*91*), and by directly changing substrate composition (*152*). By tailoring the interfacial energy to be between those of the individual blocks, the bottom surface can be neutralized ($\Delta\gamma_{Bot} \sim 0$). However, in high-$\chi$ and silicon-containing BCPs the strong interaction of the nonpolar block with air, which has a low dielectric constant, drives domain orientation to be parallel to the substrate. Several attempts have been made to circumvent this parallel orientation. Physical confinement of a BCP between two solid surfaces (*140*, *153*) and application of neutral polymeric top coats by floating (*154*) both provide top surface control but suffer from scalability issues and introduction of defects. Blending surfactants with BCPs introduces swelling and has only been demonstrated with PS-*b*-

PMMA (*155*), which does not require such processing to achieve alignment and cannot achieve sub-10 nm feature sizes. Application of polymeric top coats by spin coating from water has been reported (*156*) but materials deposited in this way are very polar and again, the process was demonstrated only with PS-*b*-PMMA. BCPs that decouple bulk and thin film thermodynamics appear promising, but require precise post-polymerization modifications that could be difficult to control on a large scale (*157*).

PS-*b*-PMMA has been the standard material for thermal thin film studies because several neutral bottom layer treatments are known and in air, $\Delta\gamma_{Top}$ becomes zero at ca. 210°C ($\gamma_{PS\text{-}Air} \approx \gamma_{PMMA\text{-}Air}$) (*158*). Thus, PS-*b*-PMMA can be readily oriented perpendicular to a substrate with thermal annealing. Unfortunately, its low χ (~0.039 at 150°C) (*42*) limits the minimum feature size to ca. 13 nm. Higher-χ BCPs that can form smaller features, such as poly(styrene-*block*-2-vinylpyridine) (PS-*b*-P2VP, χ~0.12 at 150°C) (*159*) and poly(styrene-*block*-dimethylsiloxane) (PS-*b*-PDMS, χ~0.12 at 150°C) (*41*) unfortunately have $\Delta\gamma_{Top} >> 0$ with air, which drives the orientation of domains at the top interface parallel to the substrate. Even in the presence of neutral substrate surface treatments (*43, 160*) they cannot be aligned by thermal annealing alone.

An ideal solution to the high-χ BCP orientation challenge would be to confine the BCP between bottom and top interfaces that are rendered neutral. A top coat that can be applied by spin coating has several advantages: (i) it employs the same coating equipment used to apply the BCP film, (ii) it ensures uniform coverage across large substrates, and (iii) is compatible with thermal annealing processes. Unfortunately, neutral polymers that can be spin-coated onto a BCP will necessarily only be soluble in a solvent that dissolves or is sorbed by at least one of the blocks of the BCP. Polymers that can be coated from a solvent that does not interact with the BCP will have interfacial energies that are not intermediate between those of the two blocks. Hydrophobic organic block copolymers require a top coat that can be spin-coated out of a very polar solvent such as water, but water-soluble top coats are far too polar to have an interfacial energy between that of the hydrophobic blocks.

6.2 TOP COATS FOR THERMAL ANNEALING

Our approach to solving the dilemma is to use a top coat that switches polarity after spin coating over a BCP film via a subsequent chemical reaction. The general schematic is shown in **Figure 6.3**. Application of both the substrate surface treatment and the BCP film is the same as previous literature and the work reported in Chapter 4. However, after application of the BCP, a top coat is applied out of water (or aqueous base). In its polar form, the top coat is soluble in aqueous ammonium hydroxide, which permits its application onto a water-insoluble organic BCP thin film by spin coating. Upon thermal annealing, the top coat quickly loses ammonia and undergoes a chemical transformation into a less polar state, which modulates the top-coat interfacial energy and effectively neutralizes the top interface enabling perpendicular orientation of the BCP when it is annealed above the T_g of the blocks. The top coat can then be stripped by washing with aqueous base, and selective etching of one block or pattern transfer into the underlying substrate can be performed.

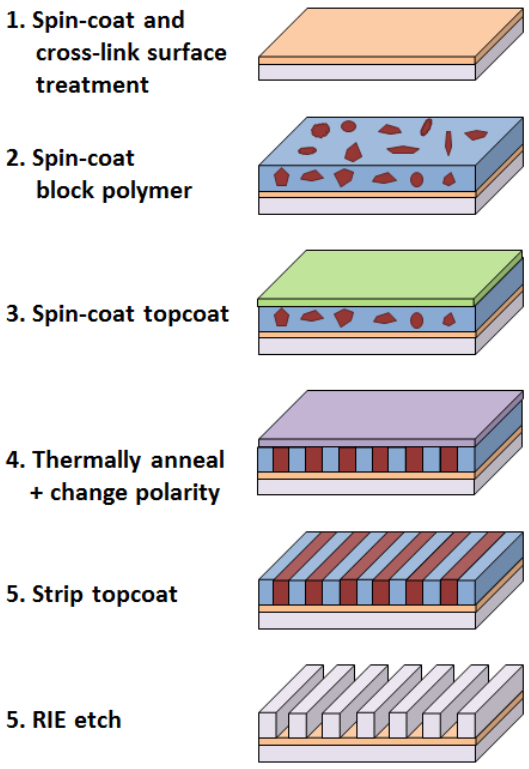

Figure 6.3: Polarity-switching top coat thin film process.

A successful top coat must be soluble in a solvent that does not interact with either block of the BCP, undergo a change in interfacial energy upon baking that renders it nearly neutral, and ideally can be stripped by solvent after BCP alignment. The top coat must also have a T_g above that of all blocks, and preferably a relatively high molecular weight. These latter requirements stem from a need to preclude intermixing of the top coat with any block during annealing. This mixing requires polymer inter-diffusion, and inter-diffusion coefficients are very low below T_g (*161*) and scale strongly and inversely to molar mass (*162*).

The polarity-switching moiety incorporated into the top coat copolymers herein is poly(maleic anhydride) (**Figure 6.4**). This polarity-switching mechanism exploits the ring-opening and closing reaction of the maleic anhydride monomer unit (**Figure 6.5A**), which has been reported previously (*163*). The ring-opened carboxylate salt form is

soluble in aqueous base and can be applied to a BCP film. Subsequent heating re-closes the anhydride ring and produces a less polar state. Norbornene was introduced as a co-monomer because it produces high $T_{g,}$ alternating copolymers with maleic anhydride by free radical polymerization (*164*). Further functionalization of the poly(maleic anhydride-*alt*-norbornene) materials to fine-tune the surface energy of the top coats turned out to be required and can be introduced in two ways (**Figure 6.4**). The norbornene can be direction functionalized through the synthesis of various monomers or a third type of monomer can be introduced into the polymerization. Each method has potential benefits and drawbacks. The synthesis of substituted norbornene monomers is relatively time consuming and many are generated through Diels-Alder reactions which can be low yielding and result in many undesired by-products. The incorporation of a third type of monomer into the maleic anhydride-norbornene polymerization generally results in a significant depression in the top coat T_g. Furthermore, in the case of the terpolymer system, the actual sequence of the polymer backbone is ill-defined. As will be demonstrated, these types of terpolymerizations often result in multi-modal polymer distributions and can be difficult to reproduce synthetically. However, many substituted styrenes and methacrylates are commercially available which makes generating a library of different top coats straightforward. Both functionalization schemes (substituted-norbornenes and terpolymers) were investigated as potential top coat materials for multiple Si-BCPs.

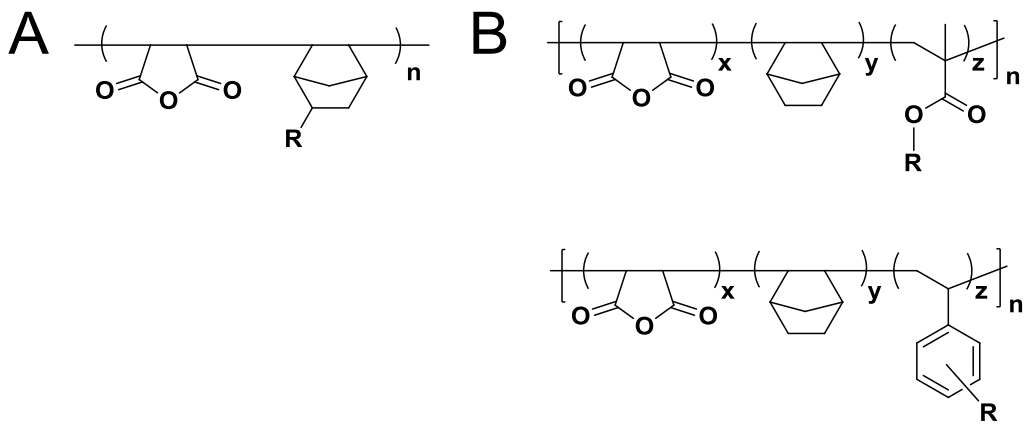

Figure 6.4: General top coat designs involving poly(maleic anhydride-*alt*-norbornene) as polarity switching materials with high T_g. Surface properties in principal can be fine-tuned with functionalization by varying the R groups **A)** attached to norbornene or **B)** through incorporation of a third monomer within the polymer backbone. A combination of both strategies is also possible.

6.3 Infrared Spectroscopy Verification of Polarity Switching Mechanism

A model top coat copolymer was synthesized to verify the ring opening and closing reactions. Conventional free radical polymerization of a mixture of maleic anhydride, norbornene, and 2,2,2-trifluoroethyl methacrylate with AIBN as the initiator at 60°C for 48 h (**Figure 6.6**) afforded a white polymer powder after precipitation and drying. The ring-opening and closing reactions were then verified with the model polymer using infrared spectroscopy (**Figure 6.5B**). A thin film (ca. 250 nm thick) of TC-MA was cast on a NaCl salt plate from 2-butanone, which should be unreactive towards the poly(maleic anhydride) moiety (i.e. it should still be ring-closed). The anhydride carbonyl out-of-plane and in-plane stretching bands (**Figure 6.5B**, blue curve) $\nu_{op}(C{=}O)_2$ = 1775 cm^{-1} (strong) and $\nu_{ip}(C{=}O)_2$ = 1850 cm^{-1} (weak) are in good agreement with reported values (*165*). Upon coating TC-MA on a new salt plate from aqueous NH_4OH (which should be reactive towards the maleic anhydride ring), infrared

spectroscopy showed (**Figure 6.5B**, red curve) complete disappearance of the anhydride carbonyl bands at 1775 and 1850 cm^{-1} and the appearance of symmetric and asymmetric carboxylate COO^- stretching bands at ν_{sym}=1400 cm^{-1} and ν_{asym}=1560 cm^{-1}, and a band attributed to the asymmetric C=O stretch of the free carboxylic acid at ν_{asym}=1660 cm^{-1} (*166*). Subsequent heating of the salt plate with TC-MA coated from aq. NH_4OH at 210°C for 1 minute (**Figure 6.5B**, green curve) caused reappearance of the anhydride carbonyl bands at 1775 and 1850 cm^{-1} and a corresponding decrease in the intensity of the ring-opened carboxylate and carbonyl stretching bands.

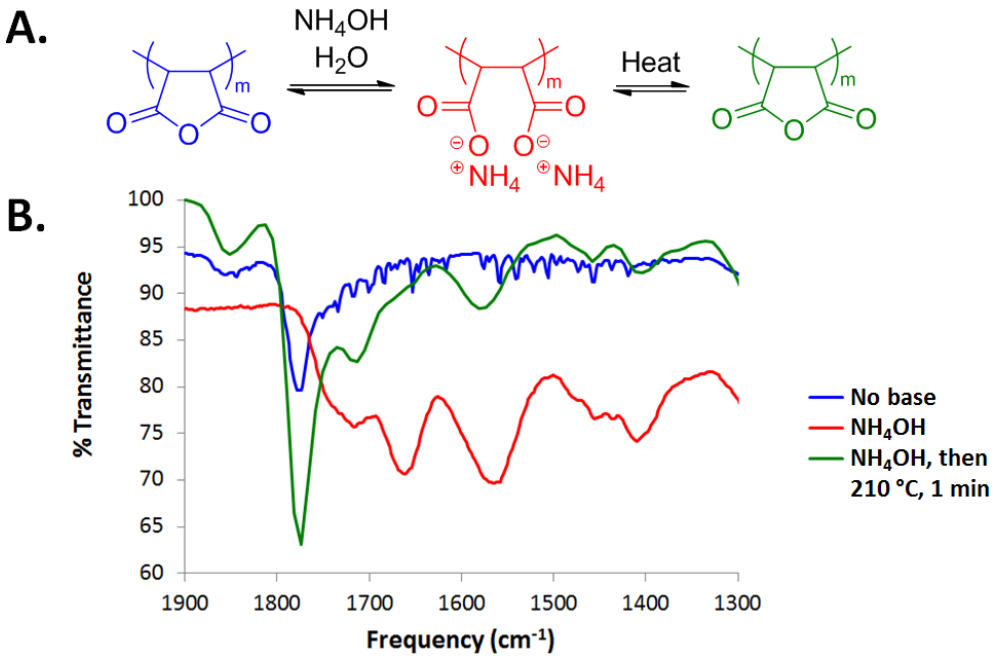

Figure 6.5: A) Ring-opening and closing reactions that modulate the polarity of the top coats. **B)** IR data from a model top coat (TC-MA that demonstrate the ring opening and closing reactions of the poly(maleic anhydride) component. Blue curve: cast from 2-butanone, red curve: cast from 30 weight% aq. NH_4OH, and green curve: aq. NH_4OH-cast sample subsequently annealed at 210°C for 1 min.

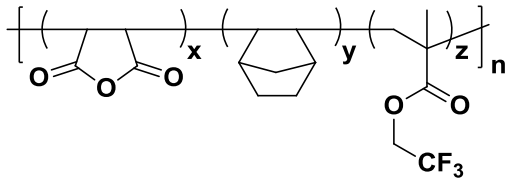

TC-MA

Figure 6.6: Top coat TC-MA was used as a model top coat to demonstrate the ring opening and closing reactions of the poly(maleic anhydride) moiety. Top coat composition (mol%) x:y:z = 50:34:16. T_g=137°C, T_d=262°C.

6.4 TOP COATS FOR POLY(STYRENE-*BLOCK*-TRIMETHYLSILYLSTYRENE-*BLOCK*-STYRENE)

PS-*b*-PTMSS-*b*-PS (**Figure 6.7**) was chosen as the initial BCP for top coat studies for two principal reasons. First, silicon-containing BCPs are notoriously difficult to orient in thin films. Neither perpendicular cylinders nor lamellae have ever been reported at the top interface of thin films of silicon-containing block copolymers when subjected only to thermal annealing (*30, 160*). Second, it is reportedly easier to form perpendicular orientations of ABA triblock copolymer architectures with relative interfacial energies $\gamma_B<\gamma_A$ compared to the AB diblocks with the same A and B chemical structures (*57, 167*). PS-*b*-PTMSS-*b*-PS appeared to be a perfect candidate for initial top coat studies; the PTMSS block contains silicon and has a significantly lower surface energy than PS ($\gamma_B<\gamma_A$). Even though the relatively small value of χ ultimately hinders the engineering utility of the material, PS-*b*-PTMSS-*b*-PS can demonstrate the efficacy of the top coat process. Lamella-forming PS-*b*-PTMSS-*b*-PS was used for the initial top coat studies. A point which was not originally appreciated is that the annealing temperature must be above the T_g of each block to allow for BCP reorganization (**Figure 6.27**, PS-*b*-PTMSS-*b*-PS: $T_{g\text{-}PS}$=106°C, $T_{g\text{-}PTMSS}$=131°C but below that of the top coat prevent inter-diffusion.

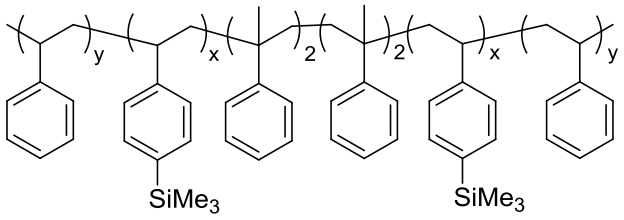

Figure 6.7: Chemical structure of PS-*b*-PTMSS-*b*-PS.

All attempts to align PS-*b*-PTMSS-*b*-PS by thermal annealing were unsuccessful as expected based on the large surface energy differences between the PS and PTMSS blocks (*69*). The lamella oriented exclusively parallel to the substrate in the absence of a top coat, so it served as an excellent demonstration vehicle for the auditioning of top coat materials. A large collection of top coats of the general design shown in **Figure 6.4** were synthesized and tested. One difficulty that was constantly encountered is the large variable space for the top coat process, including: surface treatment, top coat (composition, monomeric units), BCP film thickness, annealing temperature, and annealing time. At the outset of the experimental work, none of these variables were optimized, so some had to be held constant to isolate the effects of the others. The first experiments held the surface treatment constant as poly(4-methoxystyrene-*random*-vinylbenzyl azide) (XST-OMe). The choice of the material was basically random, but there is a good reason to hold the surface treatment constant. After coating one surface treatment over a large area (i.e. a 4" wafer), the BCP can be coated onto the entire area in one step and subsequently cut into pieces. Many different top coats can then be applied onto identical pieces of BCP. These BCP with top coat samples can then be cut up into identical pieces to probe the effects of temperature and annealing time. In contrast, varying the surface treatment increases the number of samples that must be spin coated, since each surface requires a separate application of BCPs and top coats.

Initial Orientation Control:

The first hints at successful top interface functionalization occurred using top coat CF3-Nor (**Figure 6.8**). After the process in **Figure 6.3**, very small patches of the block copolymer film showed line space patterns by SEM (**Figure 6.9**). The measured L_0 value calculated from the SEM and averaged over three lamella is 31 nm, in excellent agreement with the bulk value of 30 nm. The patchy self-assembly is in stark contrast to all control samples annealed in the absence of a top coat, which never showed line-space patterns in any region of the film. Multiple BCP thin film thicknesses were probed, with the best result observed at 44 nm. Since the annealing temperature (170°C) was slightly above the T_g of the top coat (162°C), lower temperatures were probed. Annealing temperatures < 170°C showed no signs of self-assembly. Since surface energy is a function of temperature, we surmised that 170°C is a neutral condition for this top coat, but inter-diffusion of the top coat with the BCP prevented uniform self-assembly. New top coat structures were subsequently pursued. Two important lessons were gleaned from the CF3-Nor work. First, BCP thicknesses around 44 nm produced self-assembled patterns in the presence of a top coat, and second, XST-OMe seemed to at least partially work as a substrate surface treatment. Since the variable space of the process is so large, these two pieces of information provided an important foundation to build upon with new top coat materials.

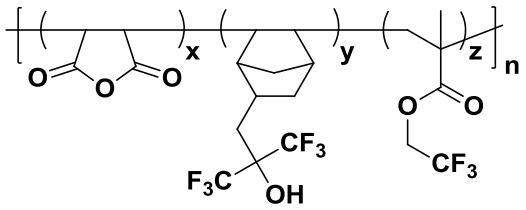

Figure 6.8: Top coat CF3-Nor. Top coat composition from combustion analysis (mol%) x:y:z = 35:27:38. T_g=162°C, T_d=278°C.

Figure 6.9: Initial hints that top coats may be effective at controlling block copolymer orientation. PS-*b*-PTMSS-*b*-PS film thickness was 44 nm (1.46*L_0) with a substrate surface treatment XST-OMe, annealed at 170°C for 19 hr 45 min.

Improvement in areal density of Perpendicular features

A considerable improvement in the areal density of self-assembled BCP was observed using top coat TC-MA (**Figure 6.6**). **Figure 6.10** shows line-space lamella patterns over large regions of the substrate. A large-field view is provided in **Figure 6.11**. Virtually the entire wafer was covered with the perpendicular lamella pattern. Some incomplete line formation defects were still observed in the form of light patches or dots. While TC-MA has a significantly lower T_g (137°C) than CF3-Nor, it was possible to produce the pattern with an annealing temperature of 131°C, which is the theoretically lowest possible temperature since the T_g of the PTMSS block is 131°C. It appears that using annealing temperatures $T<T_{g\text{-Top coat}}$ did improve the overall area in which self-assembly occurred. Unfortunately, the temperature processing window with TC-MA is quite small (131°C < T < 137°C), which has two negative consequences. First, long

annealing times were required to produce the oriented pattern. While 2 day anneals produced some success, 5 day anneals resulted in the best orientation. Annealing times this long partially negate the benefits of using thermal annealing and would seriously inhibit industrial application of the process. Second, since surface energy is a function of temperature, the accessible surface energies for a given top coat/surface treatment pair are limited. This reduces the chance of success with a given top coat. With TC-MA, the observed defects could not be removed with higher temperature. Rather than investigate even longer annealing times, alternative top coat structures were investigated.

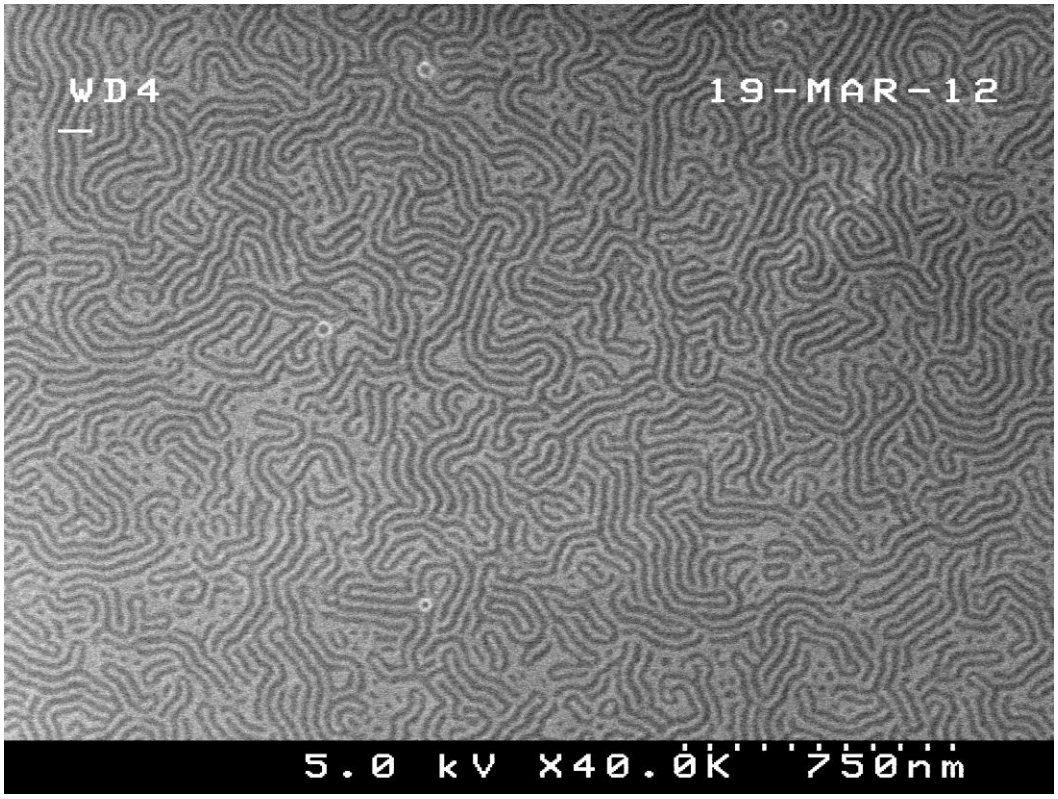

Figure 6.10: Top coat TC-MA enabled virtually whole-wafer perpendicular self-assembly of 43 nm thick PS-*b*-PTMSS-*b*-PS annealed at 131°C for 5 days and etched with O_2 RIE for 30 s. Some defectivity (large spaces and dots) was observed.

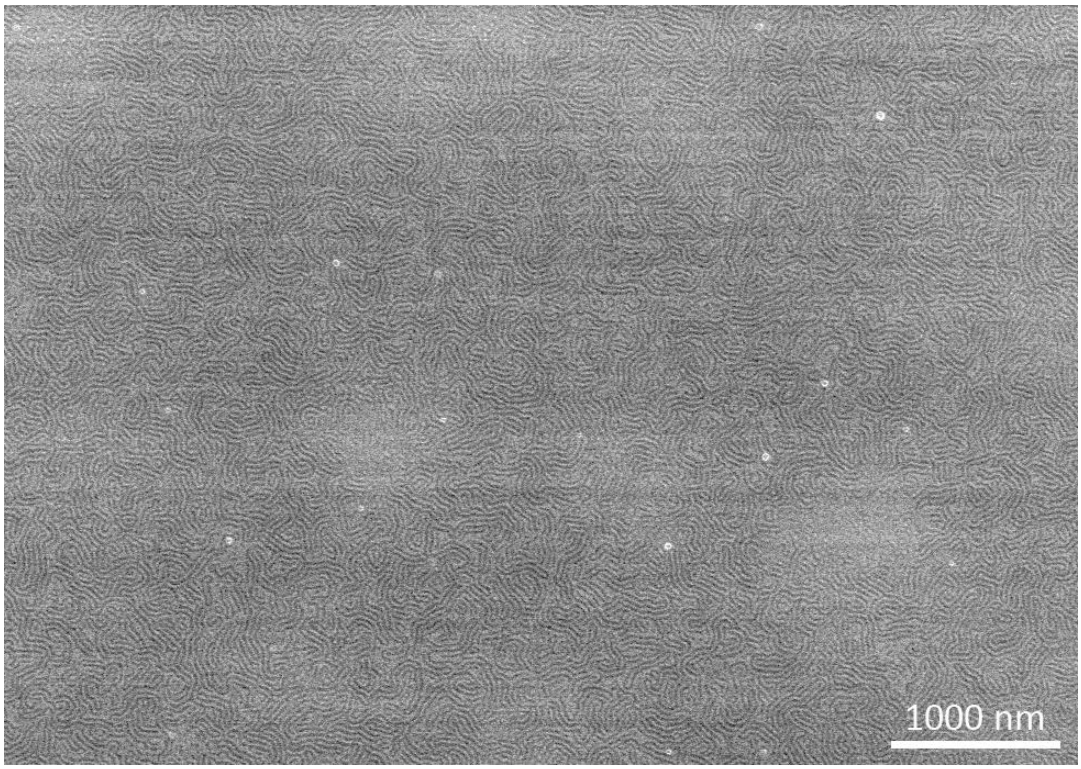

Figure 6.11: Large-field SEM of 42 nm thick PS-*b*-PTMSS-*b*-PS annealed at 131°C for 5 days in the presence of TC-MA. Samples were stripped with 75:25 wt% IPA:aq. 30 wt% NH_4OH and etched with O_2 RIE for 30 s.

Top coat TC-StyOCF3 (**Figure 6.12**) produced very similar results as TC-MA under identical annealing conditions. Slightly improved defectivity was observed (**Figure 6.13**), albeit still with long annealing times. The T_g of the top coat (180°C) is significantly higher than TC-MA and should allow for higher temperature annealing. At the same time as the development of TC-StyOCF3, top coat TC-PS was created. TC-PS was pursued instead of TC-StyOCF3 since it has an even higher T_g than TC-StyOCF3 and involves less synthetic steps to make the monomer.

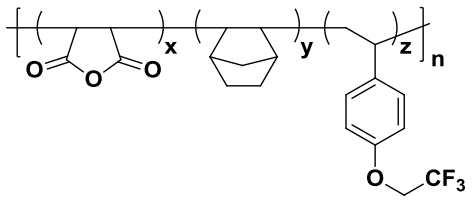

TC-StyOCF3

Figure 6.12: Top coat TC-StyOCF3. Top coat composition (mol%) x:y:z=56:17:27. T_g=180°C, T_d=296°C.

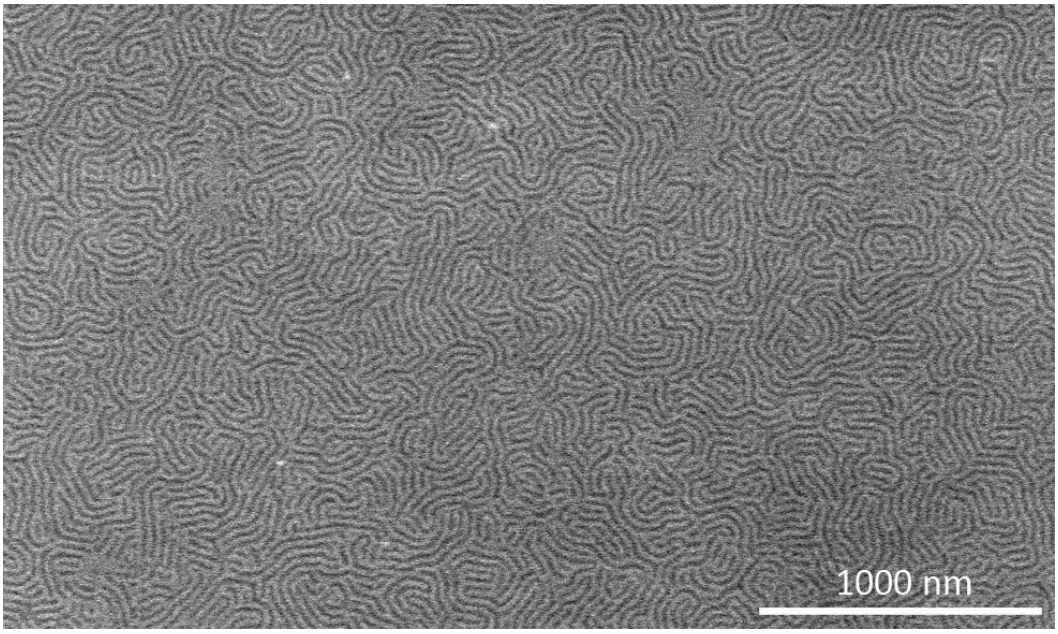

Figure 6.13: Large-field SEM of 42 nm thick PS-*b*-PTMSS-*b*-PS annealed at 131°C for 5 days in the presence of TC-StyOCF3. Samples were stripped with 75:25 wt% IPA:aq. NH_4OH and etched with O_2 RIE for 30 s.

Low Defect density perpendicular orientation

PS-*b*-PTMSS-*b*-PS triblock copolymer samples confined between a substrate surface treated with XST-OMe and the TC-PS top coat (**Figure 6.14**), annealed at 210°C for 1 min on a hot plate in an air environment, showed well-formed perpendicular

lamellae over the entire film (**Figure 6.15**). The figure shows SEM data after stripping the top coat with aqueous ammonium hydroxide and subjecting the oriented film to development by O_2 reactive ion etching. In contrast, samples annealed in the absence of a top coat (**Figure 6.15, inset**), but subjected to identical annealing, stripping, and O_2 reactive ion etch conditions show absolutely no signs of perpendicular self-assembly in any region of the film. They have parallel-oriented lamellae. The top coat very efficiently induces perpendicular orientation of the silicon-containing BCP which otherwise orients parallel to the substrate. Tilted-SEM images of samples etched with O_2 are consistent with perpendicular lamella penetrating the entire thickness of the film (**Figure 6.16**). Furthermore, the O_2-etched pattern was successfully transferred into single crystal silicon (**Figure 6.17**).

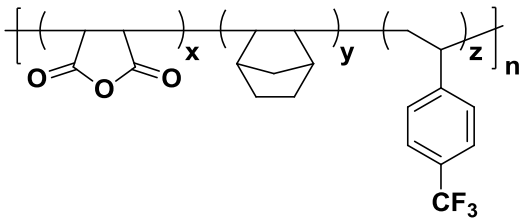

TC-PS

Figure 6.14: Top coat TC-PS. Top coat composition (mol%) x:y:z=57:26:17. T_g=214°C, T_d=230°C.

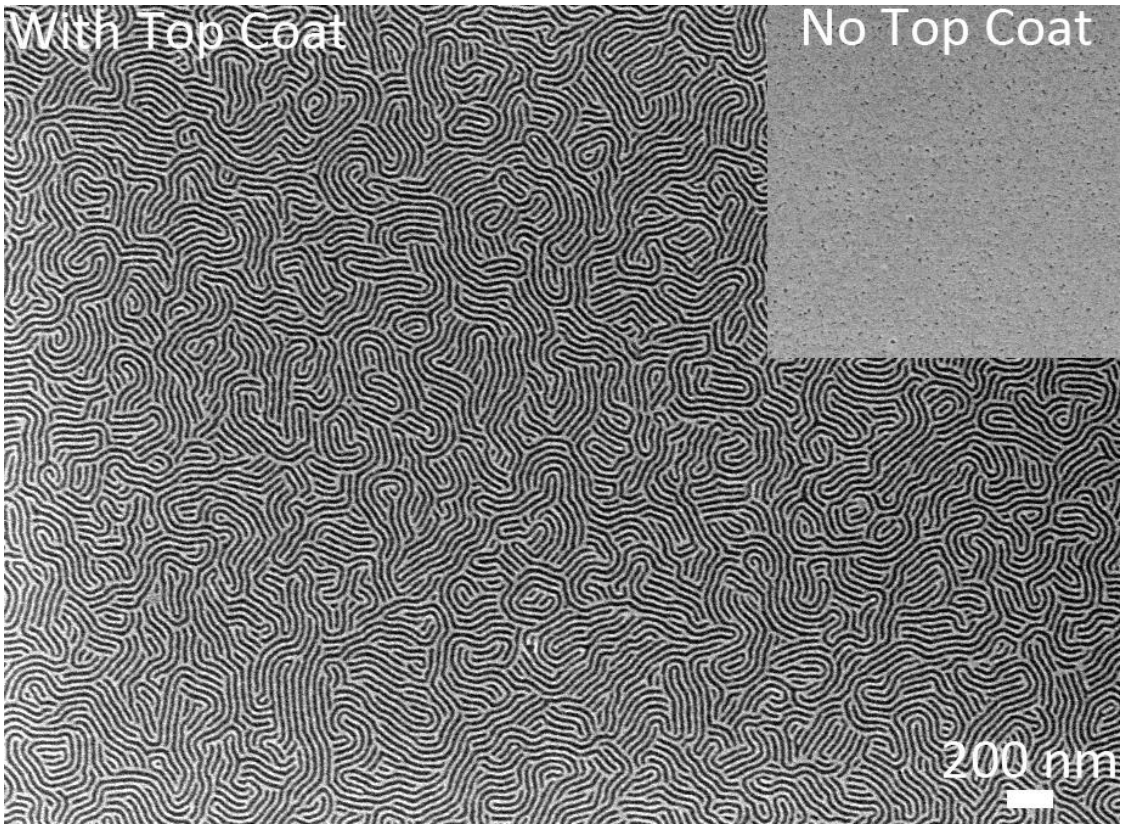

Figure 6.15: Scanning electron micrographs of PS-*b*-PTMSS-*b*-PS (L_0=29 nm as measured, 30 nm bulk) annealed at 210°C for 1 minute on a hot plate open to air with top coat TC-PS (main figure) and without top coat (inset). The BCP film thickness was 43 nm (1.4*L_0). After thermal annealing, both samples were stripped with 3:1 by weight MeOH:aq. 30 wt% NH_4OH and etched with O2 RIE for 30 s. The bottom surface treatment was an XST-OMe cross-linkable copolymer. The scale bar is valid for both the image and the inset.

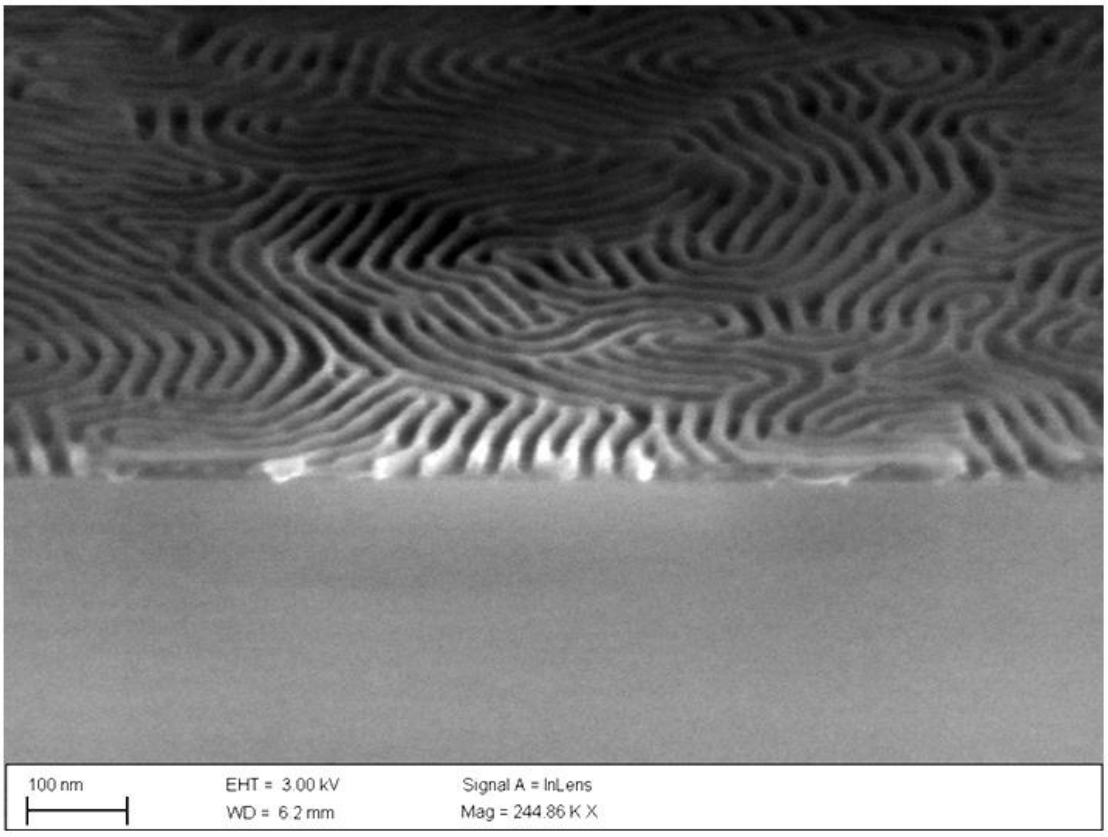

Figure 6.16: Tilted SEM demonstrating through-film perpendicular orientation of PS-*b*-PTMSS-*b*-PS triblock copolymer annealed in the presence of top coat TC-PS. The O_2 RIE time was 80 sec, which corresponds with a targeted PS etch depth of 37 nm.

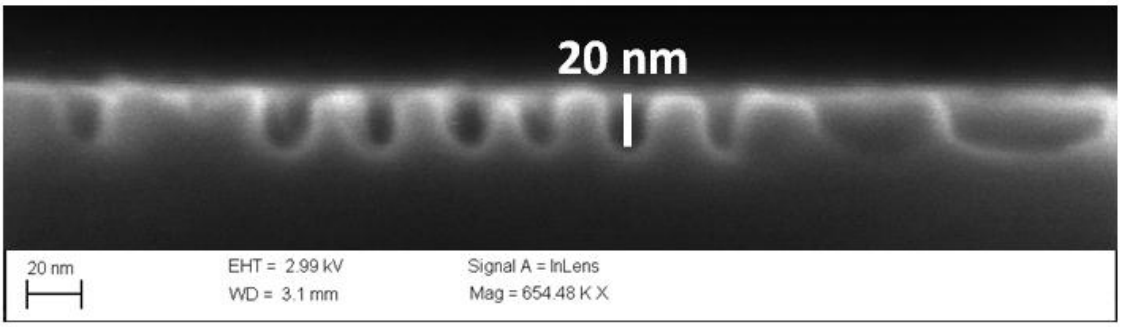

Figure 6.17: Cross-section SEM demonstrating pattern transfer of PS-*b*-PTMSS-*b*-PS triblock copolymer, annealed in the presence of top coat TC-PS, into single crystal silicon. The following sequence of etch times was used, with the aforementioned formulas: 70 sec O_2, 5 sec SF_6/C_4F_8, 45 sec O_2, 75 sec SF_6. A piranha solution was used post-etch to remove residual surface treatment.

Annealing Time and Temperature Studies

One minute thermal annealing for PS-*b*-PTMSS-*b*-PS with the top coat matches the fastest self-assembly processes reported even for PS-*b*-PMMA, which are on the order of one minute at 250°C (*168*). The L_0 value as calculated from **Figure 6.15** (29 nm) is in good agreement with the bulk value calculated from SAXS data (30 nm) (*150*). Additionally, the level of defectivity is quite low; considerably improved from the original data obtained with CF3-Nor. A series of time and temperature data were obtained with identical surface treatment and BCP thicknesses (**Figure 6.18**). The BCP orientation was virtually identical at both lower temperatures (down to 189°C) and longer times (up to 24 h). These data combined with the IR data, imply that the top coat very quickly ring-closes to the equilibrium state that is also a neutral surface for the BCP. Amazingly, annealing times as short as 10 sec produced well-oriented BCP features (**Figure 6.19**), although admittedly with slightly more defects than the samples annealed for 1 minute.

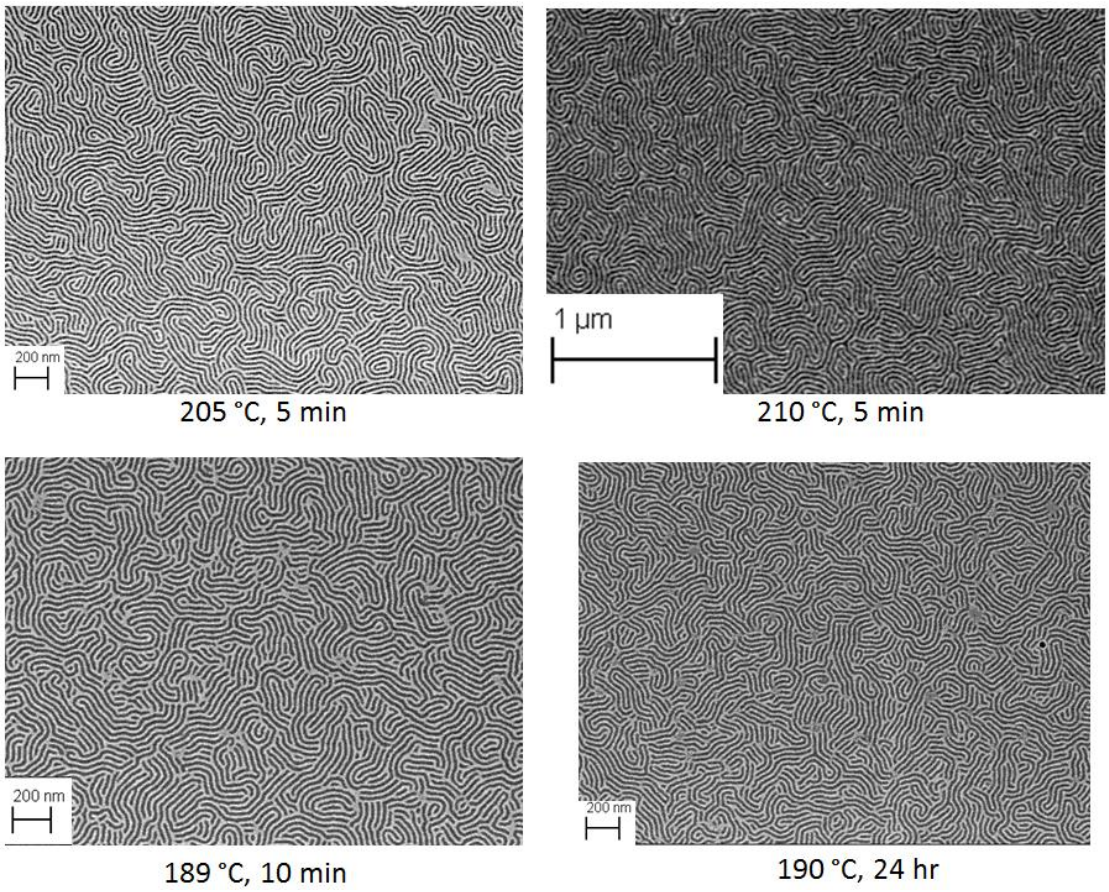

Figure 6.18: PS-*b*-PTMSS-*b*-PS annealed in the presence of TC-PS at different temperatures and times. Samples were etched with O_2 identical to Figure 6.15. All conditions yielded essentially the same pattern, which implies that the self-assembly is rapidly achieved and does not change over time.

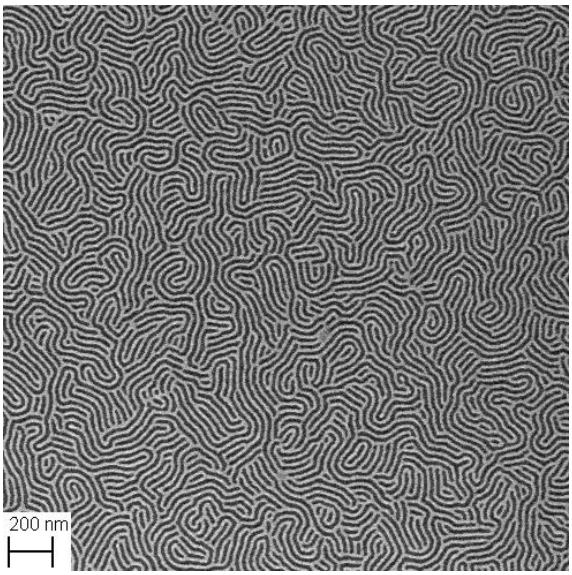

Figure 6.19: PS-*b*-PTMSS-*b*-PS annealed in the presence of TC-PS at 210°C for 10 sec.

6.5 TOP COATS FOR POLY(TRIMETHYLSILYLSTYRENE-*BLOCK*-D,L-LACTIDE)

With the top coat proof-of-principle established using the PS-*b*-PTMSS-*b*-PS triblock, attention was shifted towards utilizing a high-χ BCP that would be of engineering interest for next-generation lithography. Poly(trimethylsilylstyrene-*block*-D,L-lactide) (PTMSS-*b*-PLA) (**Figure 6.20**) was selected as a model high-χ BCP for three reasons: 1) it again incorporates silicon for etch resistance, 2) both blocks have T_g>25°C for structural stability, and 3) it has a high-χ and self-assembles into sub-10 nm features (*169*). The synthesis of the block copolymer was performed by Julia D. Cushen and is reported elsewhere (*169*). All attempts to align PTMSS-*b*-PLA by thermal annealing alone in air, nitrogen, or under vacuum were unsuccessful - it oriented exclusively parallel to the substrate in the absence of a top coat. Analogous to PS-*b*-PTMSS-*b*-PS, the annealing temperature must be above the T_g of each block to allow for BCP reorganization (**Figure 6.27**: PTMSS-*b*-PLA: $T_{g\text{-}PTMSS}$=102°C, $T_{g\text{-}PLA}$=54°C) but below that of the top coat to prevent inter-diffusion.

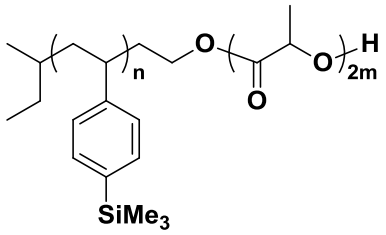

Figure 6.20: Chemical structure of PTMSS-*b*-PLA.

High-χ lamella-forming PTMSS-PLA annealed with top coat TC-PLA (**Figure 6.21**) produced relatively well-formed perpendicular lamellae after the top coat was stripped, with measured L_0 values ca. 19 nm, corresponding to line widths of <10 nm (**Figure 6.22**). In this case, the SAXS data for the bulk sample shows an even smaller L_0 (15 nm). We believe that the lack of perfect agreement between these measurements is likely the result of imprecise SEM metrology at a resolution near the limit of our instrument. Samples annealed and stripped in the absence of a top coat produced only slight surface roughness, with no perpendicular lamella in any region (**Figure 6.22**, inset).

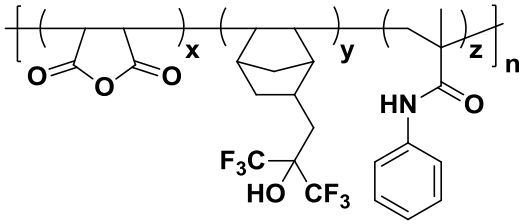

TC-PLA

Figure 6.21: TC-PLA. Maleic Anhydride:Norbornene:Methacrylate=61:19:20, T_g=180°C, T_d=260°C.

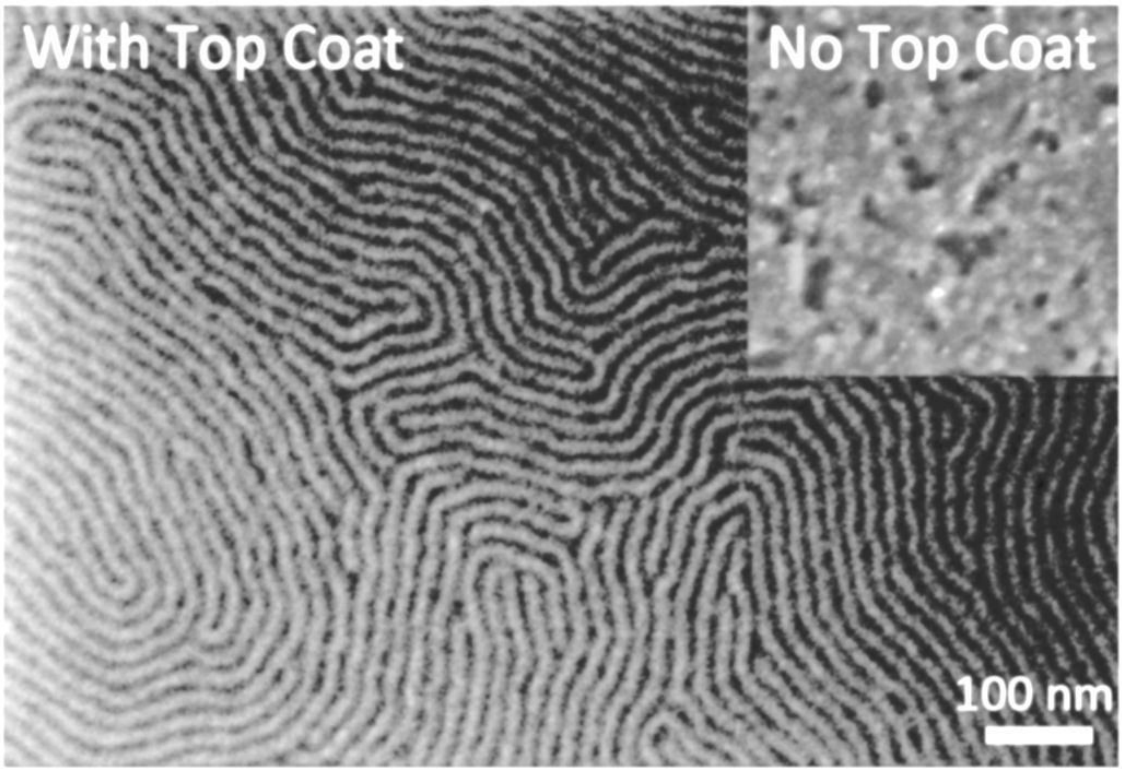

Figure 6.22: Scanning electron micrographs of PTMSS-*b*-PLA (L_0=19 nm as measured, 15 nm in bulk), annealed at 170°C for 20 h with top coat TC-PLA (main figure) and without a top coat (inset). The BCP film thickness was 10 nm (0.66*L_0). After thermal annealing, both samples were stripped with 3:1 by weight MeOH:30 wt% aq. NH_4OH. The bottom surface treatment was an XST-OMe cross-linkable copolymer. The scale bar is valid for both the image and the inset.

There were considerable difficulties associated with re-synthesizing the TC-PLA top coat. New batches failed to orient PTMSS-*b*-PLA the same as the original batch. Presumably small variations in top coat composition and chain distribution can have large effects on the BCP orientation because of its high-χ value. This problem was not encountered with the low-χ PS-*b*-PTMSS-*b*-PS – a second batch of TC-PS successfully

induced perpendicular orientation of PS-*b*-PTMSS-*b*-PS. Future work focuses on optimizing a top coat for PTMSS-*b*-PLA.

6.6 THIN FILM ORIENTATION CONTROL THEORY

The difference in orientation between a film with and without a top coat can be understood in terms of the differences in the thin film free energies of the orientations that the block copolymer can adopt. For simplicity, a symmetric AB diblock copolymer is modeled using PS and PTMSS constituents, which have bulk free energy (*28*) and interfacial interactions similar to those of the ABA triblock copolymer. The bulk free energy of the BCP must be modified in the case of thin films because of the addition of substantial interface free energies. Three orientations of the lamella-forming BCP were considered: horizontal symmetric, horizontal asymmetric and vertical (**Figure 6.1**). Turner (*170*) and Walton (*79*) introduced a thin film free energy model that evaluates the free energy of each of the three lamellar orientations F_v (vertical), $F_{H\text{-}sym}$ (horizontal symmetric), and $F_{H\text{-}asym}$ (horizontal asymmetric) relative to the bulk free energy of the BCP (F_0). These relationships are expressed as follows (**Equations 6.1-6.3**):

$$\frac{F_V}{F_0} = \frac{1}{3}\left[3 + \frac{1}{d}\left(\frac{\left(\gamma_{B-Bot} - \gamma_{A-Bot}\right) + \left(\gamma_{B-Top} - \gamma_{A-Top}\right)}{2\gamma_{AB}} + \frac{\gamma_{A-Top} + \gamma_{A-Bot}}{\gamma_{AB}}\right)\right] \qquad \textbf{Eq. 6.1}$$

$$\frac{F_{H-sym}}{F_0} = \frac{1}{3}\left[\left(\frac{d}{n}\right)^2 + \frac{2n}{d} + \frac{1}{d}\left(\frac{\gamma_{A-Top} + \gamma_{A-Bot}}{\gamma_{AB}}\right)\right] \qquad \textbf{Eq. 6.2}$$

$$\frac{F_{H-asym}}{F_0} = \frac{1}{3}\left[\left(\frac{d}{n+\frac{1}{2}}\right)^2 + \frac{2\left(n+\frac{1}{2}\right)}{d} + \frac{1}{d}\left(\frac{\gamma_{A-Top} + \gamma_{B-Bot}}{\gamma_{AB}}\right)\right] \qquad \textbf{Eq. 6.3}$$

where the normalized film thickness $d=D/L_0$ (D is the actual BCP film thickness, L_0 is the bulk periodicity), n is a series of positive integers, and $\gamma_{A\text{-}Top}$, $\gamma_{A\text{-}Bot}$, $\gamma_{B\text{-}Top}$, and $\gamma_{B\text{-}Bot}$ represent the interfacial energies of PTMSS (subscript A) and PS (subscript B) with either the bottom or top interface, with $\gamma_{A\text{-}Top} \leq \gamma_{B\text{-}Top}$ by definition. The block-block

interfacial energy $\gamma_{AB} = (k_B T \chi^{1/2})/(6^{1/2}\alpha^2)$ is dependent on the segment-segment interaction parameter χ and the statistical segment length α (*22*).

The smaller of the three normalized free energy ratios (F_V/F_0, $F_{H\text{-}sym}/F_0$, and $F_{H\text{-}asym}/F_0$) will determine the energetically-preferred orientation of the BCP at a given normalized film thickness, d. The free energy equations have been rewritten below in terms of the differences between the horizontal and vertical orientations, $(F_H\text{-}F_V)/F_0$, which depend upon the difference in the interfacial energy of each block with both the top and bottom interfaces ($\Delta\gamma_{Top} \equiv |\gamma_{B\text{-}Top} - \gamma_{A\text{-}Top}|$ and $\Delta\gamma_{Bot} \equiv |\gamma_{B\text{-}Bot} - \gamma_{A\text{-}Bot}|$), not on the absolute values of $\gamma_{A\text{-}Top}$, $\gamma_{A\text{-}Bot}$, $\gamma_{B\text{-}Top}$, and $\gamma_{B\text{-}Bot}$ (**Equations 6.4-6.6**).

$$\frac{F_{H-sym} - F_V}{F_0} = c - \frac{\Delta\gamma_{Bot} + \Delta\gamma_{Top}}{6d\gamma_{AB}} \qquad \textbf{Eq. 6.4}$$

$$\frac{F_{H-asym} - F_V}{F_0} = c + \frac{\Delta\gamma_{Bot} - \Delta\gamma_{Top}}{6d\gamma_{AB}} \qquad \textbf{Eq. 6.5}$$

$$c = \frac{d^3 + 2m^3}{3dm^2} - 1 \qquad \text{where m=n for } F_{H\text{-}sym}\text{, m=n+½ for } F_{H\text{-}asym} \qquad \textbf{Eq. 6.6}$$

We calculated the effects of $\Delta\gamma_{Top}$ on the orientation of a lamella-forming BCP using these equations. The segment-segment interfacial energy is estimated to be γ_{AB} = 0.80 mN/m using a statistical segment length α = 0.68 nm for PS (*171*) and $\chi_{PS\text{-}PTMSS}$ = 0.024, as calculated for PS-*b*-PTMSS-*b*-PS at 150°C based on absolute intensity small-angle X-ray scattering measurements (*150*). Interestingly, the results are virtually identical using the values for PTMSS-PLA, $\chi_{PTMSS\text{-}PLA}$ = 0.34 at 150°C (*169*) and γ_{AB} = 1.39 mN/m. To minimize the effect of the substrate interface on the BCP orientation, a neutral bottom interface was modeled such that $\gamma_{B\text{-}Bot} = \gamma_{A\text{-}Bot} = ½\gamma_{AB}$, implying that $\Delta\gamma_{Bot} = 0$, analogous to Walton et al. (*79*). The value of $\Delta\gamma_{Top}$ was then varied to isolate the role of the top surface on BCP orientation. A perfectly neutralizing top coat has $\Delta\gamma_{Top} = 0$. For comparison, in the case of a block copolymer composed of a silicon-containing block and a relatively non-polar organic block (such as PTMSS and PS), an air top interface results in $\Delta\gamma_{Top} \approx 20$ mN/m (*69*).

A free energy curve was generated from the superposition of the parabolic expressions at incremental values of n for both of the horizontal orientations, horizontal symmetric ($F_{H\text{-}sym}/F_0$) and horizontal asymmetric ($F_{H\text{-}asym}/F_0$). For each horizontal orientation, the minimum value of the collection of parabolas at a given $d=D/L_0$ resulted in a function for $F_{H\text{-}sym}/F_0$ or $F_{H\text{-}asym}/F_0$. The vertical orientation free energy did not depend on n and did not require the superposition of multiple curves; so the free energy F_V/F_0 could be calculated directly. To evaluate the energetically favorable orientation, the difference between the minimum horizontal orientation free energy, $F_{H\text{-}min} \equiv$ minimum $[F_{H\text{-}sym}, F_{H\text{-}asym}]$, and the vertical orientation free energy F_V/F_0 was plotted as a function of $d = D/L_0$ (**Figure 6.23**). The value $(F_{H\text{-}min}- F_V)/F_0$ should be negative if a horizontal orientation is energetically favorable and positive if a vertical or perpendicular orientation is favored. A plot of $(F_{H\text{-}min}- F_V)/F_0$ as a function of d for different values of $\Delta\gamma_{Top}$ ranging from 0 to 0.5 mN/m is also shown in **Figure 6.23**; the general trends are in good agreement with the efficacy of the top coats described herein. With $\Delta\gamma_{Top} \geq 0.5$ mN/m, a relatively modest difference in interfacial energies $\gamma_{B\text{-}Top}$ and $\gamma_{A\text{-}Top}$, $(F_{H\text{-}min}- F_V)/F_0$ is always negative and thus favors a horizontal orientation of BCP domains at all film thicknesses. This situation models silicon-organic block copolymers in contact with air, which often have $\Delta\gamma_{Top} \approx 20$ mN/m and experimentally always produce horizontal orientations at the top interface in the absence of top coats. As the $\Delta\gamma_{Top}$ value decreases ($\Delta\gamma_{Top} < 0.5$ mN/m), $(F_{H\text{-}min}- F_V)/F_0$ becomes positive at some values of d, implying that vertical features can be obtained at certain film thicknesses, as was observed in **Figures 6.15** and **6.22**. In the limit of a perfectly neutral top surface ($\Delta\gamma_{Top} = 0$), vertical orientation is favored over all film thicknesses.

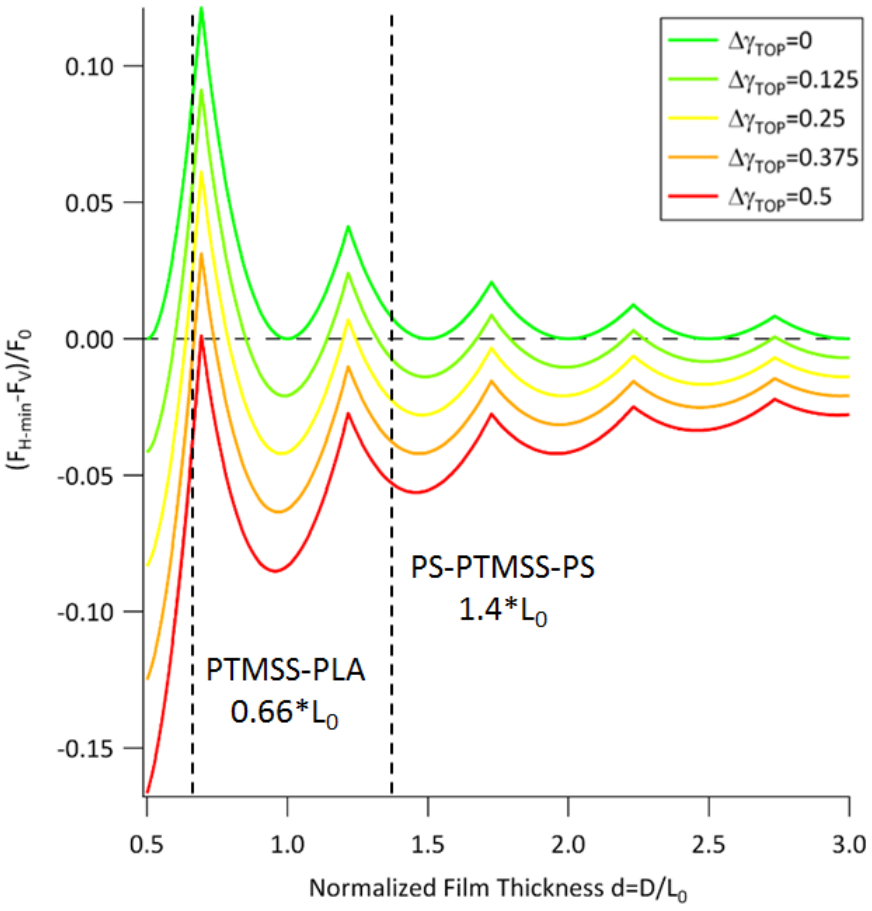

Figure 6.23: Differences in BCP thin film free energies between the horizontal and vertical orientations $(F_{H\text{-}min}\text{-}F_V)/F_0$ as a function of reduced film thickness d. For a given d, if the value of $(F_{H\text{-}min}\text{-}F_V)/F_0$ is negative, a horizontal orientation is preferred; if it is positive, a vertical orientation is preferred. Different curves represent different values of $\Delta\gamma_{Top}$ measured in mN/m. $\Delta\gamma_{Top}$ = 0 mN/m represents a perfectly neutralizing top coat. For $\Delta\gamma_{Top} \geq 0.5$ mN/m, a horizontal orientation is realized for all d. The dashed line at D = 1.4*L_0 corresponds with the 43 nm PS-*b*-PTMSS-*b*-PS film used to produce the SEMs shown in Figure 6.15; the dashed line at D = 0.66*L_0 corresponds with the 10 nm PTMSS-*b*-PLA film used to produce the SEMs shown in Figure 6.22.

The surface energy of the ring-closed, less polar form of the top coat should therefore be tuned to achieve neutrality for the specific BCP for which it was designed. The top coat for the triblock copolymer described herein seems to be nearly optimized based on its performance. We do not believe that the top coat for the high-χ diblock material is fully optimized. A top coat with a nonpolar state that is nearer to neutrality could provide a wider process window and enable shorter annealing times for this BCP. Second generation top coats for PTMSS-*b*-PLA were thus designed, synthesized, and tested (Chapter 7).

6.7 EXPERIMENTALS:

CF3-Nor:

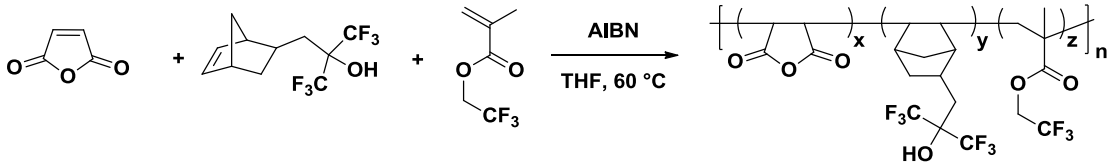

Scheme 6.1: Synthesis of top coat CF3-Nor.

A 50 mL round bottom flask was charged with a stir bar, maleic anhydride (4 eq, 1.130 g, 11.52 mmol), 3-(Bicyclo[2.2.1]hept-5-en-2-yl)-1,1,1-trifluoro-2-(trifluoromethyl)propan-2-ol (2 eq, 1.580 g, 5.762 mmol), 2,2,2-trifluoroethyl methacrylate (1 eq, 0.484 g, 2.881 mmol), and azoisobutyronitrile (0.065 eq, 0.031 g, 0.187 mmol). The RBF was fitted with a reflux condenser and 60 mL of dry ethyl acetate was added, followed by three freeze-pump-thaw cycles to remove oxygen. The RBF was submerged in an oil bath at 85°C for 4 h, quenched at 0°C. The product was precipitated in hexanes at room temperature, redissolved in ethyl acetate, and liquid-liquid extracted 6 times with H_2O to remove unreacted maleic anhydride monomer. The polymer solution was precipitated into hexanes and the fine white powder was isolated by filtration and dried *in vacuo* to give ~10% yield. SEC data is shown in **Figure 6.24**.

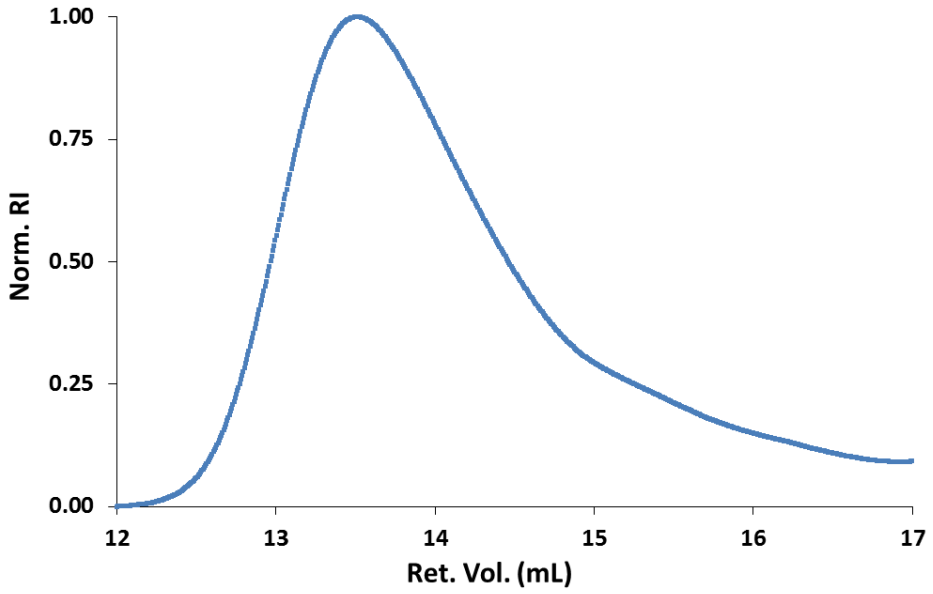

Figure 6.24: SEC trace for top coat CF3-Nor collected using PLGel columns at 70°C. Molecular weight and dispersity data compared to PMMA standards: M_n=5910 Da, M_w=10900 Da, Dispersity=1.85.

Thin Film Processing:

A 1 wt% solution of XST-OMe in toluene was spin-coated at 3500 rpm and cross-linked at 250°C for 5 minutes. The wafer was quickly cooled to room temperature followed by submersing in toluene for 2 minutes and blown dry twice to remove residual uncross-linked polymer, which resulted in a surface treatment thickness of 22 nm. Lamella-forming PS-*b*-PTMSS-*b*-PS was spin coated at 1700 rpm from a 1 wt% solution in toluene and post apply baked at 110°C for 1 minute to produce a 44 nm thick film. Top coat (CF3-Nor) was spin-coated from a 1.5 wt% solution in 30 wt% aq. NH_4OH at 3000 rpm to produce a 38 nm thick film. The samples were annealed at 170°C for 19 hr 45 min, cooled to room temperature, and stripped with 10 drops of 30 wt% aq. NH_4OH. The resulting film was etched using the following formula: pressure=20 mTorr, RF=10 W, ICP=50 W, O_2 flow rate=75 sccm, Ar flow rate=75 sccm, temperature=15°C, time=45 s.

TC-MA:

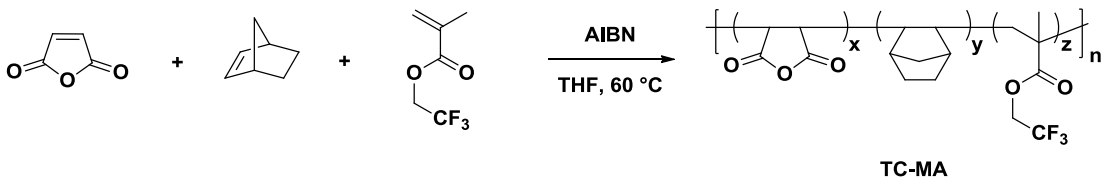

Scheme 6.2: Synthesis of top coat TC-MA.

A 50 mL round bottom flask (RBF) was charged with a stir bar, maleic anhydride (6 eq, 1.575 g, 16.06 mmol), norbornylene (3 eq, 0.756 g, 8.03 mmol), 2,2,2-trifluoroethyl methacrylate (1 eq, 0.450 g, 2.68 mmol), and azoisobutyronitrile (0.1 eq, 0.044 g, 0.268 mmol). The RBF was fitted with a reflux condenser and 20 mL of dry THF was added, followed by three freeze-pump-thaw cycles to remove oxygen. The RBF was submerged in an oil bath at 60°C under dry N_2 for 48 h, quenched at 0°C, and precipitated in hexanes at room temperature. The product was filtered and redissolved in ethyl acetate, followed by 6 liquid-liquid extractions with H_2O to remove unreacted maleic anhydride monomer. The fine white powder was isolated by filtration and dried *in vacuo* to give ca. 50% yield. The top coat was analyzed by gel permeation chromatography. TC-MA: Composition (combustion): Maleic Anhydride:Norbornene:Methacrylate=50:34:16, T_g=137°C. M_n=3490 Da, M_w=6700 Da, Dispersity=1.92 (calculated with DMF as an eluent against PMMA standards).

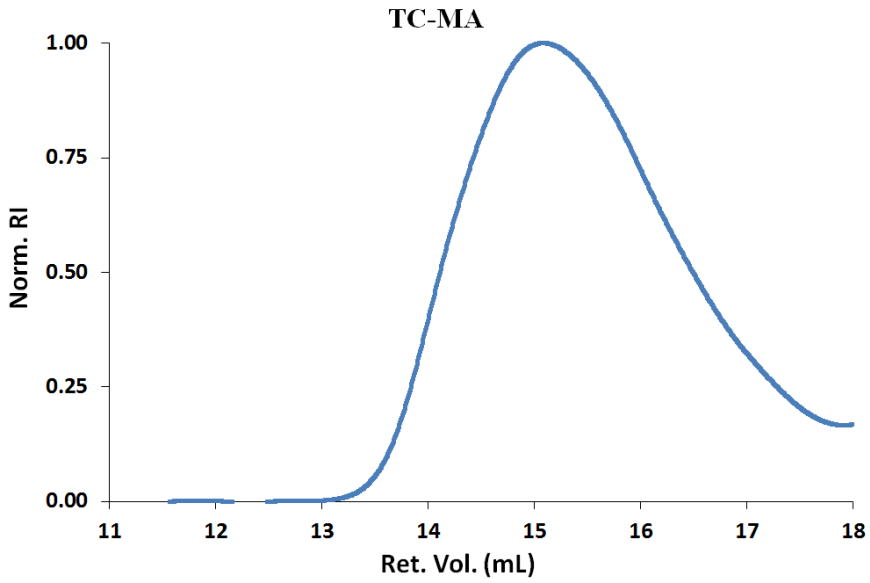

Figure 6.25: GPC data with DMF as an eluent of the representative top coat (TC-IR) used for the infrared spectroscopy ring-opening and closing equilibrium studied. Molecular weight data calculated relative to PMMA standards. TC-IR: M_n=3490 Da, M_w=6700 Da, Dispersity=1.92.

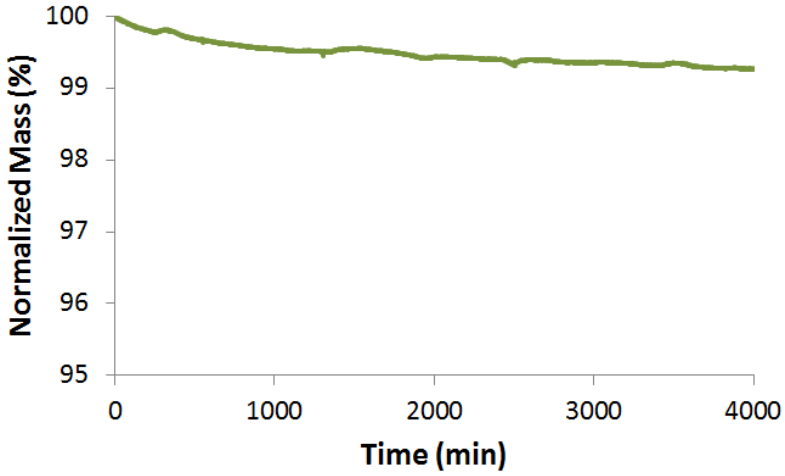

Figure 6.26: Isothermal TGA data at 131°C for 4000 min, which mimics conditions used in the thin film annealing process. No significant top coat degradation was observed. Two 10°C/min ramps to 150°C were performed prior to the isothermal run to remove residual solvent.

The thin film processing was identical to TC-Sty-OCF3. See the next section for details.

TC-StyOCF3:

Synthesis of TC-StyOCF3 precursor:

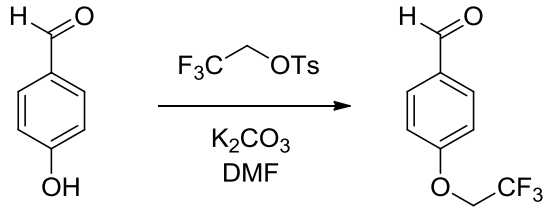

Scheme 6.3: Synthesis of *4-(2,2,2-tifluoroethoxy)benzaldehyde.*

A flame dried three-neck round bottom flask equipped with a magnetic stirbar, glass stopper, condenser, and a rubber septum was charged with 2,2,2-trifluoroethyl 4-

methylbenzenesulfonate (7.00 g, 27.5 mmol, 1.3 eq), 4-hydroxybenzaldehyde (2.52 g, 20.6 mmol, 1 eq), potassium carbonate (18.9 g, 137.6 mmol, 6.6 eq), and 50 mL of dry DMF. The cloudy solution was heated to 120˚ C and stirred under a nitrogen atmosphere for 17 hrs. The solution was diluted with 400 mL of water and the product was extract with 100 mL of ether (4x). The organic phases were combined and washed with 400 mL of water (3x) and 400 mL of brine (1x). The organic phase was dried over Na_2SO_4 and the solvent was removed to yield the crude product. Column chromatography (EtOAc/Hex) was used to yield 3.238 g (76.9%) of an off-white solid. HRMS (M/Z) [M+H] found: 205.0475, calc. 205.04. MP: 48-51°C. ^{1}H NMR (400 MHz; $CDCl_3$): δ 9.92 (s, 1H), 7.90-7.84 (m, 2H), 7.09-7.03 (d, 2H), 4.48-4.39 (q, *J*=7.9 Hz, 2H).

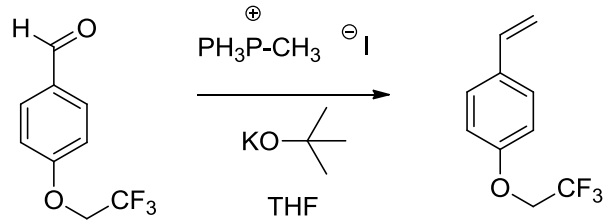

Scheme 6.4: Synthesis of *1-(2,2,2-trifluoroethoxy)-4-vinylbenzene.*

A flame dried three-neck round bottom flask equipped with a magnetic stirbar, glass stopper, condenser, and a rubber septum was charged with methyltriphenylphosphonium iodide (5.4 g, 13.5 mmol, 1.3 eq), potassium tert-butoxide (1.51 g, 13.5 mmol, 1.3 eq) and dry THF (100 mL). The solution was bright yellow and cloudy, and was stirred for 5 minutes. 4-(2,2,2-trifluoroethoxy)benzaldehyde (2.113 g, 10.35 mmol, 1 eq) was dissolved in 25 mL of THF and was cannulated into the solution of ylide. The solution was stirred for 6 hrs at room temperature. The white precipitate was filtered out of the solution, and the solvent was removed. The crude product was purified via column chromatography (10% EtOAc/Hex) to yield 1.65 g (79.1%) of pure product as an oil. HRMS (M/Z) [M+H] found: 203.0682, calc. 203.06. ^{1}H NMR (400 MHz; $CDCl_3$): δ 7.40-7.36 (m, 2H), 6.92-6.89 (m, 2H), 6.68 (dd, *J* = 17.6, 10.9, 1H), 5.66 (d, *J* = 17.6, 1H), 5.19 (d, *J* = 10.9, 1H), 4.38-4.32 (q, *J* = 8.1, 2H).

Top Coat synthesis

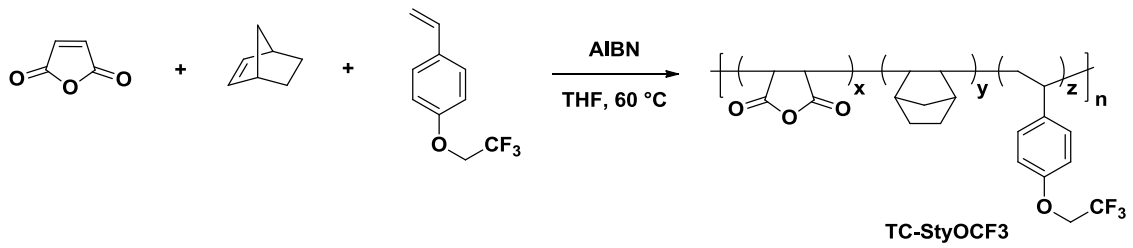

Scheme 6.5: Synthesis of top coat TC-Sty-OCF3.

A flame dried round bottom flask equipped with a magnetic stirbar and water condenser was charged with maleic anhydride (1.16 g, 11.8 mmol, 0.6 eq), 1-(2,2,2-trifluoroethoxy)-4-vinylbenzene (0.40, 1.97 g, 0.1 eq), norbornene (0.55 g, 5.9 mmol, 0.3 eq), AIBN (6.5 mg, 0.039 mmol, 0.002 eq), and dry THF (6 g). The solution was degassed by the freeze-pump-thaw method three times. The solution was heated and stirred at 60˚ C for 48 hours. The THF was removed and the polymer was dissolved in EtOAc (25 mL). It was washed with 25 mL (3x) of water. The solvent was removed until only about 2 mL of solution remained. The polymer was precipitated three times from EtOAc in hexane, 1:1 hexane/DCM, and DCM to remove any remaining monomer and impurities. The polymer was dried *in vacuo*, and 255 mg of polymer was obtained in 12% yield. Maleic Anhydride:Norbornene:Styrene (mol%)=56:17:27. T_g=185°C, T_d=230°C. M_n=6380 Da, M_w=18200 Da, Dispersity=2.85 (calculated with DMF as an eluent against PMMA standards).

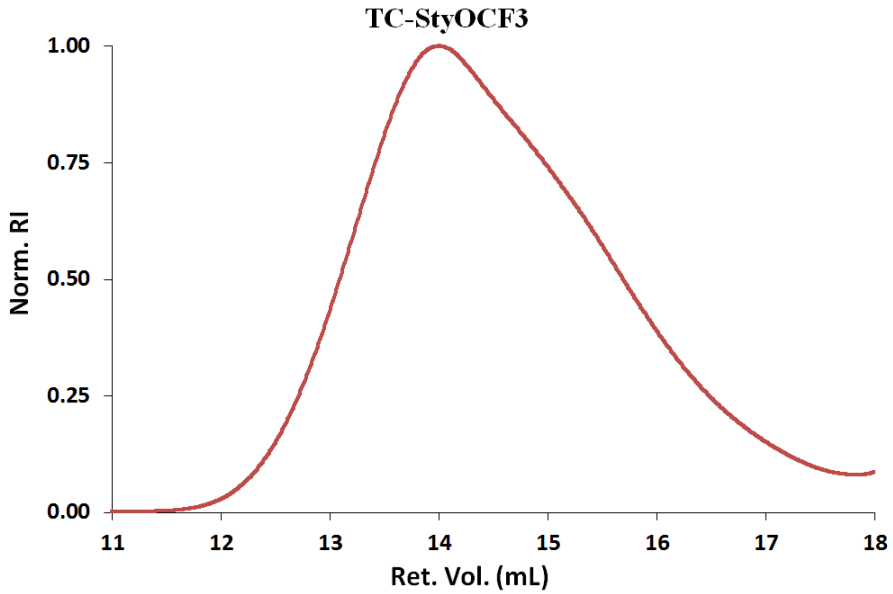

Figure 6.27: GPC data with DMF as an eluent of the representative top coat (TC-StyOCF3). Molecular weight data calculated relative to PMMA standards. M_n=6380 Da, M_w=18200 Da, Dispersity=2.85.

Thin Film Processing of TC-MA and TC-StyOCF3:

A 0.5 wt% solution of XST-OMe in toluene was spin-coated at 3500 rpm and cross-linked at 250°C for 5 minutes. The wafer was quickly cooled to room temperature followed by submersing in toluene for 2 minutes and blown dry twice to remove residual uncross-linked polymer, which resulted in a surface treatment thickness of 11 nm. Lamella-forming PS-*b*-PTMSS-*b*-PS was spin coated at 2900 rpm from a 1.1 wt% solution in toluene which produced a 42 nm thick film. Top coat (TC-MA or TC-StyOCF3) was spin-coated from a 2 wt% solution in 1:3 by wt MeOH:30 wt% aq. NH_4OH at 2500 rpm to produce a 54 nm thick film. The samples were annealed at 131°C for ca. 5 days, cooled to room temperature, and stripped with 15 drops of a 1:3 by wt solution of MeOH:30 wt% aq. NH_4OH at 2500 rpm. The resulting film was etched using the following formula: pressure=20 mTorr, RF=10 W, ICP=50 W, O_2 flow rate=75 sccm, Ar flow rate=75 sccm, temperature=15°C, time=30 s.

TC-PS:

TC-PS precursor:

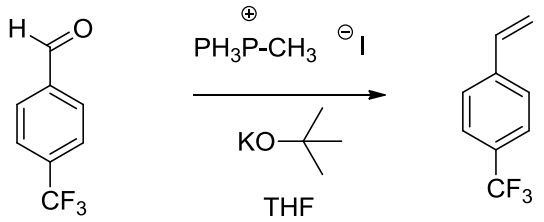

Scheme 6.6: Synthesis of 1-(trifluoromethyl)-4-vinylbenzene.

A flame dried round bottom flask equipped with a magnetic stirbar and a rubber septum was charged with methyltriphenylphosphonium iodide (9.0 g, 22 mmol, 1.3 eq), potassium *tert*-butoxide (2.5 g, 22 mmol, 1.3 eq) and dry THF (100 mL) and cooled to -78°C. The bright yellow and cloudy solution was stirred for 5 minutes. 4-(trifluoromethyl)benzaldehyde (3.0 g, 17 mmol, 1 eq) was dissolved in 25 mL of THF and was cannulated into the solution of ylide. The solution warmed to room temperature and was stirred for 5 hrs. The white precipitate was filtered out of the solution, and the solvent was removed *in vacuo*. The crude material was passed through a short column of silica gel using pentanes as the eluent. Removal of the solvent yielded 1.23 g (44 %) of pure product as an oil. ^{1}H NMR (400 MHz; $CDCl_3$): δ 7.58 (d, *J* = 8.3, 2H), 7.50 (d, *J* = 8.3, 2H), 6.75 (dd, *J* = 17.6, 10.9, 1H), 5.85 (dd, *J* = 17.6, 0.3, 1H), 5.39 (d, *J* = 10.9, 1H). HRMS (M/Z) [M+H] found 173.0213, calc. 173.05.

Top Coat Synthesis

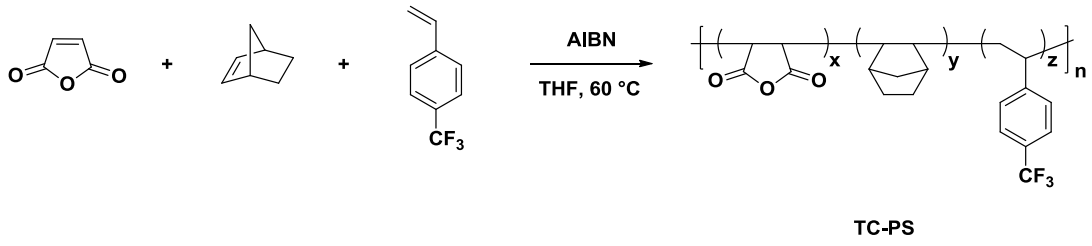

TC-PS

Scheme 6.7: Synthesis of top coat TC-PS.

A 50 mL round bottom flask (RBF) was charged with a stir bar, maleic anhydride (6 eq, 1.16 g, 11.1 mmol), norbornylene (3 eq, 0.450 g, 6.94 mmol), 2,2,2-1-(trifluoromethyl)-4-vinylbenzene (1 eq, 0.400 g, 2.32 mmol), and azoisobutyronitrile (0.02 eq, 0.0076 g, 0.046 mmol). The RBF was fitted with a reflux condenser and 20 mL of dry THF was added, followed by three freeze-pump-thaw cycles to remove oxygen. The RBF was submerged in an oil bath at 60°C under dry N_2 for 48 h, quenched at 0°C, and precipitated in hexanes at room temperature. The product was filtered and redissolved in ethyl acetate (25 mL), liquid-liquid extracted 3 times with H_2O (25 mL each time) to remove unreacted maleic anhydride monomer, and precipitated in hexanes. The polymer was subsequently redissolved and precipitated two more times in solutions of 1:1 hexane:DCM and DCM. The fine white powder was isolated by filtration and dried in vacuo to give ca. 20% yield. Low conversions help avoid monomer drift and should improve the match between the copolymer composition of the polymer and the actual monomer feed ratio. The top coat was analyzed by gel permeation chromatography (**Figure 6.30**). TC-PS: Composition (mol% from combustion): Maleic Anhydride:Norbornene:Styrene=56:18:26, T_g=214°C.

TC-PLA

TC-PLA Precursor:

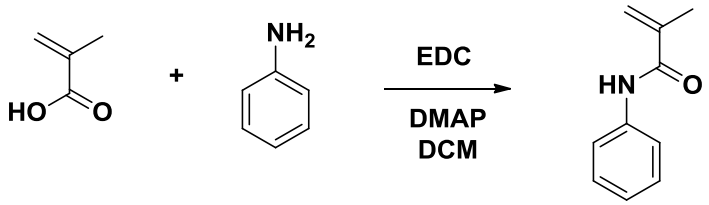

Scheme 6.8: Synthesis of N-phenylmethacrylamide.

A three-neck flask was equipped with a magnetic stir bar, 1-ethyl-3-(3-dimethylaminopropyl)carbodiimide hydrochloride (9.84 g, 51.3 mmol, 1.1 eq.) and

dichloromethane (25 g) and cooled to 0°C. Methacrylic acid (6.02 g, 69.9 mmol, 1.5 eq.) and aniline (4.34 g, 46.6 mmol, 1 eq.) were added to the flask, followed by 4-(dimethylamino)pyridine (1.14 g, 9.32 mmol, 0.2 eq.) in dichloromethane (25 g). The mixture was stirred for 3 h at room temperature, then washed with 1 N HCL (50 g) three times, saturated $NaHCO_3$ (50 g) two times, and water (50 g) three times. The final pH of the solution was 7. After removing the solvent, the residue was purified by column chromatography using 3:1 hexanes:ethyl acetate as the eluent. The product was dried *in vacuo* to give a white solid in 55% yield. M.P. 83-84°C (literature 82-84°C). ^{1}H NMR (400 MHz; $CDCl_3$): δ 7.54 (m, 3H), 7.32 (m, 2H), 7.11 (m, 1H), 5.77 (s, 1H), 5.43 (s, 1H), 2.04 (s, 3H). HRMS (M/Z) [M+H] found: 162.0919, calc. 162.08.

Top Coat Synthesis

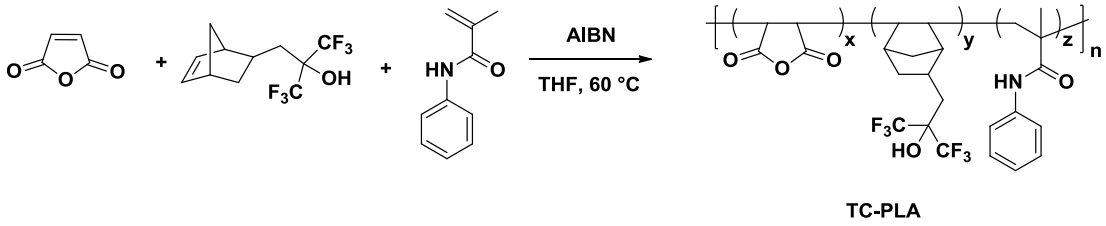

Scheme 6.9: Synthesis of top coat TC-PLA.

A 50 mL round bottom flask was charged with a stir bar, maleic anhydride (6 eq, 1.130 g, 11.52 mmol), 3-(Bicyclo[2.2.1]hept-5-en-2-yl)-1,1,1-trifluoro-2-(trifluoromethyl)propan-2-ol (3 eq, 1.580 g, 5.762 mmol), N-Phenylmethacrylamide (1 eq, 0.310 g, 1.921 mmol), and azoisobutyronitrile (0.05 eq, 0.016 g, 0.096 mmol).The RBF was fitted with a reflux condenser and 8 mL of dry THF was added, followed by three freeze-pump-thaw cycles to remove oxygen. The RBF was submerged in an oil bath at 60°C for 48 h, quenched at 0°C, and precipitated in hexanes at room temperature. The product was filtered and redissolved in ethyl acetate, followed by 6 liquid-liquid extractions with H_2O to remove unreacted maleic anhydride monomer. The polymer

solution was poured into hexane: DCM=6:4(wt/wt) mixture solvent. The fine white powder was isolated by filtration and dried *in vacuo* to give ~30% yield. The top coat was analyzed by gel permeation chromatography (**Figure 6.30**). TC-PLA: Composition (mol% from combustion): Maleic Anhydride:Norbornene:Methacrylate=68:21:11, T_g=180°C.

Thin Film Processing of TC-PS and TC-PLA:

A 0.5 wt% toluene solution of XST-OMe was spin-coated at 3000 rpm for 30 sec onto a wafer that had been rinsed with acetone and isopropanol three times, respectively. The wafer was annealed at 250°C for 5 min on a hot plate open to air to cross-link the film. Once removed from the hot plate and cooled to room temperature, the wafer was then submerged in toluene for 2 min and blown dry two times to remove uncrosslinked polymer. Typical film thicknesses were on the order of 13-15 nm, as determined by ellipsometry. Approximately 1 wt% toluene solutions of lamellar-forming PS-*b*-PTMSS-*b*-PS were applied to crosslinked XST-OMe films at various spin speeds to produce different block copolymer film thicknesses as determined by ellipsometry. The top coat was then spin-coated out of a 3:1 by wt solution of MeOH:30 wt% aq. NH_4OH (for TC-PS) or just 30 wt% aq. NH_4OH (for TC-PLA) at various concentrations, giving top coat film thicknesses ca. 18 nm (TC-PLA) and ca. 60 nm (TC-PS). Methanol was used with the application of TC-PS to produce more uniform top coat thin films. Solutions of 3:1 by weight solution of MeOH:30 wt% aq. NH_4OH were found to have no effect on the block copolymer film thickness of both PS-*b*-PTMSS-*b*-PS and PTMSS-*b*-PLA as measured by ellipsometry. The trilayer film stacks were subsequently annealed at 170°C (for PTMSS-*b*-PLA, in a vacuum oven) and 210°C (for PS-*b*-PTMSS-*b*-PS, on a hot plate open to air) for 20 h and one minute, respectively. Upon completion of annealing, the PTMSS-*b*-PLA sample annealed in the vacuum oven was cooled down to room temperature under vacuum over the course of ca. 5 h. The PS-*b*-PTMSS-*b*-PS sample annealed on a hotplate was removed and quickly cooled to room temperature on a room temperature solid metal block. The top coats were subsequently stripped with a 3:1 by

weight solution of MeOH:30 wt% aq. NH_4OH by spinning the wafer at 3000 rpm and applying 20 drops of stripping solution by pipette. In general, stripped films contained very little, if any detectable residual top coat (<4 nm) as measured by ellipsometry. Stripped samples of PS-*b*-PTMSS-*b*-PS triblock copolymer were subsequently etched with oxygen reactive ion etching. Stripped samples of PTMSS-*b*-PLA were not etched.

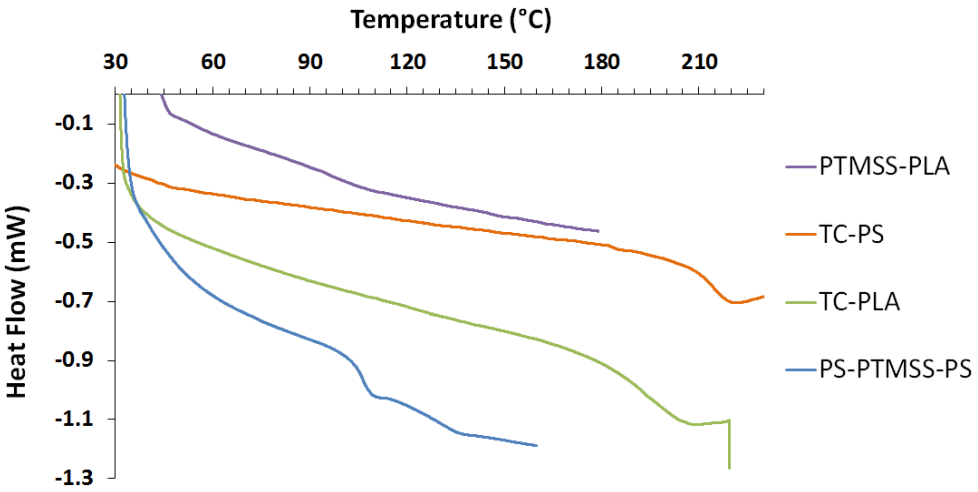

Figure 6.28: DSC data of block copolymers PS-*b*-PTMSS-*b*-PS and PTMSS-*b*-PLA and top coats TC-PS and TC-PLA. PS-*b*-PTMSS-*b*-PS: T_g(PS block)=106°C, T_g(PTMSS block)=131°C. PTMSS-*b*-PLA: T_g(PTMSS block)=102°C, T_g(PLA block)=54°C. Top Coats: T_g(TC-PS)=214°C, T_g(TC-PLA)=180°C. Heating rate=10°C/min for PS-*b*-PTMSS-*b*-PS and 5°C/min for PTMSS-*b*-PLA, TC-PS, and TC-PLA.

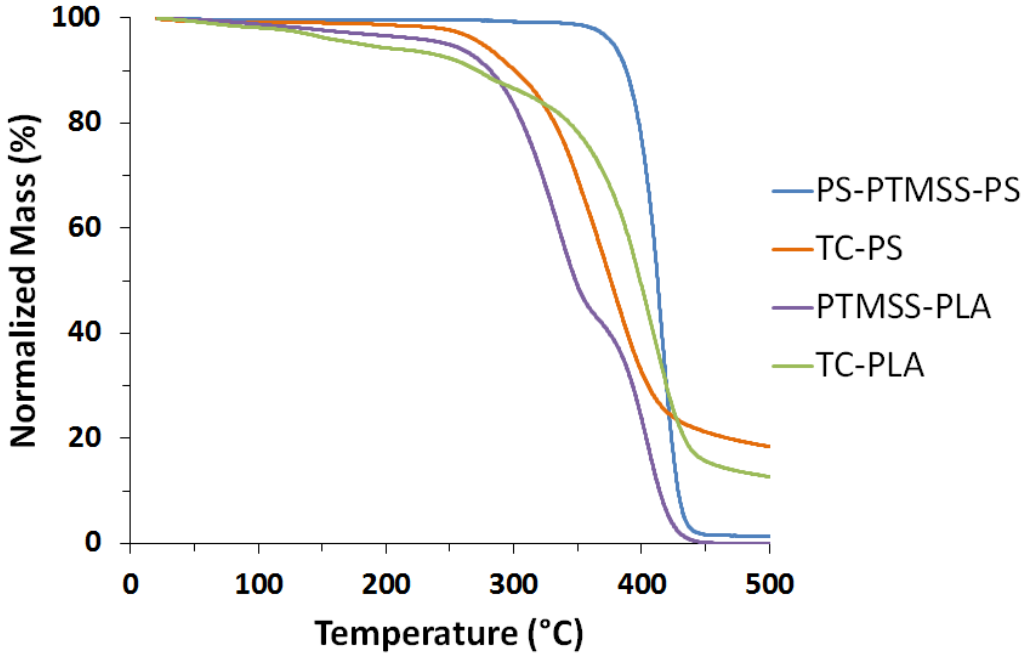

Figure 6.29: TGA data of block copolymers PS-*b*-PTMSS-*b*-PS and PTMSS-*b*-PLA and the top coats TC-PS and TC-PLA. The ramp rate for PS-*b*-PTMSS-*b*-PS was 5°C/min from 20-300°C and 20°C/min from 300-500°C; for PTMSS-*b*-PLA it was 10°C/min from 0-500°C; for TC-PS it was 10°C/min from 20-500°C; for TC-PLA it was 10°C/min from 20-300°C and 40°C/min from 300-500°C. No significant top coat decomposition is observed at the annealing conditions utilized in the present thin film study.

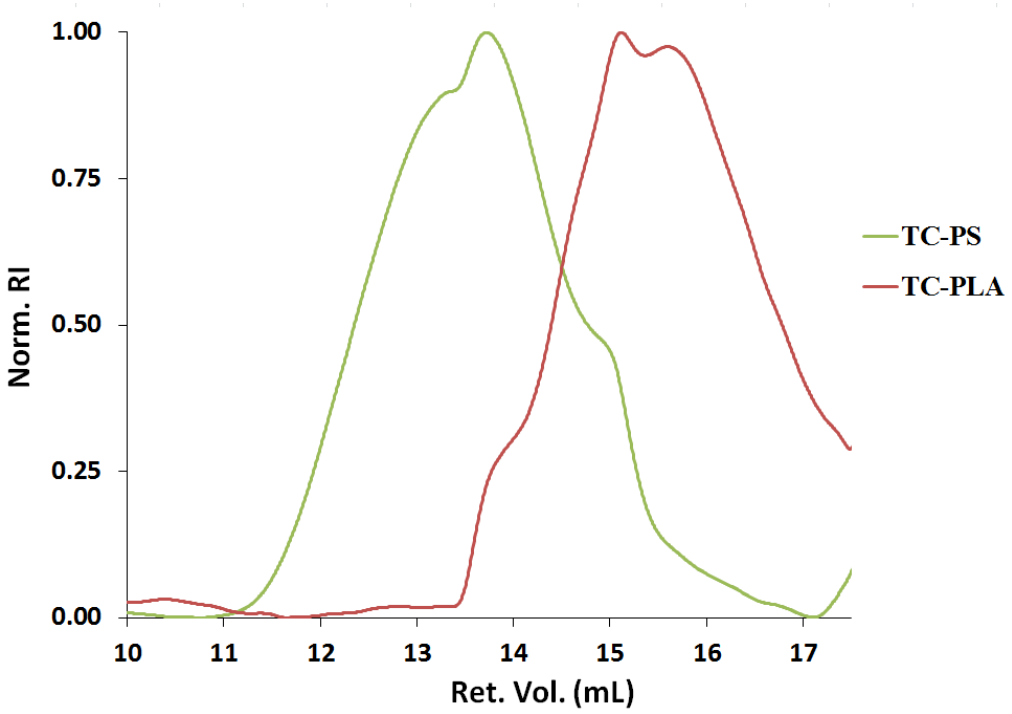

Figure 6.30: Top coat GPC data with DMF as an eluent. Molecular weight data calculated relative to PMMA standards. The small molecule peak starts at ca. 17.5 mL and has been omitted from the plot. TC-PLA: M_n=4340 Da, M_w=8350 Da, Dispersity=1.92; TC-PS: M_n=19480 Da, M_w=42050 Da, Dispersity=2.16.

Materials and Methods

Instrumentation

^{1}H NMR spectra were recorded on a Varian Unity Plus 400 MHz instrument. Chemical shifts are reported in ppm downfield from TMS using the residual protonated solvent as an internal standard ($CDCl_3$, ^{1}H 7.26 ppm). Small molecule IR data were recorded on a Nicolet Avatar 360 FT-IR. Polymeric IR data were collected on a Nicolet Magna-IR 550 Spectrometer. Polymer gel permeation chromatography (GPC) data were measured using an Agilent 1200 Series Isopump and Autosampler with an Agilent

Technologies 1100 RI detector equipped with one PLgel 5 μm, 100 Å column and one PLgel 5 μm, 1000 Å column using DMF as an eluent at 70°C and a flow rate of 1 mL/min. GPC data were measured relative to seven PMMA standards (102, 2200, 4250, 12600, 23500, 41400, and 128000 Da). Films were spin-coated on a Brewer CEE 100CB Spincoater. Film thicknesses were determined with a J.A. Woollam Co, Inc. VB 400 VASE Ellipsometer using wavelengths from 382 to 984 nm with a 65° angle of incidence. A Heraeus Vacutherm Type VT 6060 P from Kendro was used to thermally anneal the films under reduced pressure (for PTMSS-*b*-PLA) and a Thermolyne HP-11515B hot plate open to air was used to thermally anneal PS-*b*-PTMSS-*b*-PS. Oxygen reactive ion etching was performed on an Oxford Instruments Plasmalab 80+ operating in inductively coupled plasma mode. Scanning electron microscopy was performed using a Zeiss Supra 40 VP at 3 kV with the in-lens detector and a working distance of 2.3 mm for PS-*b*-PTMSS-*b*-PS and 1.9 mm for PTMSS-PLA. TGA data were collected on a TA Instruments Q500. DSC data were collected on a TA Instruments Q100. Combustion analysis was performed by Midwest Microlab LLC.

Materials

Maleic anhydride (MA), norbornylene (Nor), azobisisobutyronitrile (AIBN), magnesium, and dibromoethane were purchased from Sigma Aldrich. AIBN was recrystallized from methanol. Tetrahydrofuran (THF) and diethyl ether were purchased from Fisher Scientific. 2-((1S,4S)-bicyclo[2.2.1]hept-5-en-2-ylmethyl)-1,1,1,3,3,3-hexafluoropropan-2-ol was generously provided by Central Glass Co. 4-chlorostyrene was purchased from Alfa Aesar. Trimethylsilyl chloride was purchased from Acros Organics. All chemicals were used as received unless otherwise noted.

Substrate interface surface treatments

The substrate surface treatment poly(4-methoxystyrene-*random*-4-vinylbenzylazide) (XST-OMe) was synthesized according to previously reported literature procedure (*69*).

Infrared Spectroscopy Data

The model topcoat containing maleic anhydride, norbornene, and a fluorinated methacrylate (TC-MA, **Figure 6.6**) was used to generate thin film IR data, which were collected in transmission mode on thin films ca. 280 nm thick coated on NaCl salt plates (**Figure 6.5B**). The blue "no base" curve represents the top coat spin coated out of 2-butanone, which is unreactive towards the poly(maleic anhydride) moiety. The red "NH_4OH" curve was spin coated from a 30 wt% aq. NH_4OH solution and was subsequently heated at 210°C for 1 min to produce the green curve.

Scanning Electron Microscopy Images

SEM images had brightness and contrast uniformly and linearly enhanced across the entire image using image editing software.

Block copolymer syntheses

Synthetic details and full characterization of lamella-forming PS-*b*-PTMSS-*b*-PS block copolymer with L_0=30 nm as calculated from bulk SAXS can be found in Chapter 2. Synthetic details and full characterization of lamella-forming PTMSS-*b*-PLA block copolymer with L_0=15 nm as calculated from bulk SAXS can be found in Cushen et al. (*169*).

Etching

Oxygen plasma reactive ion etching performed on thin films of PS-*b*-PTMSS-*b*-PS used the following settings: pressure=20 mTorr, RF power=10 W, ICP power=50 W, O_2 flow rate=75 sccm, Ar flow rate=75 sccm, temperature=15°C. These settings have previously been established as effective for at least partially removing one organic block relative to a PTMSS block (*25*). The etch rate of PS homopolymer using these conditions was measured with ellipsometry to be approximately 0.46 nm/sec; this corresponds with a targeted etch depth of 14 nm in 30 sec for the PS-*b*-PTMSS-*b*-PS triblock copolymer. The SF_6/C_4F_8 etch used for pattern transfer into single-crystal silicon used the following

settings: pressure=55 mTorr, RF power=80 W, ICP power=150 W, SF_6 flow rate=20 sccm, C_4F_8 flow rate=50 sccm, temperature=15°C. Etch times were variable and are specified in figure captions.

6.8 Conclusions

The polarity-switching top coat principle has proven extremely effective at controlling Si-BCP thin film orientation. Compared to the extreme difficulties encountered with solvent annealing processes, the top coat process is simple and versatile. Two BCP architectures (AB diblocks and ABA triblocks) were oriented and the results agree well with theoretical calculations developed for confined BCP thin films.

6.9 Acknowledgements:

Visiting scientist Takehiro Seshimo (from TOK) and graduate students Michael J. Maher, William J. Durand, and Gregory Blachut made significant contributions to the top coat work reported in this chapter. TS and MJM synthesized various top coat materials and precursors. Undergraduates Leon M. Dean and Anthony Thio also contributed greatly to both top coat syntheses and thin film work.

Chapter 7: Top Coats With Composition Control

7.1 Background:

The initial successes with the first generation of top coats described in Chapter 6 were quite encouraging. However, from both synthetic and pragmatic perspectives the top coat materials were unsatisfying. The ideal top coat material will mimic crucial design characteristics of substrate surface treatments (the subject of Chapter 3). Namely, composition control of surface-attachable polymers enables precise synthesis of neutral surfaces tailored for specific block copolymer materials. In principle, the same set of monomers can be used for a wide variety of block copolymers given that the range of accessible surface energies encompasses the appropriate neutral window. This strategy is impossible with the first generation top coat design because the polymer composition is not particularly well controlled by the polymerization feed ratio. Furthermore, the low yields and multimodal character of the SEC traces imply a lack of synthetic control that is crucial for the production of well-defined surface treatment materials. The problematic component in the first generation design was norbornene; polymerizations containing norbornene resulted in poor yields (ca. 20%), while polymerizations involving only maleic anhydride and styrene monomers generally resulted in higher yields. Furthermore, as will be demonstrated, the molecular weight distributions of the polymers lacking norbornene generally appeared monomodal, in contrast to those containing norbornene which were multimodal (**Figure 6.30**). The optimization of the first generation top coat materials was achieved by changing the chemical structure of the third monomer (or the substitution of the norbornene moiety), a process guided by chemical intuition and imprecise structure-property relationships. The laborious top coat component optimization process had to be repeated for each BCP material.

This chapter seeks to establish a general top coat design strategy and to leverage it in combination with substrate surface treatments for complete BCP interfacial neutralization. The presence of two neutral interfaces theoretically decouples BCP orientation from BCP thickness - perpendicular orientation of any BCP thickness

becomes favorable (see the theory developed in **Figure 6.23**) (*149*). However, as one interface deviates even slightly from true neutrality, only specific BCP thicknesses can be oriented perpendicular to the substrate. Thick BCP films are the most difficult. The present improvement in top coat design relies upon the synthetic control of top coat composition, which is exactly analogous to the strategy used for substrate surface treatments (*86, 111, 160*).

7.2 MATERIAL DESIGN

Copolymers containing maleic anhydride and styrene have been extensively studied in the literature (*172-175*). They generally form alternating copolymers (50% maleic anhydride and 50% styrene) over a wide range of feed ratios (*173, 174*), with higher styrene incorporation occurring only at low feed ratios of maleic anhydride (*175*). Since maleic anhydride generally does not homopolymerize with itself, its maximum incorporation into the copolymer is theoretically limited to 50%. A feed composition with >50% styrene can result in increased styrene content and a reduction in the alternating structural motif of monomers, since styrene can self-propagate. Strictly alternating poly(maleic anhydride-*alt*-styrene) is reported to have a glass transition temperature around 170°C and high thermal stability, with 5% weight loss at 310°C (*172*). As styrene incorporation is increased, glass transition temperatures decrease towards the asymptotic limit of polystyrene homopolymer, which has a T_g of ~105°C. Many substituted styrene polymerizations with maleic anhydride also produce 1:1 copolymers, although many have not been extensively characterized (*176-179*). No reports were found on mixtures of styrene derivatives polymerized with maleic anhydride (i.e. styrene1-styrene2-maleic anhydride terpolymers), although some literature details terpolymers consisting of styrene, maleic anhydride, and a third type of co-monomer (*175*).

Top interface neutralization through compositional control is herein extended to polarity-switching top coats with the synthesis of poly(maleic anhydride-styrene1-styrene2), reliant upon the appropriate selection of the two styrenic monomers. In

principle, this single top coat design could be appropriate for a wide range of BCP materials, where the neutralization of the top interface for each BCP utilizes a different but synthetically accessible top coat composition.

7.3 SECOND GENERATION TOP COATS

The design strategy for the second generation top coats is shown in **Figure 7.1**. Analogous to maleic anhydride-styrene and maleic anhydride-substituted styrene polymerizations, we anticipated that a mixture of maleic anhydride and two styrene derivatives, 4-trifluoromethylstyrene and styrene, would also form an alternating copolymer (**Figure 7.1**: n=0.50, m=0.50), with the relative incorporation of each styrene (**Figure 7.1**: x:y) controlled by the polymerization feed ratio. The two styrenes were selected to have a large difference in surface energy, with the intention that a large range of top coat surface energies could be obtained between the two extremes (**Figure 7.1**: n=0.50, x=0.50, y=0 and n=0.50, x=0, y=0.50). While the precise surface energy of poly(4-trifluoromethylstyrene) (PCF3S) is unknown, polystyrene (PS) is reported (*86*) to have a value of 29.9 mN/m at 170°C and fluorinated hydrocarbons are known to have significantly lower surface energy than their non-fluorinated counterparts (*66*). Additionally, the surface energy of copolymers containing pentafluorostyrene and methyl acrylate has been shown to vary smoothly as a function of composition over a large range (*75*). It was thus anticipated that mixtures of PS and PCF3S would also produce a wide range of accessible surface energies that could be controlled during polymer synthesis.

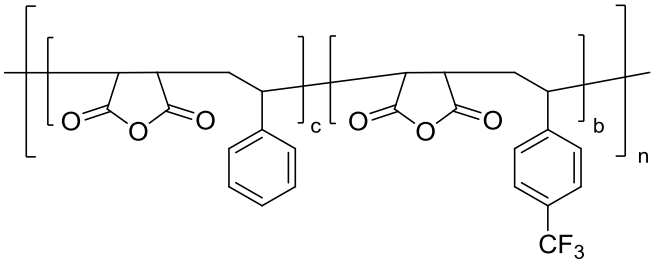

Figure 7.1: Second generation top coats poly[(maleic anhydride-*alt*-styrene)-*co*-(maleic anhydride-*alt*-4-trifluoromethylstyrene)] (TC-PMA-PS-PCF3S).

Surface energy can be quite difficult to accurately and precisely measure. However, Si-BCPs are an extremely sensitive (indirect) measurement probe since they will only orient morphological features perpendicular to the substrate when interfacial interactions are balanced at both the top and bottom interfaces. The goal of the present research is not to quantitatively measure surface energies but to orient Si-BCPs thermally. We thus eliminate the direct measurement of top coat surface energies and instead probe the effect of top coat composition on the orientation of a model Si-BCP, poly(styrene-*block*-trimethylsilylstyrene-*block*-styrene) (PS-*b*-PTMSS-*b*-PS). We expect that the interfacial neutralization principles established with PS-*b*-PTMSS-*b*-PS can be extended to high-χ BCP systems.

7.4 SYNTHESIS AND CHARACTERIZATION

Top coats were synthesized using AIBN initiator at 65°C in THF (**Scheme 7.1**). **Table 7.1** shows the synthetic results of five top coats obtained in moderate to good yield. In all cases, the feed composition is in excellent agreement with the polymer composition as calculated by combustion analysis. PMA contents were close to constant at ~50 mole%, with the relative ratio of PS to PCF3S well-controlled by the relative feed ratio. Size exclusion chromatography (**Figure 7.2**), differential scanning calorimetry (**Figure 7.3**), and thermal gravimetric analysis (**Figure 7.4**) data are summarized in **Table 7.2**. All samples have mono-modal distributions and exhibit excellent thermal stability (288-312°C). Surprisingly, all samples showed relatively high glass transition temperatures (T_g~190-200°C), in contrast to the literature reported value of 170°C for poly(maleic anhydride-*alt*-styrene) (*172*).

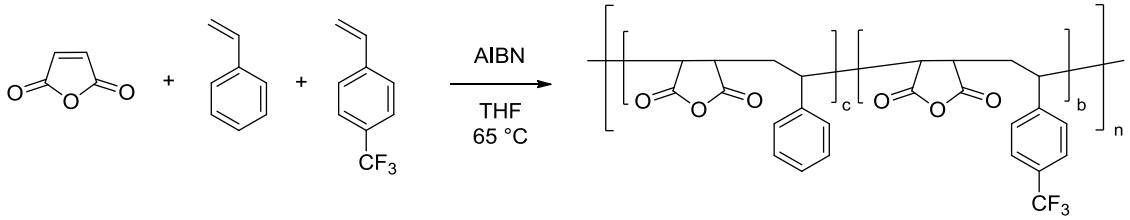

Scheme 7.1: Synthesis of TC-MA-PS-PCF3S top coats.

Table 7.1: Top coat synthesis results. Top coat names are formatted as TC- $PMA_{mol\%}$-$PS_{mol\%}$-$PCF3S_{mol\%}$.

		Feed Composition[b]			*Polymer Composition (Combustion)*[b]		
Top Coat	**Yield**[a]	**MA**	**S**	**CF3S**	**PMA**	**PS**	**PCF3S**
TC-50-43-7	79	0.50	0.43	0.07	0.50	0.43	0.07
TC-49-29-22	69	0.50	0.25	0.25	0.49	0.29	0.22
TC-46-19-35	84	0.50	0.17	0.33	0.46	0.19	0.35
TC-48-15-37	55	0.50	0.10	0.40	0.48	0.15	0.37
TC-46-1-53	49	0.50	0.03	0.47	0.46	0.01	0.53

[a] Calculated by mass% recovered.
[b] Compositions are listed as mole fractions.

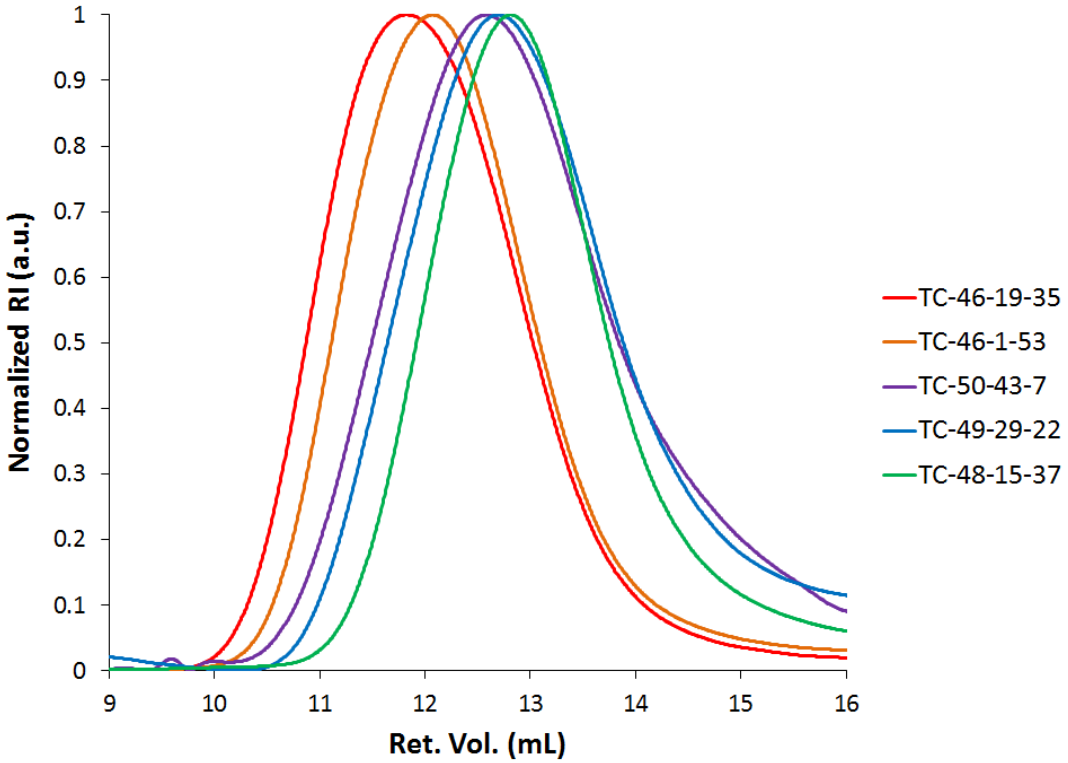

Figure 7.2: Size exclusion chromatography data collected with DMF as an eluent at 70°C. PMMA standards were used to calculate relative molecular weight data.

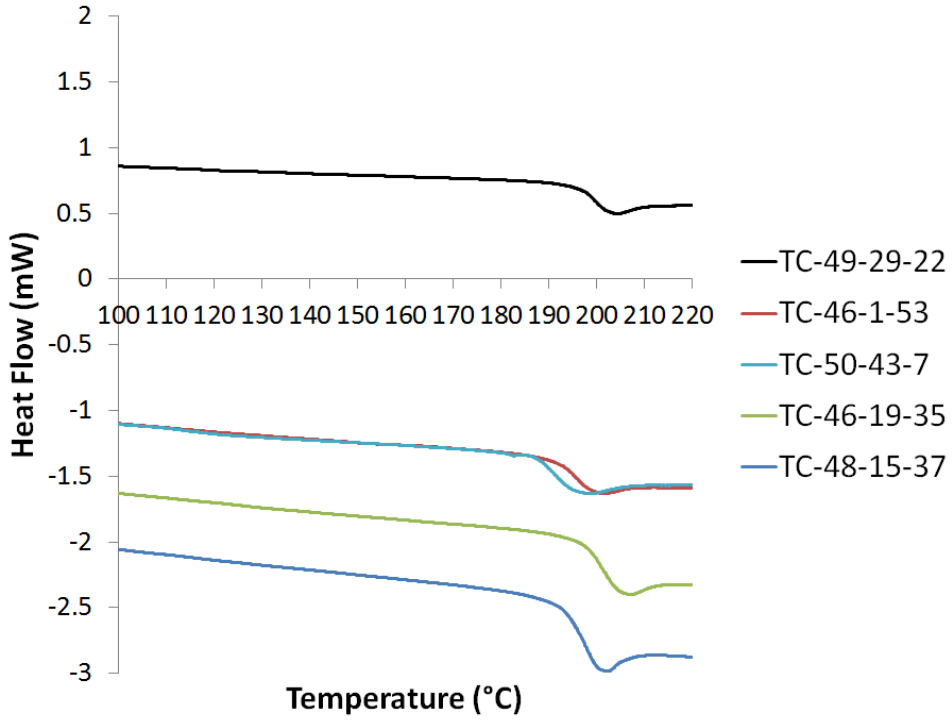

Figure 7.3: DSC data collected on the third heating cycle at 10°C/min. All T_gs are well above the literature reported values for PS-*b*-PTMSS-*b*-PS (PTMSS block=131°C, PS block=106°C).

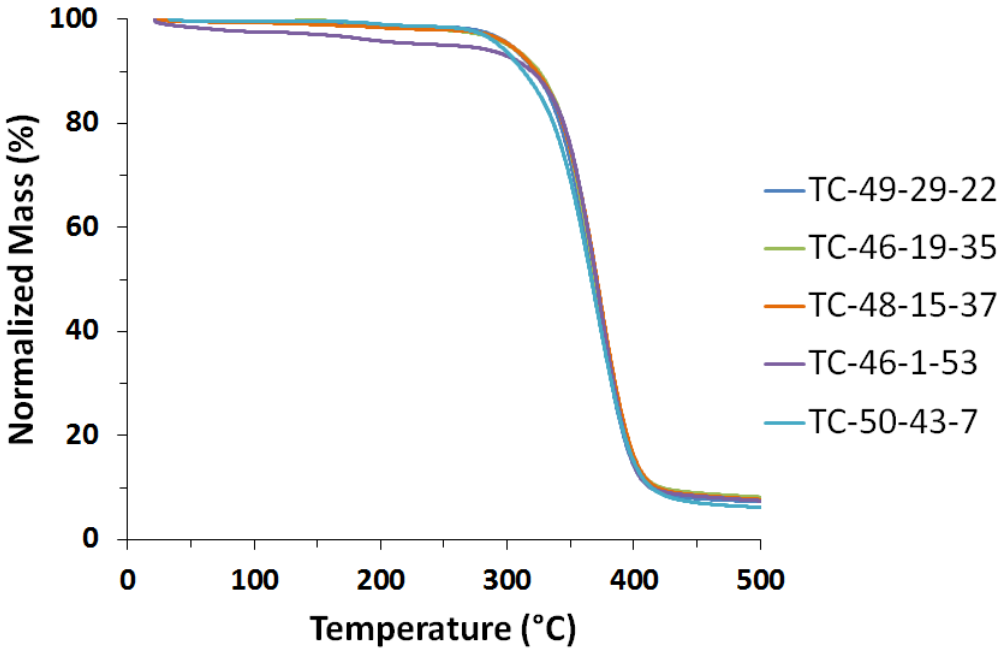

Figure 7.4: TGA data collected on heating at 10°C/min under an N_2 purge.

Table 7.2: Compiled size exclusion chromatography, differential scanning calorimetry, and thermal gravimetric analysis data.

Top Coat	M_n [a]	M_w [a]	Đ [b]	T_g	T_d
TC-50-43-7	15,350	44,900	2.93	190	288
TC-49-29-22	15,060	40,230	2.67	199	307
TC-46-19-35	38,540	85,280	2.21	200	303
TC-48-15-37	14,090	33,540	2.38	198	298
TC-46-1-53	31,290	71,480	2.28	196	312

[a] Calculated relative to PMMA standards with DMF as an eluent at 70°C, in units of g/mol.
[b] Molecular mass dispersity, M_w/M_n.

7.5 Substrate Surface Treatments

Composition-controlled top coats were evaluated in combination with PtBuS-*r*-PMMA-*r*-PVBzAz (**Figure 7.5**) cross-linkable surface treatments (XSTs) that were synthesized in Chapter 3. We were sufficiently inspired to use these XSTs for three

reasons. A recent paper by Kennemur et al. (*54*) reports the minimum lamellae full pitch of poly(4-*tert*-butylstyrene-*block*-methyl methacrylate) to be 14 nm, which suggests a large difference in surface energy between the two blocks. The lack of silicon in the XST potentially facilitates pattern transfer contingent upon successful orientation control. Analogous surfaces composed of the constituents of the block copolymer (PS and PTMSS) that would have a large range of accessible surface energies could introduce undesired difficulties in the etching process. The XSTs are also readily accessible using a combination of conventional free radical polymerization and post-polymerization functionalization to install cross-linkable azide groups (*92*). XSTs are referred to by the mole% PtBuS content as calculated by combustion analysis. Four XSTs (XST-68, XST-46, XST-34, and XST-21) with PtBuS contents 68, 46, 32, and 21 mole% PtBuS are utilized herein.

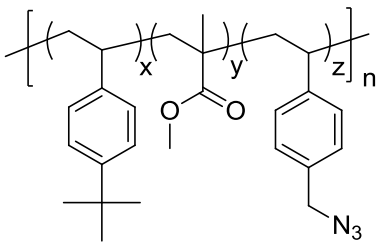

Figure 7.5: Poly(4-*tert*-butylstyrene-*r*-methyl methacrylate-*r*-4-vinylbenzyl azide) crosslinkable substrate surface treatments. Synthetic details are reported in Chapter 3.

7.6 Evaluation of Substrate Surface Neutrality

An extremely valuable analytical technique exists that can elucidate the wetting preferences of a block copolymer with the surface it is coated on (*81, 180*). The technique relies on the quantization of BCP film thickness to integer ($n*L_0$, symmetric wetting) or half-integer ($(n+0.5)*L_0$, asymmetric wetting) multiples of the natural periodicity (L_0) (see Chapter 6 for an in-depth quantization explanation). The experiment is detailed pictorially in **Figure 7.6**. A BCP is first spin coated at a non-commensurate

film thickness to both symmetric and asymmetric wetting conditions. As drawn, the as-cast film is $1.2*L_0$ in thickness, which will satisfy neither symmetric ($n*L_0$) nor asymmetric ($(n+0.5)*L_0$) wetting conditions. Importantly, the silicon block (pictured as red) will always wet the top interface because of its significantly lower surface energy. The formation of islands or holes will thus only depend upon the nature of the interactions of the BCP with the substrate surface. If the silicon-containing block also wets the substrate, symmetric wetting is achieved (pictured on the right side of **Figure 7.6**). The bulk of the film will adopt a $1*L_0$ thickness (instead of the as-cast $1.2*L_0$) and the excess material will form islands of $2*L_0$. At total film thicknesses ~50 nm, the islands appear as dark spots under an optical microscope. If the non-silicon-containing block (pictured as blue) wets the substrate, asymmetric wetting is achieved (pictured on the left side of **Figure 7.6**). The bulk of the film will adopt a $1.5*L_0$ thickness (instead of the as-cast $1.2*L_0$), but there is not enough material to fully cover the surface and thus holes form at $0.5*L_0$. At total film thicknesses ~50 nm, the holes appear as light spots under an optical microscope. A series of well-designed XSTs at various compositions should show a transition from islands to holes (at constant as-cast film thickness). The intermediate composition which exhibits neither islands nor holes is theoretically neutral towards the BCP.

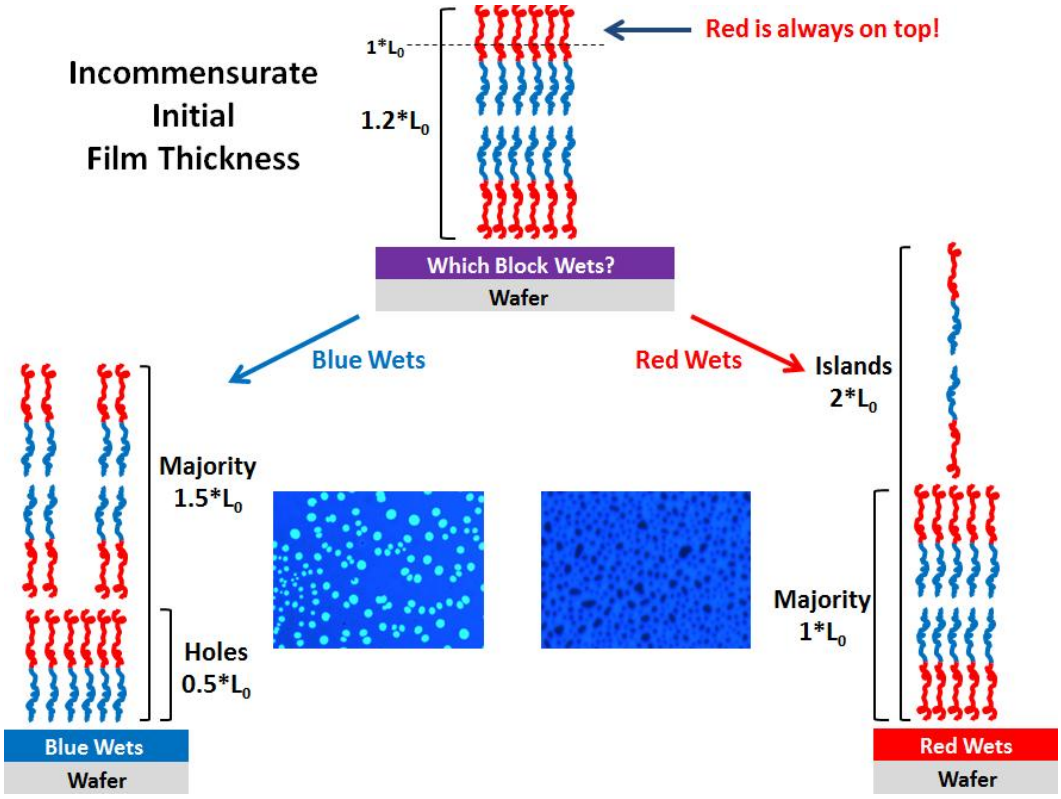

Figure 7.6: The island and hole test can be used to determine the wetting preferences of a BCP towards a given substrate surface.

The island and hole test was used to evaluate the neutrality of the PtBuS-*r*-PMMA-*r*-PVBzAz XSTs towards PS-*b*-PTMSS-*b*-PS. If the XST design works properly, the PtBuS extreme will wet the silicon-containing block and the PMMA extreme will wet the PS block. Some intermediate composition should then be a neutral surface towards the BCP. **Figure 7.7** shows the results of the island and hole tests performed with an initial as-cast BCP film thickness of approximately 1.2*L_0 (~36 nm) subsequently annealed for 30 min at 190°C. Both optical microscopy (green-colored images) and atomic force microscopy (orange-colored images) were used to unambiguously determine the formation of islands or holes on the samples. The optical microscope and AFM images have opposite color contrast. Percentages listed are the mole% of PtBuS in the XST as calculated from combustion analysis. At 21% and 34%

PtBuS, holes (bright spots in the optical image, dark spots in the AFM image) are observed with a $1*L_0$ depth, consistent with the expected "classic" film thickness quantization. The PS block preferentially wets these two substrate surface treatments. The XST with 68% PtBuS produces islands (black spots in the optical image, light spots in the AFM image) with a $1*L_0$ height, again consistent with the expected film thickness quantization. The PTMSS block wets the XST-68 surface. A surface between 34-68% PtBuS should be neutral towards PS-*b*-PTMSS-*b*-PS. The 46% PtBuS XST shows a markedly different type of macroscopic BCP pattern than any of the other tested XST compositions. The contrast observed with the optical microscope is consistent with the formation of holes, but the length scale is significantly smaller than the hole patterns observed on XST-21 and XST-34. AFM height profile measurements verify that the features are holes, but the depth of the holes quantizes to $0.5*L_0$. To the best of our knowledge, half integer film thickness quantization has not been previously reported. We believe that the "half hole" structures arise due to the presence of a single neutral interface (here, the substrate) and a single strongly preferential interface (here, the air). Further studies seeking to clarify these observations are currently underway in collaboration with Professor Frank Bates at the University of Minnesota and will be reported at a later date. Tentatively, we classify the 46% PtBuS surface as neutral or very near neutral towards PS-*b*-PTMSS-*b*-PS.

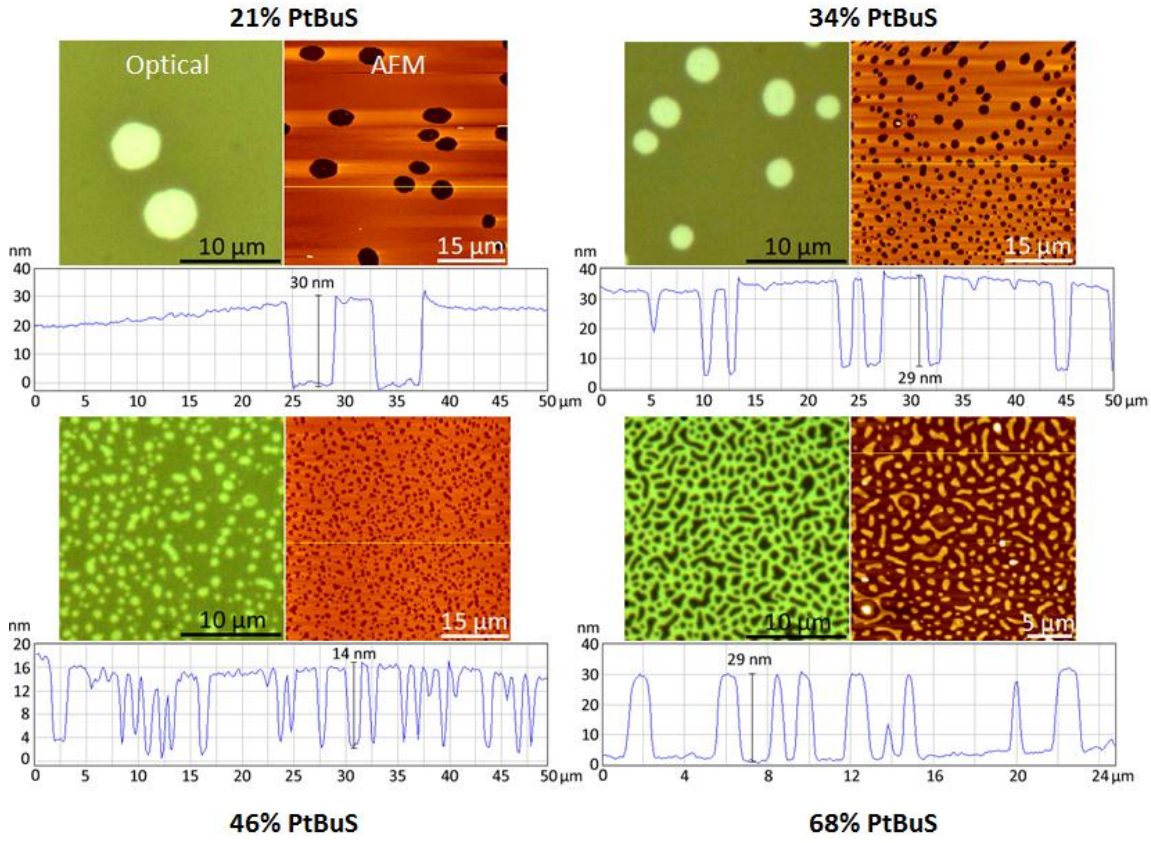

Figure 7.7: Island and hole tests with PS-*b*-PTMSS-*b*-PS on a series of PtBuS-*r*-PMMA-*r*-PVBzAz XSTs with different compositions.

At present there exists no method to probe the wetting preferences of the BCP towards the series of top coats TC-PMA-PS-PCF3. The initial experimental design to probe the effect of top coat composition utilizes four XSTs (68%, 46%, 34%, and 21%) that span the range of wetting conditions (PTMSS wetting, "neutral", and PS wetting) at various deviations from apparent neutrality. The effect of both BCP film thickness (in periodicity regimes 1, 1.5, 1.67, and 2*L_0) and top coat composition (five top coats, TC-46-1-53, TC-48-15-37, TC-46-19-35, TC-49-29-22, TC-50-43-7) were studied with each XST. A total of 80 samples were prepared, annealed concurrently at 190°C for 11 min on a hot plate, etched for 30 sec using O_2 RIE, and imaged with SEM. The results are

shown in **Figures 7.8-7.11**. Each small SEM image is meant to capture a representative region of the surface. In general, the type of pattern shown was similar over the entire sample.

7.7 THIN FILM STUDIES

The results from the top coat studies are striking. Perpendicular BCP orientation is a function of top coat composition, XST composition, and BCP film thickness. Top coat composition has a clear effect on BCP thin film orientation. Top coat TC-50-43-7 with just 7 mole% PCF3S shows no indication of perpendicular PS-*b*-PTMSS-*b*-PS lamellae on all XST surfaces, XST-68, XST-46, XST-34, and XST-21. The top coat composition is apparently not neutral. Top coat TC-49-29-22 with 22 mole% PCF3S shows some indication of perpendicular lamellae that generally occur in larger areas with the thinnest BCP film thicknesses. The $1*L_0$ BCP film on XST-68, XST-46, and XST-34 shows relatively large regions of perpendicular lamellae, while most other BCP thicknesses exhibit no surface features.

The most interesting results occur with TC-46-19-35, TC-48-15-37, and TC-46-1-53 with 35, 37, and 53 mol% PCF3S, respectively. On the "neutral" XST-46 (**Figure 7.8**), all BCP film thicknesses (1, 1.5, 1.67, and $2*L_0$) form excellent perpendicular lamellae over the entire surface of the film. In the absence of island and hole tests with the top coat materials, we cannot definitively say that one of the top coat compositions is indeed truly neutral. However, the formation of perpendicular lamellae with virtually any BCP film thickness indicates the top coat materials must be very near neutral. Theoretically the presence of neutral top and bottom interfaces energetically favors the perpendicular orientation of BCP features at all BCP film thicknesses (*149*). In contrast, even small interfacial energy deviations from neutrality (~0.5 mN/m) at the top interface (with a neutral substrate interface) will result in parallel lamellae at all BCP film thicknesses. In general, thick BCP films are more difficult to orient than thin films in the presence of slightly preferential interfaces. Perpendicular orientation of thick films of PS-*b*-PMMA has been achieved in the presence of a neutral substrate surface treatment

and surface-directing pre-patterns (*76*). PS-*b*-PMMA does not require a top coat because the PS and PMMA block interactions with the top interface can be equated at ~210°C (*158*). However, most BCPs (and all Si-BCPs) exhibit preferential interactions with the top interface at all experimentally-accessible temperatures. Such BCPs that exhibit preferential top interfacial interactions require top coats or alternative annealing techniques to orient perpendicular at the top interface.

As the substrate interface composition deviates from the neutral 46 mole% PtBuS composition (XST-46), the number of BCP film thicknesses that produce well-formed perpendicular lamellae is significantly reduced. On XST-68 (PTMSS wetting and compositionally far from neutral), well-formed perpendicular lamellae are only observed with top coats TC-48-15-37 and TC-46-19-35 at $1*L_0$ BCP thickness (**Figure 7.9**). All other BCP film thicknesses exhibit varying degrees of patchy perpendicular lamellae or no features. On XST-34, which is PS wetting but compositionally closer to neutral, top coats TC-46-19-35, TC-48-15-37, and TC-46-1-53 produce well-formed perpendicular lamellae at all BCP film thicknesses except $1.5*L_0$ with TC-46-1-53, which is slightly patchy (**Figure 7.10**). The process window is slightly smaller than the neutral XST-46 condition. All BCP films on XST-21 (PS wetting and compositionally far from neutral) show poor perpendicular orientation (**Figure 7.11**). Some unusual frustrated morphologies are observed that apparently arise from non-neutral interfacial conditions.

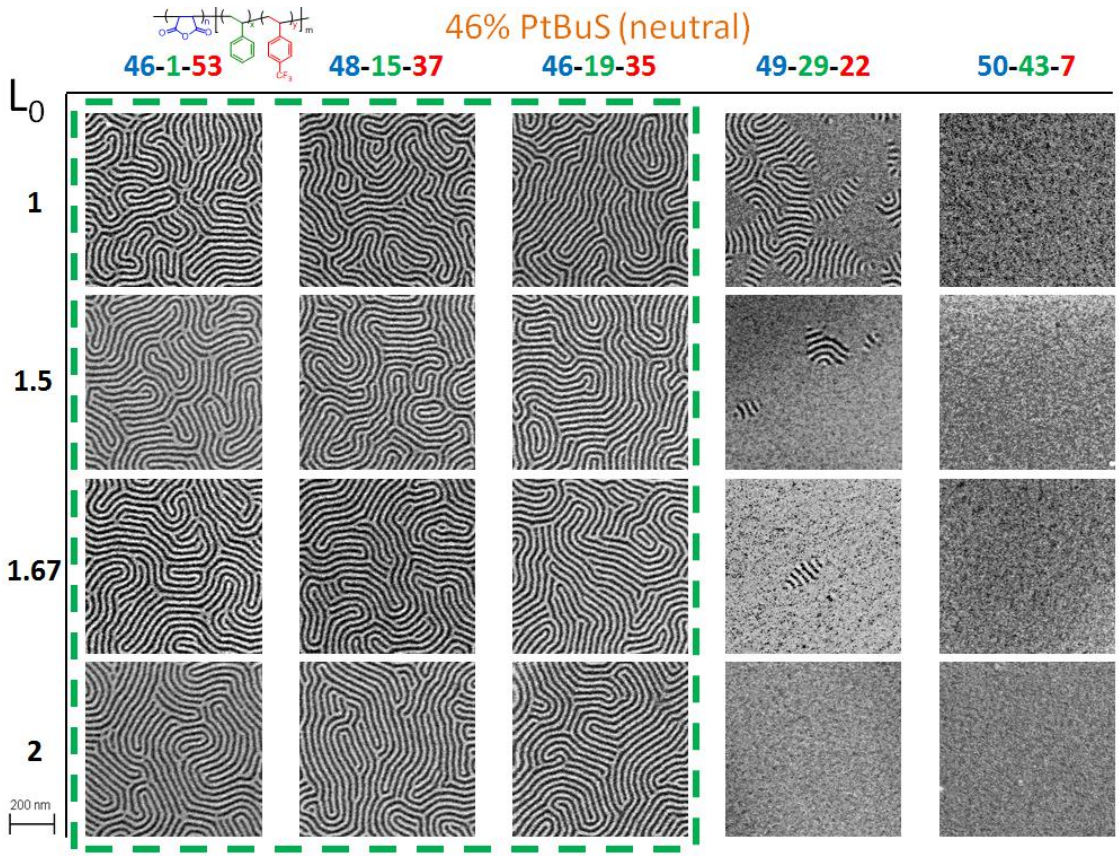

Figure 7.8: Effect of varying top coat composition and BCP thickness on the neutral substrate surface treatment with composition PtBuS:PMMA:PVBzAz=46:48:6 mol%. The green dashed box denotes well-formed perpendicular lamellae. L_0=30 nm.

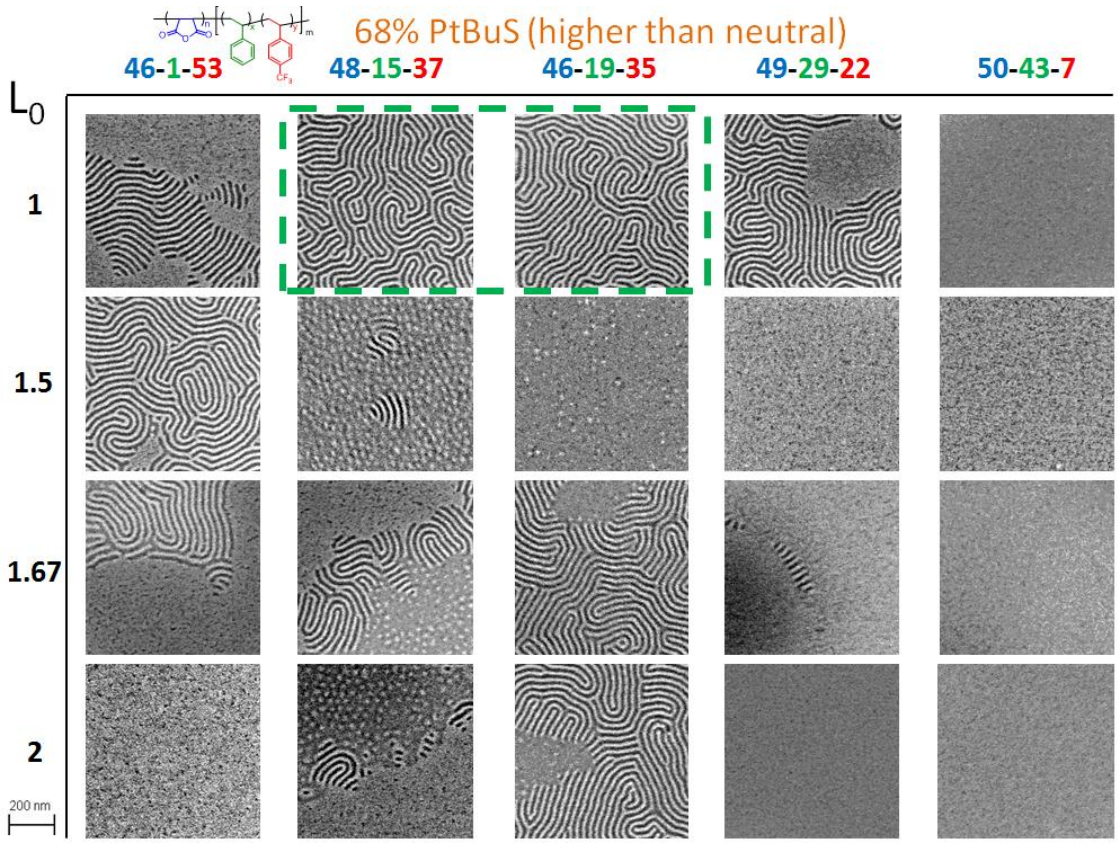

Figure 7.9: Effect of varying top coat composition and BCP thickness on the XST with composition PtBuS:PMMA:PVBzAz=68:25:7 mol%. The green dashed box denotes well-formed perpendicular lamellae. L_0=30 nm.

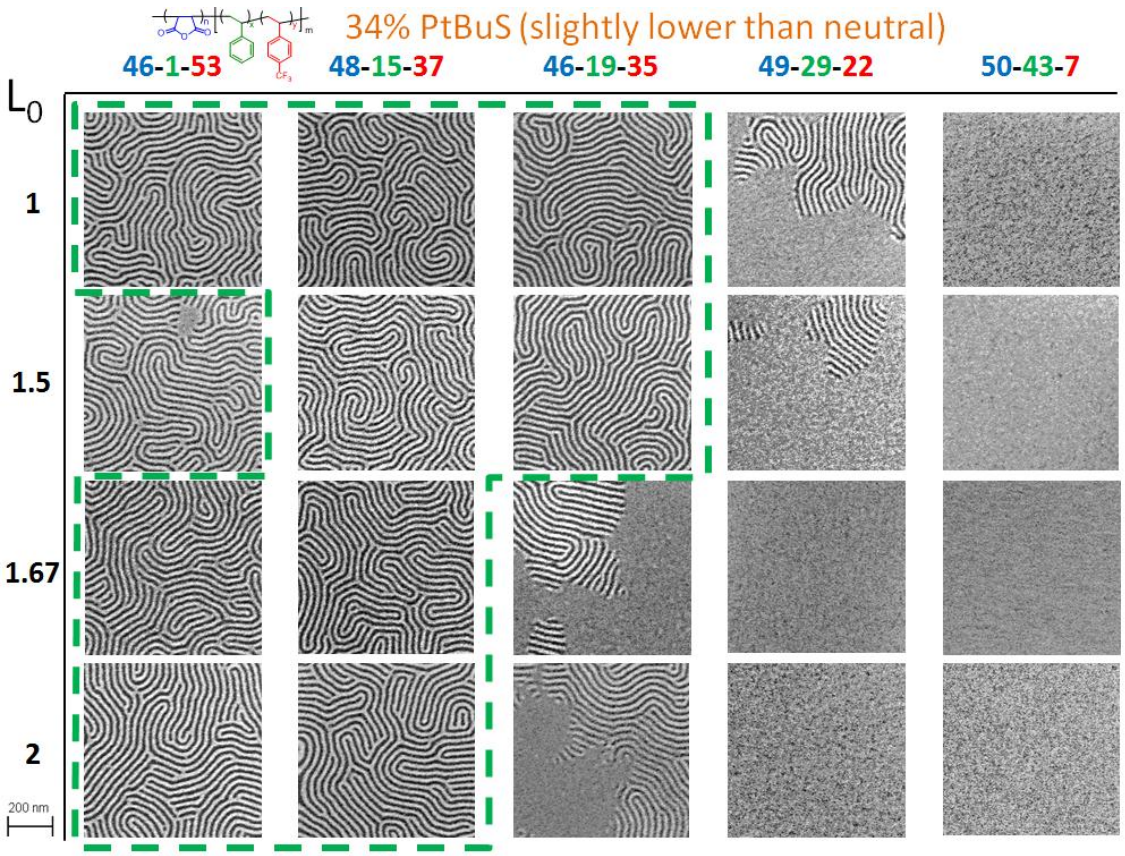

Figure 7.10: Effect of varying top coat composition and BCP thickness on the substrate surface treatment with composition PtBuS:PMMA:PVBzAz=34:59:7 mol%. The green dashed box denotes well-formed perpendicular lamellae. L_0=30 nm.

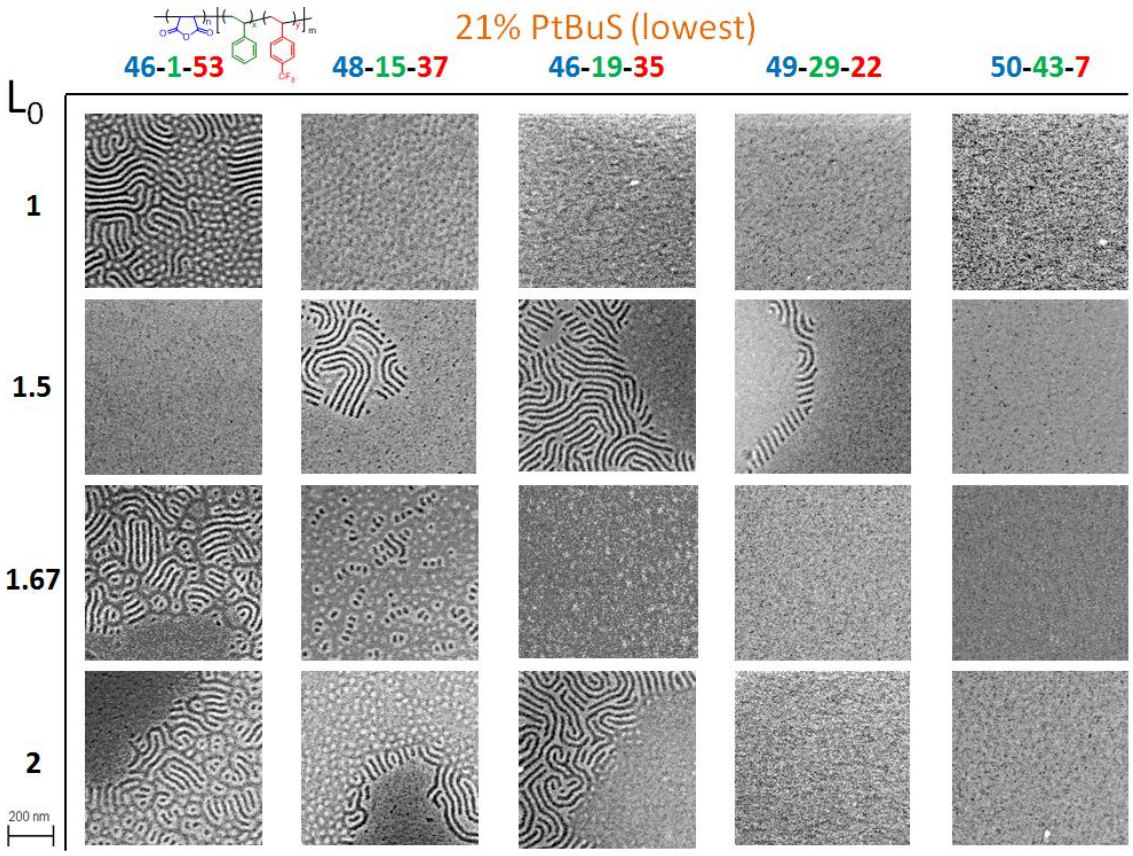

Figure 7.11: Effect of varying top coat composition and BCP thickness on the substrate surface treatment with composition PtBuS:PMMA:PVBzAz=21:71:8 mol%. No conditions produce well-formed perpendicular lamellae. L_0=30 nm.

7.8 Studies with Neutral Substrate and Top Coat

We tentatively believe that top coat TC-48-15-37 is relatively close to neutral for PS-*b*-PTMSS-*b*-PS since it exhibits the largest BCP thickness process window on the collection of tested XSTs. A BCP film thickness study was performed utilizing the "neutral" XST-46 in combination with TC-48-15-37 (**Figure 7.12**). Well-formed perpendicular lamellae are observed at 1, 1.5, 1.7, 2, 2.8, and 3.2*L_0. The 3.2*L_0 film has very slight defectivity not observed in the thinner films. A yet thicker 3.7*L_0 film (**Figure 7.13**) still shows perpendicular lamellae but exhibits markedly increased

defectivity compared to the thinner BCP films. Small deviations from true interfacial neutrality at both top and bottom interfaces makes orientation of films this thick challenging. We believe that further fine-tuning of both the top coat and XST compositions would likely eliminate the surface defectivity observed in the thickest films. Nevertheless, the simultaneous control of both top coat and substrate surface compositions has enabled the orientation of a wide range of BCP film thicknesses. The interfacial energetics must be very near neutral.

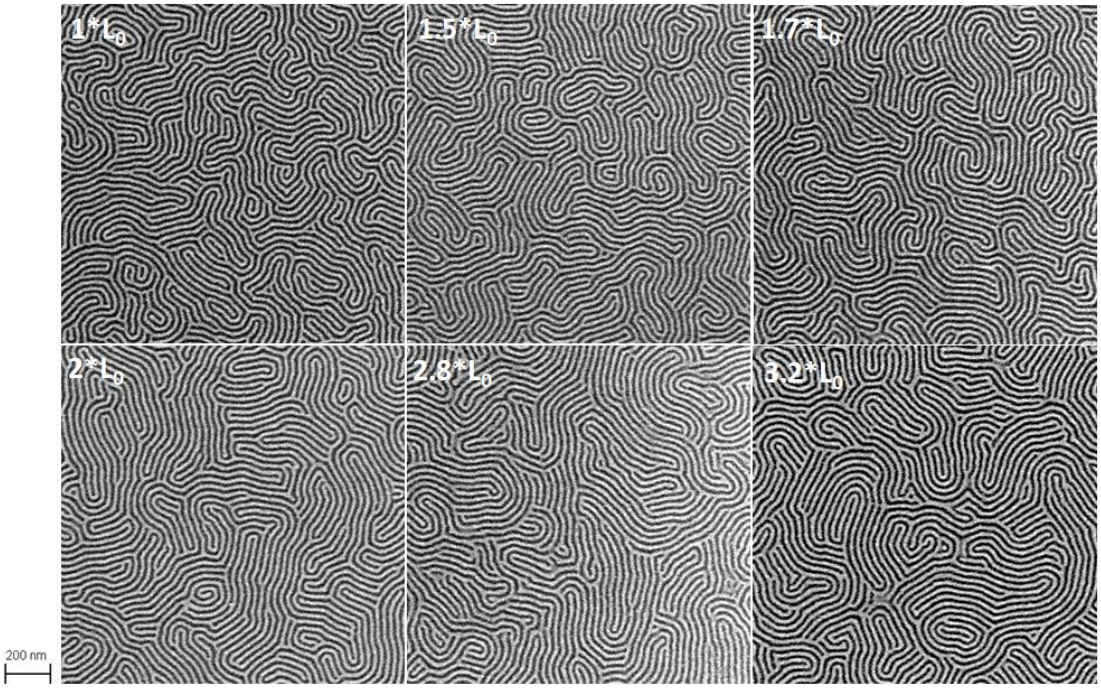

Figure 7.12: The effect of PS-*b*-PTMSS-*b*-PS film thickness when annealed in the presence of two neutral interfaces, substrate surface XST-46 (46% PtBuS) and top coat TC-48-15-37. Samples were annealed at 190°C for 11 min and O_2 etched for 30 sec.

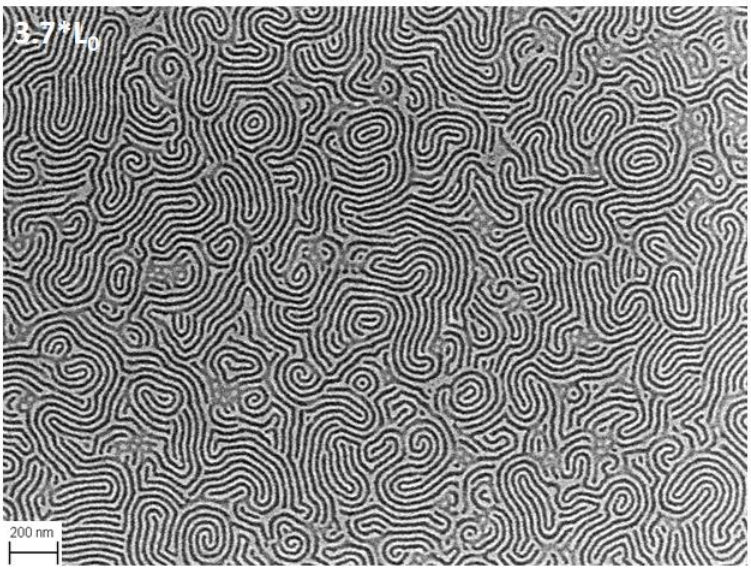

Figure 7.13: A 3.7*L_0 film (111 nm) annealed at 190°C for 11 min in the presence of substrate surface XST-46 and top coat TC-48-15-37 exhibits mostly perpendicular orientation with some defectivity not observed in thinner films. The sample was O_2 etched for 30 sec.

The 3.2*L_0 film shown in **Figure 7.12** was generously cross-section SEM imaged by Hiroshi Yoshida of the Hitachi Research Laboratory. The process pioneered by his group and recently described in the literature (*181*) utilizes argon milling in combination with polishing and O_2 RIE. The cross-section images (**Figures 7.14** and **7.15**) demonstrate the efficacy of the top coat process. A significant fraction of the perpendicular lamellae penetrate the entire thickness of the film. Some bifurcation is observed and is not surprising given the non-directed nature of the self-assembly process. Theoretical insights from the de Pablo and Nealey groups reveal a large thermodynamic driving force for the elimination of defects in the presence of surface-directing pre-patterns (*182*), predictions that are remarkably consistent with experiments. Welander et

al. have observed the elimination of PS-*b*-PMMA lamellae defects in 1 to 30 minutes when self-assembly occurs on surface chemically nano-patterned surfaces (*168*). Bencher et al. have also demonstrated extraordinarily low levels of defectivity with a PS-*b*-PMMA DSA process (*183*). We thus anticipate that the slight bifurcation observed with the top coat system will be fully eliminated when utilized in combination with directed self-assembly. Importantly, there is no wetting layer at the top interface. The top coat efficiently induces the orientation of perpendicular lamellae and is close enough to neutral to prevent the formation of a silicon-containing wetting layer.

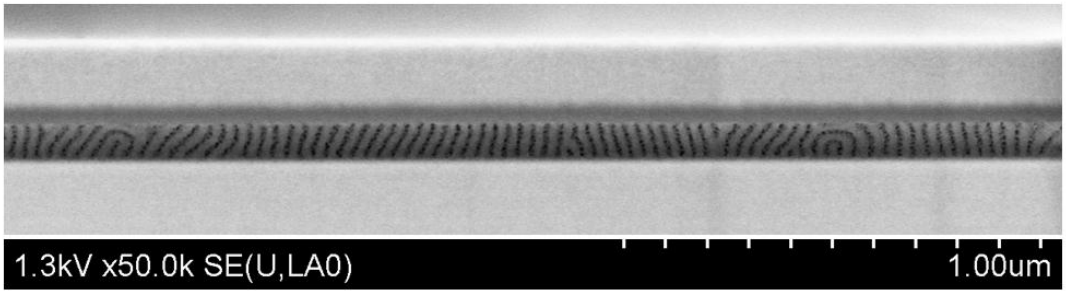

Figure 7.14: Cross-section image of 3.2*L_0 (96 nm) PS-*b*-PTMSS-*b*-PS annealed at 190°C for 11 min between XST-46 and TC-48-15-37.

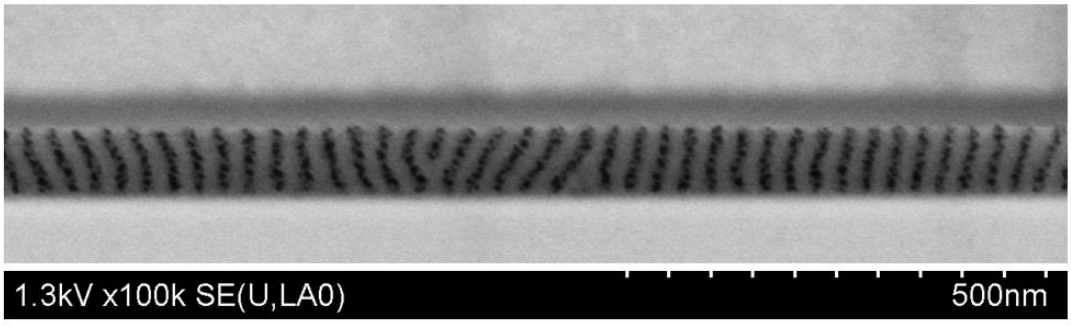

Figure 7.15: Cross-section image of 3.2*L_0 (96 nm) PS-*b*-PTMSS-*b*-PS annealed at 190°C for 11 min between XST-46 and TC-48-15-37.

7.9 Effect of Annealing Time

The effect of annealing time at constant temperature (190°C) with various BCP film thicknesses (1, 1.5, 1.67, 2*L_0) was studied using the near-neutral combination of XST-46 and TC-48-15-37 (**Figure 7.17**). After 10 sec, perpendicular lamellae are apparent at all film thicknesses but are characterized by short line patterns that are not fully formed. After 30 sec, well-formed perpendicular lamellae are observed over the entire surface of the 1, 1.5, and 1.67*L_0 films. The pattern produced from the thickest 2*L_0 film is significantly improved from 10 sec but still exhibits minor defectivity. All four film thicknesses generate well-formed perpendicular lamellae after 60 sec. Annealing times ~30-60 sec at 190°C rival the fastest thin film self-assembly processes reported to date, which are on the order of 60 sec for PS-*b*-PTMSS-*b*-PS at 210°C (*149*) and PS-*b*-PMMA at 250°C (*168*).

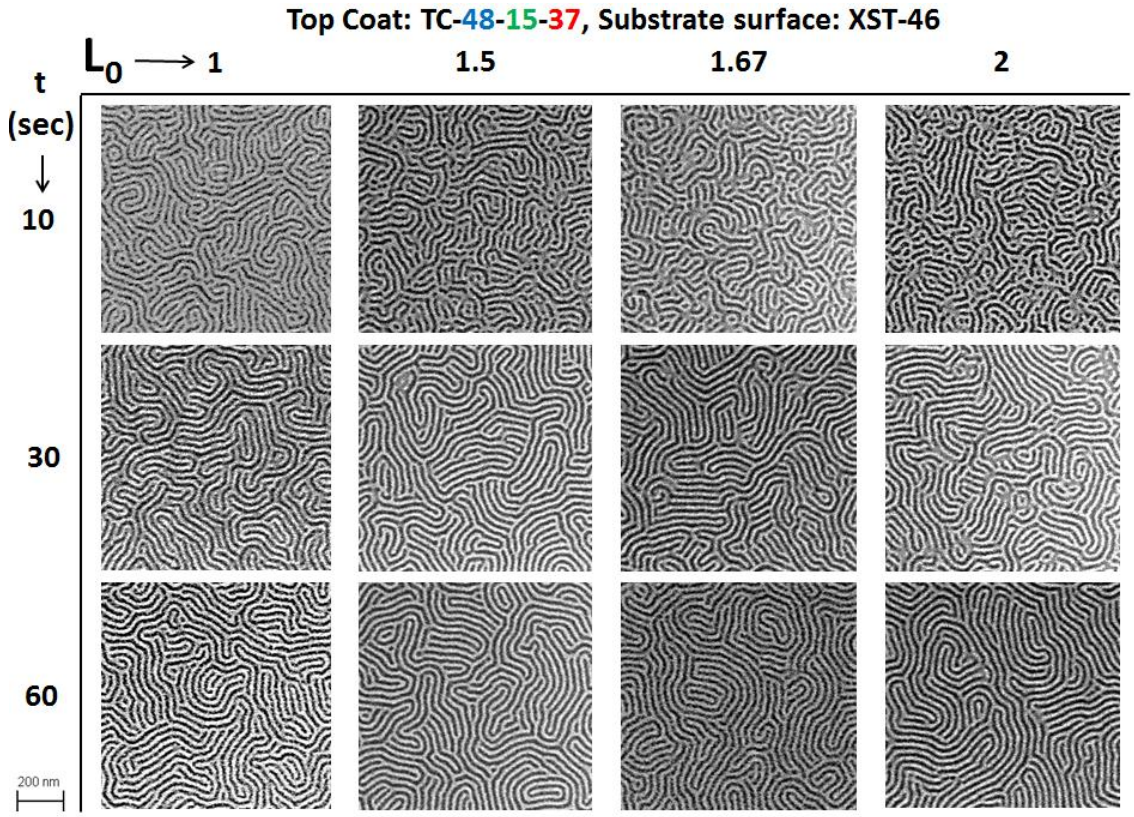

Figure 7.16: The effect of PS-*b*-PTMSS-*b*-PS film thickness and annealing time at 190°C with neutral interfacial conditions XST-46 and top coat TC-48-15-37.

7.10 EXPERIMENTAL:

Chemicals:

Azoisobutyronitrile (Sigma Aldrich) was recrystallized from methanol. Maleic anhydride (Sigma Aldrich) and tetrahydrofuran (Fischer Scientific, uninhibited) were used as received. Styrene (Sigma Aldrich), 4-*tert*-butylstyrene (Sigma Aldrich), methyl methacrylate (Sigma Aldrich) and 4-trifluoromethylstyrene (generously provided by Synquest) were stirred with basic alumina for 30 minutes to remove inhibitor and filtered.

General top coat synthetic procedure

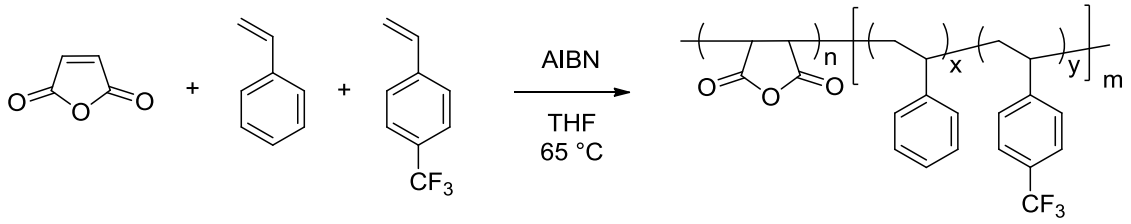

Scheme S1: Synthesis of top coats.

A round bottom flask fitted with a reflux condenser was charged with a stir bar, maleic anhydride (0.50 eq, 1.00 g, 10.2 mmol), styrene (0.25 eq, 0.531 g, 5.1 mmol), and 4-trifluoromethylstyrene (0.25 eq, 0.878 g, 5.1 mmol), azoisobutyronitrile (0.005 eq, 16.7 mg, 0.102 mmol), and tetrahydrofuran (10 mL). Feed ratios were varied as described in **Table 7.1**. The reaction mixture was degassed for 15 min with dry N_2 and heated at 65°C for 24 h. The reaction was quenched at 0°C and precipitated into a 3:1 (by vol) mixture of hexanes:DCM. The polymer was isolated by vacuum filtration, redissolved in THF and reprecipitated two more times into 3:1 (by vol) mixture of hexanes:DCM. The white powder was dried *in vacuo* and analyzed by SEC, DSC, and TGA (**Tables 7.1** and **7.2**, **Figures 7.2-7.4**).

Instrumentation:

Size exclusion chromatography (SEC) data for the top coats were collected on an Agilent 1200 Series Isopump and Autosampler with an Agilent Technologies 1100 RI detector. One PLgel 5 µm, 100 Å column and one PLgel 5 µm, 10000 Å column were used with DMF as an eluent at 70°C and a flow rate of 1 mL/min. The refractive index response of the top coats was compared to nine PMMA standards (1660, 2200, 4250, 6370, 12600, 23500, 41400, 89300, and 201000 Da), which were used to calibrate the instrument by refractive index response (conventional calibration). Substrate surface treatment SEC data were collected with an Agilent 1100 Series isopump and autosampler with a Viscotek Model 302 TETRA detector platform. Three I-series mixed bed high-

MW columns were calibrated relative to PS standards. A Brewer CEE 100CB Spincoater was used to cast all thin films. Ellipsometry was performed with a J.A. Woollam Co, Inc. VB 400 VASE Ellipsometer with wavelengths from 382 to 984 nm and a 65° angle of incidence. A Zeiss Supra 40 VP scanning electron microscope operating at 3 kV with the in-lens detector and a working distance of 3.5 mm was used to collect all SEM data. Brightness and contrast for all SEMs were uniformly enhanced using commercial image editing software.

Thin Film Preparation:

A 0.5 wt% solution of XST in toluene was filtered with a 0.2 micron Chromafil® filter and spin coated at 3000 rpm for 30 sec to yield a smooth film ca. 15 nm. The film was heated at 250°C on a hotplate for 5 minutes to crosslink the azide functionality and subsequently rinsed with toluene 3 times at 3000 rpm to remove uncrosslinked chains. The final film thickness after rinsing was ca. 14 nm as measured by ellipsometry. Various concentration solutions (1-2.5 wt%) of PS-*b*-PTMSS-*b*-PS in toluene were filtered with a 0.2 micron Chromafil® filter and cast onto the XST film at various spin speeds to produce relatively smooth films with thicknesses ~30-11 nm (1-3.7*L_0). A 1 wt% solution of a top coat was then spin-coated onto the BCP film at 3000 rpm. All top coats were applied from a 3:1 (by mass) MeOH:aq. 30 wt% NH_4OH solution, except TC-50-43-7; because it was insoluble in 3:1 solution, it was cast only from 1:3 (by mass) MeOH:aq. 30 wt% NH_4OH. Methanol was added to the casting solutions to produce more uniform films. 3:1 and 1:3 MeOH:aq. 30 wt% NH_4OH solutions were found to cause no change in PS-*b*-PTMSS-*b*-PS film thickness as measured by ellipsometry. Samples were annealed on a Thermolyne HP-11515B hot plate at 190°C for various times. They were quickly removed and cooled to room temperature on a solid metal block. The top coat was stripped with the same casting solvent used to apply the top coat (i.e. 3:1 MeOH:aq. 30 wt% NH_4OH solution for all top coats except TC-50-43-7, which was stripped with 1:3 MeOH:aq. 30 wt% NH_4OH). Stripped samples contained little (<=5 nm) residual top coat layer.

Reactive Ion Etching:

Etching was performed on an Oxford Plasmalab 80+ in inductively coupled plasma mode with the following formula: pressure=20 mTorr, RF power=10 W, ICP power=80 W, Ar flow rate=75 sccm, O_2 flow rate=75 sccm. These settings have previously been established as effective for the selective removal of the organic PS block without causing significant damage to the PTMSS block (*149*).

Combustion Analysis:

Combustion analysis was performed by Midwest Microlab, LLC.

7.11 CONCLUSIONS

Top coats composed of poly[(maleic anhydride-*alt*-styrene)-*co*-(maleic anhydride-*alt*-4-trifluoromethylstyrene)] are introduced that provide synthetic access to a range of polystyrene:poly(4-trifluoromethylstyrene) compositions with T_gs ~ 190-200°C. Additionally, a new class of non-silicon-containing substrate surface treatments, poly(4-*tert*-butylstyrene-*random*-methyl methacrylate-*random*-4-vinylbenzyl azide) are described that apparently provide access to a wide range of interfacial energies. The combination of these top coats and substrate surface treatments enables independent tuning of the characteristics of both the top and bottom interface of BCP thin films. A neutral or near-neutral condition was established for PS-*b*-PTMSS-*b*-PS that decouples BCP thin film thickness from lamellae thin film orientation. BCP film thicknesses ranging from 1-3.2*L_0 produced well-formed perpendicular lamellae, many of which penetrate the entire thickness of the film. We believe that independent control of top coat and substrate surface compositions is a general process that will enable the orientation of a plethora of BCPs. Increased BCP design flexibility afforded by relaxed thin film limitations could usher in a new era of BCP materials relevant to a wide swath of applications that demand controlled interfacial interactions.

7.12 ACKNOWLEDGEMENTS:

Graduate students Michael J. Maher, William J. Durand, and Gregory Blachut contributed to the development of the second generation top coats. Undergraduates Anthony Thio, Leon M. Dean, and Litan Li also helped synthesize top coats and analyze their thin film properties.

GLOSSARY:

AFM: Atomic force microscopy

Ar: Argon

BCP: Block copolymer

BPM: Bit patterned media

CMM: Conventional multigrain media

DMF: Dimethylformamide

HSQ: Hydrogen silsesquioxane

PMMA: Poly(methylmethacrylate)

PMTMSMA: Poly(methyltrimethylsilylmethacrylate)

PDMS: Poly(dimethylsiloxane)

PS: Polystyrene

PS-*b*-PI: Poly(styrene-*block*-isoprene)

PS-*b*-PMTMSMA: Poly(styrene-*block*-methyltrimethylsilylmethacrylate)

PS-*b*-PTMSS-b-PS: Poly(styrene-*block*-trimethylsilylstyrene-*block*-styrene)

PTMSS-b-PLA: Poly(4-trimethylsilylstyrene-*block*-D,L-lactide)

PVBzAz: Poly(vinylbenzyl azide)

PVBzCl: Poly(vinylbenzyl chloride)

RIE: Reactive Ion Etching

SEC: Size exclusion chromatography

SEM: Scanning electron microscopy

Si: Silicon

Si-BCP: Silicon-containing block copolymer

THF: Tetrahydrofuran

XST: Cross-linkable substrate surface treatment

REFERENCES:

1. E. W. Pugh, *RAMAC in Historical Perspective*. (2005).
2. Bitman. (Wikipedia, 2009), vol. 2013.
3. E. D. Daniel, C. D. Mee, M. H. Clark, *Magnetic Recording: The First 100 Years*. (IEEE Press, New York, NY, 1999).
4. U. S. A. R. R. Arsenal. (Wikipedia, ca. 1956).
5. N. A. Spaldin, *Magnetic Materials*. (Cambridge University Press, 2010).
6. Wikimedia. (2009).
7. Z. Ye *et al.*, *Proc. SPIE* **8323**, 1 (2012).
8. H.G.S.T. (2011).
9. S. Y. Chou, *Proc. IEEE* **85**, 652 (1997).
10. S. X. Wang, A. Taratorin, M., *Magnetic Information Storage Technology*. (Academic Press, San Diego, CA, 1999).
11. C. Ross, *Annual Review of Materials Research* **31**, 203 (2001).
12. F. Hossein-Babaei, A. L. Koh, K. Srinivasan, G. A. Bertero, R. Sinclair, *Nano Letters*, (2012).
13. R. Sbiaa, S. N. Piramanayagam, *Recent Pat. Nanotechnol.* **1**, 29 (2007).
14. D. Weller, A. Moser, *IEEE Trans. Magn.* **35**, 4423 (1999).
15. T. Vandeweyer *et al.*, *Proc. SPIE* **7521**, 752102/1 (2010).
16. M. Colburn *et al.*, *Proc. SPIE-Int. Soc. Opt. Eng.* **3997**, 453 (2000).
17. F. Hua *et al.*, *Nano Letters* **4**, 2467 (2004).
18. S. Y. Chou, P. R. Krauss, *Microelectronic Engineering* **35**, 237 (1997).
19. J. K. W. Yang, K. K. Berggren. (AVS, 2007), vol. 25, pp. 2025-2029.
20. R. Ruiz *et al.*, *Science* **321**, 936 (2008).
21. F. S. Bates *et al.*, *Science* **336**, 434 (2012).
22. F. S. Bates, G. H. Fredrickson, *Physics Today* **52**, 32 (1999).
23. S. Park *et al.*, *Science* **323**, 1030 (2009).
24. F. S. Bates, *Science* **251**, 898 (1991).
25. J. D. Cushen *et al.*, *ACS Nano* **6**, 3424 (2012).
26. Y. S. Jung, J. B. Chang, E. Verploegen, K. K. Berggren, C. A. Ross, *Nano Letters* **10**, 1000 (2010).
27. P. C. Heimenz, Lodge, T. P., *Polymer Chemistry, 2nd Ed.*, (CRC Press, Boca Raton, Pl, 2007).
28. E. Helfand, Z. R. Wasserman, *Macromolecules* **9**, 879 (1976).
29. Y.-L. Loo, R. A. Register, A. J. Ryan, *Macromolecules* **35**, 2365 (2002).
30. C. A. Ross *et al.*, *J. Vac. Sci. Technol., B* **26**, 2489 (2008).
31. J. Y. Cheng *et al.*, *Advanced Materials (Weinheim, Germany)* **13**, 1174 (2001).
32. I. Bita *et al.*, *Science* **321**, 939 (2008).
33. Y. S. Jung, C. A. Ross, *Nano Letters* **7**, 2046 (2007).
34. J. W. Jeong, W. I. Park, M.-J. Kim, C. A. Ross, Y. S. Jung, *Nano Letters* **11**, 4095 (2011).

35. M. D. Rodwogin, C. S. Spanjers, C. Leighton, M. A. Hillmyer, *ACS Nano* **4**, 725 (2010).
36. T. Hirai *et al.*, *Adv. Mater.* **21**, 4334 (2009).
37. C. Kloninger, D. Knecht, M. Rehahn, *Polymer* **45**, 8323 (2004).
38. S.-M. Park, O.-H. Park, J. Y. Cheng, C. T. Rettner, H.-C. Kim, *Nanotechnology* **19**, 455304/1 (2008).
39. S. Park, J.-Y. Wang, B. Kim, J. Xu, T. P. Russell, *ACS Nano* **2**, 766 (2008).
40. R. Ruiz *et al.*, *J. Vac. Sci. Technol., B: Nanotechnol. Microelectron.: Mater., Process., Meas., Phenom.* **30**, 06F202/1 (2012).
41. C. M. Hardy, F. S. Bates, M.-H. Kim, G. D. Wignall, *Macromolecules* **35**, 3189 (2002).
42. Y. Zhao, E. Sivaniah, T. Hashimoto, *Macromolecules* **41**, 9948 (2008).
43. L. Wan, X. Yang, *Langmuir* **25**, 12408 (2009).
44. H. L. Hsieh, R. P. Q., *Anionic Polymerization: Principles and Practical Applications*. (Marcel Dekker Inc., New York, 1996).
45. T. S. Bailey, H. D. Pham, F. S. Bates, *Macromolecules* **34**, 6994 (2001).
46. A. J. Meuler *et al.*, *J. Chem. Phys.* **130**, 234903/1 (2009).
47. H. Sakurai *et al.*, *Tetrahedron* **39**, 883 (1983).
48. J. R. Strahan, The University of Texas at Austin (2010).
49. I. W. Hamley, V. Castelletto, *Prog. Polym. Sci.* **29**, 909 (2004).
50. S. Zhu, W. F. Edmonds, M. A. Hillmyer, T. P. Lodge, *J. Polym. Sci., Part B: Polym. Phys.* **43**, 3685 (2005).
51. S. Ndoni, C. M. Papadakis, F. S. Bates, K. Almdal, *Review of Scientific Instruments* **66**, 1090 (1995).
52. R. P. Quirk, B. Lee, *Macromol. Chem. Phys.* **204**, 1719 (2003).
53. S. K. Varshney, Z. Gao, X. F. Zhong, A. Eisenberg, *Macromolecules* **27**, 1076 (1994).
54. J. G. Kennemur, M. A. Hillmyer, F. S. Bates, *Macromolecules* **45**, 7228 (2012).
55. M. Harada *et al.*, *J. Polym. Sci., Part B: Polym. Phys.* **43**, 1486 (2005).
56. T. P. Russell, R. P. Hjelm, Jr., P. A. Seeger, *Macromolecules* **23**, 890 (1990).
57. M. W. Matsen, *Macromolecules* **43**, 1671 (2010).
58. V. Khanna *et al.*, *Macromolecules* **39**, 9346 (2006).
59. L. J. Fetters, D. J. Lohse, D. Richter, T. A. Witten, A. Zirkel, *Macromolecules* **27**, 4639 (1994).
60. D. Uhrig, J. W. Mays, *J. Polym. Sci., Part A Polym. Chem.* **43**, 6179 (2005).
61. A. J. Meuler, M. K. Mahanthappa, M. A. Hillmyer, F. S. Bates, *Macromolecules* **40**, 760 (2007).
62. P. Chaumont, G. Beinert, J. E. Herz, P. Rempp, *Makromol. Chem.* **183**, 1181 (1982).
63. M. A. Hillmyer, F. S. Bates, *Macromolecules* **29**, 6994 (1996).
64. N. Hadjichristidis, H. Iatrou, S. Pispas, M. Pitsikalis, *Journal of Polymer Science, Part A: Polymer Chemistry* **38**, 3211 (2000).

65. G. Cao, Y. Wang, *Nanostructures and Nanomaterials: Synthesis, Properties, and Applications*. (World Scientific, 2010).
66. L. J. Hayes, *Journal of Fluorine Chemistry* **8**, 69 (1976).
67. J. N. Israelachvili, *Intermolecular and Surface Forces*. (Elsevier Science & Technology, 2011).
68. T. W. G. Solomons, C. B. Fryhle, *Organic Chemistry*. (John Wiley & Sons, Inc., Hoboken, N.J., ed. 8th, 2006).
69. C. M. Bates *et al.*, *Langmuir* **27**, 2000 (2011).
70. J. R. Strahan, The University of Texas at Austin (2010).
71. M. Strobel, C. S. Lyons, *Plasma Processes and Polymers* **8**, 8 (2011).
72. J. T. Koberstein, *Journal of Polymer Science Part B: Polymer Physics* **42**, 2942 (2004).
73. E. V. Anslyn, D. A. Dougherty, *Modern Physical Organic Chemistry*. (University Science Books, Sausalito, CA, 2006).
74. S. S. Batsanov, *Inorganic Materials* **37**, 871 (2001).
75. J. W. P. Lin, L. P. Dudek, D. Majumdar, *J. Appl. Polym. Sci.* **33**, 657 (1987).
76. E. Han *et al.*, *Macromolecules* **42**, 4896 (2009).
77. B. K. Mueller *et al.*, *Abstracts of Papers, 239th ACS National Meeting, San Francisco, CA, United States, March 21-25, 2010*, POLY (2010).
78. D. Y. Ryu *et al.*, *Macromolecules* **40**, 4296 (2007).
79. D. G. Walton, G. J. Kellogg, A. M. Mayes, P. Lambooy, T. P. Russell, *Macromolecules* **27**, 6225 (1994).
80. H.-C. Kim, S.-M. Park, W. D. Hinsberg, *Chem. Rev.* **110**, 146 (2010).
81. R. D. Peters, X. M. Yang, T. K. Kim, B. H. Sohn, P. F. Nealey, *Langmuir* **16**, 4625 (2000).
82. A. Niemz, K. Bandyopadhyay, E. Tan, K. Cha, S. M. Baker, *Langmuir* **22**, 11092 (2006).
83. P.-H. Liu, P. Thebault, P. Guenoun, J. Daillant, *Macromolecules* **42**, 9609 (2009).
84. J. N. L. Albert, T. Epps, *Materials Today* **13**, 24 (2010).
85. G. J. Kellogg *et al.*, *Physical Review Letters* **76**, 2503 (1996).
86. P. Mansky, Y. Liu, E. Huang, T. P. Russell, C. Hawker, *Science* **275**, 1458 (1997).
87. S. T. Milner, *Science (Washington, DC, United States)* **251**, 905 (1991).
88. S. Ham *et al.*, *Macromolecules* **41**, 6431 (2008).
89. D. Y. Ryu *et al.*, *Macromolecules* **42**, 4902 (2009).
90. E. Han *et al.*, *Advanced Materials* **19**, 4448 (2007).
91. D. Y. Ryu, K. Shin, E. Drockenmuller, C. J. Hawker, T. P. Russell, *Science* **308**, 236 (2005).
92. J. Bang *et al.*, *Advanced Materials* **19**, 4552 (2007).
93. J. R. Knowles, *Accounts of Chemical Research* **5**, 155 (1972).
94. R. A. Abramovitch, B. A. Davis, *Chem. Rev.* **64**, 149 (1964).
95. L. Cao *et al.*, *Advanced Functional Materials* **13**, 271 (2003).
96. J. K. Bosworth *et al.*, *ACS Nano* **2**, 1396 (2008).

97. J. Y. Cheng *et al.*, *Applied Physics Letters* **91**, 143106/1 (2007).
98. H. J. Busscher, A. W. J. van Pelt, P. de Boer, H. P. de Jong, J. Arends, *Colloids and Surfaces* **9**, 319 (1984).
99. C. W. Extrand, Y. Kumagai, *Journal of Colloid and Interface Science* **191**, 378 (1997).
100. C. N. C. Lam *et al.*, *Journal of Colloid and Interface Science* **243**, 208 (2001).
101. G. Odian, *Principles of Polymerization*. (John Wiley & Sons, Inc., Hoboken, NJ, ed. 4th, 2004).
102. F. R. Mayo, C. Walling, *Chem. Rev.* **46**, 191 (1950).
103. J. Brandrup, E. H. Immergut, E. A. Grulke, A. Abe, D. R. Bloch, Eds., *Polymer Handbook*, (John Wiley and Sons, 2005).
104. L. Wan *et al.*, *Journal of Micro/Nanolithography, MEMS, and MOEMS* **11**, 031405 (2012).
105. C. T. Black, *Applied Physics Letters* **87**, 163116 (2005).
106. B. Xin-Yu *et al.*, in *Electron Devices Meeting (IEDM), 2011 IEEE International*. (2011), pp. 7.7.1-7.7.4.
107. R. D. Peters, X. M. Yang, Q. Wang, J. J. de Pablo, P. F. Nealey, *J. Vac. Sci. Technol. B* **18**, 3530 (2000).
108. M. Somervell *et al.*, H. S. Mark, I. W. Thomas, Eds. (SPIE, 2012), vol. 8325, pp. 83250G.
109. R. A. Segalman, H. Yokoyama, E. J. Kramer, *Adv. Mater.* **13**, 1152 (2001).
110. M. P. Stoykovich *et al.*, *Science* **308**, 1442 (2005).
111. E. Han, K. O. Stuen, Y.-H. La, P. F. Nealey, P. Gopalan, *Macromolecules* **41**, 9090 (2008).
112. E. W. Edwards, M. P. Stoykovich, H. H. Solak, P. F. Nealey, *Macromolecules* **39**, 3598 (2006).
113. C. M. Bates *et al.*, *Journal of Polymer Science Part A: Polymer Chemistry* **51**, 290 (2013).
114. J. N. L. Albert *et al.*, *ACS Nano* **6**, 459 (2011).
115. M. Y. Paik *et al.*, *Macromolecules* **43**, 4253 (2010).
116. P. Mansky, T. P. Russell, C. J. Hawker, M. Pitsikalis, J. Mays, *Macromolecules* **30**, 6810 (1997).
117. V. Mishra, G. H. Fredrickson, E. J. Kramer, *ACS Nano* **6**, 2629 (2012).
118. S. Caron. (John Wiley & Sons, Inc., 2011), pp. 805-818.
119. A. J. Gordon, R. A. Ford, *The Chemist's Companion: A Handbook of Practical Data, Techniques, and References*. (John Wiley & Sons, New York, N.Y., 1972).
120. D. R. Lide, *Handbook of Organic Solvents*. (CRC Press, Boca Raton, FL, 1995).
121. S. Bank, *The Journal of Organic Chemistry* **37**, 114 (1972).
122. . (Shell Chemicals, 2007).
123. Y. S. Jung, C. A. Ross, *Advanced Materials* **21**, 2540 (2009).
124. J. Y. Cheng, C. T. Rettner, D. P. Sanders, H.-C. Kim, W. D. Hinsberg, *Adv. Mater.* **20**, 3155 (2008).

125. J. Y. Cheng, C. A. Ross, E. L. Thomas, H. I. Smith, G. J. Vancso, *Adv. Mater.* **15**, 1599 (2003).
126. A. M. Welander, P. F. Nealey, H. Cao, R. Bristol. (AVS, 2008), vol. 26, pp. 2484-2488.
127. S. Pujari, M. A. Keaton, P. M. Chaikin, R. A. Register, *Soft Matter* **8**, 5358 (2012).
128. D. Sundrani, S. B. Darling, S. J. Sibener, *Nano Letters* **4**, 273 (2004).
129. Y. S. Jung, J. H. Lee, J. Y. Lee, C. A. Ross, *Nano Letters* **10**, 3722 (2010).
130. D. E. Johnston, M. Lu, C. T. Black, *Journal of Micro/Nanolithography, MEMS, and MOEMS* **11**, 031306 (2012).
131. H. C. Kim *et al.*, *Advanced Materials* **13**, 795 (2001).
132. K. Shin *et al.*, *Nano Letters* **2**, 933 (2002).
133. T. Xu *et al.*, *Advanced Functional Materials* **13**, 698 (2003).
134. S. P. Delcambre, R. A. Riggleman, P. J. J. de, P. F. Nealey, *Soft Matter* **6**, 2475 (2010).
135. T. Tanaka, M. Morigami, N. Atoda, *Journal of the Electrochemical Society* **140**, L115 (1993).
136. M. A. Mohammad *et al.*, *Microelectronic Engineering* **87**, 1104 (2010).
137. R. A. Farrell *et al.*, *Macromolecules* **43**, 8651 (2010).
138. M. A. Lieberman, A. J. Lichtenberg, *Principles of Plasma Discharges and Materials Processing*. I. John Wiley & Sons, Ed., (Wiley-Interscience, Hoboken, New Jersey, ed. 2, 2005).
139. M. Somervell, The University of Texas at Austin (2000).
140. S.-X. Ji, C.-C. Liu, G.-L. Liu, P. F. Nealey, *ACS Nano* **4**, 599 (2010).
141. M. E. Colburn, The University of Texas at Austin (2001).
142. M. Colburn *et al.*, *J. Vac. Sci. Technol. B* **19**, 2162 (2001).
143. C.-C. Liu, P. F. Nealey, Y.-H. Ting, A. E. Wendt. (AVS, 2007), vol. 25, pp. 1963-1968.
144. B. Rathsack *et al.*, M. T. William, Ed. (SPIE, 2012), vol. 8323, pp. 83230B.
145. Y. J. Lii, J. Jorne, K. C. Cadien, J. E. Schoenholtz, Jr., *Journal of the Electrochemical Society* **137**, 3633 (1990).
146. D. L. Flamm, V. M. Donnelly, J. A. Mucha, *J. Appl. Phys.* **52**, 3633 (1981).
147. S. A. Campbell, *Fabrication Engineering at the Micro- and Nanoscale*. (Oxford University Press, New York, N.Y., ed. 3rd, 2008).
148. X. Gu *et al.*, *Advanced Materials*, n/a (2012).
149. C. M. Bates *et al.*, *Science* **338**, 775 (2012).
150. T. Seshimo *et al.*, *Journal of Photopolymer Science and Technology* **25**, 125 (2012).
151. T. P. Russell, A. Menelle, S. H. Anastasiadis, S. K. Satija, C. F. Majkrzak, *Macromolecules* **24**, 6263 (1991).
152. H.-S. Suh, H. Kang, C.-C. Liu, P. F. Nealey, K. Char, *Macromolecules* **43**, 461 (2010).
153. G. Liu *et al.*, *Physical Review Letters* **108**, 065502 (2012).

154. E. Huang *et al.*, *Macromolecules* **31**, 7641 (1998).
155. J. G. Son, X. Bulliard, H. Kang, P. F. Nealey, K. Char, *Advanced Materials* **20**, 3643 (2008).
156. Panasonic, Patent JP 2011-78978 (2011).
157. S. Kim, P. F. Nealey, F. S. Bates, *ACS Macro Letters* **1**, 11 (2012).
158. P. Mansky *et al.*, *Physical Review Letters* **79**, 237 (1997).
159. H. Yokoyama, E. J. Kramer, *Macromolecules* **31**, 7871 (1998).
160. S. Ji *et al.*, *Macromolecules* **41**, 9098 (2008).
161. J. L. Duda, *Pure Appl. Chem.* **57**, 1681 (1985).
162. P. T. Gilmore, R. Falabella, R. L. Laurence, *Macromolecules* **13**, 880 (1980).
163. T. Higuchi, L. Eberson, J. D. McRae, *J. Am. Chem. Soc.* **89**, 3001 (1966).
164. F. M. Houlihan, T. I. Wallow, O. Nalamasu, E. Reichmanis, *Macromolecules* **30**, 6517 (1997).
165. R. A. Nyquist, *Interpreting Infrared, Raman, and Nuclear Magnetic Resonance Spectra: Variables in data interpretation of infrared and Raman spectra*. (Academic Press, San Diego, CA, 2001), vol. 1.
166. R. M. Silverstein, F. X. Webster, D. J. Kiemle, Eds., *Spectrometric Identification of Organic Compounds*, (John Wiley & Sons, Hoboken, NJ, ed. 7th, 2005), 7th.
167. T. Vu, N. Mahadevapuram, G. M. Perera, G. E. Stein, *Macromolecules* **44**, 6121 (2011).
168. A. M. Welander *et al.*, *Macromolecules* **41**, 2759 (2008).
169. J. D. Cushen *et al.*, *Macromolecules* **45**, 8722 (2012).
170. M. S. Turner, *Physical Review Letters* **69**, 1788 (1992).
171. G. E. Stein, J. A. Liddle, A. L. Aquila, E. M. Gullikson, *Macromolecules* **43**, 433 (2010).
172. E. Moore, *Industrial & Engineering Chemistry Product Research and Development* **25**, 315 (1986).
173. P. F. Barron, D. J. T. Hill, J. H. O'Donnell, P. W. O'Sullivan, *Macromolecules* **17**, 1967 (1984).
174. J. M. G. Cowie, *Alternating Copolymers*. (Plenum Press, New York, N. Y., 1985).
175. B. C. Trivedi, B. M. Culbertson, *Maleic Anhydride*. (Plenum Press, New York, N. Y., 1982).
176. A. Zerroukhi, C. Cincu, J. P. Montheard, *Journal of Applied Polymer Science* **71**, 1447 (1999).
177. C. Cincu, J.-P. Montheard, *J. Appl. Polym. Sci.* **61**, 1847 (1996).
178. P. G. Brown, K. Fujimori, D. J. Tucker, *Polym. Bull.* **27**, 543 (1992).
179. M. C. Davies, J. V. Dawkins, D. J. Hourston, *Polymer* **46**, 1739 (2005).
180. T. P. Russell, G. Coulon, V. R. Deline, D. C. Miller, *Macromolecules* **22**, 4600 (1989).
181. C.-C. Liu *et al.*, *Macromolecules* **46**, 1415 (2013).
182. U. Nagpal, M. Müller, P. F. Nealey, J. J. de Pablo, *ACS Macro Letters* **1**, 418 (2012).

183. C. Bencher, *Proc. of SPIE, Alternative Lithographic Technologies III* **7970**, (2011).